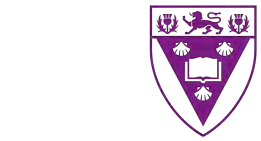

New insights on classical radio galaxies from MeerKAT and uGMRT

A thesis submitted for the degree of

DOCTOR OF PHILOSOPHY

of

RHODES UNIVERSITY

By

LEGODI POTASI PORTIA

ORCID ID
https://orcid.org/0000-0001-8242-7582

November 23, 2024

Supervisor: Prof. Oleg Smirnov
Co-Supervisor: Dr. Tiziana Venturi

Abstract

New insights on classical radio galaxies from MeerKAT and uGMRT

The morphology of low and high-power sources has been the subject of a classification method for over four decades, leading to a comprehensive understanding of extragalactic radio sources. The morphological classification of radio galaxies is again a hot topic. This project aims to revisit the current classification scheme for classical radio galaxies and investigate the properties and origin of the new filamentary features which are becoming standard within and outside the radio lobes and which are suggestive of so far unexplored interactions between the radio plasma and the external medium.

This thesis presents high-resolution and sensitivity studies of the nature of ten known radio galaxies: three FR Is (4C -03.43, 3C 403.1, 3C 198), three FR IIs (3C 105, 3C 227, 3C 445), tailed radio sources (CGCG 046-067, NGC 7503) and the FR 0s (SDSS J 09157+1331, SDSS J 1120+0407). The total sample was selected from the 4C catalogue with well-defined criteria. To this aim, we are using the μJy sensitivity offered by the combination of uGMRT and MeerKAT in a frequency range from $500 - 1712$ MHz.

The radio images present several new morphological features in the radio emission at a $\sim 4'' - 10''$ angular resolution. Our radio maps validate the morphological classification.

The sources exhibit remarkable features that raise new questions regarding the complex interaction between radio plasma emitted by host galaxies and the surrounding medium through which the jet propagates. The wealth of morphological details includes, for example, the detection of filaments in the emission from the lobes, the existence of diffuse emission beyond the hotspots, and multiple knot-like structures along the jet spine in some sources in the sample. Detailed descriptions of the overall radio structures are presented.

We derived the equipartition parameters for each source in the sample, and after fitting their integrated spectrum, we estimated their global radiative ages. We find a broad range of radiative ages, i.e. $40.19 - 242.85$ Myr.

We derived in-band spectral index imaging for a few radio galaxies in the sample. This allowed us to make some preliminary considerations on the origin of the various

radio features.

Contents

List of Figures

List of Tables

Acknowledgements

These three years of research have been an experience that allowed me to grow personally and professionally. The path to the end of this research has been an adventure. I could not have reached this end without the people who made it possible.

First, many thanks to my incredible supervisor, Prof. Oleg Smirnov. Without the valuable input and guidance, this research would not have concluded. Most importantly, Dr. Tiziana Venturi for always being present and available and pushing me when I needed a push.

My quest has been to learn and be acquainted with the science and its interpretation towards radio galaxies. By so saying, my sincere thank you goes to Dr. Bernie Fanaroff and Dr. Dharam Vir Lal for taking your precious time to assist in this research, teaching and answering all questions with great patience.

I have also benefited greatly from working with the Radio Astronomy Techniques and Technologies postgraduate students, and I thank them for their assistance whenever I call on them.

Finally, I thank my family for their love; this work would not have been possible without your support.

My gratitude goes to you all.

Abbreviations

AGN	Active Galactic Nuclei
ASKAP	Australian Square Kilometre Array Pathfinder
BLRGs	Broad Line Radio Galaxies
CASA	Common Astronomy Software Applications
CHPC	South African Centre for High Performance Computing
CMB	Cosmic Microwave Background
DD	Direction Dependent (Telescope or atmospheric effects)
DDRGs	Double Double Radio Galaxies
DI	Direction Independent (Telescope or atmospheric effects)
DSS-II	Digitized Sky Survey II
EMU	Evolutionary Map of the Universe
FAST	Five hundred metre Aperture Spherical Telescope
FR 0	Fanaroff Riley Class 0
FR I	Fanaroff Riley Class I
FR II	Fanaroff Riley Class II
GBT	Green Bank Telescope
GRGs	Giant radio galaxies
HERGs	High Excitation Radio Galaxies
HST	Hubble Space Telescope
HYMORS	HYbrid MOrphology Radio Sources
ICM	Intracluster medium
IGM	Intergalactic Medium
LERGs	Low Excitation Radio Galaxies
LOFAR	Low Frequency Array
LoTSS	LOFAR Two-metre Sky Survey
MIGHTEE	MeerKAT International GigaHertz Tiered Extragalactic Exploration
MeerKAT	Meer Karoo Antenna Telescope
NAT	Narrow-angle tail
NED	NASA Extragalactic Database
NLRG	Narrow Line Radio Galaxies
NRAO	National Radio Astronomical Observatories
NVSS	NRAO VLA Sky Survey
PSF	Point Spread Function
RFI	Radio Frequency Interference

RLAGN	Radio Loud Active Galactic Nuclei
RIME	Radio Interferometry Measurement Equation
RMS	Root Mean Square
SDSS	Sloan Digital Sky Survey
SMBH	Supermassive black hole
TDRGs	Triple-double radio galaxies
uGMRT	upgraded Giant Metrewave Radio Telescope
WAT	Wide-angle tail

Chapter 1

Introduction

Since the first discovery of a signal that proved to be from the Milky Way [Jansky, 1933], radio observational techniques have evolved dramatically. These advancements provided means to probe both the local and distant universe, becoming crucial tools for understanding the physics governing radio-emitting regions in large-scale structures.

The development of radio interferometry (see Chapter 2) and its applications (see Chapter 3) led to the discovery and study of countless extragalactic sources whose emission is synchrotron in origin (Section 1.1), thereby uncovering the nature of these powerful radio sources. It also led to the discovery of hotspots (Section 1.2) and the systematic cataloguing of radio sources, such as the 3C and 4C surveys.

These studies revealed well-defined structures in powerful extragalactic objects (Figures 1.4 and 1.3), leading to their morphological classification by Fanaroff and Riley [1974] based on images obtained by the 1970s Cambridge interferometer operating at 178 MHz, 408 MHz, and 5 GHz. Fanaroff and Riley [1974] introduced a clear separation into high and low-power radio sources (FR II and FR I, respectively) based on apparent morphological differences (Section 1.3). This morphological classification has laid the foundation for the study and comprehensive understanding of extragalactic radio sources over the past decades. However, our knowledge of these radio sources, including the physics of radio plasma propagation in the intergalactic medium, still needs to be completed.

Against this backdrop, our study aims to construct high-resolution and high-sensitivity (total intensity and spectral index maps) observations of these radio sources. By exploring the unprecedented sensitivity of a few μJybeam^{-1} at resolutions of a few arcseconds, we hope to uncover new features that necessitate revising our current classification scheme for classical radio galaxies.

This chapter provides the background and introduction to the present study. Key highlights include the origin of radio emission in radio galaxies, an overview of their components, a discussion of their morphology, and the scientific grounds for conducting this study.

1.1 Synchrotron radiation

The radio emission detected from extragalactic radio sources, such as star-forming and AGN-dominated galaxies in 1.4GHz radio surveys, is primarily due to synchrotron radiation. The synchrotron radiation is generally generated by charged particles spiralling within a magnetic field at a relativistic speed governed by the Lorentz force. This mechanism is also responsible for the radio emission observed from our galaxy, supernova remnants (e.g., Crab Nebula) and cluster halos.

For a particle with a charge q, rest mass m, and Lorentz factor

$$\gamma = \frac{1}{\sqrt{1 - \frac{v^2}{c^2}}}, \tag{1.1}$$

traveling through a static and uniform magnetic field $\vec{B}$, the force experienced by the particle can be described by

$$\frac{d}{dt}(\gamma m_o \vec{v}) = q(\vec{v} \times \vec{B}), \tag{1.2}$$

where c represents the speed of light in a vacuum.

Since the force described in equation 1.2 is perpendicular to the magnetic field and in the same direction as the centripetal acceleration, both the velocity (v) and Lorentz factor (γ) remain constant. Additionally, the particle is constrained to move in a circular or helical trajectory around the magnetic field lines, leading to the emission of a specific frequency known as gyrofrequency

$$\nu_g = \frac{qB}{2\pi\gamma mc}, \tag{1.3}$$

indicative of the circular motion's rate.
The energy emitted due to this motion can be quantified by

$$W = \frac{2}{3}\frac{q^4}{m^2c^3}\gamma^2 B^2. \tag{1.4}$$

In astrophysical events, the radiation from a single particle provides a foundational understanding of synchrotron radiation; however, the radiation we observe encompasses a more complex scenario that involves a population of relativistic particles. Synchrotron emission is a common phenomenon observed in AGNs, which are highly energetic. We make a generic assumption that the radiation follows a simple power-law relation

$$S_\nu = \nu^{-\alpha}, \tag{1.5}$$

where S_ν is the observed flux density in units of Jansky (Jy)[1], ν is the frequency measured in Hertz (Hz) and α is the spectral index. Consider an energy distribution for electrons

$$N\epsilon\, d\epsilon = N_0 \epsilon^{-\delta} d\epsilon \tag{1.6}$$

[1]The flux density unit, Jansky, is equivalent to 10^{-23}erg cm^{-2}sr^{-1}Hz^{-1}.

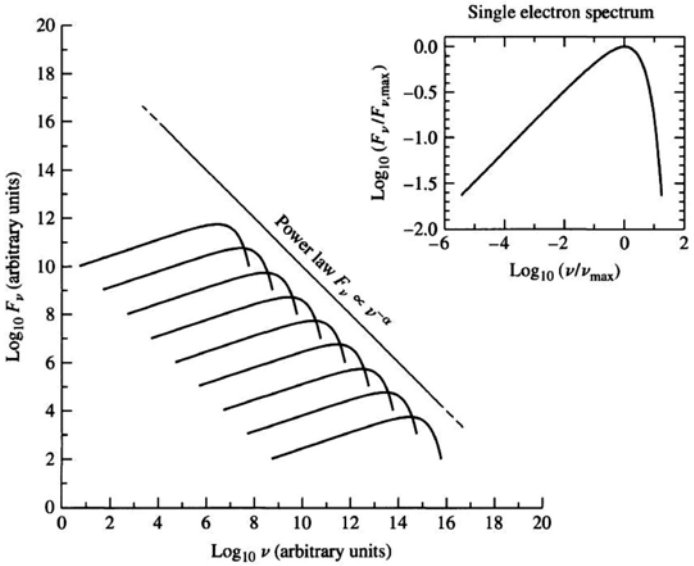

Figure 1.1: Power law spectrum of synchrotron radiation in terms of flux density and frequency $S_\nu \propto \nu^{-\alpha}$. The synchrotron spectrum of a single electron is shown separately in the top panel.

where $\epsilon = \gamma mc^2$ represents the energy of a moving particle and N_0 is the number density of the particle. A pure power-law spectrum is a clear signature of synchrotron radiation. Assuming that all particles emit radiation at a specific frequency v, the monochromatic power per unit volume per unit frequency per unit time is

$$\frac{dW_s(\nu\epsilon)}{dt} N(\epsilon) \frac{d\epsilon}{d\nu} \approx N_0 \vec{B}^{\frac{\delta+1}{2}} \nu^{-\frac{\delta-1}{2}} = N_0 \vec{B}^{\frac{\delta+1}{2}} \nu^{-\alpha} \tag{1.7}$$

where δ is the slope of the power-law distribution of energy radiated by electrons related to the spectral index, i.e., $\alpha = \frac{\delta-1}{2}$. Figure 1.1 shows a typical synchrotron spectrum interpreted as the superposition of the various contributions of each single electron emitting at its specific frequency. The spectrum may deviate from a single power law with equation 1.5 at both high and low frequencies. Notably, the spectrum steepens at higher frequencies due to the radiative losses that are more significant at high electron energies (see Chapter 5). Synchrotron radiation is also polarized, and its strength is the most effective way to measure the magnetic field values of a radio source.

Moreover, the spectral index α of extragalactic radio sources typically ranges from 0 to -2, with a median spectral index of $\sim$ -0.7 to -0.8, corresponds to an exponent value $\delta \sim 2.4$; this applies to higher frequencies where synchrotron self-absorption is insignificant.

1.2 Radio Loud AGNs

Radio galaxies are the greatest manifestation of supermassive black holes (SMBHs). They bear information on the astrophysics at play in the inner regions of active galac-

tic nuclei, where the energy is extracted, and on the mechanisms transporting the relativistic plasma out to distances which can cover up to Mpc scales. Moreover, the interaction of the radio emission and the surrounding medium (interstellar or intergalactic, depending on the scale under consideration) is a fundamental ingredient in the formation and evolution of large structures (i.e. properties of their nuclear component and the thermal gas in the groups and clusters in which these objects reside [Fabian, 2012]). Although the radio galaxies exhibit significant differences in their physical scales and origins, they all share a common source of radio wave emission fueled by synchrotron radiation. Radio Loud AGNs comprise a small fraction of the known AGN population [Dermer and Giebels, 2016], extending from pc to Mpc scales, constituting among the largest known physical structures in the universe.

A complete system of a radio galaxy consists of an SMBH at the centre of the galaxy, jets and lobes; comparatively powerful jets give rise to different morphological classifications (see below).

- **Core** – the core serves as a main origin of non-thermal radio emission in radio galaxies. These compact cores are typically located at the same position as the optical host of a radio galaxy, frequently remaining unresolved on arcsecond scales. Furthermore, they exhibit a flat spectrum and are most effectively detected at GHz frequencies.

- **Jets** are collimated outflows of plasma carrying a long stream of material from the core outwards in opposite directions. They are often observed as symmetrical and may reach far beyond the host galaxy (extending from kpc to Mpc scale). The decelerating end of the jet inflates in the extragalactic medium or large lobes of material Longair [2011]. Typically, they have a flatter spectrum than the surrounding lobe material (-0.5 $< \alpha <$ -1.0). In most cases, jets frequently contain compact, bright radio feature structures interpreted as 'knots' embedded deep in the radio lobes, believed to indicate an internal disruption in radio jets [Hardcastle et al., 2007a]. These knots can be observed as non-terminal spots along the spine of the jet, appearing in extended emission at both radio and X-ray wavelengths. They are often associated with particle acceleration in strong shocks within the outflow, whereby these shocks may be caused by the recollimation of the jet by the surrounding medium, inhomogeneities introduced by the central engine activity, or instabilities in the outflow. Other theories explaining knot formation in jets include non-uniform Doppler boosting and sudden large-scale expansions in the outflow [Bridle and Perley, 1984].

- **Radio lobes** are one of the most common large-scale extended structures in a typical radio source. Extending on either side of the AGN with filamentary substructures (e.g. Leahy et al. [1997]). The lobe spectral index depends on the radiative age of the source and the observing frequency, ranging from -1.0 $< \alpha <$ -0.7 [Schoenmakers et al., 2000]. They exhibit morphological features such as plumes, tails, bridges and wings. The origin of the lobes in powerful and less powerful radio galaxies is different. For the former, it is backflow emission from the hotspots while they advance in the intergalactic medium. Lobes in radio

galaxies with prominent jets and no hotspots (FR I) are fainter than those formed by the flaring of the jets.

  - **Plumes** are described as peculiar lobe structures, extended regions with a low luminosity that disperses away from the whole source. The diffuse linear region is mostly associated with FR I radio galaxies probably representing outflow, and therefore, difficult to separate from jets.
  - **Tails** are structures formed due to deflected plasma interacting with the external medium. They are similar to plumes but are substantially curved away from the original outflow axis, leading to a non-linear source structure.
  - **Bridges** occur in the inner lobes region of the radio galaxies. They are low surface brightness regions of radio sources, particularly in FR IIs.
  - **Wings** are parts of lobes in FR II that are curved significantly away from the axis of the source.

- **Hotspots** are features that arise from the interaction between jets and the surrounding medium in extragalactic radio sources, a concept first introduced by [Blandford and Rees, 1974]. These regions show enhanced brightness near the edges of radio lobes, representing areas where a significant portion of jet energy is transformed into accelerating relativistic particles that fuel the radio lobes. While typically composed of single particles and spanning a few hundred parsecs in size, hotspots display a wide variety of complex shapes, challenging a simple classification as regions solely driven by shocks for particle acceleration. Their power law spectrum is generally flat, with values around $-0.5 - -0.6$, and rarely steeper. In cases like Cygnus A [Carilli et al., 1998], a pair of hotspots can be observed within a single lobe. High-resolution imaging techniques have enabled the identification of multiple components within highly luminous radio source hotspots, referred to as complex structures or multiple hotspots [Laing, 2005, Leahy et al., 1997]. The presence of multiple hotspots may indicate jet movement or precession [Cox et al., 1991]. Laing and Bridle [2012] has classified hotspot regions into primary (compact) and secondary (more diffuse) categories, associating the former with jet termination point (either original or current). The diverse structures of hotspots have spurred the development of various models to explain their origin, considering the subjective nature of morphology and resolution limitations.

  For instance, the dentist drill model, as described by Scheuer et al. [1982], illustrates how the jet can alter its direction through precession or abrupt changes in orientation on timescales shorter than required for the initial hotspot to fade [Ekers et al., 1978]. Additionally, the splatter spot-splitting model suggests that a secondary hotspot forms due to the continuous supersonic outflow from the primary hotspot, potentially deflected obliquely by the lobe boundary, creating a contact discontinuity between the jet plasma and the surrounding medium [Williams, 1985]. The dentist drill and the splatter spot splitting models propose a jet structure terminating in a concentrated "primary" hotspot, accompanied by a more diffuse "secondary" hotspot. Horton et al. [2023] explored the additional mechanisms for multiple hotspot formation in radio galaxies, including Chevron

splitting, which generates Chevron-shaped hotspot regions or complexes at the base of the disrupted jet. Chevron splitting is characterised by the emergence of transient hotspots from a larger, dynamic structure, resulting in a series of shocks rather than one or more terminal hotspots. Alternatively, the stream-splitting model bifurcates the jet into two stable, enduring flows, potentially entraining material and splitting the jet's path. In this model, both hotspots are active termination points. The hotspot splitting model elucidates a process in which a terminal hotspot is divided into two segments through hydrodynamic forces, resulting in "passive" and "active" components (i.e., the secondary and primary hotspots, respectively). The active hotspot signifies the termination point of the jet, characterised by ongoing shocks pushed back towards the core. This process commonly occurs in slowly precessing jets, resulting in a noticeable differentiation between the two components as time progresses.

1.3 The Morphological Classification

Fanaroff and Riley [1974] introduced a clear division of large-scale radio sources into two main classes, namely, the high-power Fanaroff and Riley type II (FR II) and low-power type I (FR I). The two classes are morphologically distinct, famously known as the core-brightened FR I and edge-brightened FR II radio galaxies. The pivotal publication of the classical morphological classification [Fanaroff and Riley, 1974] has been a foundational framework for extragalactic radio source studies. Widely adopted and applied in numerous catalogues throughout the years, the citation record, surpassing 2000 references, attests to its profound significance in shaping our understanding of these extragalactic radio sources.

Fanaroff and Riley [1974] discovered that the transition of FR morphology occurs at a radio power of $P_{178\ \mathrm{MHz}} \sim 10^{25}$ W Hz^{-1} sr^{-1} (at 178 MHz frequency). Over the decades, several attempts have been made to understand the remarkable morphology of FR I and FR II radio sources. Different models have been proposed to explain the morphology, with some attribution to the jet power and environmental conditions in which the radio source propagates and others to the fundamental central engine (AGN) parameters [Gopal-Krishna and Wiita, 2000]. The jet deceleration paradigm explains the appearance of the FR I and FR II jets; jets are thought to start supersonically and slow down to a subsonic flow due to the entertainment of the plasma in the host galaxy leading to different morphology [Bicknell, 1984, Kaiser and Best, 2007]. Rees et al. [1982] proposed that properties of the central black hole, such as its spin and the accretion of matter, play a role in determining the morphology of the radio sources.

An exciting discovery was made by Ledlow and Owen [1996], that the division between the FR I and FR II morphology strongly correlates with the optical luminosity of the host galaxy (see Figure 1.2 Owen and Ledlow [1994]).

Advancing on this, Mingo et al. [2019] reaffirmed this discovery, expanding on the understanding of classification through the LOFAR Two-metre Sky Survey (LoTSS) observation of a low luminosity FR II population, challenging the dependent use of

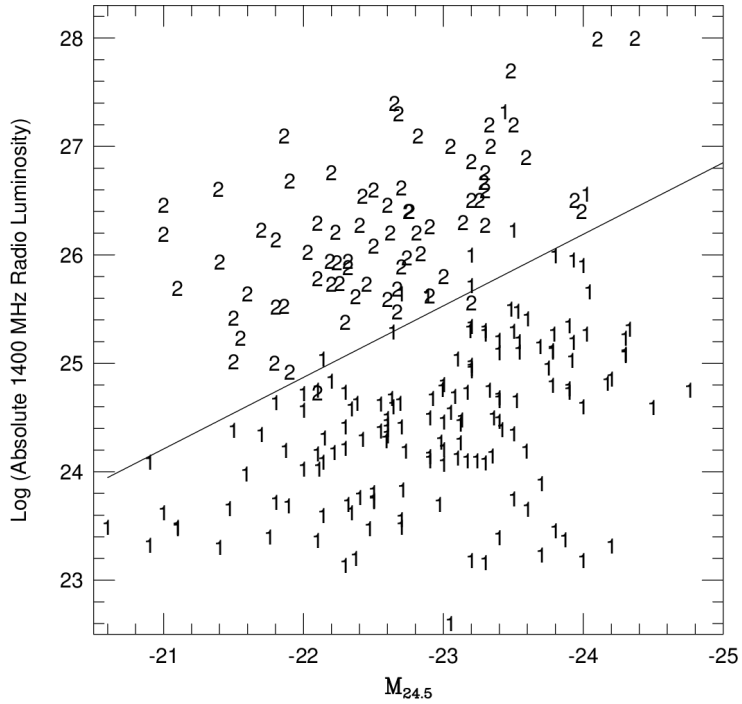

Figure 1.2: The radio luminosity vs the host optical magnitude plane reproduced from Ledlow and Owen [1996]. The y axis represents the radio luminosity in W Hz^{-1}, and the x axis represents the R-band absolute magnitude. Numbers 1 and 2 indicate the FR I and FR II classes respectively.

luminosity as the sole predictor of morphology. The study revealed complexities, including ambiguous cases and hybrid radio sources that display characteristics of both FR I and FR II categories, blurring the once clear-cut boundary between the two categories [Gopal-Krishna et al., 2023]. More complex morphologies have been introduced in previous studies, including types such as wide or narrow-angle tail sources (WATs or NATs respectively); e.g., [Owen and Rudnick, 1976], S/Z-shaped sources [Florido et al., 1990], X-shaped sources [Leahy and Williams, 1984] and others, such as double-double sources that consist of two pairs of lobes with a common centre [Schoenmakers et al., 2000]. These complexities challenge the classical standard of FR classification to modern radio observation of extragalactic source populations, prompting a revisit of its limitations, thanks to the advancement of interferometers that make it possible by revealing new features in radio emission. Rudnick [2021] recently pointed out the need to revise the approach to the classification of radio galaxies to account for the increasing complexity and the often ambiguous and conflicting terminology used. A new scheme was proposed whereby radio galaxies are not classified following sharp categories (i.e., FR I, FR II, compact, wide-angle and narrow-angle tail and so on), but are rather given "descriptors" labelled #tags. Finally, a newly identified classification, Fanaroff-Riley (FR) type 0, describes compact radio sources lacking significantly extended emissions on kiloparsec scales, setting them apart from conventional FR classifications [Baldi et al., 2019].

1.3.1 FR II

FR II are edge-brightened radio sources emitting radio power above 10^{25} W Hz^{-1} at 178 MHz. These sources are commonly referred to as "classical doubles" due to their distinct characteristics: a compact core optically linked to the nucleus of the optical host galaxy or quasar positioned amidst emission lobes fed by the backflow from the hotspots. The surface brightness of the source peaks at these hotspots located at the ends of its emission (see Figure 1.3.) The nuclear activity of the optical host usually shows high excitation emission lines. The jets of these sources are interpreted as a focused supersonic outflow of radio plasma consisting of relativistic particles originating near the central engine. An interesting observation is the presence of symmetrical lobes on both sides of the AGN, with typically only one visible jet, possibly explained by the relativistic beaming mechanism (i.e., if the jet plasma travels at relativistic speeds, the flux density of the jet facing the observer is significantly amplified compared to the counter jet moving away from the observer, leading to substantial asymmetries).

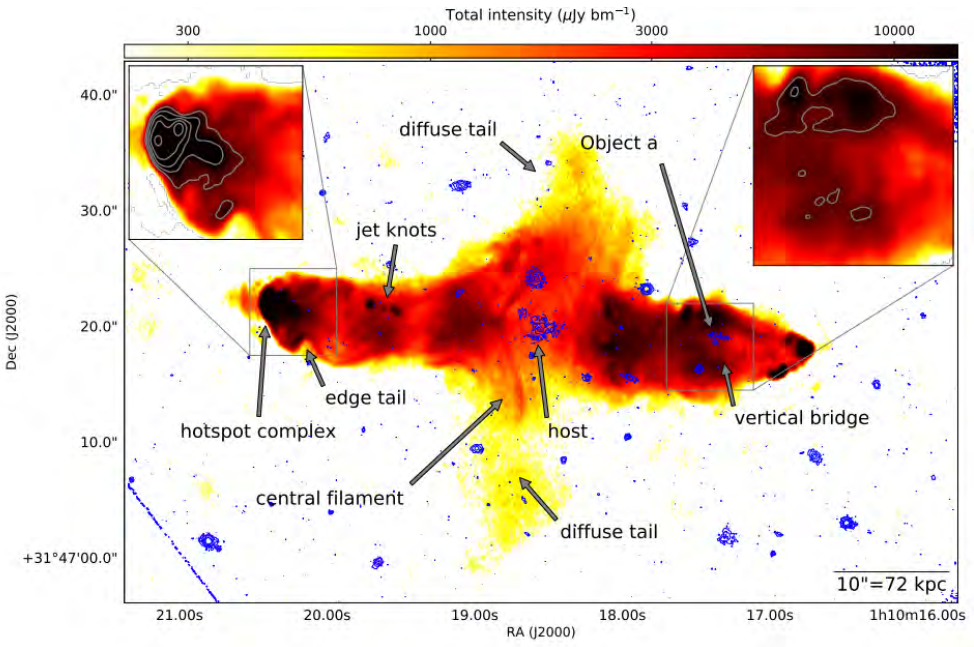

Figure 1.3: The LOFAR 144MHz image of the source 3C 34 at $\sim 0.3''$, with optical HST contour (blue) and the F785LP filter (λ =8620 Å). The insets show zoomed-in regions of the eastern hotspot complex and the limb brightening overlaid with the LOFAR contours (grey), describing the 50σ multiplied by 2 to the power of the numerals 1-10 chosen to highlight the compact structures [Mahatma et al., 2023]. 3C 34 is a typical detailed illustration of an FR II radio source with multiple components in both lobes.

FR II galaxies are typically found in less populated environments [Hardcastle, 2005]. However, there is a notable exception in the case of Cygnus A, a representative example of the FR II class located within a galaxy group. The distribution of FR II radio galaxies in the universe extends to significantly higher redshifts compared to FR I radio

galaxies, a trend likely influenced by biases in the radio interferometers used in radio surveys [Hardcastle, 2005].

1.3.2 FR I

Contrary to the FR II class of radio galaxies, these classical radio sources are of lower radio power compared to FR II ($P_{178\ \mathrm{MHz}} \lesssim 10^{25}$ W Hz^{-1}) at 178 MHz. However, possess richer, more complex and abundant structures. Twin symmetric jet morphologies, diffuse plumes, and peak emissions close to the central core characterize the radio sources. The surface brightness of these emissions decreases and loses coherence with distance, leading to a widening and dimming effect. This morphology is initially thought to be driven by jets with highly relativistic bulk speeds that decelerate over kpc scales [Bicknell, 1984, Komissarov and Falle, 1998]. FR I sources are frequently associated with giant elliptical galaxies situated within dense environments of galaxy clusters or groups. This environmental context plays a key role in shaping the distinct morphology of FR I radio galaxies, particularly influencing their jet dynamics and the diffuse tail-like structures that emerge due to interactions with the intergalactic medium (IGM).

Observational studies further elucidated the nature of FR I radio galaxies, revealing the presence of complex filamentary structures within their jets and tails and detailing their spectral behaviour across different wavelengths. Notably, the jets disruptions or knots-like structures near the core, akin to the hotspots found in FR II galaxies, albeit manifesting differently due to the intrinsic properties of the jets and their interaction with the surrounding environment [Kumari and Pal, 2022]. The distribution and intensity of radio emissions in FR I source, as exemplified by observations of specific galaxies, e.g., 3C 31 Figure 1.4, highlights the significant influence of both the jets' intrinsic properties and environmental conditions on their morphology. In 3C 31, the jets extend outward until reaching a bright flaring point, beyond which they expand and become less intense, indicative of a transition from laminar to turbulent flow. This observed behaviour reflects the complex dynamics at play, including the impact of dense intergalactic gas on the deceleration of jet material and the progressive dimming of radio emissions as they propagate from the nucleus.

In addition to the two broad classes, some galaxies also show more complex morphology. For instance, suppose the angle between the jet is significantly less than 180°. In this case, it can be classified as a bent-tail galaxy further categorized as narrow-angle tail (NAT) and wide-angle tail (WAT) based on the opening angle between the jets [Owen and Rudnick, 1976]. The phenomenon is attributed to large ram pressure exerted on the radio jet as a result of the motion of the galaxy or a turbulent movement of the IGM during a merger; these factors can result in their unique morphologies [Miley et al., 1972, Burns, 1990].

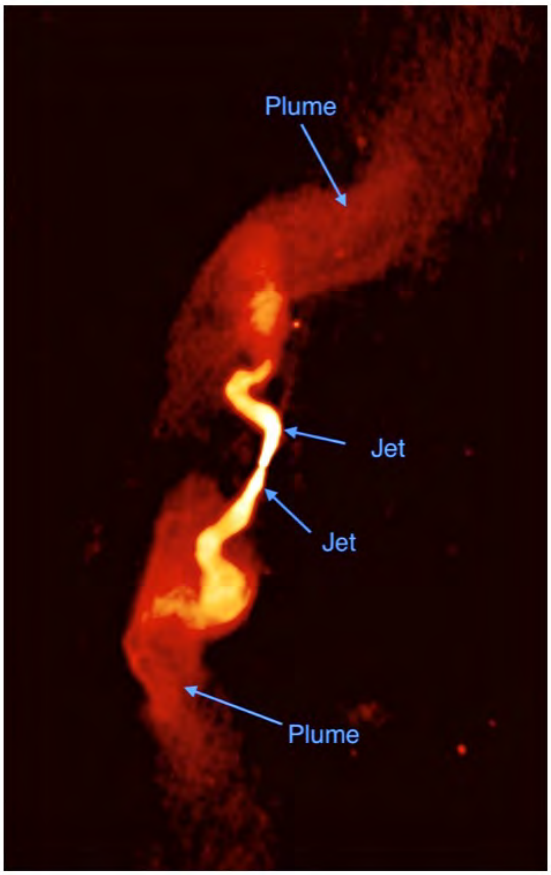

Figure 1.4: The VLA (Very Large Array) radio map of an FR I type radio source 3C 31, with a compact core with weak jets. Credit NRAO/AUI. The observation of this source can be obtained from [Laing et al., 2008]

1.3.3 Tailed radio galaxies

A subclass of FR I morphology type characterized by radio jets bent in a common direction, thus resembling tails generally recognized with a 'V' or 'C' shape of the bent tails [Owen and Rudnick, 1976, Saikia, 2022, Pal and Kumari, 2023]. Tailed radio galaxies are classified into two categories based on their degree of bending or the opening angle between the Jets. The larger opening angle is named the wide-angle tail (WAT), while the small opening is labelled NAT, primarily found in galaxy clusters and serves as a tracer of the latter [Giacintucci and Venturi, 2009].

The radio jets of these radio galaxies are exposed to a combination of effects, contributing to their peculiarity and morphology, such as the motion of the host galaxy through the intracluster medium [Owen and Rudnick, 1976], cluster weather [Burns, 1998], turbulence, shocks in the (ICM) [Nolting et al., 2019], and other dynamical systems related to the formation or cluster-cluster mergers [Pal and Kumari, 2023]. As such, NATs are believed to be formed by ram pressure due to the motion of the host galaxy through the intracluster medium (ICM), while WAT is thought to be formed by cluster weather [Klamer et al., 2004].

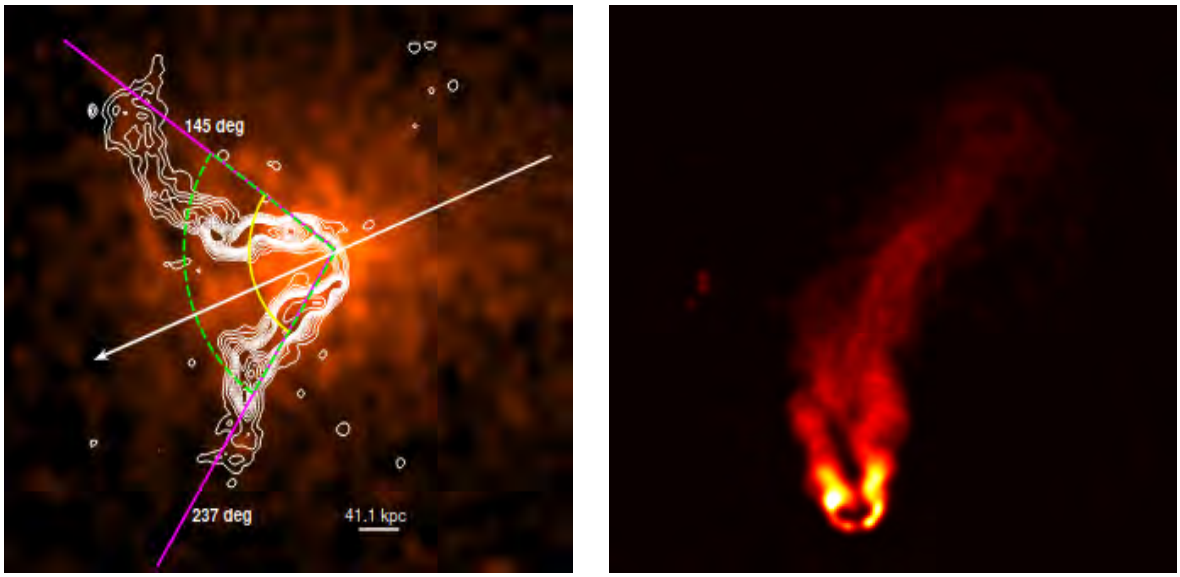

Figure 1.5: Illustration of the tailed radio galaxies; WAT 1233+168 (left) located in a merging cluster A1569 [O'Dea and Baum, 2023], the arrow indicates the angle bisecting the two tails of the WAT, the image shows the angles between jets configuration. The NAT source is NGC 1265 (right) [Ryle and Windram, 1968, O'Dea and Owen, 1986].

A typical example of a NAT radio source is shown in Figure 1.5 (right) NGC 1265 located in Perseus cluster [Gendron-Marsolais et al., 2021], which shows evidence of bending tails in the same direction likely due to the ram pressure from the ICM [Jones and Owen, 1979]. Furthermore, Figure 1.5 (left) illustrates a clear example of a wide-angle tail WAT 1233+168 located in a merging cluster A1569 [O'Dea and Baum, 2023], indicating a large angle of separation between two tails of the WAT.

1.3.4 Compact radio sources

Among the variety of observed morphologies of radio sources in the local universe, the most common one is the presence of a single compact emitting region [Baldi and Capetti, 2008]. The radio sources are associated with low redshift galaxies Heckman and Best [2014] are compact and located in massive red early-type galaxies ($-21 <$ $m_r < -23$) with high massive SMBH masses ($\sim 10^7 - 10^9 M_\odot$) [Giovannini et al., 2023].

A recently identified group of compact radio galaxies with low power, FR 0, has been brought to light [Baldi et al., 2015]. These compact radio sources do not possess extended radio lobes but instead display core characteristics akin to those of FR I (see Figure B.4) [Baldi et al., 2019]. FR 0s are defined differently and could be regarded as FR Is without the extended emission [Miraghaei and Best, 2017].

The understanding of the evolution of FR 0 has significantly improved, with high-resolution observations using Very Long Baseline Interferometry (VLBI) revealing a symmetrical yet intricate structure in FR 0 sources, exhibiting two-sided jets that ex-

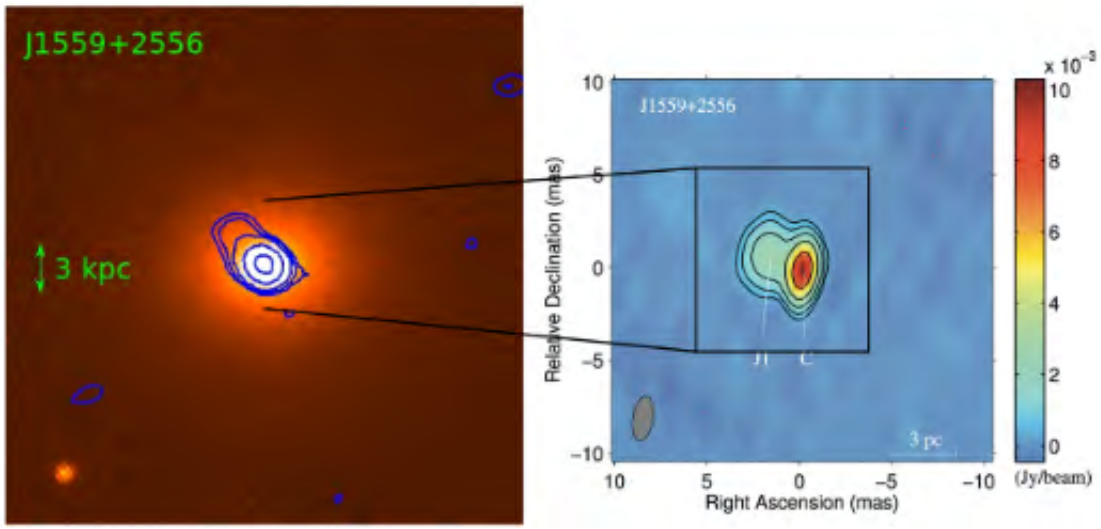

Figure 1.6: Example of an FR 0 radio source.The left panel exhibits an image captured from the r-band of the Sloan Digital Sky Survey (SDSS), which hosts the FR 0. The image is complemented by the VLA 4.5 GHz radio contours and is scaled to a distance of 3 kpc [Baldi et al., 2019]. The right panels depict a region of the radio core at a higher resolution, offering a closer view of the object at a scale of 3 parsecs. Courtesy of Baldi [2023].

tend from their cores, suggesting that the radio emission in FR 0 results from the ejection of material in opposite directions from the core [Giovannini et al., 2023].

Regarding classification, compact radio sources are not exclusive to FR 0s. When observed at small angles relative to the line of sight, these sources often exhibit significant variability due to Doppler boosting effects and frequently showcase superluminal motions. These compact radio sources can appear as either low-power or high-power radio galaxies and represent the beamed population of FR I and FR II, respectively [Blandford and Znajek, 1977].

On a different note, Fanti et al. [1995] studied compact sources with steep spectra. These sources, known as compact steep spectrum sources, generally have high to intermediate-power ranges and are not subjected to orientation effects. They are currently believed to be young radio sources and are considered the progenitors of FR Is and FR IIs.

1.3.5 HERGs and LERGs

In addition to morphological classification, radio galaxies are classified into two broad categories based on the relative intensity of high and low excitation lines in the optical spectra of their host galaxies [Laing et al., 2008, Hine and Longair, 1979]: High Excitation Radio Galaxies (HERGs) and Low Excitation Radio Galaxies (LERGs). Almost all FR I-type sources have low excitation, with a small number of low-luminosity FR II,

whilst many FR II have high excitation emission lines and a small population of high-luminosity FR I [Hardcastle et al., 2007a]. This classification is based on the existence or lack of [OIII] emission lines that provide insights regarding the galaxy's active and ionisation processes. HERGs are recognisable by strong, high-ionisation emission lines in their optical spectra that are thought to represent a classical image of an optically thick and radiatively efficient AGN [Shakura and Sunyaev, 1973]. Figure 1.7 shows a schematic representation of two types of radio sources: HERGs (left panel) and LERGs (right panel).

Furthermore, HERGs are commonly referred to as radiative or quasar mode AGN. The high radiative luminosities are fueled by a substantial supply of cold gas for accretion, resulting in strong emission across all wavelengths and an accretion rate of 1% - 10% Eddington luminosity. The Eddington rate represents the maximum rate at which a black hole (BH) can accrete matter.

On the contrary, LERGs contain fewer to non-existent emission lines in their optical spectra, indicating a relatively quiescent state in their centre region compared to high-excitation galaxy populations. LERGs' accretion rate is below 1% of the Eddington rate. Subsequently, it was found that LERGs have a radiatively inefficient accretion flow [Narayan and Yi, 1994], also known as jet mode AGNs. The fuelling mechanisms of both HERGs and LERGs are thought to be fundamentally different, and the difference in their fueling accretion modes results in a bimodal distribution in AGN accretion rates [Best, 2004]. The HERG and LERG populations reside in galaxies with different host properties.

HERGs dominate luminosities at $L_{1.4\ \mathrm{GHz}} \sim 10^{26}\ \mathrm{WHz}^{-1}$, with a preference for FR II sources [Best and Heckman, 2012], and are hosted by less massive galaxies with young stellar populations in sparser environments. LERGs are hosted by massive galaxies located in the centre of a group or cluster with older stars. Both populations exhibit varied levels of cosmic evolution at various luminosities, with HERGs exhibiting rapid cosmic evolution and LERGs exhibiting little or no redshift evolution [Best, 2004].

Recent studies of deep radio surveys have significantly altered our understanding of the relation between morphological classes, HERGs, LERGs and the features of the host galaxies, discovering subtle and captivating connections (e.g. Mingo et al. [2019], Mingo et al. [2022]). Miraghaei and Best [2017] identified and distinguished parameters that impact radio morphology from those that affect spectrum characteristics. For example, the enriched environment of FR I LERGs and their high mass density hosts support Fannaroff and Riley's classification driven by external variables such as jet disruption, indicating a relation between jet power and environmental density.

Most conclusions from radio galaxies' studies indicate that the Fanaroff-Riley morphologies overlap across all luminosities and accretion modes (e.g., Gendre et al. [2013], Mingo et al. [2019], Mingo et al. [2022]). In particular, lower luminosity LERGs can exhibit both FR I and FR II morphologies. The compelling findings presented by Mingo et al. [2022] regarding the luminous FR II LERGs show no systematic disparities in

the large-scale radio structure compared to FR II HERGs, suggesting that accretion mode does not significantly influence the large-scale morphology of these sources. The existence of low-luminosity FR II sources, also known as FR II-low [Best, 2009, Miraghaei and Best, 2017, Capetti et al., 2017], further implies that jet power is not the sole determinant of radio morphology, aligning with the conclusions drawn in Mingo et al. [2019]. A closer look at LERGs (both FR I and FR II) within the same luminosity range reveals that the likelihood of a low-power jet transitioning into either FR I or FR II depends on the host galaxy's stellar mass (e.g., Perucho et al. [2014]). This supports the notion that the surrounding environment plays a key role in jet formation within FR I radio galaxies [Bicknell et al., 1994, Laing and Bridle, 2002, 2014].

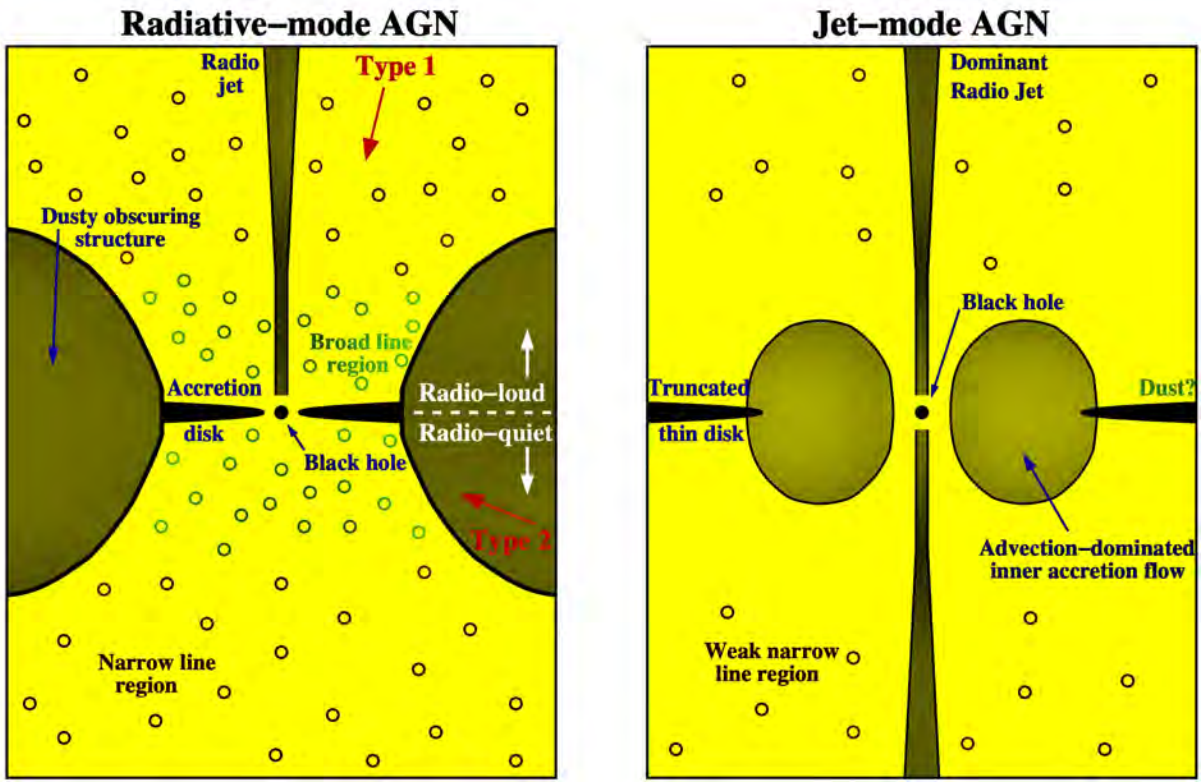

Figure 1.7: A schematic diagram of the distinction between HERGS (left panel) and LERGS (right panel) [Heckman and Best, 2014].

1.3.6 Hybrid radio galaxies

Hybrid radio sources exhibit FR I structure and FR II-like morphology on the opposite side, blurring the distinction of the morphological classification. This behaviour is believed to be influenced by a combination of jet power and environmental density on minor scales [Bicknell, 1995, Ledlow and Owen, 1996, Mingo et al., 2019]. Hercules A (Figure 1.8) is an illustrative example of this ambiguity. The radio source shows unusual features, i.e., the standard characteristic of FR II type jets diffusing into lobes. It lacks the presence of hotspots or a weak plume lobe FR I feature, which adds to the

complexity of its classification, resembling both types [Sadun and Morrison, 2002]. Perucho et al. [2023] suggests that Hercules A's observed morphology could result from a disrupted outflow of relativistic hot plasma, leading to the formation of hot lobes that expand isotropically against a decreasing intergalactic medium pressure.

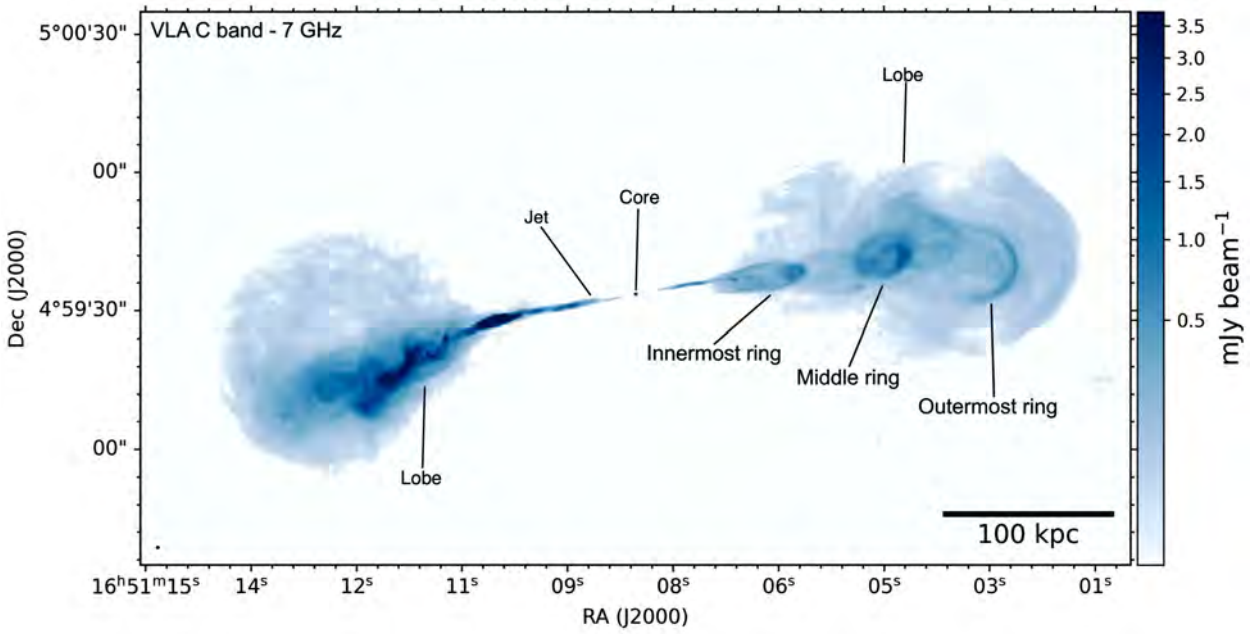

Figure 1.8: Hercules A (3C 348) observed with VLA C band (7 GHz), a luminous radio galaxy at redshift, z=0.154 [Dreher and Feigelson, 1984, Mason et al., 1988], displays a complex structure in its lobes, characterised as an intermediate FR I and FR II radio galaxy. The lobe in the eastern direction is dominated by the bright jet that slowly diffuses into the lobe, while the western lobe shows three distinct structures (labelled as rings) at a projected distance from the core [Timmerman et al., 2022].

Gopal-Krishna [1995], identified such sources using the VLBI and suggested that differences in the FR morphologies are due to the variations in the interaction between the jets and the external medium rather than the fundamental differences in their central engine. More studies of these sources, known as HYMORS (HYbrid MOrphology Radio Sources), are reported by multiple authors [Gawroński et al., 2006, de Gasperin, 2017, Cegłowski et al., 2013, Wiita et al., 2002, Kapińska et al., 2017], observed the sample of HYMORS, where one lobe appears darkened at the edge (FR I), while the other lobe displays a well-defined emission peak near its outer edge (edge-brightened, FR II), believed to be evolving in a non-uniform high-density environment [Cegłowski et al., 2013]. Results of these observations provided strong support for the existence of the different types of jets in the HYMORS on the FR morphology [Gopal-Krishna, 1995].

More recent studies of HYMORS samples are made in detail by Harwood et al. [2020], Stroe et al. [2022], Kumari and Pal [2022], studied the spectral analysis of the radio sources, that the HYMORS are a result of the orientation effect of the intrin-

sically FR II lobes. Thus, the apparent lobes of the HYMORS are centre brightened; however, they are not indicative of the typical FR I morphology; instead, it is by a compact acceleration region resembling hotspots (example in J 1348+28 radio map) [Harwood et al., 2020]. Stroe et al. [2022] observed consistency of HYMORS with the typical host galaxies of FR II radio sources are based on the galaxy's orientation, making one side of the galaxy appear similar to FR I jet.

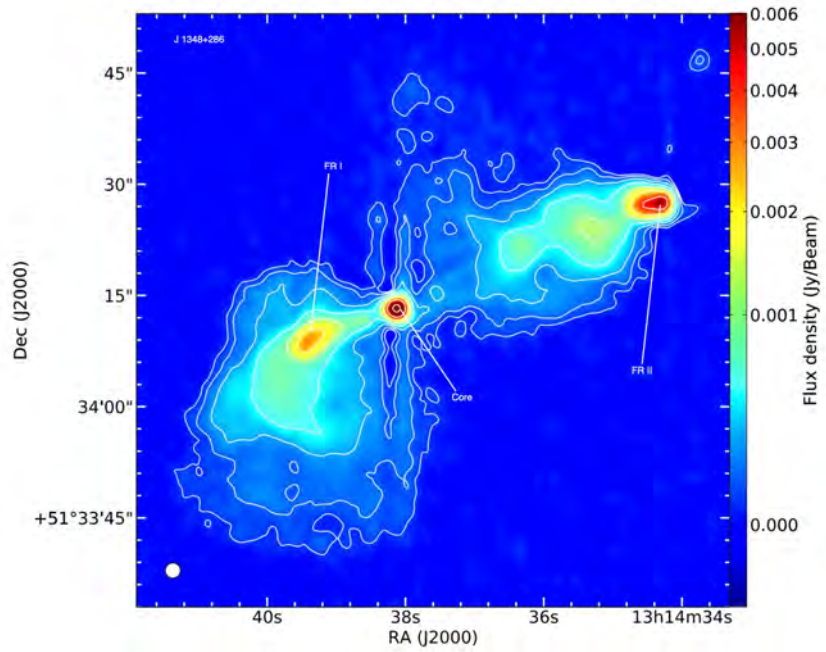

Figure 1.9: HYMORS radio maps from VLA at 1.52 GHz of J 1315+516 and J 1348+28 showing the FR II like jets, lobes and hotspots and FR I plume on one side [Harwood et al., 2020, Stroe et al., 2022].

Figure 1.9 gives examples of two HYMORS with an archetypal hybrid morphology: J 1315+516, with both lobes that follow a typical distribution associated with FR II and FR I lobes, and J 1348+28, with a hotspot-like feature on the FR I lobe. It is proposed that HYMORS may not constitute a distinct class of radio galaxies but rather exhibit characteristics akin to variations observed within FR II galaxies from specific observational perspectives. Recent high-resolution, detailed mapping has shown that radio sources previously classified as HYMORS, such as 4C +63.07, demonstrate characteristics in line with a standard FR II classification rather than truly being HYMORS [Gopal-Krishna and Dusmanta., 2023].

1.3.7 Double Double Radio Galaxies (DDRGs)

An atypical class of objects detected by Schoenmakers et al. [2000], christened Double Double Radio Galaxies (DDRGs), consists of double radio lobes with a common centre that appears at the opposite sides of the source [Scheuer et al., 1982, Saikia and Jamrozy, 2010]. This morphology distinguishes DDRGs from typical FR II objects.

These sources are the most explicit or episodic indications of recurrent jet activity. In the context of the DDRGs, their activity cycle, also known as the duty cycle, can be recognised by prior nuclear activity (i.e., a remnant emitting plasma) co-occurring with a new young jet restart, known as the new activity [Saikia and Jamrozy, 2010]. We identify the young radio source embedded in the old structure. The radio observations sometimes reveal the new pair separated from the old lobes, indicating multiple cycles, e.g., J 0041+3224 [Saikia and Jamrozy, 2010]. The new set of jets originates within the older lobes surrounded by diffuse emission and propagates through the existing cocoon material, yet not in ICM or ISM.

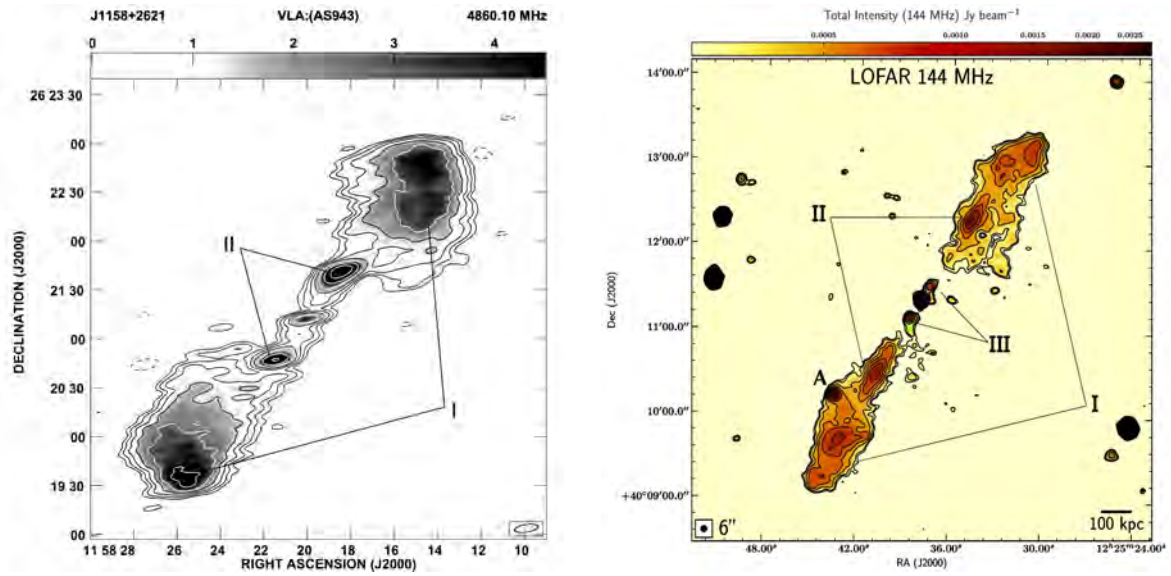

Figure 1.10: J1225+4011 a giant FR II referred to as a triple-double radio galaxy (TDRG). The image shows three distinct episodes of jet activity with the radio core. The most recent or the innermost double (III), the second double (II) and the first or the oldest double (I) [Chavan et al., 2023].

DDRGs are believed to be likely due to a disruption in the central jet production, with the older lobes lacking hotspots. In contrast, new ones show hotspots, indicating a disruption. However, unambiguous examples of DDRGs tend to have an edge-brightened structure at the extremities, which is easily explained by the standard FR II models (see Figure 1.10 left panel). Brocksopp et al. [2011] explored the formation of the inner hotspots of the radio galaxies, stating that the inner lobes are formed by relativistic electrons within the outer lobes, compressed and re-accelerated again by a bow shock in front of the reactivated jets within the outer lobes. The evolution of these sources can be probed through structural and spectral analysis of their extended emission.

An AGN can have multiple episodes of activity; an example is the Triple Double Radio Galaxies (TDGRs) [Chavan et al., 2023], with three distinct episodes of jet activity shown in Figure 1.10 (right panel).

Radio galaxy morphology can be classified differently depending on the orientation of the source. The reorientation events resemble the dynamics of the surrounding external medium, as seen in several cases, such as the X and S/Z shapes below. This suggests that orientation has a substantial impact on morphological classification.

1.3.8 Other Morphologies

X- shaped radio galaxies (XRGs) are known to constitute a considerable proportion (to $\sim 10\%$) of the population of powerful radio galaxies [Leahy and Williams, 1984, Leahy and Parma, 1992], also known as the 'winged' radio galaxies. They are a subclass of extragalactic radio sources with an additional pair of low surface brightness emissions detected in wings. The defining characteristic is plasma's backflow (i.e., hydrodynamical) from the hotspot into the surrounding medium [Leahy and Williams, 1984, Capetti et al., 2002]. Their morphological characteristics can also be ascribed as a consequence of the orientation of the jet or an abrupt flip in the spin of the supermassive black hole (SMBH) following the merger of a pair of galaxies [Biermann et al., 2003, Gopal-Krishna et al., 2010]. The radio source PKS 2014- 55 is an exceptional example of an X-shaped radio galaxy [Saripalli et al., 2008, Cotton et al., 2020]. Its observations reveal a double boomerang morphology of hydrodynamical backflows (see Figure 1.11), resulting from the main jet deflection by the large host galaxy. Its spectrum steepens in the lobes while flattening near the regions inside the apex of the boomerang, yet steepens in its cocoons due to a dominance of ageing electrons of the source.

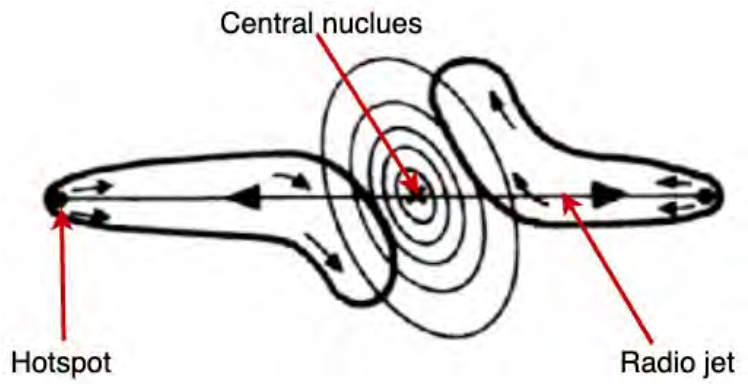

Figure 1.11: A schematic representation of the hydrodynamical backflow model of XRGs by Leahy and Williams [1984].

S/Z- shaped radio galaxies. The bending of the radio jets on kpc or larger scales is not a rare occurrence amongst radio galaxies, especially those of the FR I type. Their morphology can show curvature or sharp turns in their jets or lobes [Riley, 1972]. Several mechanisms were proposed to explain the occurrence of their morphology, i.e., jets

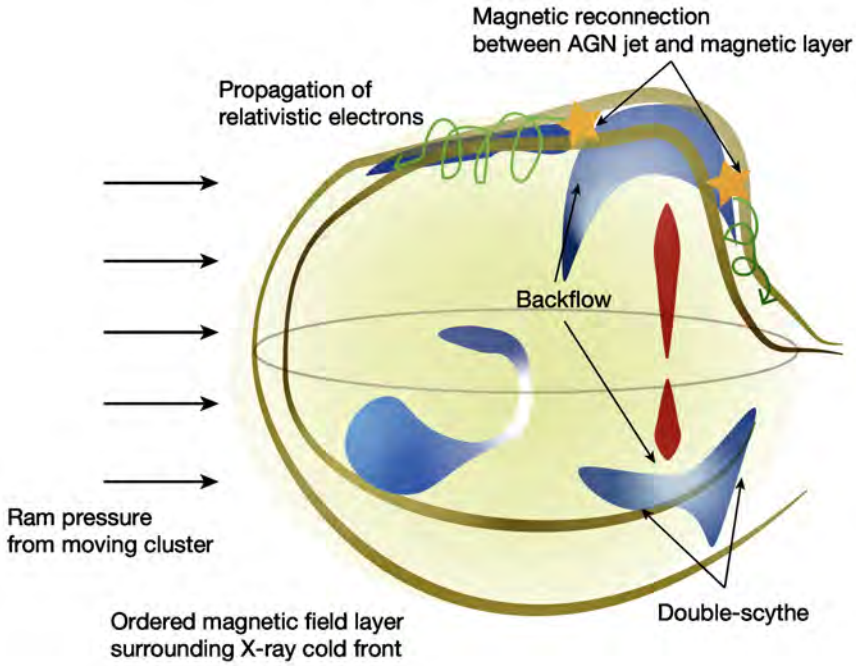

Figure 1.12: Schematic drawing proposed as a possible mechanism by Chibueze et al. [2021] representing an interaction of a radio jet with the magnetized surrounding medium.

may follow bent S-shaped trajectories due to strong interactions with the magnetized surrounding medium, or the jet structure can also be affected by ram pressure [Blanton et al., 2001], or else the galaxy is subjected to jet precession [Ekers et al., 1978].

Figure 1.12 shows a schematic drawing of a proposed scenario for the possible morphology of an S-shaped structure. The radio jet experiences density contact discontinuity in the cool, dense plasma or experiences ram pressure as the galaxy moves through the ICM.

1.4 Filaments

Filaments are thin, elongated structures increasingly seen in the intracluster medium [Rudnick et al., 2022, Yusef-Zadeh et al., 2022]. However, they are becoming more common both within and outside radio lobes, tails, and cluster radio relics, implying that unknown interactions between radio plasma and the external medium exist outside these areas. It is unclear if these filaments are physically related to radio galaxies or what they reveal about the ICM's underlying magnetic field [Ramatsoku et al., 2020]. There are multiple documented occurrences of filaments connected to radio lobes and jets. Notably, in Figure 1.13, the narrow, long and straight faint radio filament branching from the tail of a radio galaxy J 1333-3141 in galaxy cluster A3562 [Giacintucci et al., 2022, Venturi et al., 2022], is presumed to be blown by the tangential wind in that region stretching the radio plasma from the galaxy and forming the

filamentary structure.

Such features have become more common in radio galaxies, frequently detected as interferometers are becoming more sensitive, indicating their visibility across a range of radio frequencies, capturing emissions from ageing cosmic-ray electrons [Giacintucci et al., 2022]. Ramatsoku et al. [2020] proposed a potential cause, suggesting a magnetic field reconnection around radio lobes (e.g., ESO 137–006). Condon et al. [2021] support the potential reason that coherent magnetic field structures possibly result from relativistic electrons escaping helical Kelvin–Helmholtz instabilities in radio jets found (i.e., observed in highly polarized filaments of IC 429). In the context of clusters, Knowles et al. [2022] speculated on the possibility of the radio filaments illuminating magnetic flux tubes in the intracluster medium (ICM), echoing that synchrotron emission reflects the underlying magnetic field structure. Intriguingly, simulations suggest cosmic-ray electron convection by ICM "weather" flows may shape these filamentary patterns [ZuHone et al., 2021]. Despite these findings, the exact origin of these filaments is still unknown.

Remarkable progress has been made in imaging extragalactic radio sources thanks to the advanced imaging capabilities of interferometers. LOFAR [van Haarlem et al., 2013], JVLA[Perley et al., 2011], MeerKAT [Jonas, 2016], ASKAP [Johnston et al., 2007], and uGMRT [Gupta et al., 2017], with their superb sensitivity and *uv*-coverage, as well as a broad range of simultaneous angular resolutions, now offer a unique view of radio galaxies on scales from sub-arcsecond to tens of arcseconds in a seamless range of frequencies, from 144 MHz (LOFAR, Dutch stations and international baselines) to 8 GHz and beyond (JVLA). At the same time, the large samples of radio galaxies delivered by the continuum sky surveys carried out with LOFAR (LoTSS, Shimwell et al. [2017], ASKAP (EMU, Norris et al. [2011]) and MeerKAT (i.e. MIGHTEE, MGCLS, Jarvis et al. [2016], Knowles et al. [2022], allows studying such objects' cosmological evolution using solid statistical samples.

High-fidelity images of radio galaxies reveal a wealth of complex structures in radio emission: multiple hotspots observed in several sources (e.g. 3C 403 and 3C 227 Hardcastle et al. [2007b]), including wiggles along the ridge of radio jets (e.g. CGCG 044–046: Fanaroff et al. [2021]), IGC 4296: Condon et al. [2021] and 3C 129 Lal and Rao [2004]) and how they interact with the surrounding medium. In addition to the detected complex structures, thin filaments of radio emission originating from the lobes and jets (e.g. Velović et al. [2023]), thin tubes of emission detected in different regions of the radio galaxies at least in projection, and the low surface brightness emission detected the lobes and some hotspots.

This increased level of complexity in the morphology of FR I and FR II radio galaxies raises the question of whether this classification is still meaningful.

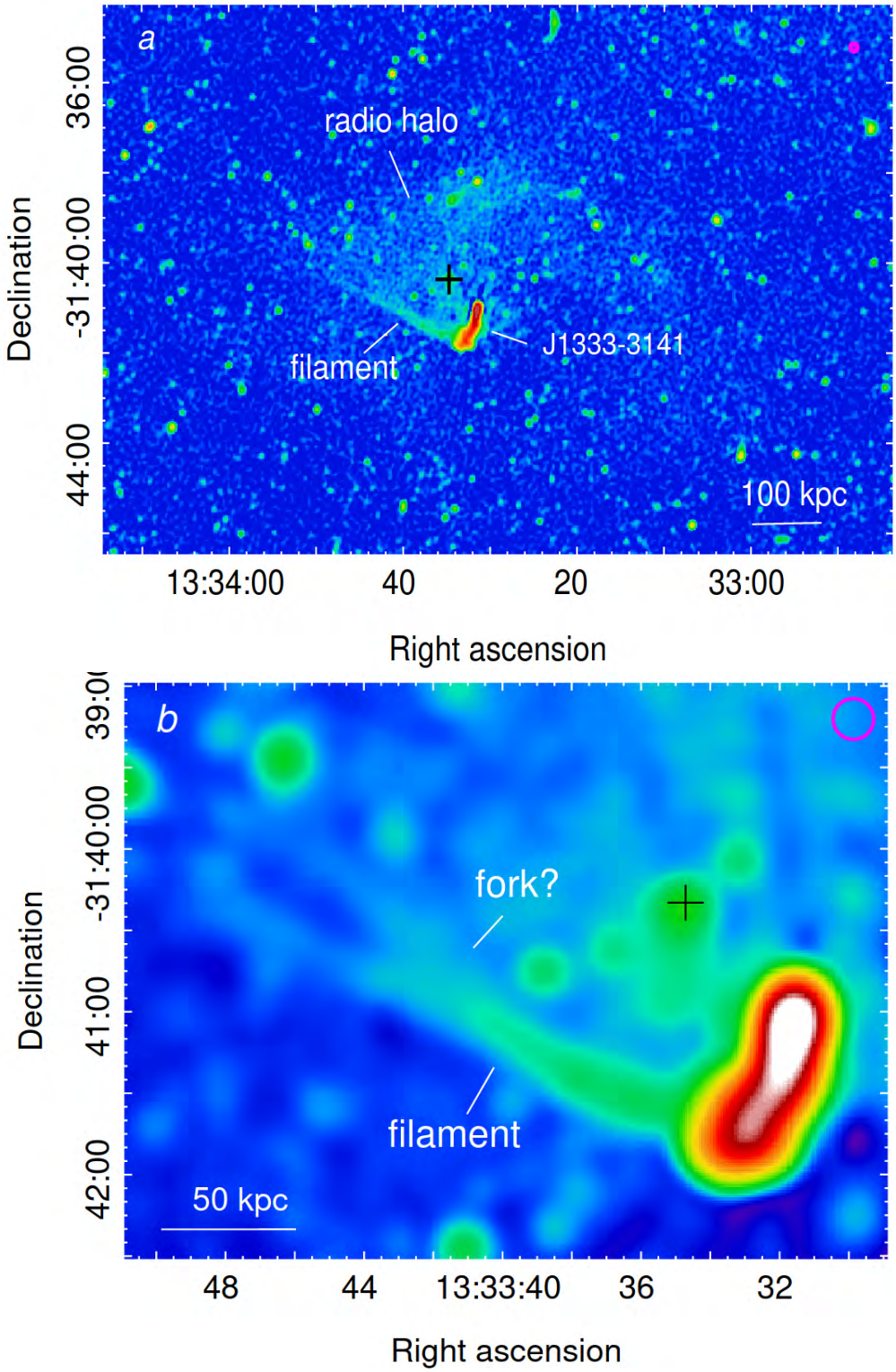

Figure 1.13: MeerKAT image of the radio filament from the end of the J 1333-3141 extending eastward, showing a possible fork-like structure seen ∼kpc from the tail [Giacintucci et al., 2022].

1.5 Background studies for the present thesis

Fanaroff et al. [2021] provide a systematic study of the first set of four radio galaxies we consider in this work, i.e 4C 12.02, 4C 12.03, CGCG 044-067 (4C 07.32) and CGCG 021-063 (4C 00.36), exploring the unprecedented sensitivity and resolution of the upgraded Giant Metrewave Radio Telescope (uGMRT) and the MeerKAT array. The combination of μJy beam^{-1} sensitivity and high ($\sim$5″ to 7″) angular resolution over the entire 550−1712 MHz range revealed a wealth of morphological details that could necessitate a revision of the classical radio galaxy classification scheme from extensively rich structures, such as filaments in the emission from the lobes, to the existence of diffuse emission beyond the hotspots. Based on the first four radio sources, the classical FRI and FR II morphological schemes still hold with improved imaging capabilities. However, the richness in details suggested caution in the systematic morphological classification carried out with automatic procedures in surveys with poorer sensitivity and angular resolution.

The high-resolution images revealed detailed structures such as filamentary emissions and misalignments. For instance, 4C 12.02, identified as a FR II galaxy, showed back-flows from the lobes and multiple hot spots, with flux densities at 0.69 GHz and 1.28 GHz measured as 3.50± 0.19 Jy and 2.15±0.07 Jy, respectively. 4C 12.03, an X-shaped radio galaxy, displayed signs of restarted activity and inner double structures, with total flux densities of 3.14 ± 0.18 Jy at 0.69 GHz and 2.06 ± 0.06 Jy at 1.28 GHz. CGCG 044–046, a wide-angle tail (WAT) radio galaxy, exhibited an asymmetric bent morphology with filamentary structures in the tails and flux densities of 3.24 ± 0.16 Jy at 0.69 GHz and 2.05 ± 0.07 Jy at 1.28 GHz. CGCG 021–063, characterized by a compact core and extended lobes, typical of FR II morphology, revealed a cocoon of fainter emission suggesting back-flow from the jets, with total flux densities of 3.77 ± 0.20 Jy at 0.69 GHz and 2.80 ± 0.09 Jy at 1.28 GHz.

1.6 Project objectives

Our understanding of the FR division and its relation to the source dynamics has evolved considerably over the past four decades. To enhance our understanding of the radio galaxy phenomena and the interaction between the radio plasma and the surrounding medium in light of current interesting imaging capabilities in the radio band, we aim to address questions that have remained unanswered. In particular:

1. Does the classical morphological scheme of FR I and FR II type still hold with the current imaging capabilities of interferometers?

2. Does very low surface brightness emission exist beyond the known boundaries of radio galaxies, or can it be detectable around FR 0 radio galaxies?

3. Do we need more morphological classes or a refined scheme for extragalactic radio galaxies?

4. As more details are revealed, how can we explain the details, like the hotspots, filaments, and other details observed in the radio galaxies?

1.7 Thesis structure

The thesis is structured as follows:

Chapter 2 gives a brief review of basic radio interferometry using a two-element interferometer and a description of the uGMRT and MeerKAT arrays. **Chapter** 3 presents the radio galaxy selection criteria for radio sources and provides particular descriptions of radio galaxies from the literature. We also give a detailed discussion of the data reduction, data calibration, and imaging techniques used in this work from the uGMRT and MeerKAT.

Chapter 4, the science chapter, summarises the important findings of our work. First, we present the intensity maps, high resolution and high sensitivity maps of the science targets derived from the calibration and imaging process derived in Chapter 3, and the comprehensive description of the radio sources.

Chapter 5 gather details of the various parameters inherent in the galaxies, using common arguments to derive the physical parameters from the total intensity distributions. In addition, we present the integrated spectrum of the radio galaxies from the literature and derive the inband spectral index for the MeerKAT data.

Chapter 6 gives the estimated radiative ages of the radio galaxies using parameters estimated in Chapter 5.

Chapter 7 gives the discussion of the work, finally **Chapter** 8 draws relevant conclusions about the work's purpose based on the primary findings and provides prospects for future work that was not covered in the current study.

Chapter 2

Radio interferometry, and MeerKAT and upgraded GMRT

The early eras of radio astronomy were dominated by single-dish (or, in any case, single receiving element) observations, following on the groundbreaking telescope of Grote Reber. These typically consist of a single radio telescope with a steerable or non-steerable dish reflector. Steerable dishes that can track a source across the sky are desirable but complex in construction, with the largest being the 100 m Green Bank Telescope (GBT) [Srikanth et al., 1999], while the largest non-steerable dish telescope is the 500m Five hundred-meter aperture spherical radio telescope (FAST) [Nan, 2006]. Two common metrics are used to qualify the performance of a telescope: sensitivity – which roughly determines how faint a signal the telescope can detect – and angular resolution – its ability to distinguish between two sources separated by a given angular distance. The sensitivity of a single dish is proportional to the size of the dish collecting area (aperture), while its angular resolution is determined by the dish diameter, D, using the Rayleigh criterion: $\theta = 1.22\frac{\lambda}{D}$, where λ is the observing wavelength. Therefore, a larger dish results in both improved sensitivity and resolution. However, due to wavelengths being significantly longer in the radio regime, even the largest radio dishes cannot achieve the resolution available to optical telescopes. Moreover, there is also a practical limit to the size of telescopes that can be built, with larger ones presenting significant engineering challenges. Obtaining a meaningful sensitivity and resolution improvements would require a massive telescope. The technique of radio interferometry offers a solution. By combining signals from multiple spatially separated elements (typically, but not restricted to , dishes), it forms an *synthesis array*, functioning as one large telescope with a resolution given by the largest separation between two antennas (baseline) b_{max}.

The following section discusses the basics of interferometry techniques and principles governing aperture synthesis for imaging the data from radio observation (see Section 3.4). This discussion is rooted in Taylor et al. [1999] and Thompson et al. [2001].

2.1 Basic Radio Interferometry

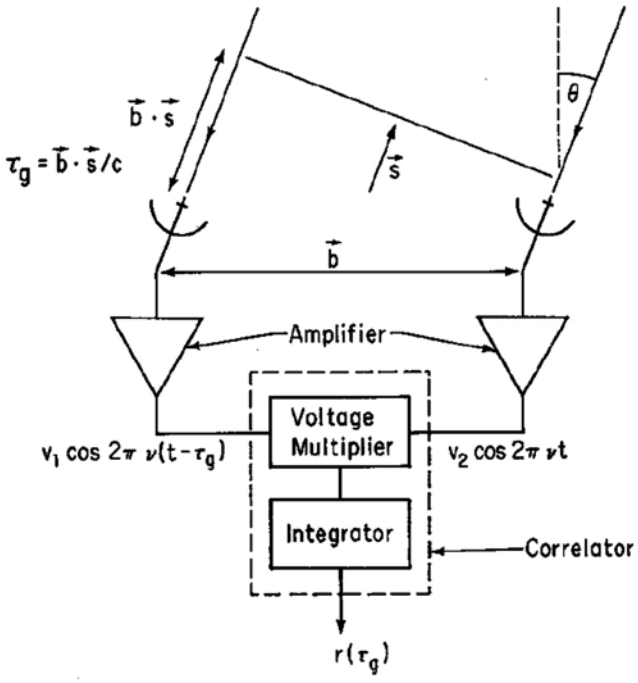

Figure 2.1: Two element interferometer [Taylor et al., 1999].

For simplicity, consider a quasi-monochromatic signal emitted from an astronomical radio source at a far distance observed from earth-based antennae. Figure 2.1 illustrates a two-element interferometer, separated by a single baseline in the array defined by vector **b** and a unit vector **s** pointing in the direction of the source. The signal from the astronomical source arrives at slightly different times at the two antennas given by

$$\tau_g = \frac{\mathbf{b}\cdot\mathbf{s}}{c} \tag{2.1}$$

introduced as the geometric delay, where c is the speed of light given as c = 3×10^5 km s^{-1}. As a result, if one antenna receives an input signal $V_1 = v_1(t) = v_1\, cos\, 2\pi\, \nu(t)$, the geometric delay means the other antenna will receive the signal as $V_2 = v_2(t) = v_2\, cos\, 2pi\, \nu(t-\tau_g)$. The correlated voltages V_1 and V_2 are then averaged over time as $\langle V_1 V_2\rangle_t$, and $< \cdot >$ denote the time average. The sky consists not only of point-like sources but also extended sources; as such, the signal from extended sources can be computed by treating the source as a series of infinitesimally small points. The overall response of the interferometer can be obtained as

$$r = \int_s A(s)I(s)\Delta\nu cos\left(2\pi\nu\frac{\mathbf{b.s}+\sigma}{c}\right)d\Omega \tag{2.2}$$

where $I(s)$ is the spatial intensity distribution of the produced by the astronomical source at a particular frequency, $d\Omega$ is the solid angle of a source at point **s** received at bandwidth $\Delta\nu$ and $A(s)$ is the collecting area of the antenna. The components of

the baselines are measured in units of wavelength, λ denoted as (u, v, w), such that u and v axes form a plane in which the interferometer samples visibilities often adverted to as the (u, v) plane, perpendicular to the line of sight with w axis. The observed quantities of radio interferometry observations are the complex visibilities $V(u, v, w)$, and it is related to the true sky distribution $I(l, m, n)$ by the relation

$$V(u,v,w) = \int\int A(l,m,n)I(l,m)\frac{e^{-2\pi\, i[ul+vm+w(\sqrt{1-l^2-m^2}-1)]}}{\sqrt{1-l^2-m^2}}dldm; \tag{2.3}$$

where $(l, m) = (l, m, \sqrt{1 - l^2 - m^2})$ are the direction cosines in the sky and $d\Omega = \frac{dl\mathrm{dm}}{\sqrt{1-l^2-m^2}}$. The above relation is known as the van Cittert-Zernike theorem. For a small field of view, the third exponential term is ignored, and the simplification leads to a form

$$V(u,v) = \int\int I(l,m)e^{-2\pi\, i[ul+vm]}dldm. \tag{2.4}$$

Given a sufficiently sampled uv-plane and ignoring the complexities of gridding for the moment, Equation 2.4 can be inverted, using Fourier Transforms to recover the actual sky distribution of the astronomical source,

$$I(l,m) = \int\int V(u,v)e^{2\pi\, i[ul+vm]}dudv. \tag{2.5}$$

The above formulation (vCZ) assumes a perfect instrument with no distortions. In reality, we have instrumental and atmospheric effects, which must be dealt with in calibration (see Section 3.3.2). The RIME is a mathematical framework for describing these effects [Hamaker et al., 1996, Hamaker, 2006, Smirnov, 2011a]. The two-dimensional Fourier transform using the RIME is given as

$$V_{pq} = \mathbf{G}_p\left(\int\int_{lm}\mathbf{B}_{pq}(l,m)e^{-2\pi I(ul_{pq}+v_{pq}m)}dldm\right)\mathbf{G}_q^H \tag{2.6}$$

$$\mathbf{B}_{pq} = \mathbf{E}_p\mathbf{B}\mathbf{E}_q^H$$

V_{pq} is the measured visibility by antenna by antennas p and q, $\mathbf{E}_p$ represents the direction-dependent effects in the direction of the source. $\mathbf{B}_{pq}$, the assumed sky distribution, $\mathbf{G}_p$ represents the Direction independent instrumental gains, accounting for the properties of the antenna and other instrumental effects independent of the direction of the source. Each baseline samples a Fourier component of the observed sky. These patches represent Fourier components of the observed sky intensity (i.e., the components vary for each baseline).

The most ubiquitous DDE is the primary beam, which represents the sensitivity pattern of the antenna projected onto the sky. In principle, it does vary in time and per-antenna due to pointing errors and parallactic angle rotation. However, for the purposes of this work (since all our targets are observed at the centre of each field), we ignore these subtleties and treat the primary beam as time- and antenna-invariant. In other words, we treat it as a *trivial* DDE. Assuming a trivial DDE, all baselines will measure the same sky as $\mathbf{EBE}^H$. Consequently, the apparent sky intensity will be

consistent across all baselines, corresponding to the observed intensity attenuated by the power beam. This can then be corrected in the image plane (see Section 3.5.3).

2.2 Observational Instruments

In the following, we provide an overview of the radio interferometers used in our study.

2.2.1 The MeerKAT radio telescope

The MeerKAT radio telescope is a precursor of the Square Kilometre Array (SKA) located in the Northern Cape, Karoo region of South Africa (30.713° S, 21.4430° E) [Jonas, 2009]. The array comprises 64 antennas with an effective diameter of 13.5 m and an offset Gregorian-designed dish that ensures an unobstructed aperture and outstanding sensitivity to extended emission observation. The array comprises 48 antennas scattered within the 1 km core and 16 others scattered around the surrounding region, giving a maximum baseline of 8 km.

Each dish encompasses a receiver indexer that can accommodate up to 4 receivers below the reflector. The L-band receiver covers a frequency range of 900 to 1670 MHz, the UHF-band receiver covers a frequency range of 580 to 1015 MHz, and the S-band covers a frequency range of 1.75 to 3.5 GHz. The receivers capture the radio signal, convert it into voltage signals, and amplify them. The voltages are further digitized from the receivers into digital signals. Once converted into digital data, they are sent to the correlator/ beamformer (CBF) within the Karoo Array Processing Building [Camilo et al., 2018]. Furthermore, the F-engine aligns the voltages coarsely to make amends for geometric and instrumental delays and then splits them into frequency channels. The X-engine performs cross-correlation of the digitized voltage streams. The visibilities produced by the correlator are then transferred to the archives hosted by the Centre for High-Performance Computing (CHPC) in Cape Town.

2.2.2 The uGMRT radio telescope

The Giant Metrewave Radio Telescope (GMRT) is the most extensive, sensitive low-frequency array in Pune, India [Swarup, 1991, Gupta et al., 2017]. The interferometric array consists of 30 steerable parabolic radio telescopes, each with a diameter of 45 meters. The GMRT's major upgrade with the new receivers and wideband correlator system has significantly improved its performance operating in four frequency bands: band 2 (120 - 240 MHz), band 3 (250 - 500 MHz), band 4 (550 - 850 MHz) and band 5 (1000 - 1450 MHz). The upgraded GMRT (uGMRT) is a SKA pathfinder with unprecedented sensitivity and low frequency. Its hybrid configuration (Figure 2.4) also fulfils both the high resolution and detection of extended radio emission at lower frequencies. The uGMRT array comprises 14 antennas scattered around the $\sim$1km central square region. The central square region provides many shorter baselines, which are well situated for imaging the extended emission of radio sources. The remaining 16

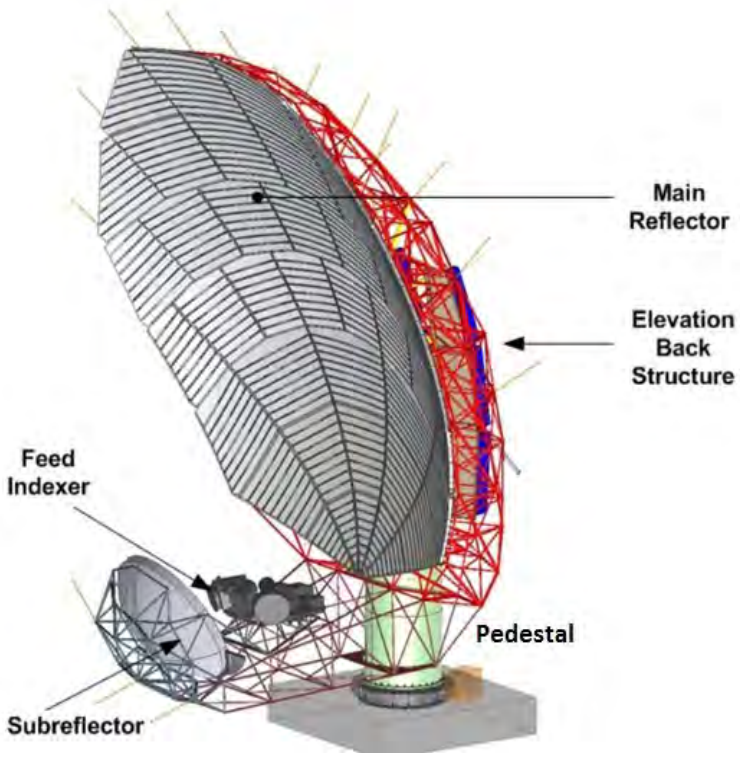

Figure 2.2: A schematic diagram of the MeerKAT antenna [Jonas, 2016].

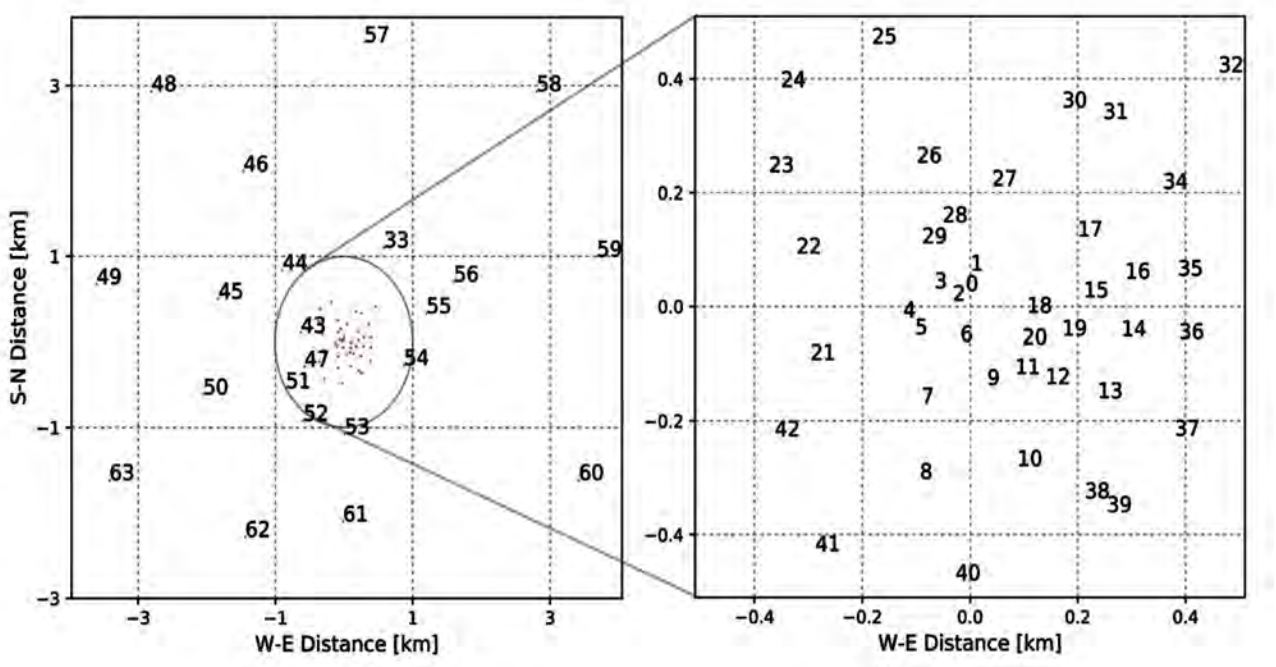

Figure 2.3: The MeerKAT array configuration, The array comprises 48 antennas scattered within the 1 km core and 16 others scattered around the surrounding region, giving a maximum baseline of 8 km [Booth et al., 2009]

antennas are distributed in a Y-shaped configuration with the East-West and South arms. Subsequently resulting in a maximum baseline length produced by the arms antennas of $\sim$25 km. The long baselines provided by the arms' antennas are suitable for high-resolution imaging. Table 2.1 gives the system parameters of uGMRT.

Table 2.1: The uGMRT system parameters.

Bands	Band-2	Band-3	Band-4	Band-5
Frequency (MHz)	125 - 250	250 - 500	550 - 850	1000 - 1460
System Temperature (K)	760 - 240	165 - 100	$\sim$ 100	$\sim$ 75
Primary Beam (arcmin)	120	75	38	23
RMS noise (μJybeam^{-1})	500	10	6	2.5
Gain of an antenna (K/Jy)	0.33	0.38	0.35	0.22 - 0.28

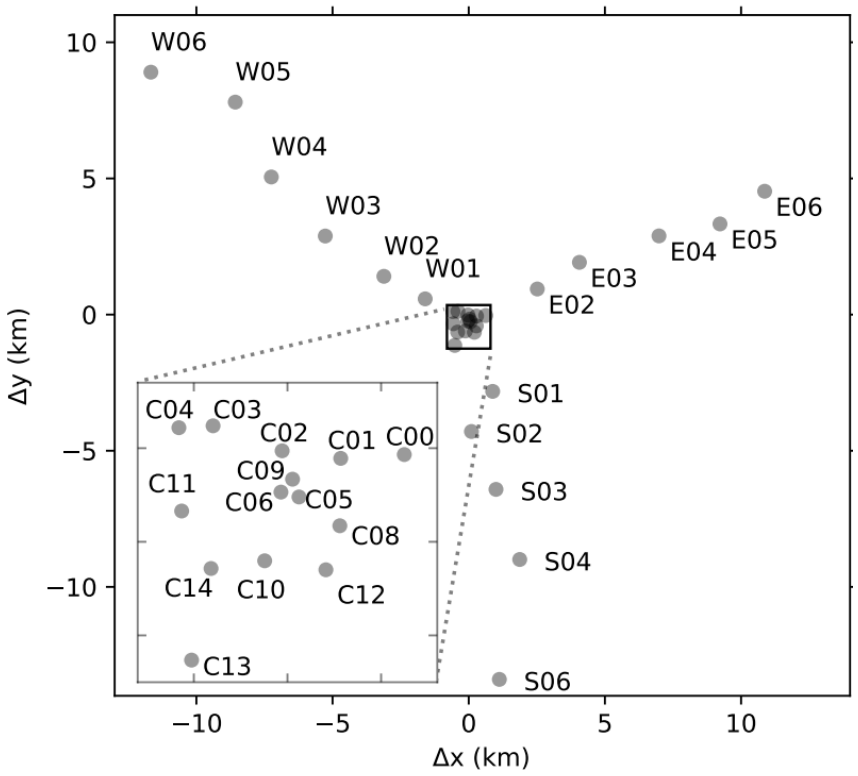

Figure 2.4: The GMRT array hybrid configuration, with the antennas shown in circled and labelled. The 30 antennas are arranged in a Y configuration, consisting of 16 antennas within the Y configuration's east, west and south arms. The remaining 14 antennas are gathered at the central core of the array [Dokara et al., 2023].

Chapter 3

Sample selection, Observations and Data processing

3.1 Sample selection

To address the questions raised in Section 1.6, we selected a sample of radio galaxies from the 4C catalogue [Pilkington and Scott, 1965]. The 4C survey of radio sources was carried out at the frequency ν= 178 MHz between declination -7° < δ >+80° to a limiting flux density of $S_{178\ MHz}$ =2.0 Jy [1] [Gower, 1966] . We selected our sample of interest based on the following criteria:

1. Optical galaxies hosting the radio galaxies, with a spectroscopic redshift in the range of 0.04 to 0.20 to ensure the detection of Mpc scale extended emission using uGMRT band-4. This results in a similar fraction of FR Is and FR IIs.

2. The radio source is in a declination range of [-15°: +20°] to ensure proper visibility and comparable (u, v) coverage with both uGMRT and MeerKAT and,

3. they show a clear double radio morphology, including traces of further surrounding emission at the 45 arcsecs [2] angular resolution of the NRAO VLA Sky Survey (NVSS) [Condon et al., 1998] [2].

The criteria resulted in a total of selected 17 radio sources, of which two were FR 0s from the catalogue of compact sources known as FR0CAT Baldi et al. [2019] in the same redshift of z $\sim$0.05 and declination range δ. Of 17 radio sources, six are FR IIs, six FR Is, three FR Is with tailed morphology and two FR 0s.

We restrict the number of radio sources to ten in this work. These add to the four radio galaxies presented in Fanaroff et al. [2021]. The basic properties of the sample, including the name, coordinates, redshift, radio power at 1.4 GHz and the radio morphology type, are listed in Table 3.1; amongst them are three FR Is (4C -03.43, 3C 403.1,

[1] 1 flux unit = 10^{-26} W m^{-2} Hz^{-1}

[2] NRAO VLA sky survey (NVSS) is at 1.4 GHz continuum survey covering the entire sky north of -40° declination with a resolution of 45″ FWHM.

3C 198), three FR IIs (3C 105, 3C 227, 3C 445), two-tailed radio sources (CGCG 046-067, NGC 7503) and the FR0s (SDSS J 09157+1331, SDSS J 1120+04). The redshift distribution is bimodal with three sources at the redshift z= 0.081:0.089, and the remaining at redshift z = 0.044:0.056.

Radio contours are provided in Figure 3.1 – 3.3 to visualise the selected sample of radio sources. The contours represent radio images from NVSS spanning 0.3°x 0.3° large fields for their large-scale structure and extended components, which were used to aid the morphological selection of the source. The flux densities values are above 1 Jy (however less than 0.01 Jy FR 0 radio sources) at 1.4GHz the radio power range between $22 < log_{10} P_{1.4\ \mathrm{GHz}} < 26$.

Table 3.1: Sample of radio galaxy candidates

Object Name	RA_{J2000}	Dec_{J2000}	z	Type	$P_{1.4} WHz^{-1}$
3C 105	04 07 16.5	+03 42 26	0.089	FR II	7.79e+25
3C 198	08 22 31.9	+05 57 07	0.081	FR I	4.12e+25
3C 227	09 47 45.1	+07 25 21	0.085	FR II	1.43e+26
4C -03.43	11 33 05.1	−04 00 48	0.0519	FR I	3.12e+24
CGCG 047-067	14 29 55.4	+07 15 13	0.0548	FR I (WAT)	1.10e+25
3C 403.1	19 52 30.5	01 17 21	0.055	FR I	1.65e+25
3C 445	22 23 49.6	−02 06 12	0.0562	FR II	4.32e+25
NGC 7503	23 10 42.3	+07 34 04	0.044	FR I (NAT)	6.61e+25
SDSS J 09157+1331	09 17 54.3	+13 31 45	0.05	FR 0	1.40e+23
SDSS J 1120+0407	11 20 29.2	+04 07 42	0.05	FR 0	4.63e+21

We measured the flux density of the radio sources from the low-resolution survey (NVSS) at 1.4 GHz to calculate the radio emission power of the radio sources. The flux densities of the multiple components of the radio sources are added together to obtain the total flux density of a source $S_{1.4\ \mathrm{GHz}}$. The projected angular size was derived according to the redshift of the optical galaxy using the cosmological calculator, and the luminosity distance was computed using the cosmology parameters with the Hubble constant $H_0 = 69.6$ km s^{-1}Mpc^{-1}, Ω_m= 0.286 and $\Omega_\lambda = 0.714$. The luminosity distance was calculated following [Hogg, 1999].

$$D_L(z, H_0, \Omega_m, \Omega_\lambda) = \frac{c(1+z)}{H_0}) \times \int_0^2 [(1+z')^2(1+\Omega_m^{2'}) - z'(1+z')\Omega_\lambda]^{-\frac{1}{2}}\, dz'\, [Mpc] \quad (3.1)$$

Where c is the speed of light. The computed radio power $P_{1.4\ GHz}$ of a source from the flux density $S_{1.4\ GHz}$ and redshift z is

$$P_{1.4\ GH}z = 4\pi D_L^2 S_{1.4\ GHz}\, [WHz^{-1}]. \quad (3.2)$$

Owing to the low redshifts, no k-corrections were necessary for our sample radio galaxies.

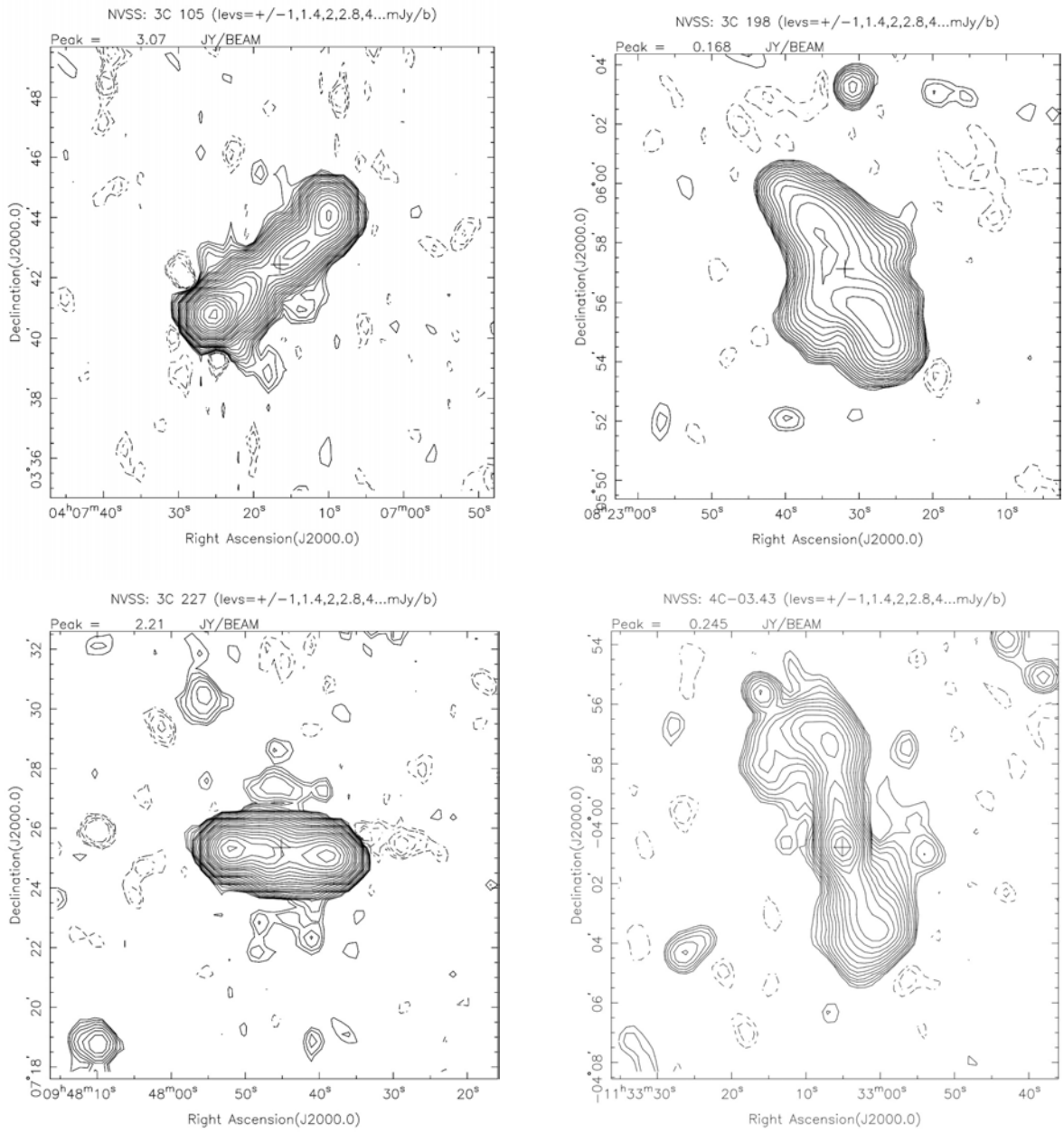

Figure 3.1: The NVSS images of our source sample. Individual sources are, from top row-by-row, 3C 105 (FR II), 3C 198 (FRI), 3C 227 (FR II) and 4C -03.43 (FR I).

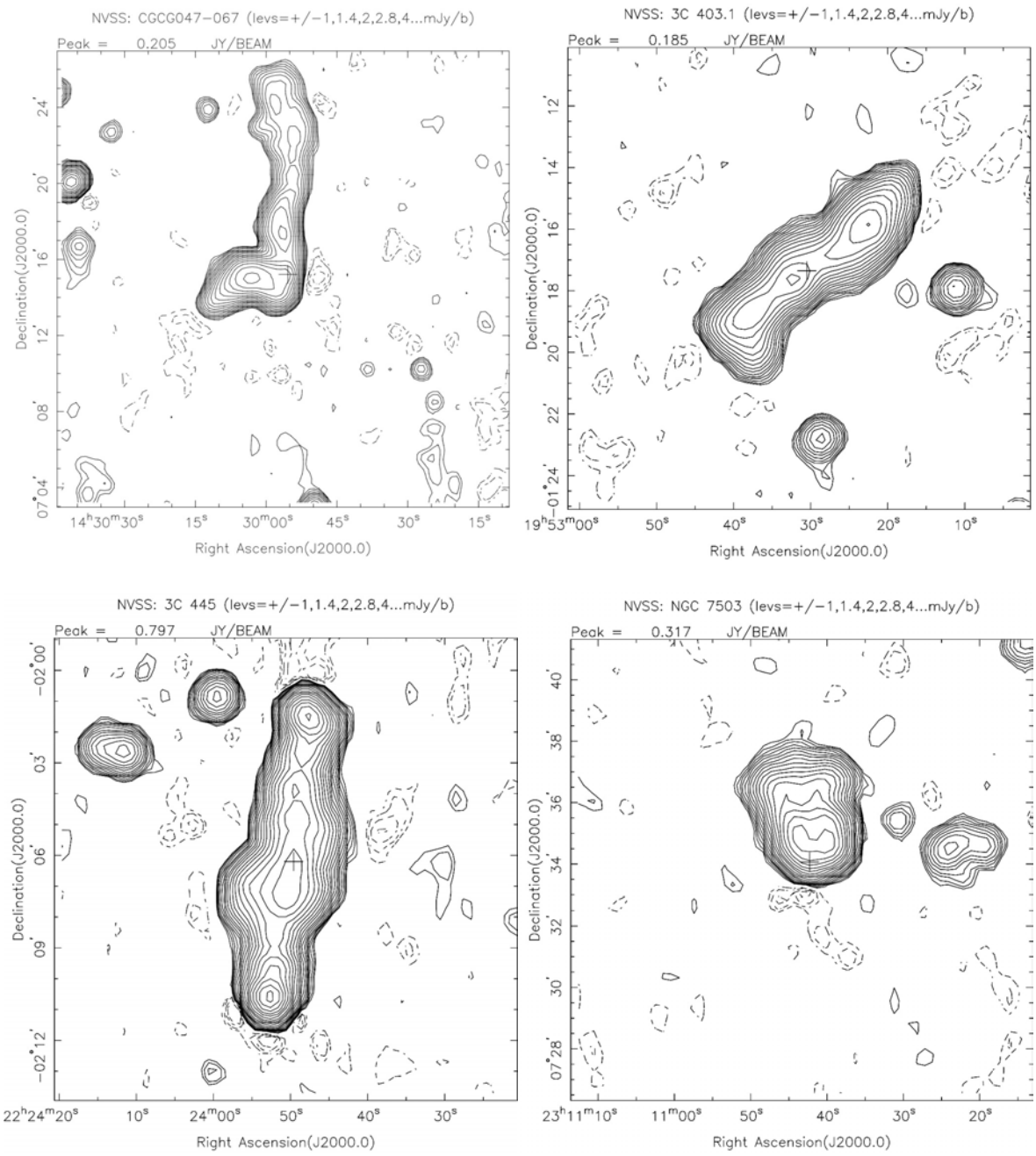

Figure 3.2: The NVSS images of our source sample. Individual sources are, from top row-by-row, CGCG 047-067 (WAT FR I), 3C 403.1 (FR I), 3C 445 (FR II) and NGC 7503 (NAT FR I).

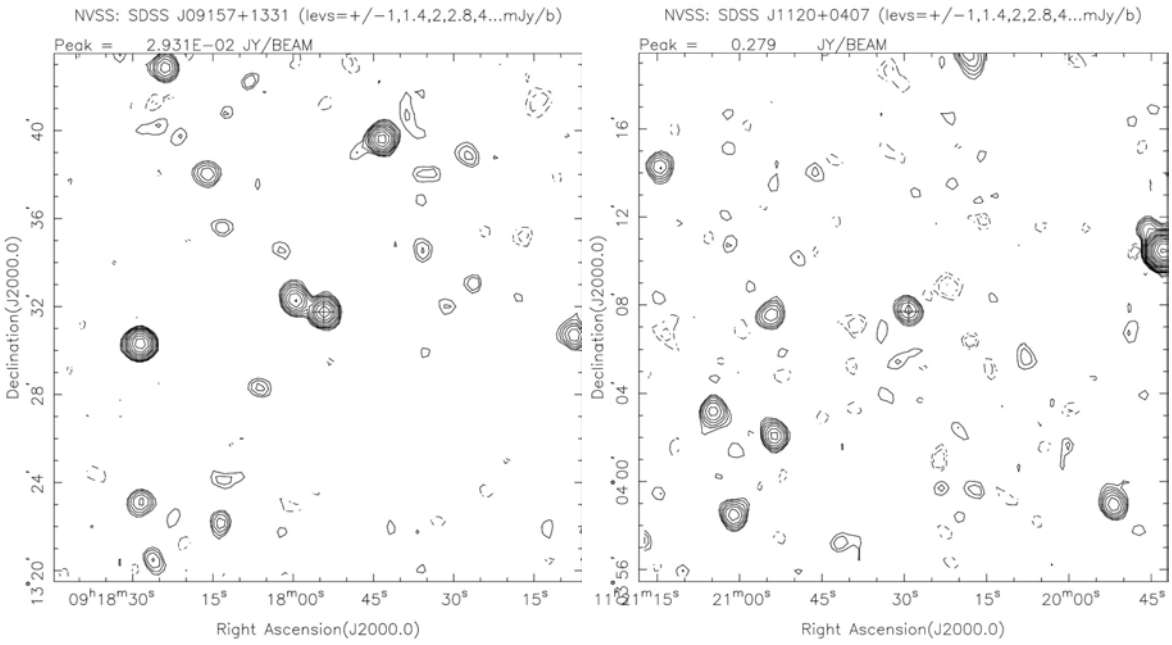

Figure 3.3: The NVSS images of our source sample. Individual sources are, from top row-by-row, SDSS J09157+1331 (FR 0), SDSS J1120+0407 (FR 0).

3.2 Radio data

This section describes the data collection procedures used to investigate the radio source. Here, we present the MeerKAT L-band and the uGMRT band-4 observations. Data observations are at frequencies ranging from 550 MHz to 1.67 GHz, offering imaging capabilities with a sensitivity of μJy beam^{-1} and an angular resolution of a few arcseconds. The synergy of the two instruments provides consistent resolution and sensitivity across the entire source structure. Given the typical spectrum of such features, it is ideal for the spectral structure of extended source studies (i.e., jets, lobes and extended emission in radio galaxies). A summary of observations is presented in the Table 3.3.2.

3.2.1 The MeerKAT Observations

We observed the sources 3C 105, 3C 445, 4C -03.43, CGCG 047-067, SDSS J 09157+1331 and SDSS J 1120+0407 with the MeerKAT in May 2019 and August 2021 in all four correlations [3]. The observation used at least 63 of 64 antennas, and each session spanned $\sim$5 hours, including scans of the calibrator sources.

The correlator was configured for 8 seconds of integration time. For the observing sequence, a typical strategy was used which includes 10 minutes tracks on the bandpass calibrator (i.e., J 1939-6342 or J 0408-6545) and regular visits to the gain calibrator (i.e., J 0323+0534, J 1150-0023, J 1445+0958, J 2225-0457 or J 1008+0730).

Figure 3.4 illustrates tracks for the bandpass calibrator and tracks, target field and the gain calibrator. The total MeerKAT bandwidth, centred on 1.28 GHz, was 856 MHz with 4096 spectral channels of 0.209 MHz width, covering the L-band (856 − 1712 MHz).

3.2.2 The uGMRT Observations

The uGMRT observations complement the MeerKAT observations. The observations were proposed in 2 cycles, first submitted in set 3C 105 and 4C −03.43 were observed in September 2019 (proposal code 36_32). The remaining radio sources (3C 445, 3C 198, 2C 227, CGCG 047-067, 3C 403.1 and NGC 7503) were later proposed for observation from November 2022 to March 2023 carried out under the proposal code 43_058. The total allocated telescope time to the proposal was approximately 20 hours. Full on-source time was $\sim$4 hours for each source. The bandpass and flux calibrators, depending on the target (3C 468.1, 3C 147, 3C 286), were observed at least once during observation for 10 minutes, and the gain calibrator (2011-067, 087-198, 1445+099, 2212+018) observed once every 20 to 25 minutes of the target field observation. The integration time was 5.83 seconds, and the bandwidth was 292.965 MHz. All the uGMRT data were recorded in spectral line mode, typically 8192 channels in the new dual-polarisation (RR and LL).

[3]Full polarisation data was taken; however, polarimetric analysis remained outside the scope of this work.

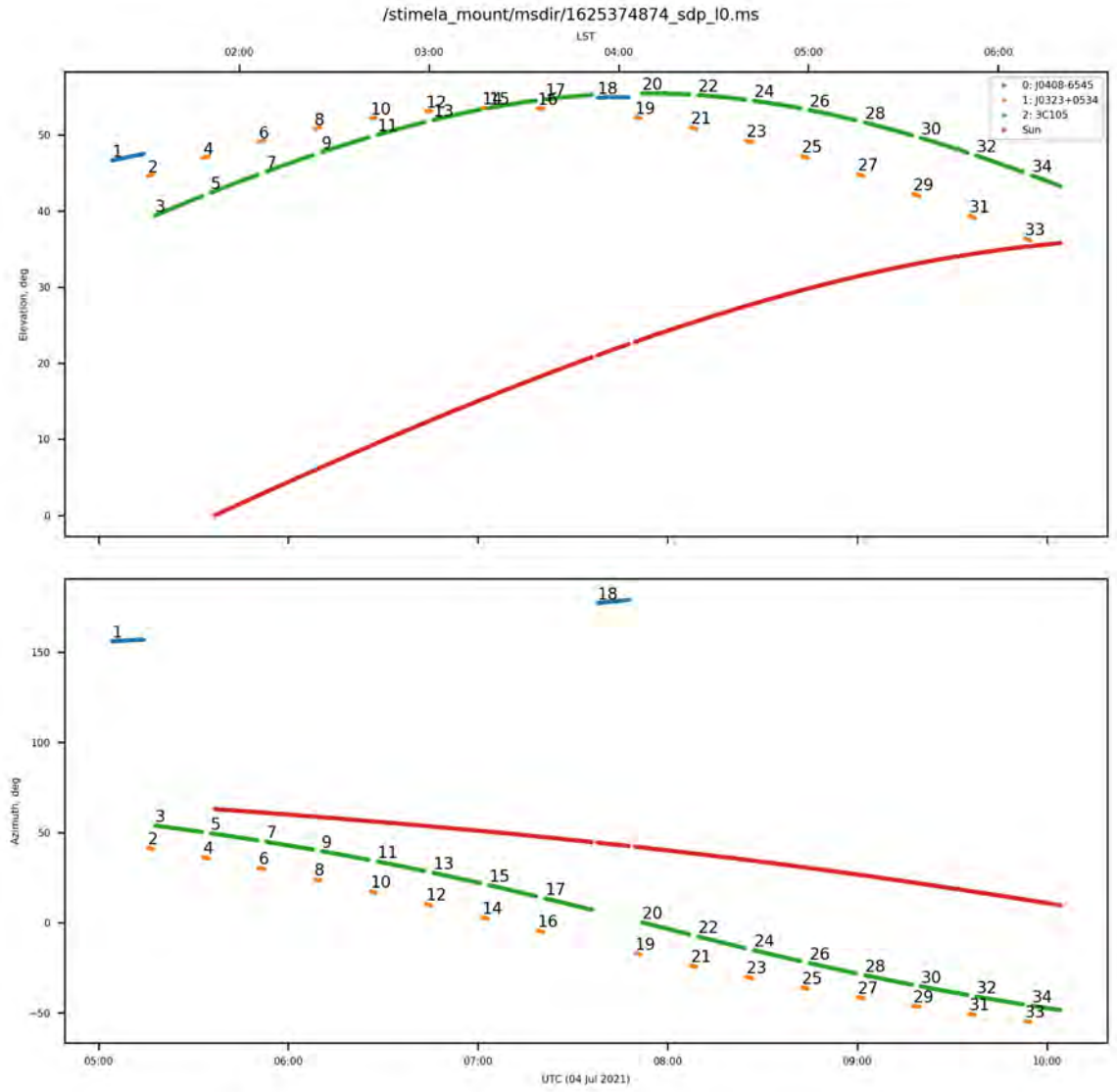

Figure 3.4: Example of the MeerKAT track for the bandpass calibrator J 0408-6545, gain calibrator J 0323+0534 and the target field 3C 105.

3.3 Data processing

The quantity measured by equation 2.6 is not the actual brightness distribution $V_{pq}(u, v)$ but rather affected by the corruption terms introduced by the atmosphere and by the instrumentation. As such, the data reduction processes transform this raw visibility data into a synthesised image of celestial objects in the sky. This process entails identification and excision of Radio Frequency Interference (RFI), calibration (including self-calibration), and aperture synthesis imaging.

3.3.1 RFI excision

RFI is inevitable when dealing with non-sensitive and highly sensitive instruments, presenting significant challenges, particularly in measuring the astrophysical signals that interest researchers. The signals due to RFI typically surpass the levels of natural emission from astronomical sources. Its causes vary, ranging from satellites passing overhead to various human-made sources. In some cases, the intensity of RFI can be several orders of magnitude higher than the natural emission from astronomical sources. However, there is a silver lining: RFI tends to manifest itself at specific frequencies and time intervals, making its localisation feasible. The general principle is to mitigate the RFI effects (normally seen as spikes or outliers) by flagging (see Offringa et al. [2012]). In particular, we use different pipelines to detect spikes and flag data. Under the hood, our pipelines utilise the Tricolour[4] package and AOflagger [Offringa et al., 2010], which employ Sumthreshold algorithm methods developed to improve the speed and efficiency of RFI identification and flagging [Offringa et al., 2010]. Additionally, the pipelines use CASA's tfcrop task McMullin et al. [2007] in some contexts (particularly when flagging calibrator data).

The outliers may be identified and masked. However, the remaining challenge lies in weaker RFI, which can be difficult to separate from the desired signal, especially when utilising automated flagging algorithms within data processing pipelines, especially flagging algorithms that necessitate meticulous fine-tuning to ensure accurate detection and isolation of the signal from the interfering RFI. At times, manual intervention becomes imperative for effective flagging of the data. Thankfully, the adverse effects of weak RFI on calibration solutions can be lessened by adopting appropriate calibration formulations.

3.3.2 A general view of calibration

In interferometry, calibration involves correcting instrumental variations, i.e., the time-dependent and frequency-dependent parameters within the observational data embedded in the propagation signal. In principle, the objective is to generate an accurate sky model and minimise disparities between the model-based estimates and the interferometer's actual observed measurements.

In simple RIME formalism, the RIME predicting the observed visibilities given a model can be written as

[4]https://github.com/ska-sa/tricolour

$$\mathbf{V}_{pq}^{\text{obs}} = \mathbf{J}_p \mathbf{V}_{pq}^{\text{model}} \mathbf{J}_q^H \tag{3.3}$$

where $\mathbf{V}_{pq}^{\text{model}}$ is the model visibilities corresponding to our sky model. We, therefore try to find the set of gain matrices J that minimises:

$$\chi^2 = \sum_{pq} \left\| \mathbf{V}_{pq}^{\text{obs}} - \mathbf{J}_p \mathbf{V}_{pq}^{\text{model}} \mathbf{J}_q^H \right\| \tag{3.4}$$

Generally, $\mathbf{J}_p$ is separated into a sequence of Jones terms, for example

$$\mathbf{J}_p = \mathbf{B}_p \mathbf{G}_p \mathbf{D}_p \mathbf{E}_p \mathbf{P}_p \mathbf{T}_p \tag{3.5}$$

Where $\mathbf{B}_p$ Jones term is the bandpass, $\mathbf{G}_p$ represents the antenna/receiver gain term, $\mathbf{E}_p$ is the beam gain and $\mathbf{D}_p$, $\mathbf{P}_p$, $\mathbf{T}_p$ are the polarisation leakage, parallactic angle rotation and atmospheric phase terms respectively. The order of RIME represents the causal order of effects.

The Jones term is determined through a non-linear fit to the measured visibilities. Corrected visibilities can then be obtained by applying the inverse of the estimated Jones matrices to the observed visibilities as

$$\mathbf{V}_{pq}^{\text{corr}} = (\mathbf{J}_p)^{-1} \mathbf{V}_{pq}^{\text{obs}} \left(\mathbf{J}_q^H\right)^{-1} \tag{3.6}$$

Calibration is commonly classified into three categories: reference calibration (see Section 3.3.2, DI self-calibration (Section 3.3.3) and DD self-calibration (Section 3.3.3). Consistent with the Noordam and Smirnov [2010] terminology, the categories are referred to as the first, second, and third generation calibration, respectively.

Reference Calibration

Reference calibration solves for direction-independent effects by using observations of a calibrator source. $\mathbf{V}_{pq}^{\text{model}}$ in equation 3.4 then originates from a calibrator source model. A good calibrator is typically a bright point-like source reasonably isolated from other bright sources. A primary calibrator establishes the flux scale and bandpass and must have a well-known flux and spectrum. Since such well-known sources are relatively few, a secondary calibrator nearer to the target field can constrain antenna gains and phases. A secondary need only be reasonably bright and point-like.

The instrumental correction, in particular the bandpass (incorporated in equation 3.5), complex gains and the delay errors, are estimated using these known parameters of the primary calibrator. They can then be interpolated onto the secondary, refined, and further interpolated onto the visibilities of the target field.

In practice, we use the following two pipelines, CAPTURE (CAsa Pipeline-cum-Toolkit for Upgraded Giant Metrewave Radio Telescope data REduction) [Kale and Ishwara-Chandra, 2020] and CARACal (Containerized Automated Radio Astronomy Calibration) [Jozsa and Perkins, 2021]. Both pipelines use CASA tasks under the hood for this purpose. Furthermore, CARACal offers alternatives for using calibrator models

through Meqtrees [Noordam and Smirnov, 2010] or Crystalball[5]. Typically, there are three effects solved for during reference calibration[6] regardless of the pipeline employed: delay, gain and bandpass, corresponding to the three types of Jones matrices above.

Delay calibration The physical nature of interferometers introduces a time difference in the radio signals received by different antennas defined in equation 2.1. The delay errors appear in frequency $\Delta\nu$ as a constant phase slope across the band $\Delta\phi$. We can define the difference across the band as

$$\Delta\phi = 2\pi\Delta\nu\left(\Delta\tau_g - \Delta\tau_r\right), \tag{3.7}$$

where $\Delta\tau_g$ is the differential geometric delay and $\Delta\tau_r$, the residual instrumental delay. The calibration is mostly achieved using a calibrator scan to solve for time-based antenna variations and deliver high signal-to-noise measurements. Appendix A.1 indicates the delay solutions. The delays range from One hundred picoseconds for all observations of the primary field. The vertical spread is the time variation in the solutions.

Bandpass calibration Understanding the spectral behaviour of a radio source is essential, therefore for calibration purposes it is important to measure and correct the frequency-dependent instrumental response, i.e. the bandpass. Its diagonal Jones matrix is given as

$$\mathbf{B} = \begin{pmatrix} b_x(\nu) & 0 \\ 0 & b_y(\nu) \end{pmatrix} \tag{3.8}$$

Bandpass corrections are generally derived by making scans of the primary calibrator, averaging the scans in time and solving for the complex gain in each channel against a model of the calibrator source $\mathbf{V}_{pq}^{\text{model}}$ in equation 3.4. The bandpass solutions in this work are displayed in Appendix A.2, indicating the amplitude variation and the phase across the band per antenna and correlation.

Gain calibration Freuency-independent antenna-based gains are determined as a function of time. The complex gains function $\mathbf{G}_{pq}(t)$ is approximated by a product of two associated antenna-based complex gains $g_p(t)$ and $g_q(t)$ whose amplitude and phase are determined via calibration. Phases are typically more variable than the instrument's amplitude and have an atmospheric component. It is therefore, important to use a calibrator source near the target field (hence, secondary calibrator), thus observing nearly the same atmosphere as at the centre of the observation field. The diagonal matrix of the complex gains function is given as

$$\mathbf{G} = \begin{pmatrix} g_x(t) & 0 \\ 0 & g_y(t) \end{pmatrix} \tag{3.9}$$

Appendix A.3 gives examples of the gain solutions for amplitude and phase corrections as a function of time.

[5]https://github.com/caracal-pipeline/crystalball

[6]Ignoring polarisation calibration, as it is outside the scope of this work.

uGMRT and MeerKAT observation overview.

Object name	Array	Obs_Date	ν (MHz)	$\Delta\nu$ (MHz)	Ch.-width (kHz)	t_{int} (∼hr)	FWHM $''\times''$,$^\circ$	RMS mJybeam^{-1}
3C 105	uGMRT	06 Sep 2020	700	300	48.82	3.86	7.67×2.84, -70	0.069
	MeerKAT	4 July 2021	1283	856	208.98	5.0	7.62×6.03, 0.89	0.110
3C 198	uGMRT	18 Nov 2022	700	300	48.82	5.54	4.39×3.46, 61.62	0.026
3C 227	uGMRT	18 Nov 2022	700	300	48.82	5.55	3.88x2.57, 64.05	0.116
4C -03.43	uGMRT	25 May 2019	700	300	48.82	3.16	4.96×4.12, 71.3	0.034
	MeerKAT	23 May 2021	1283	856	208.98	1.89	8.64×7.12, 145	0.023
		21 Aug 2021				6.94		
CGCG 047-067	uGMRT	08 Feb 2023	700	300	48.82	4.17	3.90×3.23, 45	0.018
	MeerKAT	31 July 2021	1283	856	208.98	5.04	10.03×6.93, 164.13	0.010
3C 403.1	uGMRT	10 Mar 2023	700	300	48.82	3.98	3.99×3.16, 50	0.021
3C 445	uGMRT	13 Dec 2022	700	300	48.82	6.21	4.42×3.45, 49.34	0.081
	MeerKAT	29 May 2021	1283	856	208.98	4.9	8.30×6.69, 151.7	0.020
NGC 7503	uGMRT	13 Dec 2022	700	300	48.82	6.60	4.43×3.54, 47	0.021
SDSS J 09157+1331	MeerKAT	25 June 2021	1283	856	208.98	5.20	10.75×6.09, 159.05	0.006
SDSS J 1120+0407	MeerKAT	23 May 2021	1283	856	208.98	1.89	9.524×5.52, -19.55	0.005
		21 Aug 2021	1283	856	208.98	6.53		

Column 1: Radio source name.
Column 2:The array used for observations.
Column 3: Observation dates
Column 4,5: Frequency and bandwidth using in observation MHz.
Column 5:Target source observation time.
Column 6:Full Width at Half Maximum of the Gaussian restoring beam's major and minor axis in arc seconds and the position angle (PA) in degrees quoted for each image.
Column 8: RMS noise of each image

3.3.3 DI Self-calibration

Self-calibration (often called Self-cal) involves refining the complex gain (amplitude and phase) over time. In principle, self-cal solves the complex gains while progressively refining the visibility model $\mathbf{V}_{pq}^{\text{model}}$. The process can be described as follows:

1. The initial model is derived from the corrected visibilities obtained by applying the reference calibration gains.
2. Find a gain matrix $\mathbf{J}_0$ that minimises equation 3.4 with a least square method, and compute a new set of corrected visibilities using equation 3.6.
3. Extract an improved model, $\mathbf{V}^{\text{model}}$ from the corrected visibilities,
4. Use the improved $\mathbf{V}^{\text{model}}$ from step 2 for another round of self-cal step and find the new gain matrix $\mathbf{J}$, then compute the corrected visibilities.
5. Since the procedure is iterative, repeat steps 3 and 4 till the corrected visibilities are satisfactory.

Specifically for self-cal pipelines for MeerKAT, we use CubiCal [Kenyon et al., 2018], QuartiCal [Kenyon et al., 2023] and WSClean imager (see Section 3.5.2). For the uGMRT self-cal, we refine the gains using CASA following the method described above.

DD self calibration

Traditional self-calibration assumes that all errors disturbing the visibilities are associated with the individual antennas [Pearson and Readhead, 1984]. However, this assumption is no longer valid when considering the impact of directional effects (DDEs) [Smirnov and De Bruyn, 2011]. DDEs introduce signal variations depending on the source's position relative to the field of view. These variations are not uniform across the entire view [Noordam and Smirnov, 2010]. Direction-dependent effects commonly encountered include the primary beam, atmospheric and ionospheric effects. DDEs can manifest as artefacts around dominant sources [Bhatnagar and Cornwell, 2017] and are addressed explicitly through a correction in a particular direction. Various techniques are deployed to calibrate the DDEs:

- Faceting − The basic principle of this technique is dividing the sky into multiple directions (facets) and solving for an independent gain term within a facet. This technique is implemented in the killMS[7] package. killMs implement the complex non-linear least-square solver ideas for the complex N-directional optimisation (COHJONES) algorithm [Smirnov and Tasse, 2015]. COHJONES accounts for interactions among directions, but it ignores antenna interactions. The gains are generally solved with a solution interval larger than the DI solutions [Smirnov and Tasse, 2015] to avoid overfitting and flux absorption.

[7] https://github.com/saopicc/killMS

The gain solutions for each direction are applied during imaging by the DDFacet [8] package.

- Peeling −Is a simpler technique for addressing DDEs. It generally follows the following sequence of steps:

  1. Derive the $\mathbf{G}_p$, the independent gain terms in equation 3.4, and simultaneously derive direction-dependent solutions for a small number (could be as small as one) of individual sources. An illustrative measurement equation for this can be given as

  $$\mathbf{V}_{pq} = \mathbf{G}_p \left(\sum_s \mathbf{E}_{s_0 p} \mathbf{X}_{spq} \mathbf{E}^H_{s_0 q} \right) \mathbf{G}^H_q, \tag{3.10}$$

  where $\mathbf{X}_{s_0pq}$is the coherency matrix of the source in the direction s_0.
  The resulting **E**-gain solutions tend to contain DD effects in the direction of the source s_0.
  2. The model of the problem source(s) is subtracted from the visibilities, using the **E** solutions, while the residual visibilities containing the whole sky are corrected for with $\mathbf{G}_p$.
  3. Optionally repeat steps 1 and 2.

  The CubiCal and QuartiCal packages solve the direction-independent gain term $\mathbf{G}_p$ while simultaneously solving for additional gain term $\mathbf{E}_{s_0p}$.

3.4 Synthesis Imaging

Radio synthesis imaging, at its simplest, entails transforming sampled visibilities into a representation of the sky. This procedure is grounded in the van Cittert Zernike theorem [Thompson et al., 2001], which establishes a connection between the observed visibilities and the actual distribution of sky brightness. Imaging is operated in three steps: 1) the inverse Fourier Transformation, 2) deconvolution and 3)iteration with self-calibration (Section 3.3.3 and 3.3.3).

We use Equation 3.11 to represent the observed visibility $\mathbf{V}(u, v)$.

$$A(l, m)I(l, m) = \int_{-\infty}^{\infty} \int_{-\infty}^{\infty} \mathbf{V}(u, v) e^{-2\pi I(ul+vm)} du dv. \tag{3.11}$$

Where $A(l, m)I(l, m) = I'(l, m)$ denotes the modified sky brightness distribution due to the antenna response pattern $A(l, m)$. The observed visibilities are sampled at discrete points within the u, v plane, therefore, only a certain fraction of Fourier modes are sampled. Hence, the observed visibilities can be given as

$$\mathbf{V}(u, v) = S(u, v) \int_{-\infty}^{\infty} \int_{-\infty}^{\infty} I'(l, m) e^{2\pi i(ul+vm)} dl dm. \tag{3.12}$$

[8] https://github.com/saopicc/DDFacet

i.e. as the sampling function $S(u, v)$ times the Fourier transform of true sky brightness. Due to the incompleteness of the u, v plane sampling, we have a corresponding structure in response to a point source known as the Point Spread Function (PSF). The PSF is the Fourier transform of the weighted (u, v) coverage. Thus, we can write it as

$$PSF(l, m) \rightleftharpoons S(u, v). \tag{3.13}$$

The equivalent of equation 3.12 in the image domain is the convolution of the $PSF(l, m)$ and the true sky brightness $I'(l, m)$, resulting in a so called dirty image $I^D(l, m)$:

$$I^D(l, m) = PSF(l, m) * I'(l, m). \tag{3.14}$$

where $*$ represents the convolution operator.

The radio synthesis imaging process also involves deconvolution, a subsequent way of compensating for the effect of the PSF (equivalently, for interpolating the missing Fourier modes of the sky that the array does not sample). Deconvolution is typically performed as a combination of minor and major cycles. The minor cycle is purely image-based, and updates a model of the sky. The major cycle inverts the accumulated sky model into visibilities and subtracts it from the data, producing a dirty residual image for the next minor cycle. The most widely-used deconvolution algorithms are based on CLEAN [Högbom, 1974] for deconvolution. The CLEAN algorithm is summarised as follows:

1. The peak intensity of a potential source is located in the dirty image $I^D(l, m)$.
2. The PSF, scaled up by the source flux, and multiplied by loop gain γ (typically 0.1), is subtracted from the dirty image at each source's location.
3. The model $I^m(l, m)$ is updated with the flux that is subtracted at the source's position.

This forms the minor cycle of deconvolution. Note that the minor cycle iterations halt when the peak pixel within a mask falls below the threshold or when the maximum number of iterations is reached.

In practice, Multiscale [Cornwell, 2008] extension and Multiscale with Multi-frequency extensions are implemented by t-clean and WSClean. The difference lies in the peak identification and subtraction. Instead of identifying and subtracting individual delta functions, Multiscale CLEAN extends the approach by considering the different spatial scales and subtracting blobs [Offringa and Smirnov, 2017, Rich et al., 2008].

3.5 Visibility weighting

Weighting functions (applied in the u, v plane) change the PSF structure to maximise an image's sensitivity or resolution. Commonly employed weighting schemes are:

Natural weighting: Every visibility in the u, v grid is given a weight inversely proportional to its variance (thermal noise). This results in the highest sensitivity, but for

core-dense arrays like MeerKAT, produces a very wide PSF main lobe (compromising resolution) and high PSF sidelobes.

Uniform weighting: the u, v plane is divided into grid cells, and each cell's visibilities are weighted so that each cell has equal (uniform) total weight. Since the inner part of the u, v plane has more samples, uniform weighting will aggressively down-weight the short baselines. This scheme achieves the highest resolution and low PSF sidelobes but significantly trades off resolution.

Briggs weighting is a commonly used compromise scheme [Briggs, 1995]. The method trades off between maximizing resolution and minimizing PSF sidelobes using a robustness parameter r, which smoothly varies between effectively natural weighing ($r = 2$) and effectively uniform weighting ($r = -2$) [Rau et al., 2009]. A typical value used for MeerKAT and uGMRT imaging is $r = 0$.

The imaging parameters are modified depending on the data as follows:

3.5.1 t-clean

The uGMRT images are produced with t-clean, imaged the field in at least $\sim 2.3^\circ \times 2.3^\circ$ to deconvolve bright sources outside the primary beam. We use the Multi-term Multi-Frequency Synthesis (MT-MFS) deconvolution algorithm that accounts for the frequency dependence variations [Rau and Cornwell, 2011], complemented by the multiscale clean. To model the emission around the extended source structure, the number of iterations was set to 2500, increasing each cycle by a factor of 2. The procedure yielded more improved images due to better residual construction per cycle. Masking was set to auto-multi threshold, which automatically determines the threshold for cleaning, with the minimum threshold set to 0.01. We used a Briggs robustness parameter of $r = 0$ to image the large-scale structure without compromising sensitivity and resolution.

Table 3.2: t-clean parameters used in CASA. Where their different parameter values were used. Default parameters are not listed.

Clean keyword	value
`Threshold`	0.001 mJy
`Specmode`	'mfs'
`Deconvolver`	'mtmfs'
`nterms`	2
`Multiscale`	0, 5, 15
`Robust`	0.0

3.5.2 WSClean

We use the CARAcal pipeline for imaging; it incorporates the WSClean imager for deconvolution and imaging purposes. WSClean implements multiscale and wideband

deconvolution algorithms suitable for imaging extended radio galaxies with diffuse emission. Deconvolution was carried out jointly in eight subbands; each band was deconvolved separately using the joint-channel deconvolution mode. A Briggs weighting scheme was used with a robustness parameter $r = 0$. The resulting angular resolution is given in Table 3.3.2. Below, we give the parameters for imaging the visibility data for uGMRT and MeerKAT.

Table 3.3: Summary of the WSClean imaging parameters used in making the radio maps within this work. Column 2: the WSClean parameter name that takes the values stated in Columns 3 and 4.

Parameter	WSClean name	uGMRT Value	MeerKAT Value
Image size	-size	10000, 10000	10240, 10240
Polarization	-pol	I	I
Cell size	-scale	0.5asec	1.0asec
Weighting	-briggs	0	0
Deconvolution	-multiscale-scales	0,5,15 × beam	0,10,20,40 × beam

3.5.3 Primary beam corrections

By definition, the primary beam is a trivial DD effect Smirnov [2011b] if it is identical for every antenna in an array and constant in time; as such, it can be treated as part of the sky. The process corrects the flux scales of sources while increasing the map's noise from the centre to the beam edge.

The attenuations caused due to the primary beam response are corrected using the CASA task wbpbgmrt[9] for the uGMRT corrections. An eighth-order polynomial equation can typically represent the uGMRT or MeerKAT's primary beam. The fitted polynomial is given by

$$f(x,y) = 1 + \left(\frac{a}{10^3}\right)x^2 + \left(\frac{b}{10^7}\right)x^4 + \left(\frac{4}{10^{10}}\right)x^6 + \left(\frac{d}{10^{13}}\right)x^8 \qquad (3.15)$$

Here, x represents the separation from the pointing position in arc-minutes times the frequency in GHz. The coefficients a, b,c and d determine the shape of the polynomial curve. For band-4 (550-850 MHz), the values of the coefficients are $a = -3.190$, $b = 38.642$,$c = -20.471$ and $d = 3.964$. We use these primary beam parameters provided to make corrections.

For the MeerKAT primary beam corrections, a traditional approach was followed involving the division of the final image by a pre-existing model of the primary beam pattern generated through the KATBEAM package[10], incorporated within the OXKAT script[11].

[9]https://github.com/ruta-k/uGMRTprimarybeam.git
[10]https://github.com/ska-sa/katbeam
[11]https://github.com/IanHeywood/oxkat/tree/master/oxkat

3.6 Individual radio sources

This Section briefly summarises the literature review of the individual galaxies presented in this work.

- 3C 105 is a classical FR II radio source, associated with an elliptical galaxy of magnitude m_r=17.6 (NED) located at redshift z=0.089 [Madrid et al., 2006]. The radio source is a typical narrow-line radio galaxy (NLRG) with only nuclear emission lines [Baum et al., 1995, Smith and Heckman, 1989, Tadhunter et al., 1998]. The classical radio source was first classified as a type 2 Seyfert galaxy, subsequently as a highly absorbed and highly luminous FR II source with luminosity of 4.45×10^{44} erg sr^{-1} [Ajello et al., 2008]. 3C 105 have been detected in X-ray observations, Massaro et al. [2010] detected the X-ray emission from the core and the southern hotspot; the two regions are locations where the radio jets appear to enter the hotspot region, as well as from the brightest radio emission at the terminal hotspot, itself. Orienti et al. [2012] reported on the emission associated with low-power southern radio hotspots in a radio source, where they detected optical emission in the same hotspots, which implies the presence of continuous re-acceleration of particles in these regions. Recently, Murray et al. [2021] detected the HI absorption in this galaxy, including the nuclear-extended outflows of ionised gas in the radio galaxy.

- 3C 198 is classified as FR I radio source associated with an elongated elliptical galaxy, m_g=17.3 (NED) located at redshift, z=0.081. No recent deep imaging and detailed study of this source has been conducted in the radio band. The optical emission lines of the optical counterpart are consistent with star formation [Buttiglione et al., 2010, Baldi and Capetti, 2008].

- 3C 227 is an FR II radio galaxy associated with a m_g =16.7 quasar at z=0.085 (NED). It is aligned east-west, with multiple emission peaks in each hot spot. It exhibits a nuclear outflow [Speranza et al., 2021]. The multiple hotspots are detected up to very high energy as a result of particle re-acceleration (NIR, optical, X-ray emission, see Migliori et al. [2020] and Orienti et al. [2020], respectively). The hotspots are polarised Orienti et al. [2020].

- 4C -03.43 is a classical FR I radio galaxy at z=0.0554 (m=15.22, NED). It is characterised by two symmetric jets which open up and spread into two lobes. The extension of both lobes gives the source an S shape and suggests that projection effects play a relevant role here. The radio galaxy is associated with the brightest cluster galaxy (BCG) in the cluster Abell 1308 at z=0.0519 [Postman and Lauer, 1995]. Very little literature information is available for this radio galaxy.

- CGCG 047-067 is an FR I radio galaxy hosted by an optical counter- part with magnitude m_g=14.9 at redshift z = 0.055901 (NED). Very little information is

available in the literature for this radio galaxy, and no detailed radio studies exist. Kuźmicz et al. [2018] included it in a sample of giant radio galaxies, reporting a total size of 0.7 Mpc. The source appears in the G4 Jy sample as G4 Jy 1173, classified as a bent tail morphology, with double elongated and possibly L-shaped structure [White et al., 2020a,b]. Very little is known about its environment. A galaxy group is reported in the literature at the redshift and position of CGCG 047-067 (MSPM 01896, Smith et al. [2012]).

- 3C 403.1 is an FR I radio galaxy associated with a magnitude m_g=17.5 (NED) at redshift z=0.055. Missaglia et al. [2022] recently conducted a radio/optical study and concluded that the radio galaxy is part of a low-mass poor group. The radio galaxy belongs to the MURALES sample Speranza et al. [2021], Balmaverde et al. [2019, 2021], which was investigated for nuclear outflows. None was detected.

- 3C 445 is another nearby FR II radio galaxy, located at z=0.0568 [Kronberg et al., 1986]. The associated optical counterpart, a m_r =15.2 (NED) elliptical galaxy possessing an exceptionally bright and compact central region [Madrid et al., 2006]. A typical BLRG, with a broad emission spectrum in its optical spectrum [Eracleous and Halpern, 1994]. With a linear size of ∼630 kpc, it belongs to the class of giant radio galaxies. It is aligned along the north-south direction, and the northern hotspot has multiple peaks [Kronberg et al., 1986]. 3C 445 has been a subject of X-ray observation (e.g., Perlman et al. [2010], Grandi et al. [2007], Sambruna et al. [2007], Grandi et al. [2004], Orienti et al. [2012]). Moreover, both the hot spots of 3C 445 are observed in multiple optical and near-IR bands [Prieto et al., 2002, Mack et al., 2009] and have been investigated in detail with the Jansky Very Large Array (JVLA) at 22 GHz to study the distribution of the strong shocks in the hotspot region [Orienti et al., 2020]. The radio galaxy was imaged at high angular resolution with the Very Large Array (VLA) in Leahy et al. [1997], where the two inner compact components located north and south of the core and aligned along the jet direction (labelled N1 and S1 in their paper) were identified. These two components and their alignment with the direction of the outer hot spots suggest a double-double radio galaxy.

- NGC 7503 is a narrow-angle-tailed radio galaxy associated with a bright (V= 13.5) galaxy at z= 0.044 in the Pegasus II cluster (Zw 2307.6+0713, Z8852). The cluster shows X-ray emission (MCXC J2310.4+0734, Piffaretti et al. [2011]). The optical counterpart lies at $\sim 5'$ in projection from the cluster centre, dominated by the BCG NGC 7499 (V= 13.00), and only ∼ three from NGC 7501, (V= 13.4).

- SDSS J 1120+0407 is associated with the galaxy CGCG 039-127, with a m_g = 15.4 and z=0.049655 (NED), and

- SDSS J 09157+1331 is associated with WISEA J091754.26+133145.5, with magnitude $1m_g$=7.79 and located at a similar redshift (z=0.049932, NED). The op-

tical counterpart is an early-type galaxy in both cases, and the radio source is classified as FR 0. They are both characterised by the lack of extended radio lobes and have the same core properties as FRI [Baldi et al., 2019]. [Capetti et al., 2020] reported on the LOFAR detection of SDSS J 091754+133145 at 144 MHz, while no emission was revealed for SDSS J 112029+040742.

Chapter 4

The MeerKAT and uGMRT view of the radio sample

The uGMRT and MeerKAT observations provide detailed state-of-the-art images of the radio galaxies in our sample. The angular resolution of the uGMRT offers valuable insights into the structure of the hotspots. At the same time, the MeerKAT image is more effective in showcasing the intricate features and overall extent of the lobes. The overlay of uGMRT and MeerKAT contours on the DSS-II (red band) optical image and the contours with MeerKAT data provide a comprehensive view of our capability to capture detailed radio morphologies. Complemented by a colour scale indicating contour levels, these images affirm the detailed radio features for nearly all the observed sources. The salient features of the radio morphologies belonging to the most prominent and prevailing radio sources have been meticulously detailed in Tables 4.1 and 4.2. Furthermore, we offer a supplementary description of the radio morphologies exhibited by the radio sources, presented in the sequence provided in Table 3.1.

4.1 The morphology

Each source presented in this thesis shows features that deserve attention, individually discussed in the next subsections.

4.1.1 Radio flux density measurements

Having produced the radio images, the initial task is typically to use those images to determine the flux density of the source as well as the background noise in the images. We measure the background noise in the images by taking the RMS of the pixel values in clean and source-free regions in the images before primary beam corrections given in Table 3.3.2.

Measuring the flux densities requires specifying the polygon region enclosing the radio source emission. Since source extraction methods using Gaussian fitting algorithm methods lead to a possible underestimation of the integrated flux densities, significantly if the emission is extended, to measure the flux densities, we manually select

the radio source emission region using CARTA[1] and obtain the source statistics. Optionally, the region can be saved into a CASA region file with the extension ".crtf" used to determine the fluxes in alternative methods. The alternative way of manually measuring flux density is to define the radio source regions and estimate the fluxes using the *imfit* CASA task, which automatically fits a single Gaussian to the peak emission and provides the statistical information as *imstat* favourably works for point sources (e.g. FR 0). However, radio galaxies are generally not Gaussian, as information derived from a single Gaussian fit may not accurately represent the source. The total flux density of each radio source and its component are given in Table 4.1 centred at 1.28 GHz ($S_{1.28\ GHz}$) and Table 4.2 at 700 MHz ($S_{700\ MHz}$).

4.1.2 Flux density error estimates

The corresponding measurements of uncertainties for the flux density (ΔS_ν) consist of three factors following Klein et al. [2003]:

- The calibration error $\xi_{\rm cal}$: the calibration error of the maps are estimated at $\sim 3\%$ and 5% for the MeerKAT and uGMRT, respectively [2]. It includes the flux scale uncertainty, primary beam uncertainty, and possible signal loss due to missing spatial scales.
- The noise uncertainty σ: taking the local rms noise extracted from the source free region of the image multiplied by the square $N_{\rm beam}$ defined below.
- The number of beams covering the extended source $N_{\rm beam}$: the number of points in the entire radio emission of the source divided by the beam area ($A_{\rm beam}$) in pixels.

The flux density error can be estimated using the equation.

$$\Delta S_\nu = \sqrt{(\sigma \cdot \sqrt{N_{beam}})^2 + (\xi_{cal} \cdot S)^2}, \tag{4.1}$$

Where S_ν is the total flux density of a source.

[1] https://github.com/CARTAvis/carta/releases/tag/v4.1.0

[2] The residual errors for MeerKAT and uGMRT in each image are 3% and 5%, respectively.

Table 4.1: MeerKAT observation parameters

Object ID	z	Scale kpc/″	LS Mpc	$S_{1.28\,GHz}$				$P_{1.28\,GHz}$ WHz^{-1}
				S_{tot} Jy	Core mJy	Hotspot mJy	Lobes mJy	
3C 105	0.089	1.673	0.61	6.60±0.3	50±4.8	NW: 28.7±4.1 SW: 3080±130	NW: 340±12 SW: 1093±49	1.31×10^{26}
3C 198	0.081	1.537	0.71	2.12±0.01			SW: 939±23 NE: 683±15	3.94×10^{25}
4C −03.43	0.0519	1.019	0.64	1.08±0.05	271±17		N: 127±3.8 S: 249.8 ± 7.6	6.91×10^{24}
CGCG 047-067	0.0548	1.072	0.9	2.39±0.01			N: 3530±120 SE: 1741±68	1.71×10^{25}
3C 403.1	0.055	1.076	0.49	1.93±0.03				1.39×10^{25}
3C 445	0.0562	1.098	0.63	6.46±0.32	83.3±7.8	$N_{Outer_{pr}}$: 461±8.7 $N_{Outer_{Se}}$: 273±24 N_{Inner}: 64.9±5.5 S_{Outer}: 658±25 S_{Inner}: 88.4 ±8.1	N: 1401±23 S: 2240±37	4.89×10^{25}
SDSS J 09157+1331	0.055	1.076		2.20e-02	22±0.72			1.30×10^{23}
SDSS J 1120+0407	0.055	1.076		6.96e-03	6.96±0.21			4.12×10^{22}

Scale: kpc/″ to kpc conversion. LS represents the linear size of the radio sources in Mpc.

Table 4.2: uGMRT observation parameters

Object ID	z	Scale kpc/″	LS Mpc	$S_{700\,MHz}$				$P_{700\,MHz}$ WHz^{-1}
				S_{tot} Jy	Core mJy	Hotspot mJy	Lobes mJy	
3C 193	0.081	1.537	0.74	3.91±0.07			NE: 576±12	6.36×10^{25}
3C 227	0.085	1.606	0.51	12.56±0.02	58±5	$W_{Primary}$: 570±34 $W_{Secondary}$: 239±83	W: 4950±120	2.24×10^{26}
4C −03.43	0.0519	1.019	0.64	1.45±0.62	321±25	SE: 3000±240	SE: 2967±16 N: 134.9±4.8 S: 281±13	9.26×10^{24}
CGCG 047-067	0.0548	1.072	0.89	3.54±0.17	47.5±1.5		N: 2272±57 SE: 2755±56	2.53×10^{25}
3C 403.1	0.055	1.076	0.48	1.65±0.01	15.1±1.7			1.19×10^{25}
NGC 7503	0.044	0.872	0.01	2.58±0.02	53.6±2.3			1.17×10^{25}

4.1.3 3C 105

The flux density of the radio galaxy as detected by MeerKAT is $S_{1.28\ GHz}$=6.60±0.30 Jy, corresponding to a radio power $P_{1.28\ GHz} = 1.32\times10^{26}$ WHz^{-1}. Its total size is $\sim$ 485 kpc. The total intensity image reported in Figure 4.1 shows a north-western jet is fairly straight. It shows several emission peaks before ending in the hotspot, which extends perpendicularly to the direction of the jet. Leahy et al. [1997] described this hotspot as a hammerhead structure, possibly indicating a recent escape of the lobe from a strongly bounded halo surrounding the host galaxy. The southeastern jet shows a substructure with two parallel ridges of emission (or trail of emission) from the hot spots back towards the centre, interpreted as backflow emission, possibly due to a potential contact discontinuity.

4.1.4 3C 198

Only the uGMRT image is available for this radio galaxy. Its total flux density at 700 MHz is $S_{700\ MHz}$= 3.91± 0.07 Jy. for a radio power of $P_{700\ MHz} = 6.36\times10^{25}$ WHz^{-1}. The MeerKAT flux density of the radio galaxy is $S_{1.28\ GHz}$= 2.42± 0.01 Jy for the radio power of $P_{1.28\ GHz} = 3.94\times10^{25}$ WHz^{-1} [Sejake et al., 2023]. The uGMRT and MeerKAT images are similar regarding the emission extent and details of the source, e.g., the filaments embedded in the lobes and the extension perpendicular to the source major axis (see Figure 4.2).

The uGMRT and MeerKAT radio contours, including the radio-optical overlay, are shown in Figures 4.2 and 4.3. The source has the largest linear size of $\sim$ 650 kpc and can be considered a giant radio galaxy. Our observations reveal an intriguing morphology: no bright hot spots are visible, even though the surface brightness shows edge brightening at the extreme end of the lobes. Table 4.2 outlines the lobes with a diffuse low surface brightness emission. The source shows no compact features, which can be associated with the core or hot spots, and the lobes show very low surface brightness. The optical counterpart is not apparent. Such diffuse radio emission is extremely filamentary. At low frequencies, we are unable to detect radio nuclei.

4.1.5 3C 227

Only uGMRT imaging is available for this FR II radio galaxy. The radio emission is aligned in the east-west direction for a total size of $\sim$ 505 kpc. Its total flux density at 700 MHz is $S_{700\ MHz}$ =12.46± 0.02 Jy, for a radio power of $P_{700\ MHz} = 2.24\times10^{26}$ WH^{-1}. Our total intensity image is shown in the top panel of Figure 4.4. The high angular resolution of the uGMRT images confirms that the western hot spot has multiple peaks (double hotspots); the twin hotspots in 3C 227 could be explained by the mechanism of stream splitting, where the jet splits into two stable and long-lasting flows, indicating an ongoing high energy particle acceleration [Horton et al., 2023, Hardcastle et al., 2007]. The two parallel ridges detected at 22 GHz in the eastern hot spot [Orienti et al., 2020] are not resolved at our angular resolution, which, on the other hand, highlights a trail of emission from the hot spot towards the core. The diffuse backflow

emission from the lobes broadens as they propagate away from the hot spots. The two lobes are not symmetric in flux density, the eastern being stronger (with a flux density equivalent to $S_{700\ MHz}$= 4.95±0.12 Jy) and characterised by filamentary emission.

4.1.6 4C -03.43

The flux density of the radio galaxy is $S_{1.28\ GHz}$=1.08± 0.07 Jy, for a radio power of $P_{1.28\ GHz}$ = 6.91×10^{24} WHz^{-1}. The uGMRT flux density of the radio galaxy is $S_{700\ GHz}$=1.45± 0.07 Jy. Figure 4.5 and Figure 4.6 show an intriguing orientation of jets within a radio galaxy. The jets connect to the outer lobes while displaying a faint backflow directed towards the central region. The bending of the lobes with respect to the jet orientation, which gives rise to an S-shape, suggests a wide-angle-tailed radio galaxy seen face-on. The overall linear size of the source measures approximately 408 kpc. The source is overall symmetric, with radio jets of comparable length. The radio galaxy belongs to the galaxy cluster A 1308. It is associated with a m=15.22 galaxy, which could well be the dominant galaxy in the cluster, in support of a possible WAT seen face-on. Rector et al. [1995] suggests that the orientation rises due to the source's rotational dynamics, as opposed to motion through the surrounding external medium when viewed in projection. The jets' alignment is particularly noticeable as they extend towards the southwest and northeast ends. The radio galaxy shows bright spots resembling "knots," likely caused by clumpiness in the underlying medium, leading to turbulence within the jet, further enriching the details of the jet morphology. The 4C -03.43 morphology arrangement shares similarities with the structure observed in the radio galaxy M 84. The jets in M 84 are speculated to have undergone a possible precession [Bambic et al., 2023]. The observed system's aspect is the radio galaxy's interaction with its environment. The southern lobe of 4C -03.43 appears to experience compression due to ram pressure as the galaxy moves through the intracluster medium (ICM). The northern jet bend point also exhibits a possible interaction with a density contact discontinuity, suggesting a change in density within the surrounding medium influences the jet's trajectory [Chibueze et al., 2021].

4.1.7 CGCG 047-067

The flux density of the radio galaxy is $S_{1.28\ GHz}$=2.39± 0.01 Jy, for a radio power of $P_{1.28\ GHz}$ = 1.71×10^{25} WHz^{-1}. The uGMRT flux density of the radio galaxy is $S_{700\ GHz}$=3.54± 0.17 Jy. The MeerKAT and uGMRT images are shown in Figures 4.7 and Figure 4.8. The total size of CGCG 047–067 (i.e. the sum of the length of the northern and southern lobe) reaches a value of $\sim$ 950 kpc; hence, it can be considered a giant radio galaxy. The radio galaxy exhibits the characteristics of a typical wide-angle tail (WAT) radio galaxy. A pronounced elongated jet extends towards the north, spanning an impressive linear size of approximately 725 kpc. The opposite radio jet is bent towards the south-east of the source, giving an overall L-shaped appearance. The radio emission of the southeastern lobe has a very bright region, which lacks an optical counterpart, so we consider this a feature of the radio lobe itself. One possible explanation for this high brightness emission region is that we view the lobe edge-on and the radio emission results from integration along the line of sight. The radio

galaxy has a bright optical counterpart, with m_g=14.9, which, combined with the radio morphology, suggests that the source is associated with the dominant member of the group to which it belongs (MSPM 01896, [Smith et al., 2012]).

4.1.8 3C 403.1

The radio galaxy's flux density at 1.28 GHz is measured at $S_{1.28\ \mathrm{GHz}}$ = 1.93± 0.03 Jy, corresponding to a radio power of $P_{1.28\ \mathrm{GHz}} = 1.39\times10^{25}$ WHz−1. At 700 MHz, the uGMRT flux density is recorded at $S_{700\ \mathrm{MHz}}$=1.45± 0.08 Jy. The uGMRT and MeerKAT radio contours, including the radio-optical overlay bottom panel, are shown in Figure 4.9 and 4.10. The observations indicate a peculiar morphology, extending approximately 389 kpc in the south-east and north-west directions. A large-scale structure at high and low frequencies reveals faint hotspots; the brightness peak in the north-western jet might indicate a potential hot spot. This could potentially be categorised as FR II, although it remains ambiguous. The FR IIs typically have nearly invisible jets, suggesting higher efficiency, but in the case of 3C 403.1, apparent jets are visible, favouring classification as FR I. An interesting diffuse emission feature is observed, a ridge north of the western jet and the starting point of the southeastern jet, possibly linked to the nuclear emission at a particular stage of the source's lifespan. Despite the uncertainty, this feature is deemed significant and warrants inclusion in the analysis as it is unlikely to be an artefact of the imaging process (observed in 3C 465 [Eilek et al., 1984]).

4.1.9 3C 445

The flux density of the radio galaxy is $S_{1.28\ \mathrm{GHz}}$ = 6.46± 0.32 Jy, for a radio power of $P_{1.28\ \mathrm{GHz}} = 4.89\times10^{25}$ WHz^{-1}. The source has a total size of $\sim$ 630 kpc, thus a giant radio galaxy based on this criterion. The total intensity image reported in Figure 4.11 and Figure 4.12 shows a north-south alignment, with a substructure in the northern hot spot. In particular, as already noted by [Leahy et al., 1997], beyond the most compact component, a more diffuse secondary shock is present north-west of the source. This could be explained in the scenario of splatter splitting, where a secondary shock is formed due to the deflection of the supersonic collimated jet interacting with the ambient medium. Moreover, a third, fainter small component is situated between the initial and secondary hotspots. It is worth mentioning that none of these compact features displays an obvious optical counterpart, which argues in favour of emission associated with 3C 445. Our images show that the southern hotspot is a single feature at the resolution of a few arcseconds. One of the most intriguing features of this radio galaxy is the presence of two inner hot spots aligned along the same major axis. Both of them are resolved along the major axis. If we are in front of a double-double radio galaxy, the size of the restarted emission is $\sim$ 150 kpc.

4.1.10 NGC 7503

The radio emission associated with NGC 7503 is shown in the top left panel of Figure 4.13. It exhibits an amazing narrow-angle tail radio emission, with fairly collimated

jets and the tails extending in the northern direction for $\sim$ 160 kpc. The jets propagate for $\sim 55 - 78$ kpc for the eastern and western jets, respectively. The western jet culminates in a feature which could be considered a hot spot, after which collimation is lost, and the tail propagates towards the north. The radio emission in both tails shows fine structure at the angular resolution of our observations, with wiggles and thin filaments. In particular, a thin filament extends from the eastern jet into the corresponding lobe (see Figure 4.13, and another extends from the western lobe into the ICM. This filament shows a "fork", a feature which is becoming common when radio galaxies are imaged at high sensitivity and angular resolution. The total flux density of this source is $S_{700\ \mathrm{MHz}}= 2.58\pm 0.02$ Jy, corresponding to a radio power of $P_{700\ \mathrm{MHz}} = 1.17\times10^{25}$ WHz^{-1}. This radio power is high for narrow-angle-tailed radio galaxies but consistent with the asymmetric morphology of the jets and the presence of one hot spot. The optical counterpart is quite bright, too.

The local environment of NGC 7503 is extremely interesting. The two bright nearby galaxies, i.e. the BGC NGC 7499 (V=13.00, z=0.039) and NGC 7501, (V=13.4, z=0.043), are radio loud, too. NGC 7499 is a typical FR I radio galaxy (see also Hogan et al. [2015]) $\sim$ 70 kpc in size, with total radio power $P_{700\ \mathrm{MHz}} = 4 \times 10^{23}$ WHz^{-1}. The two lobes are detached from the nuclear emission coincident with the optical host, with thin and weak filaments bridging the gap with the radio core. The two lobes are not perfectly aligned but form an angle of $\sim 120^{\circ}$, suggestive of motion towards the north in the plane of the sky. NGC 7501 is charachterised by compact radio emission with $P_{700\ \mathrm{MHz}} = 2.6 \times 10^{22}$ WHz^{-1}. It could be an FR 0 radio galaxy.

4.1.11 SDSS J 09157+1331

Only MeerKAT imaging is available for this FR 0 radio galaxy. The radio emission superposed on the optical frame is shown in Figure 4.14 top panel, and the radio-optical overlay are shown in Figure 4.15. At this resolution and frequency, we detect the compact radio galaxies with a flux density of 23.98±0.72 mJy and the radio power of $P_{1.28\ \mathrm{GHz}}=1.42 \times 10^{23}$ WHz^{-1} with a deconvolved angular size of $40''$.

4.1.12 SDSS J 1120+0407

The MeerKAT images lack obvious spatial extended emission around the source, the main defining property of the FR 0 class. The MeerKAT radio contours and the radio-optical overlay are shown in Figure 4.14 and 4.15 bottom panel. This radio source is as bright as 7.20±0.21 mJy, and the radio power of $P_{1.28\ \mathrm{GHz}}=4.22\times 10^{22}$ WHz^{-1}. The measured flux density measurements agree with the values from the 1.4 GHz NVSS Table 3.3.2, implying a consistency of fluxes between the 1.28 GHz and the 1.4 GHz.

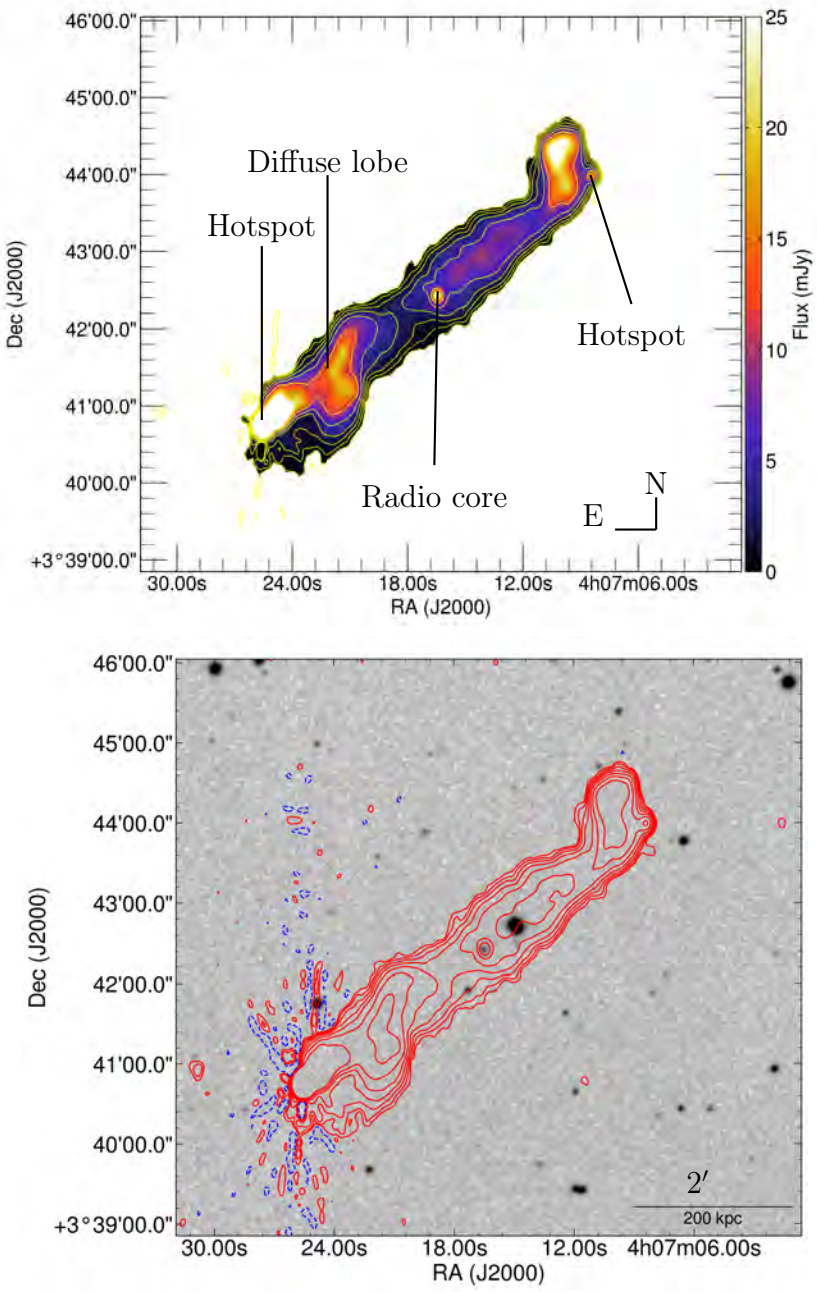

Figure 4.1: The MeerKAT total intensity image of 3C 105 (top panel). The lowest radio contour plotted is three times the total RMS noise (see Table 3.3.2 and increases by a factor of two. The MeerKAT radio contours are overlaid on the DSS-II (red band) optical image in a grey scale. The red surface brightness contours are plotted in the image, including the first negative surface brightness contours. The levels are drawn as RMS=0.069 mJy/beam × -1,1,2.., increasing by a factor of 2.

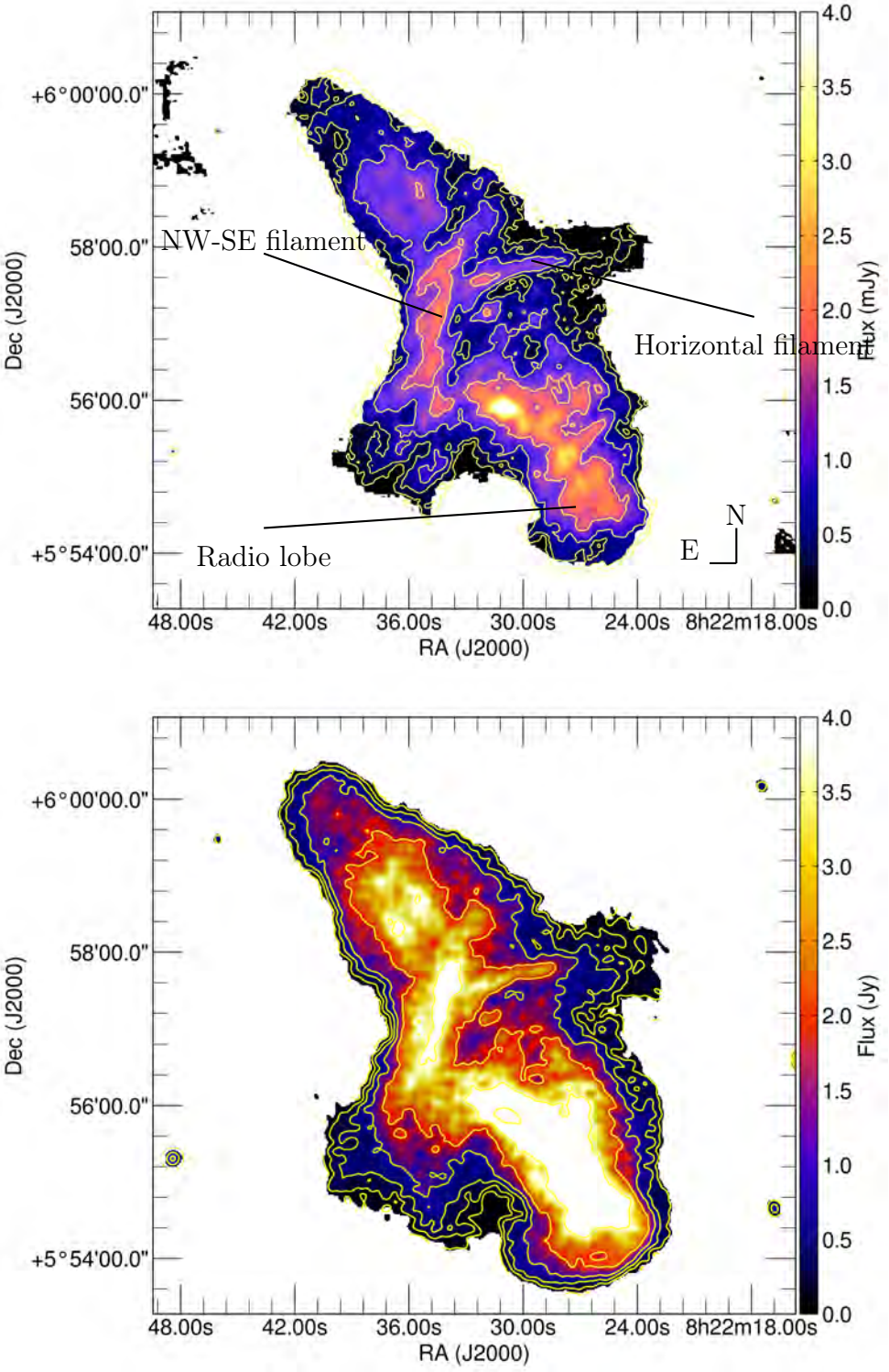

Figure 4.2: The uGMRT Band-4 (top panel) and MeerKAT (bottom panel) radio image of 3C 198, the contours are three times multiple of the RMS noise in the image, increasing by a factor of two.

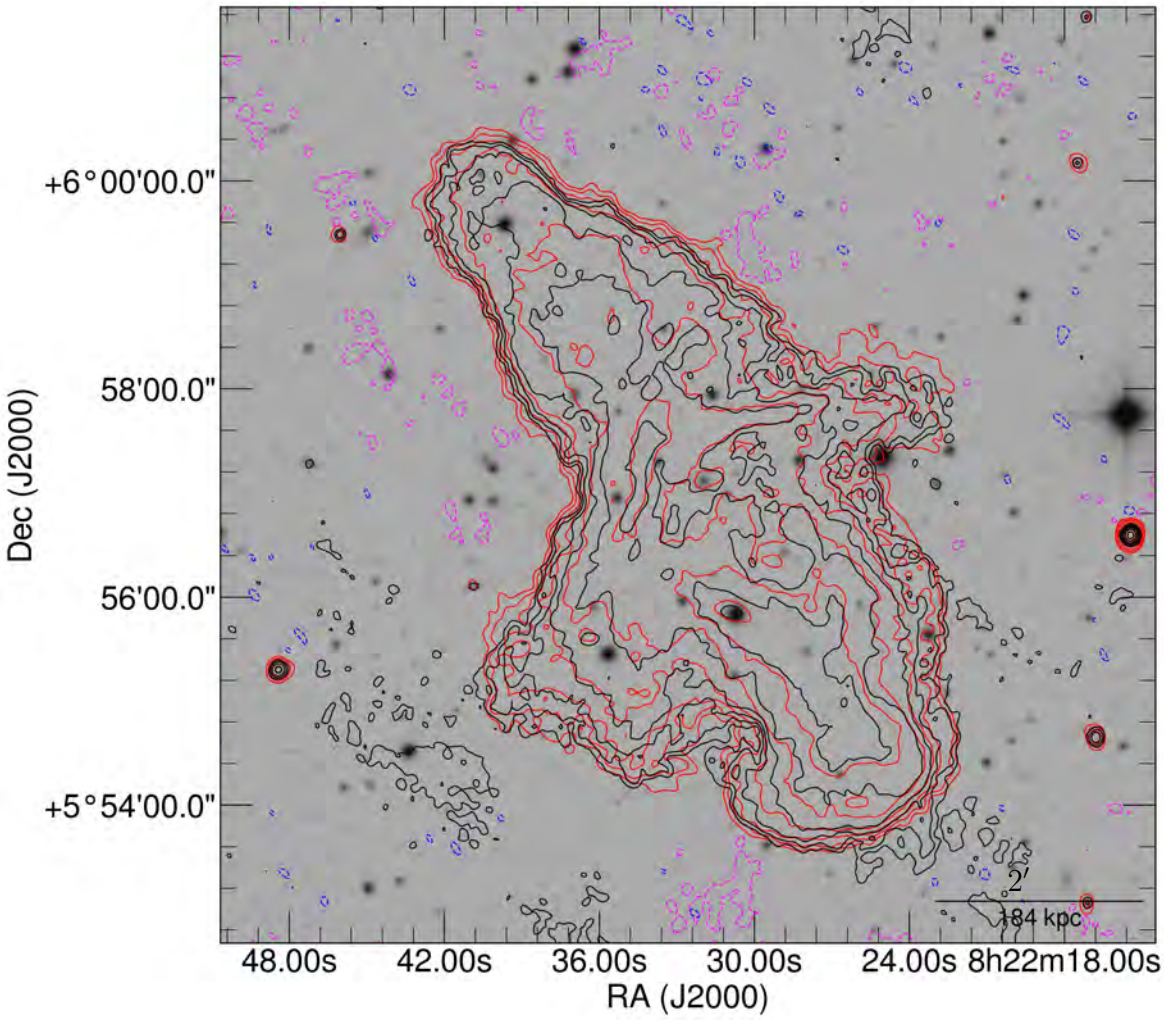

Figure 4.3: The uGMRT and MeerKAT radio contours of 3C 198 are overlaid on the DSS-II (red band) optical image in a grey scale. The black (uGMRT) and red (MeerKAT) surface brightness contours are plotted in the image, including the first negative surface brightness contours (magenta and blue). The levels are drawn as the RMS=0.026 mJy/beam × -1,1,2,4 etc, increasing by 2.

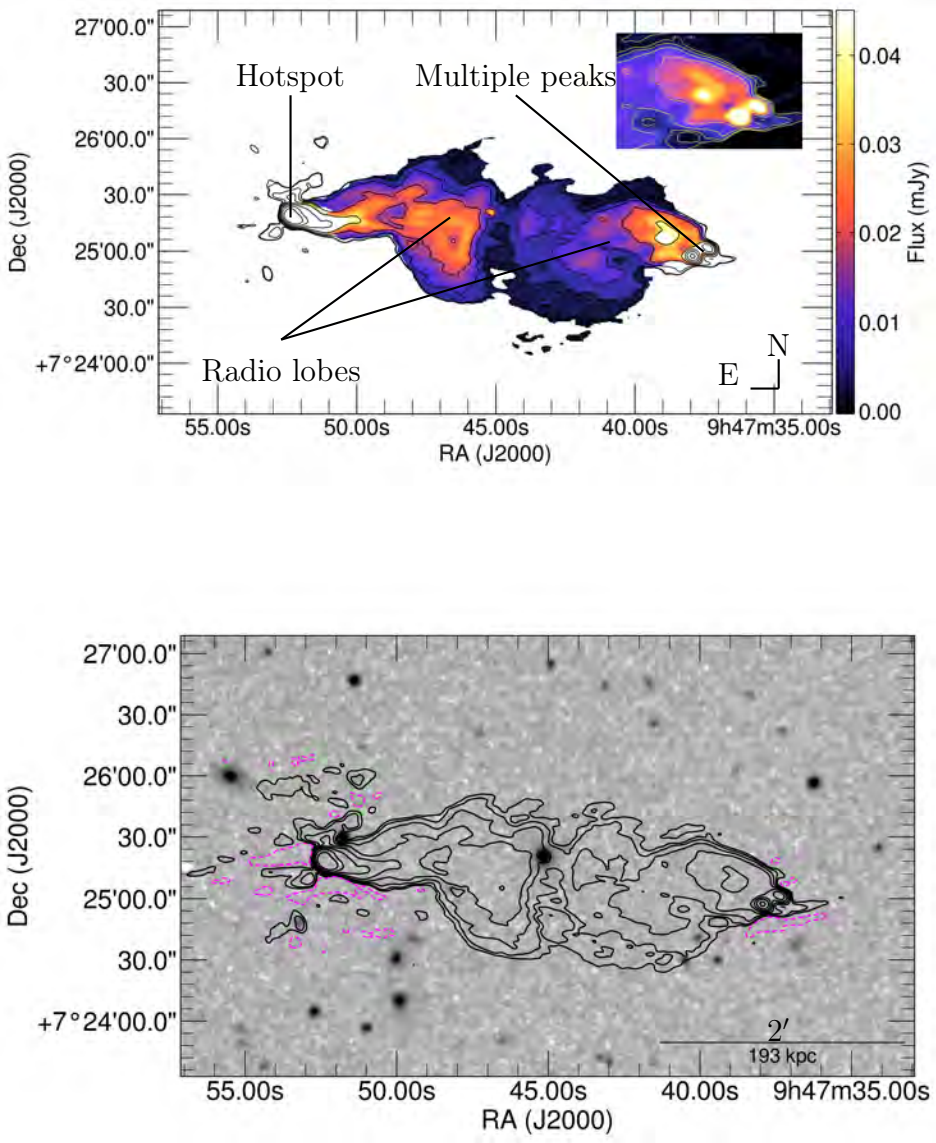

Figure 4.4: The uGMRT Band-4 total intensity image of 3C 227 (top panel). The lowest radio contour plotted is three times the total RMS noise (see Table 3.3.2 and increases by a factor of two. The MeerKAT radio contours are overlaid on the DSS-II (red band) optical image in a grey scale. The red surface brightness contours are plotted in the image, including the first negative surface brightness contours. The levels are drawn as RMS=0.116 mJy/beam × -1,1,2.., increasing by a factor of 2.

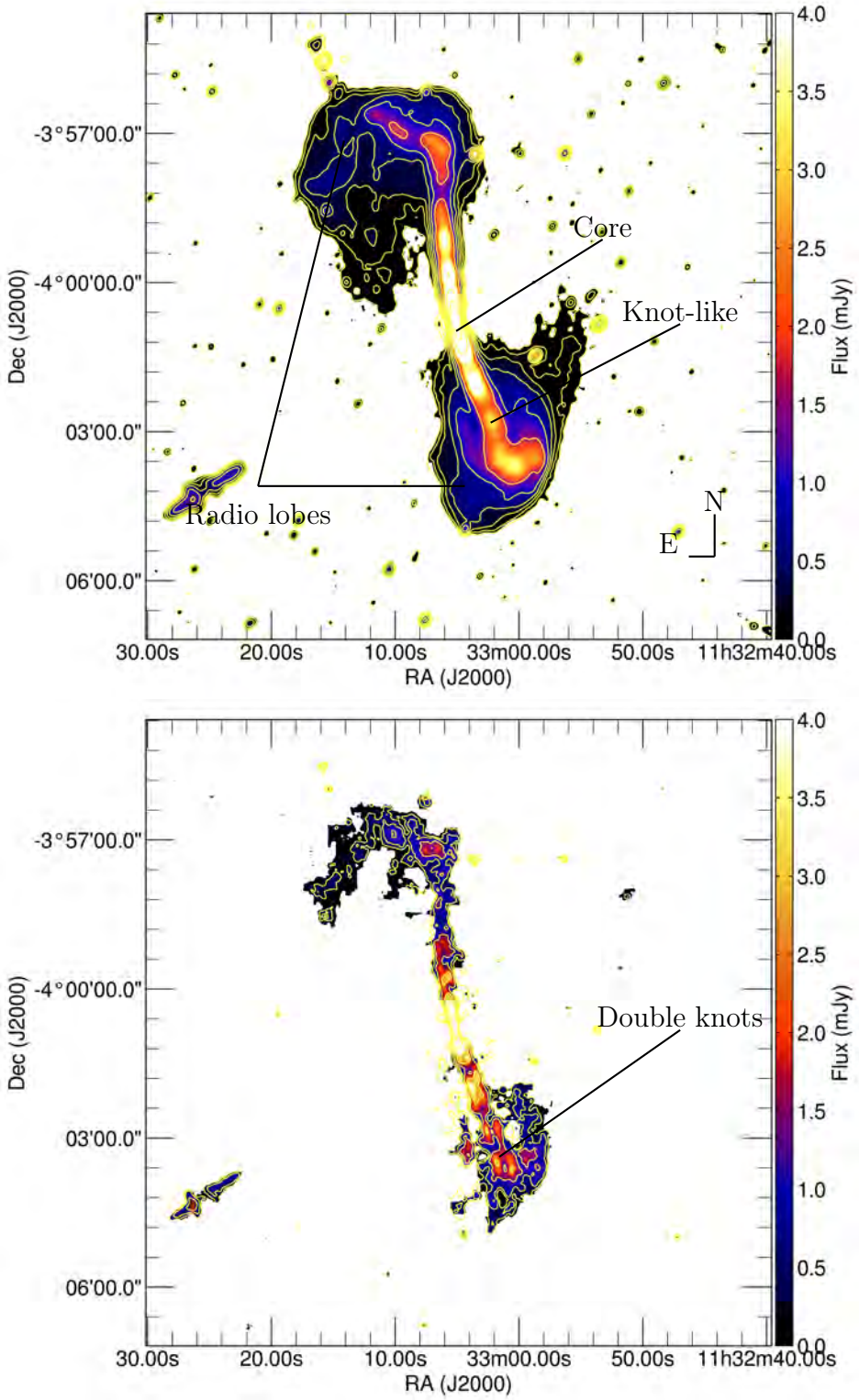

Figure 4.5: The 4C -03.43 radio source maps at the L-band using MeerKAT (top panel) and at Band-4 using uGMRT (bottom panel). The lowest radio contour plotted is three times the total RMS noise (see Table 3.3.2) and increases by a factor of two.

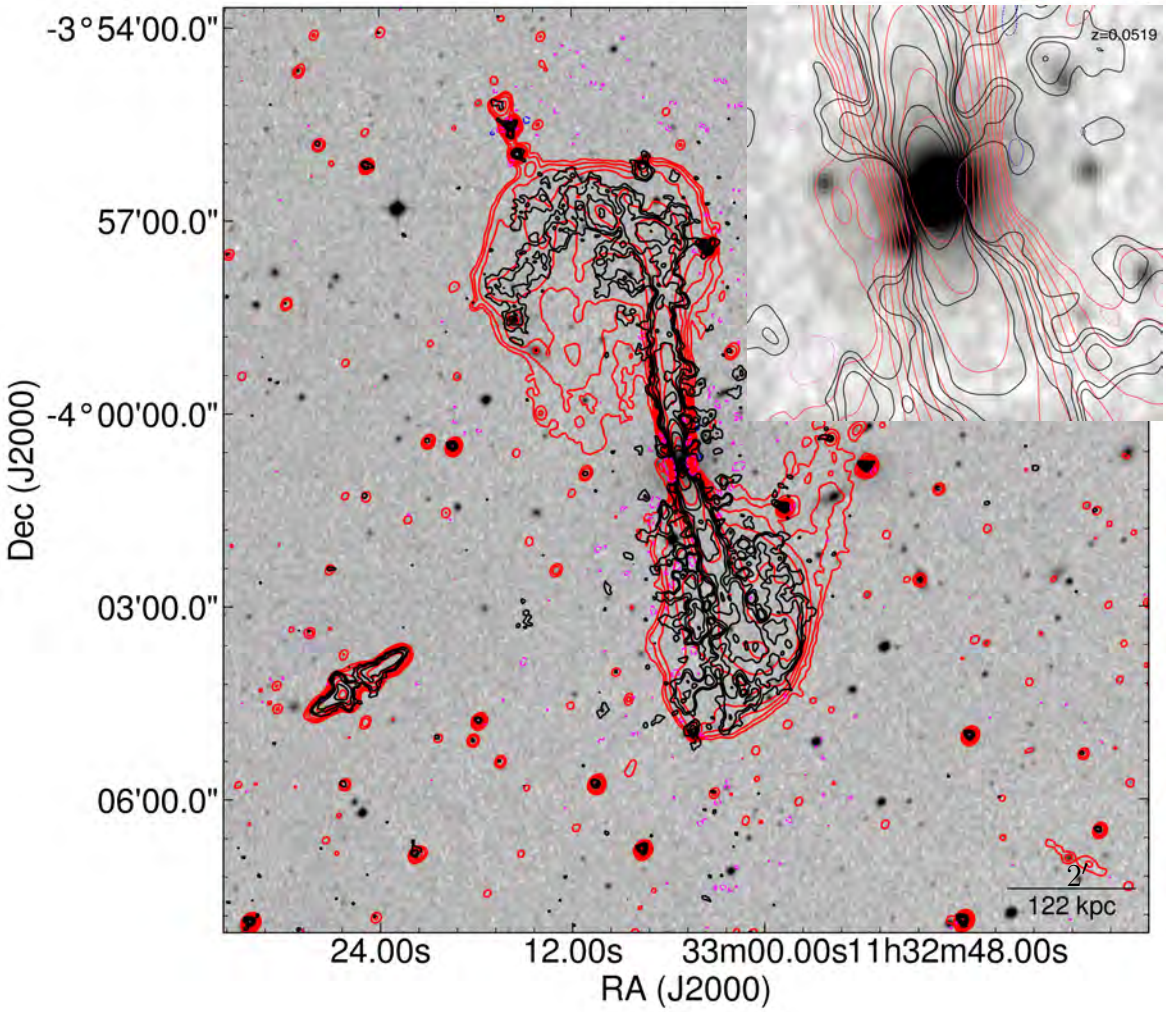

Figure 4.6: The uGMRT and MeerKAT radio contours of 4C −03.43 overlaid on the DSS-II (red band) optical image in a grey scale. The black (uGMRT) and red (MeerKAT) surface brightness contours are plotted in the image, including the first negative surface brightness contours (magenta and blue). The levels are drawn as the RMS=0.034 and 0.023 mJy/beam × -1,1,2,4..., increasing by 2 for the uGMRT and MeerKAT, respectively. The top right is the zoom-in region of 4C −03.43 core region.

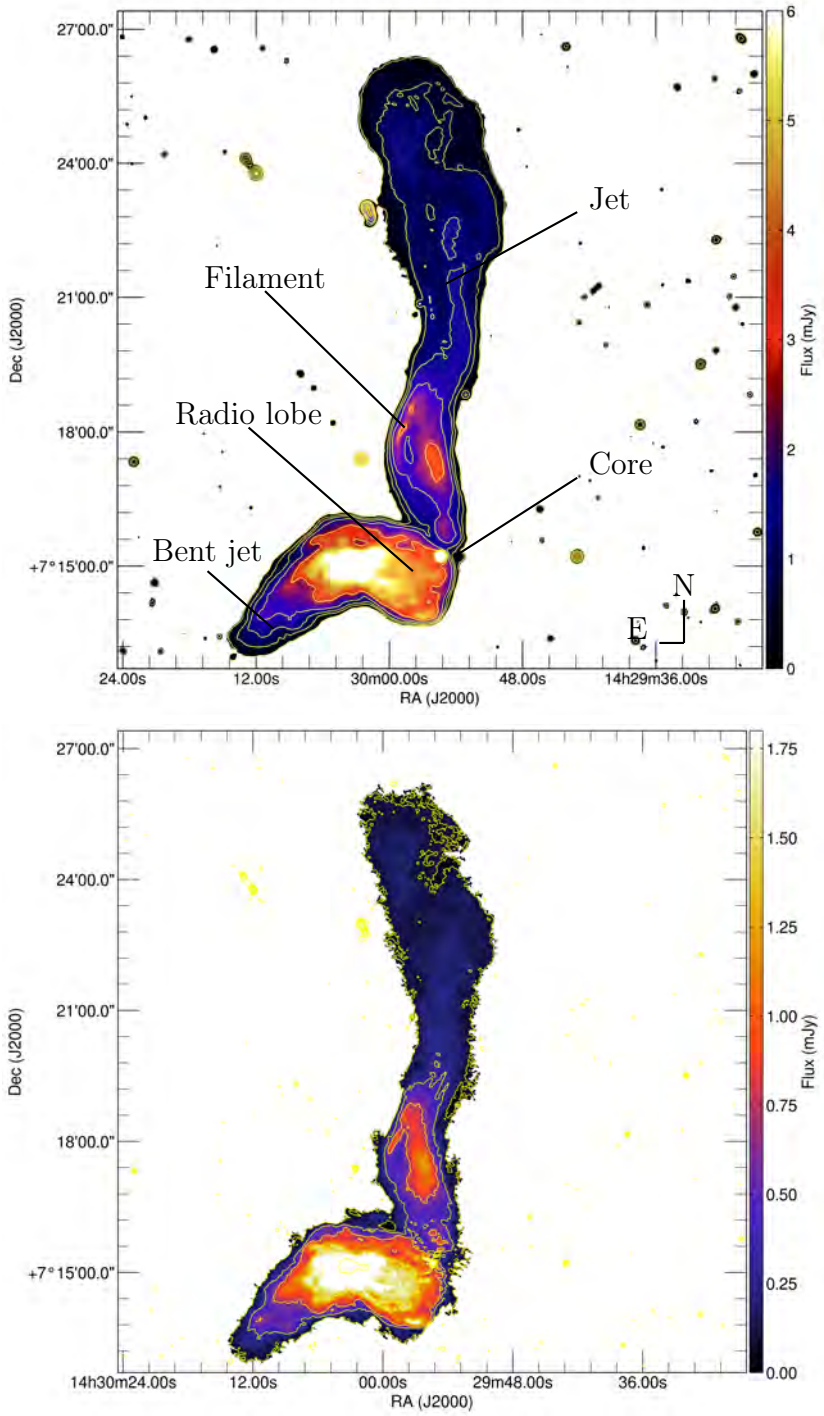

Figure 4.7: The CGCG 047-067 radio source maps at the L-band using MeerKAT (top panel) and at Band-4 using uGMRT (bottom panel). The lowest radio contour plotted is three times the RMS noise and increases by a factor of two. Table 3.3.2 denotes the RMS, beam size, and position angle.

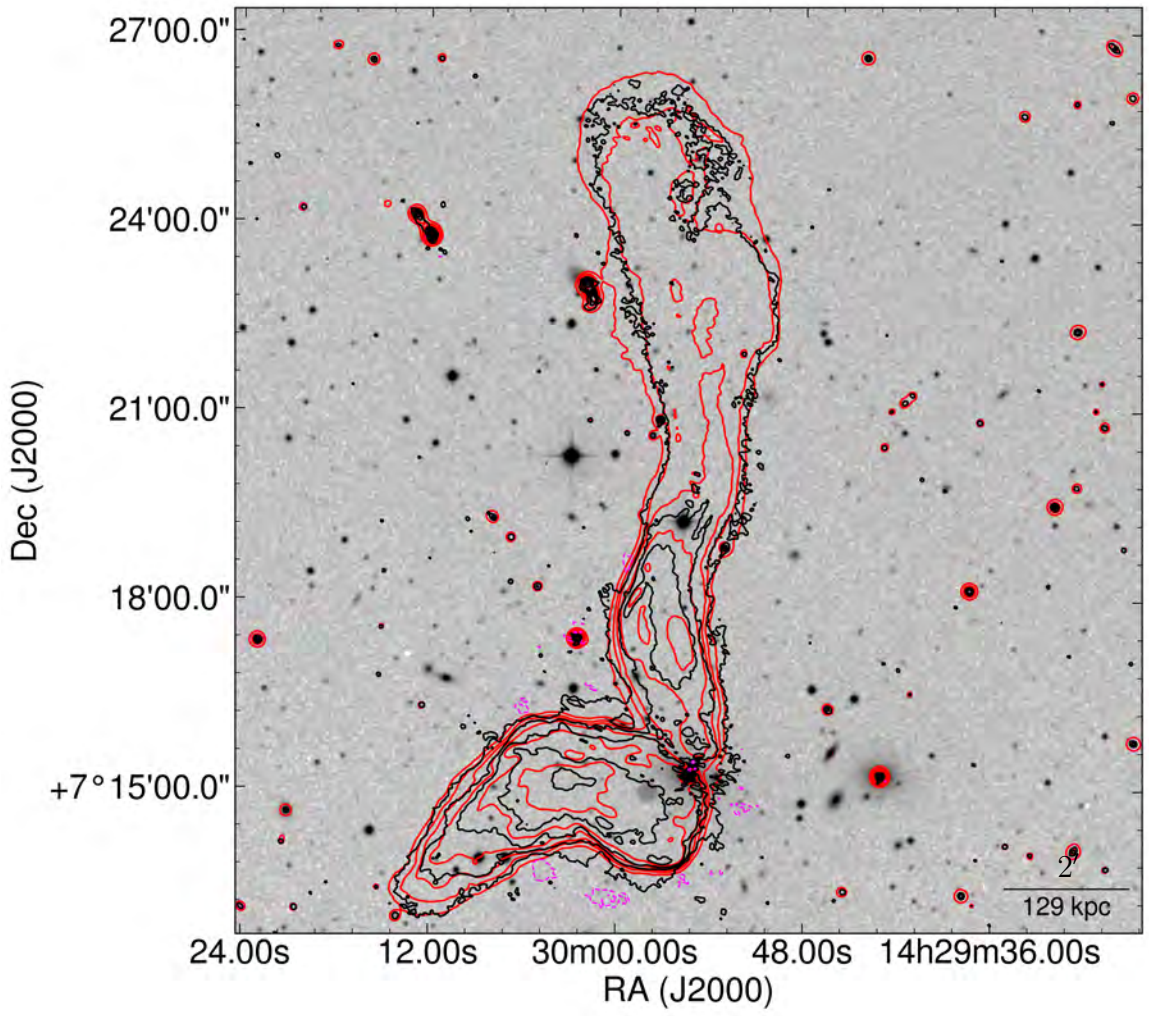

Figure 4.8: The uGMRT and MeerKAT maps of the giant radio source CGCG 047-067. The uGMRT (black) and MeerKAT (red) radio contours are overlaid on the DSS-II (red band) optical image in greyscale, including the first negative uGMRT surface brightness contours (magenta). The levels are drawn as the RMS=0.018 and 0.010 mJy/beam × -1,1,2,4..., increasing by 2 for the uGMRT and MeerKAT.

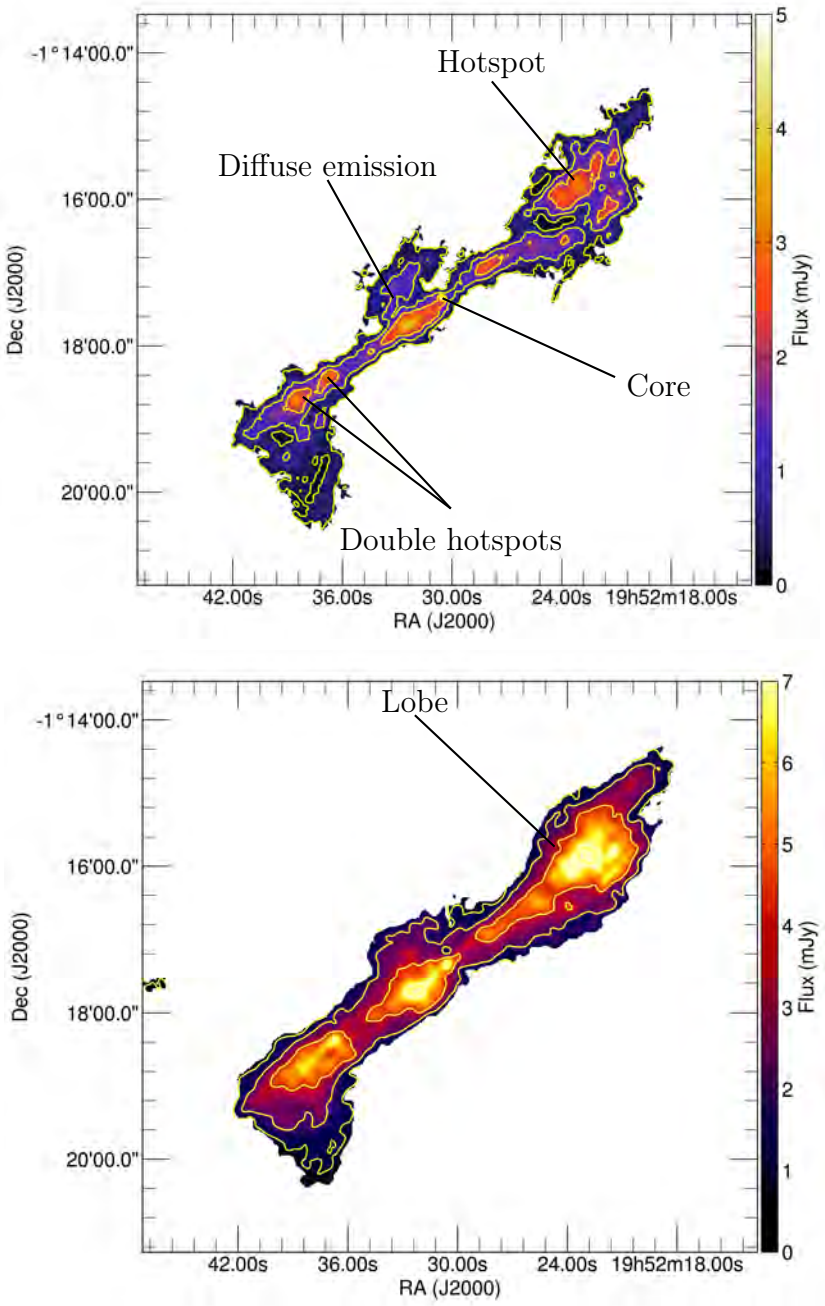

Figure 4.9: The 3C 403.1 radio source maps at the L-band using MeerKAT (bottom panel) and at Band-4 using uGMRT (top panel). The lowest radio contour plotted is three times the RMS noise and increases by a factor of two. Table 3.3.2 denotes the RMS, beam size, and position angle.

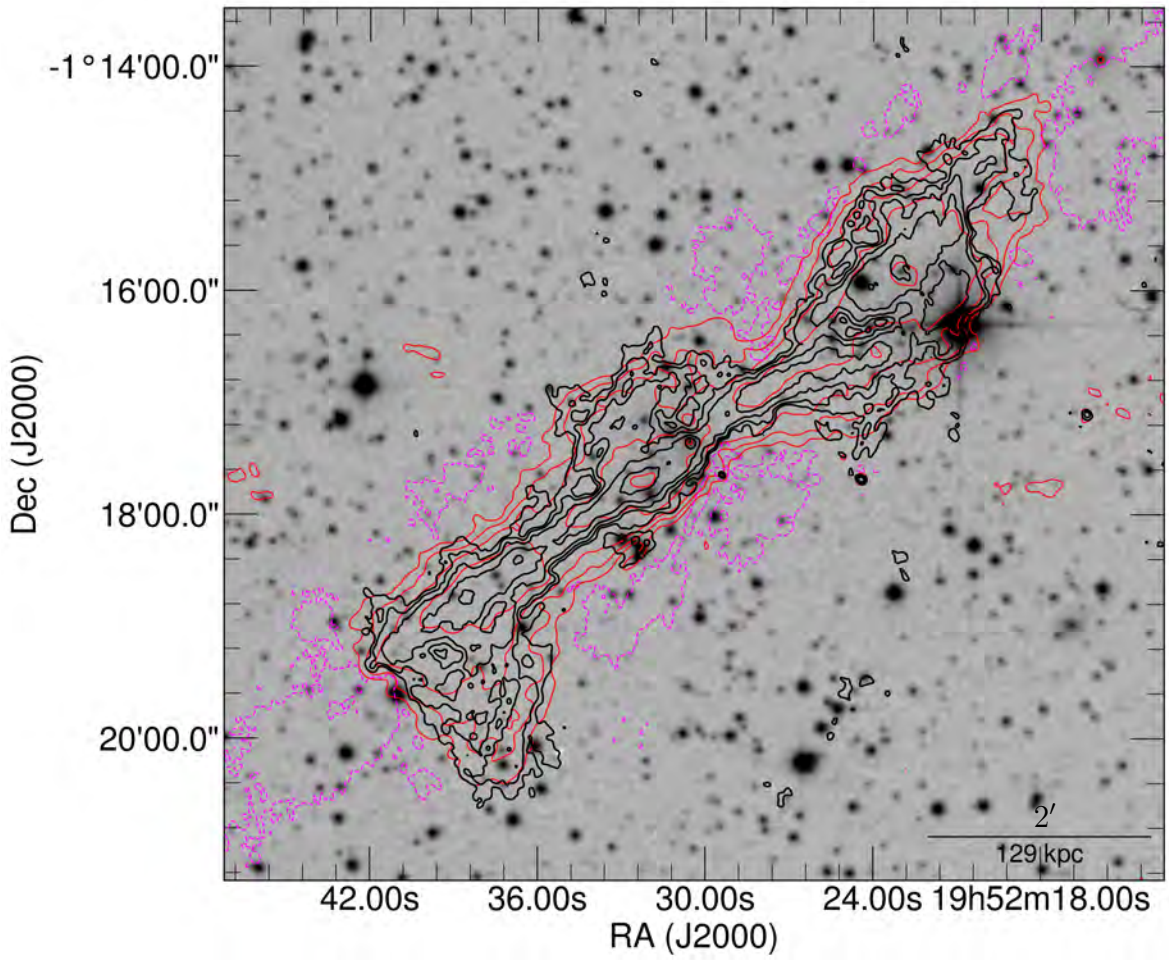

Figure 4.10: The uGMRT and MeerKAT maps of the giant radio source 3C 403.1. The uGMRT (black) and MeerKAT (red) radio contours are overlaid on the DSS-II (red band) optical image in greyscale, including the first negative uGMRT surface brightness contours (magenta). The levels are drawn as the RMS=0.021 mJy/beam × -1,1,2,4..., increasing by 2.

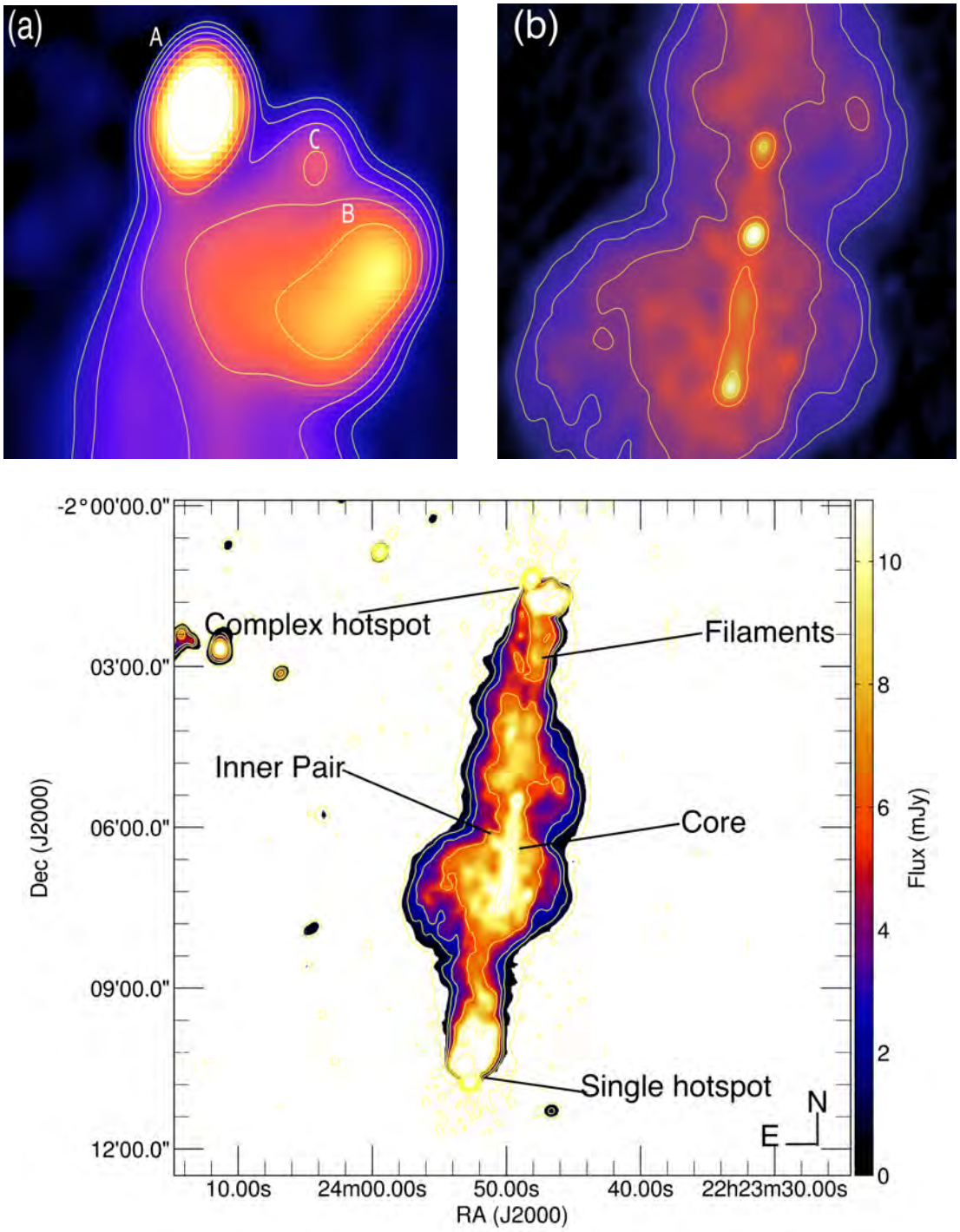

Figure 4.11: The MeerKAT total intensity image of 3C 445. The lowest radio contour plotted is three times the total RMS noise (see Table 3.3.2 and increases by a factor of two). The cutout labelled (a) above shows the multiple hotspots: A– is defined as a primary hotspot, B– the secondary hotspot, and C– jet knot. (b) shows the cutout of the inner air of the lobes.

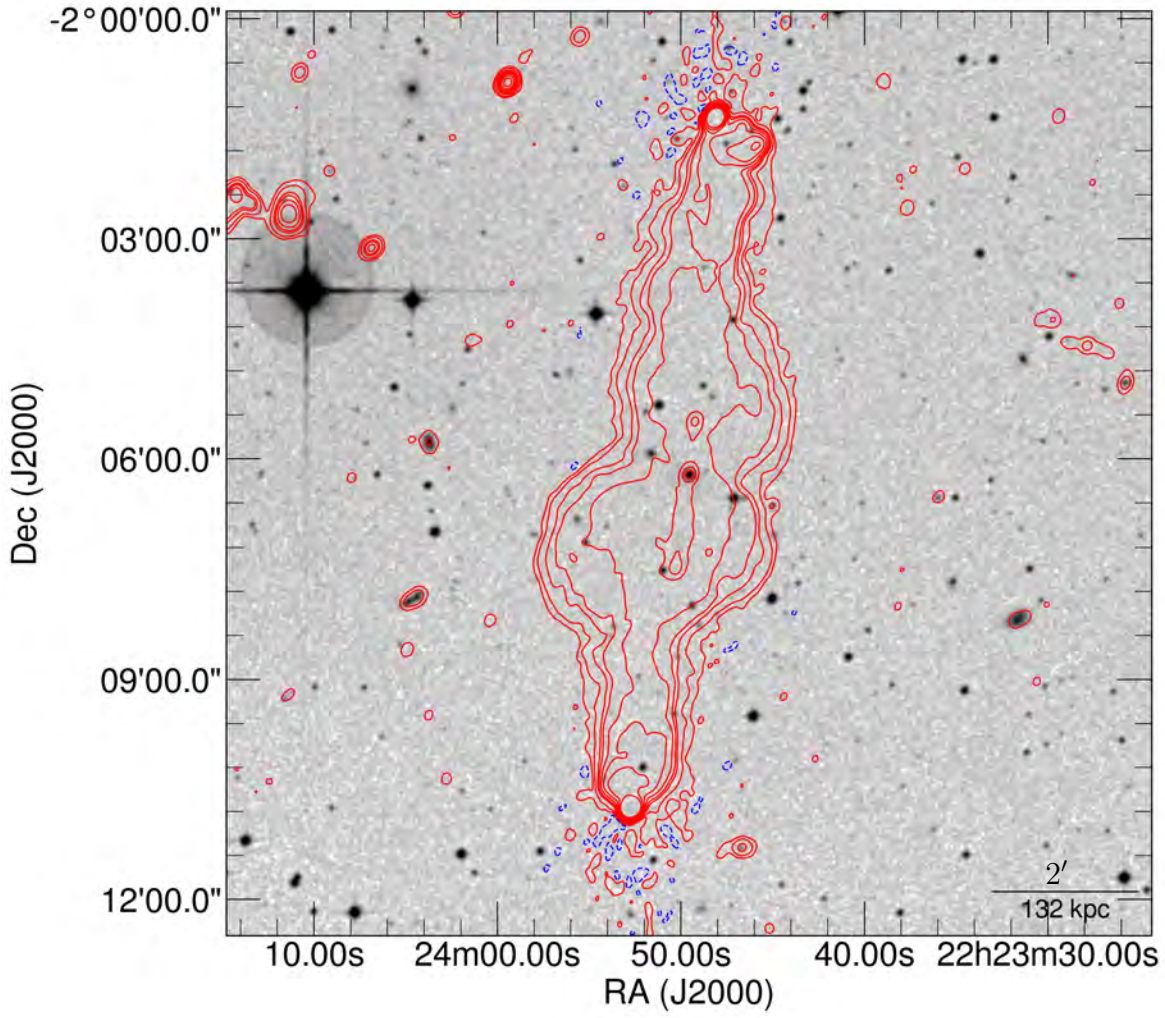

Figure 4.12: The MeerKAT radio contours of 3C 445 are overlaid on the DSS-II (red band) optical image in a grey scale. The red surface brightness contours are plotted in the image, including the first negative surface brightness contours. The levels are drawn as RMS=0.081 mJy/beam × -1,1,2.., increasing by a factor of 2. The bar at the bottom right corner depicts the physical scale of the source.

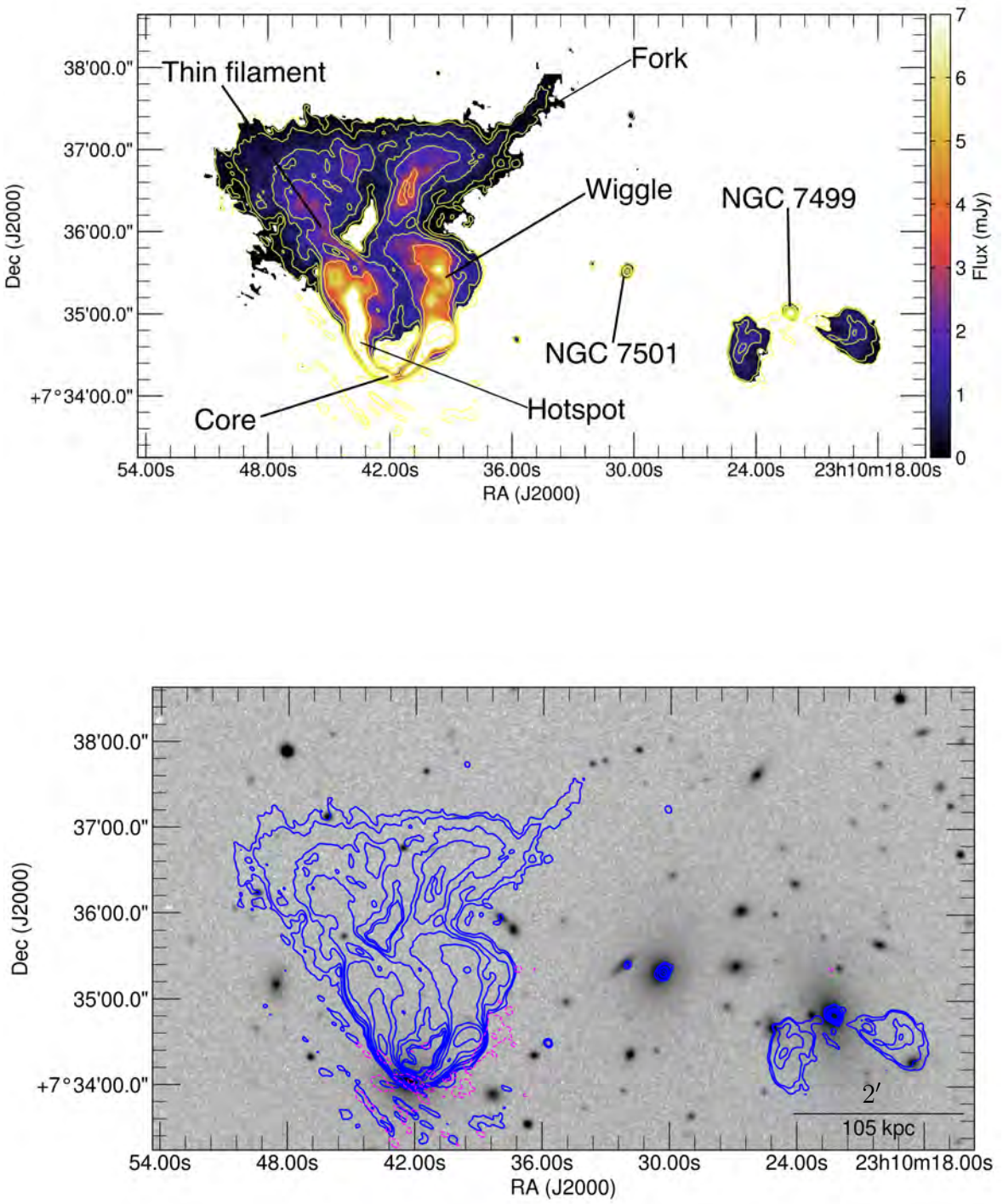

Figure 4.13: The uGMRT total intensity image of NGC 7503 (top panel). The lowest radio contour plotted is three times the total RMS noise (see Table 1.3.2 and increases by a factor of two. The uGMRT radio contours are overlaid on the DSS-II (red band) optical image in a grey scale. The blue surface brightness contours are plotted in the image, including the first negative surface brightness contours (magenta). The levels are drawn as RMS=0.021 mJy/beam × -1,1,2.., increasing by a factor of 2.

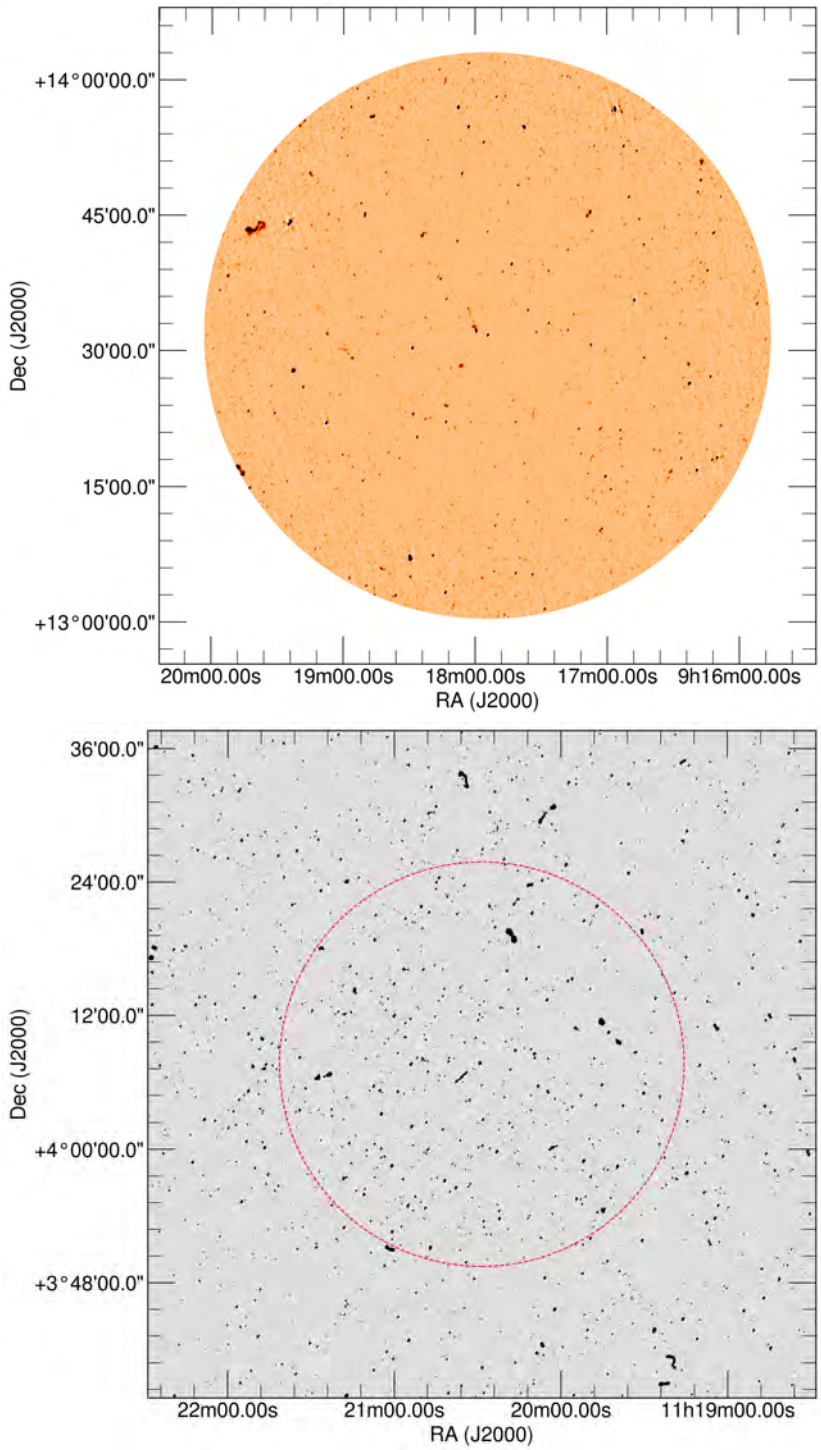

Figure 4.14: The MerKAT primary beam corrected radio maps of SDSS J 09157+1331(top panel) and SDSS J 1120+0407 (Bottom panel: inverted greyscale image). The contours are three times multiples of the RMS noise in the image, increasing by a factor of two. The local RMS noise is 5.640 μJybeam^{-1} and 5.042 μJybeam^{-1} respectively.

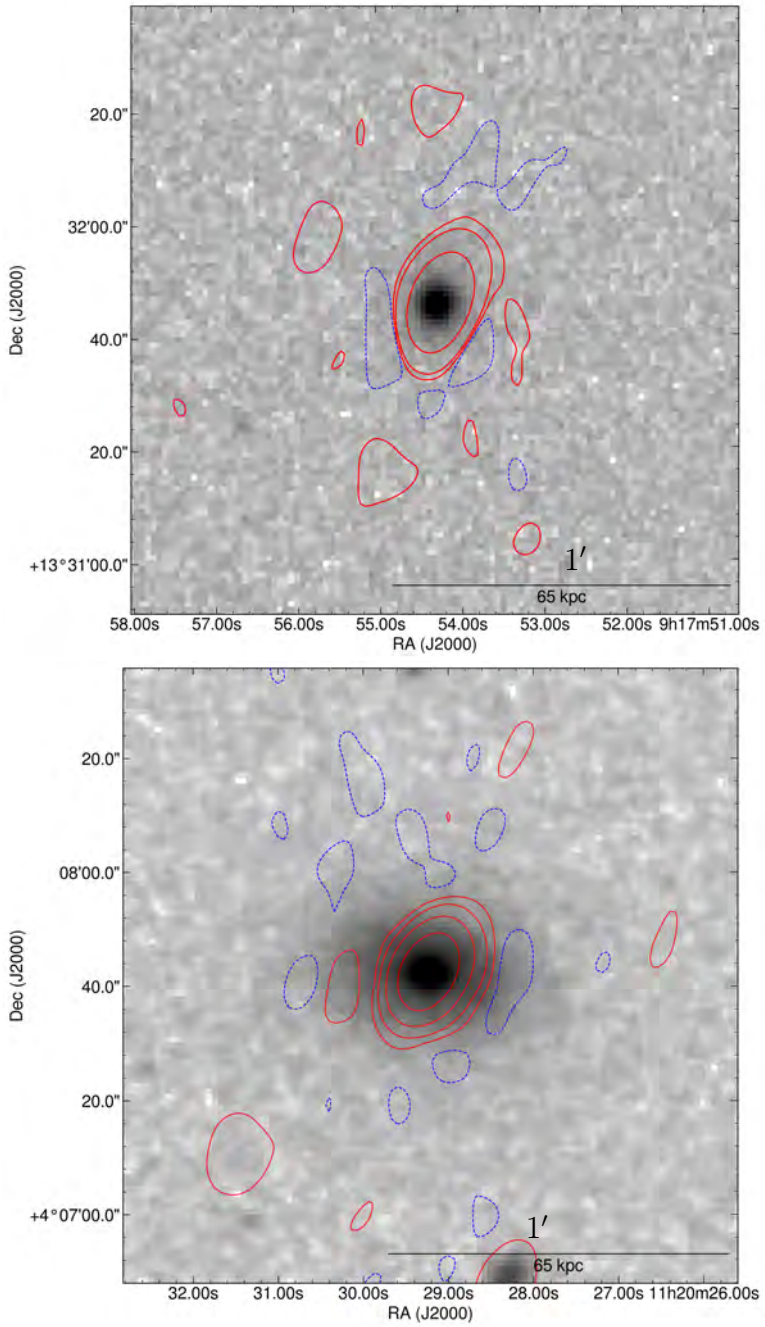

Figure 4.15: The MeerKAT radio contours of SDSS J 09157+1331(top panel) and SDSS J 1120+0407 (bottom panel) are overlaid on the DSS-II (red band) optical image in a grey scale. The red surface brightness contours are plotted in the image, including the first negative surface brightness contours (blue). The levels are drawn as RMS × -1,1,2.., increasing by a factor of 2. The RMS= 5.640 μJybeam^{-1} and 5.042 μJybeam^{-1} respectively

4.2 Generality on the radio sources

Radio galaxies' images display diverse morphological and dynamical characteristics that hint at the fundamental physical mechanisms influencing their evolution. In this context, we look into various aspects related to dead/dying radio galaxies, giant radio galaxies, restarted radio galaxies, radio galaxies featuring multiple peaks and tailed radio galaxies, providing insights into the dynamic nature of these radio galaxies.

4.2.1 Tailed Radio Galaxies

Tailed radio galaxies feature lobes or jets that bend and extend away from the central galaxy, resembling tails. These morphologies often arise from the galaxy's motion through the intergalactic medium, causing the jets to bend due to ram pressure. Our observation also includes tailed radio galaxies, both NAT (NGC 7503), WAT (CGCG 046-067) and a possible WAT seen face-on (4C −03.43). The diverse array of shapes exhibited by the jets and tails can be attributed to a combination of the galaxy's motion and the intricate dynamics of the intergalactic medium. Moreover, projection effects significantly impact how these structures appear, adding another layer of complexity to their interpretation. Recent investigations into tailed radio sources within clusters have revealed unique features, presenting intriguing challenges in comprehending these phenomena, as evidenced by studies such as Gendron-Marsolais et al. [2021] and related works. When these jets are being pushed backwards, the inner knots of the jet display the highest luminosity at the leading or 'front' edge, accompanied by a greater fractional polarisation and a distinct magnetic field orientation along the structure. Furthermore, the jets exhibit distinct regions of varying expansion rates as they move away from the core, displaying fluctuations or wiggles along their path.

4.2.2 Giant radio galaxies (GRGs)

Giant radio galaxies are traditionally defined as >1 Mpc in extent [Schoenmakers et al., 2000]. The current cosmological parameters recently adopted a canonical threshold of 0.7 Mpc for a better alignment with updated cosmology [Konar et al., 2004]. Most of the giant radio sources fall into the FR II class; an intermediate fraction of hybrid radio sources and a small fraction are classified as FR I, including tailed morphologies.

FR I sources have jets that lose energy as they propagate outward; therefore, fewer of them may grow larger > 0.7 Mpc compared to FR II, or partially due to the difficulties in detecting weak diffuse emission, especially in distant galaxies. We detect a giant FRI radio galaxy CGCG 047-067, consistent with the standard definition from the literature with a projected linear size of 950 kpcs. The projected linear size can be measured approximately from the ends of the two radio lobes. In practice, we measure the projected linear size at the 9σ level contour of each source to avoid picking spurious features. Moreover, we detected two intermediate GRGs, 3C 198 (650 kpc) and 3C 445 (630 kpc). These giant radio galaxies indicate the significant impact of AGN jets on their surroundings and call into question long-held assumptions regarding AGN activity's lifetime and energy output.

4.2.3 Dead or Dying Radio Galaxies

The length of the active phase is related to the possible existence of its duty cycles of nuclear activity. If nuclear activity is not continuous, the radio source's energy supply reduces significantly, referred to as the remnant/dying phase [Parma et al., 2007, Murgia et al., 2011]. In this phase, the plasma outflow can no longer be sustained. As such, structures that define a continuous activity, such as the core, well-defined jets, and hotspots, soon fall below the detection threshold; however, they undergo a period of fading. Radio lobes, however, may remain detectable longer if they are subjected to radiative losses. The source typically shows amorphous morphologies and low-surface brightness extended emissions in this phase. Some dying radio sources may not exhibit a visible core due to inadequate sensitivity, presenting an intriguing yet largely unexplored class of sources. Detection of these sources requires a combination of sensitivity, resolution and frequency coverage.

3C 198 is considered a genuine dead/dying radio galaxy in our sample, as it perfectly fulfils the above-mentioned criteria. The fossil radio lobes remain detectable despite significant radiative losses of relativistic components.

4.2.4 Restarted Radio Galaxies

We report the identification of restarted activity in 3C 445. The detection of two hotspots closer to the core and the outer ones and aligned with the overall orientation of the radio galaxy suggests that they are from restarted activity. These findings are crucial for understanding the episodic nature of AGN jet activity, showcasing the conditions under which the central engine can reignite and produce new jets, leading to complex radio morphologies. Active galactic nuclei (AGNs) show episodic activity that can be observed in galaxies with restarted radio jets. The restarted jets have the potential to interact with their surroundings, imprinting distinctive signatures on the radio spectral energy distribution. Tracing these signatures provides a route to delve into the evolutionary history of radio galaxies. Episodic AGNs show signs of multiple active and quiescent phases throughout their history, evidenced by the structure of their radio lobes and jets. This episodic behaviour can result from cycles of accretion onto the central supermassive black hole, leading to repeated bursts of jet activity.

4.3 Emphasis on the morphological features

4.3.1 Multiple hotspots

Hotspots are a consequence of some type of impact, such as the working surface of the jets where they interact with the interstellar medium or the IGM, resulting in a termination shock, and this is referred to as the standing or reflected shock front Hardcastle et al. [2007a]. Radio galaxies containing multiple hotspots have long been recognised, with hotspots being observed even at wavelengths beyond radio frequencies [Valtaoja, 1984, Hardcastle et al., 2007b]. Within this study, the targets 3C 227 and 3C 445 present at least two clear shows double peaks where the primary and secondary

hotspots are identifiable. Our results suggest possibilities such as the propagation of the jet through contact discontinuities or possible standing shock. The secondary hotspots could be explained as a collimated outflow from the primary hotspot. However, in a typical multiple hotspot depiction, the smaller element in 3C 445 might likely be classified as a jet knot (see Figure 4.12).

4.3.2 Features in 3C 403.1

It is challenging to associate 3C 403.1 with a clear morphological class (i.e. FR I or FR II). The source has twin jets and lobes on the kpc scale, which show different features. The southeastern jet is clearly visible and blobby throughout its length, with several emission peaks. The north-western jet is less bright and culminates in a high-brightness region, which could be a hotspot, though it is not as compact as typical hotspots and shows a couple of ridges of emission parallel to the source axis. It is noteworthy that a filament of radio emission is detected beyond the north-western hotspot. In contrast, the emission at the end of the southeastern lobe deviates from the axis and bends towards the south. To summarise, the southeastern jet is similar to FRI jets, while the north-western jet resembles FR II's.

Finally, this radio galaxy shows another interesting feature, i.e. a region of diffuse emission parallel to the source axis, just north of the core and inner part of the south-western jet.

A spectral index imaging would be beneficial in classifying this source, but unfortunately, it is not available due to the effects of residual artefacts. As such, the spectral index is not reliable.

4.4 Comparison with literature information

In several cases, MeerKAT and uGMRT observations generally confirm previously reported structures, such as those seen in the VLA total intensity maps of 3C 105 and 3C 445 at 8.23 and 8.46 GHz [Leahy et al., 1997]. However, the high resolution and sensitivity of the MeerKAT and uGMRT images provide a more refined view of these structures. Our observations of 3C403.1 corroborate the findings of Missaglia et al. [2022] and confirm its categorisation as a powerful radio galaxy, albeit at a lower power level relative to standard FR II radio sources. This lower power, combined with other source properties, leads to an ambiguous classification for 3C 403.1 in our analysis. It is worth noting that for 3C 198, 4C -03.43, CGCG 047-067, NGC 7503, SDSS J09157+1331, and SDSS J1120+0407, no previous radio observations have been reported.

Chapter 5

Physical Parameters and Spectral Analysis

Radio galaxies evolve during their lifetime [Turner and Shabala, 2015], due to several factors, such as (1) changes in the accretion mechanisms which ultimately produce the radio emission, (2) interaction with the external environment (intracluster or intergalactic medium), which may confine the radio emission, shape the morphology of jets and lobes, (3) magnetic fields within and outside the radio galaxies.

While the details of the evolution of radio galaxies are not fully understood, substantial simulation efforts have been made to reproduce their complex structures to varying degrees successfully (e.g., Burns et al. [1991], Hardcastle and Croston [2020], Perucho et al. [2014].

In this chapter, we derive some quantities intrinsic to radio galaxies, allowing a comparative analysis of the sources in our sample. In particular, we will estimate the total energy content, energy density and magnetic field assuming equipartition conditions for all sources, and we will derive an estimate of their age in Chapter 6.

5.1 Energy Content

Since injection as a power law spectrum, relativistic electrons in a fluid element have suffered synchrotron loss in the magnetic field of varying strength. A simple method to detect the magnetic field in radio sources is to minimize its total energy content. The minimum energy condition is closely related to the energy equipartition between relativistic particles and the magnetic field required for the observed synchrotron emitting plasma (first proposed by Burbidge [1956]).

The total energy is the sum of the magnetic and relativistic particle energies given as

$$E_{tot} = E_B + E_P = E_B + (1 + k)E_e \tag{5.1}$$

Where k is the ratio of the total energies of protons (E_p) and electrons (E_e), $\sim \frac{E_e}{E_p}$ and E_B is the energy in the magnetic field.

The energies in the magnetic field and electrons are given within a volume V of a source

$$E_B = \frac{B^2}{8\pi}\phi V \tag{5.2}$$

B is the magnetic field strength, and ϕ is the filling factor (known as the fraction of the volume by relativistic particles and the magnetic field).

The total electron energy is given as

$$E_e = B^{-3/2} L_{rad} c_{12}(\alpha, \nu_1, \nu_2) \tag{5.3}$$

expressed as a function of the total radio luminosity, L_{rad}. $c_{12}(\alpha, \nu_1, \nu_2)$ is a constant defined by [Pacholczyk, 1970].

Finally, the total energy in the system is calculated as a function of the magnetic field with

$$E_{tot} = (1+k) c_{12} L_{rad} B^{-3/2} + \frac{B^2}{8\pi}\phi V \tag{5.4}$$

Traditionally, equipartition occurs when the magnetic field and particle contribution are roughly equal. The magnetic field for which the total energy content is minimum

$$B_{eq} = \left(6\pi(1+k) c_{12} L_{rad} \phi^{-1} V^{-1}\right)^{2/7} \tag{5.5}$$

Now, we can solve for the total energy as

$$E_{tot,min} = C_{13} \left(\frac{3}{4\pi}\right)^{\frac{3}{7}} (1+k)^{\frac{4}{7}} \Phi^{\frac{3}{7}} V^{\frac{3}{7}} L_{1.4Ghz}^{\frac{4}{7}} [erg] \tag{5.6}$$

$$\approx 2.5 \times 10^{41} (1+k)^{\frac{4}{7}} P_{1.4GHz}^{\frac{4}{7}} V^{\frac{3}{7}}$$

and the total minimum energy density

$$u_{min} = 8.6 \times 10^{-24} (1+k)^{\frac{4}{7}} \left(\frac{P_{1.4GHz}}{V_{kpc^3}}\right)^{\frac{4}{7}} [\frac{erg}{kpc^3}] \tag{5.7}$$

$c_{13} = 0.921 c_{12}^{\frac{4}{7}}$ Pacholczyk [1970]. The radio power $P_{1.4GHz}$ is derived from equation 3.2.

Consequently, the calculation leads to an equipartition magnetic field of

$$B_{eq} = \sqrt{\frac{24\pi}{7} u_{min}}\, [\mu G] \tag{5.8}$$

which is a good approximation of the average magnetic field within a radio source. The outcomes of these calculations are shown for each source in table 5.1.

Assuming a simple cylindrical geometry, the volume of the radio sources is obtained from the relation

$$V = \pi \frac{d_{min}^2}{2} d_{max} \, [kpc^3] \tag{5.9}$$

d_{min} and d_{max} are the linear sizes of the minor and major axes, respectively. We have estimated the volume by aggregating individual components corresponding to various source regions due to the complex morphology of the sources. The determination of source diameters has been accomplished using radio maps at 1.28 GHz unless the image is unavailable, in which case 700 MHz maps are used. The volumes are predicated on cylinder geometry expressed in kpc^3 accounting for the source redshift and corresponding luminosity distance and angular to linear scale conversion factor (see Tables 4.2 ans 4.1).

Table 5.1: Global physical parameters of radio galaxies

Object ID	z	α	V kpc^3	$E_{tot,min}$ ergs	u_{min} erg/cm^3	B_{eq} μG
3C 105	0.089	-0.64±0.02	4.43×10^{6}	2.02×10^{59}	1.57×10^{-12}	4.11
3C 198	0.081	-1.01±0.02	3.54×10^{7}	2.39×10^{59}	2.32×10^{-13}	1.58
3C 227	0.085	-0.78±0.02	2.38×10^{6}	1.71×10^{59}	2.47×10^{-12}	5.16
4C-03.43	0.0519	–	1.26×10^{7}	6.03×10^{58}	1.65×10^{13}	1.33
CGCG 047-067	0.054	-0.57±0.03	1.63×10^{7}	1.08×10^{59}	2.27×10^{-13}	1.56
3C 403.1	0.055	-0.99±0.04	2.04×10^{6}	3.93×10^{58}	6.62×10^{-13}	2.67
3C 445	0.056	-0.80±0.02	8.85×10^{6}	1.51×10^{59}	5.87×10^{-13}	2.51
NGC 7503	0.044	-0.66±0.03	1.36×10^{6}	2.57×10^{58}	6.49×10^{-13}	2.64

5.2 Spectral analysis

5.2.1 Integrated radio spectrum

To derive the integrated spectrum for the sources in our sample, we collected their flux density measurements using the NASA Extragalactic Database NED. These are heterogeneous values taken with different radio telescopes at various resolutions. At the same time, an accurate spectrum study should rely on measurements integrated over the same region and with u-v planes that are as similar as possible. Nevertheless, our analysis is a good starting point for a comparative study of the sources in our sample.

The integrated spectrum for each source was fitted using the programme Synage Murgia [1996], which offers fits with power law, continuum injection, Kardashev-Pacholczyk (KP) and Jaffe-Perola model (JP) models. A CI model with a fixed α_{inj}=0.5 provides the best fit for all sources.

[0] 1 kpc^3 $\approx$ 2.93799×10^{64} cm^3

– The Kardashev-Pacholczyk (KP) model– the pitch of radiating electrons is considered to be constant with time [Kardashev, 1962, Pacholczyk, 1970].

– Jaffe-Perola model (JP) model – assumes the single particle to be subject to many scattering events that randomize its pitch angle, assuming a timescale for the isotropic of the electrons much longer than the radiative timescale Jaffe and Perola [1973].

– The continuous injection model (CI) [Kardashev, 1962] – assumes a mixed population of electrons of different ages.

Below, we provide the CI model results shown in Figures 5.1 to 5.8. The results are summarized in Table 6.1, where we list the break frequency ν_{br}, the equipartition magnetic $B_{\rm eq}$ and the radiative source age $t_{\rm rad}$. In all cases, we report the results from the fit of the integrated spectrum in Section 5.2.2.

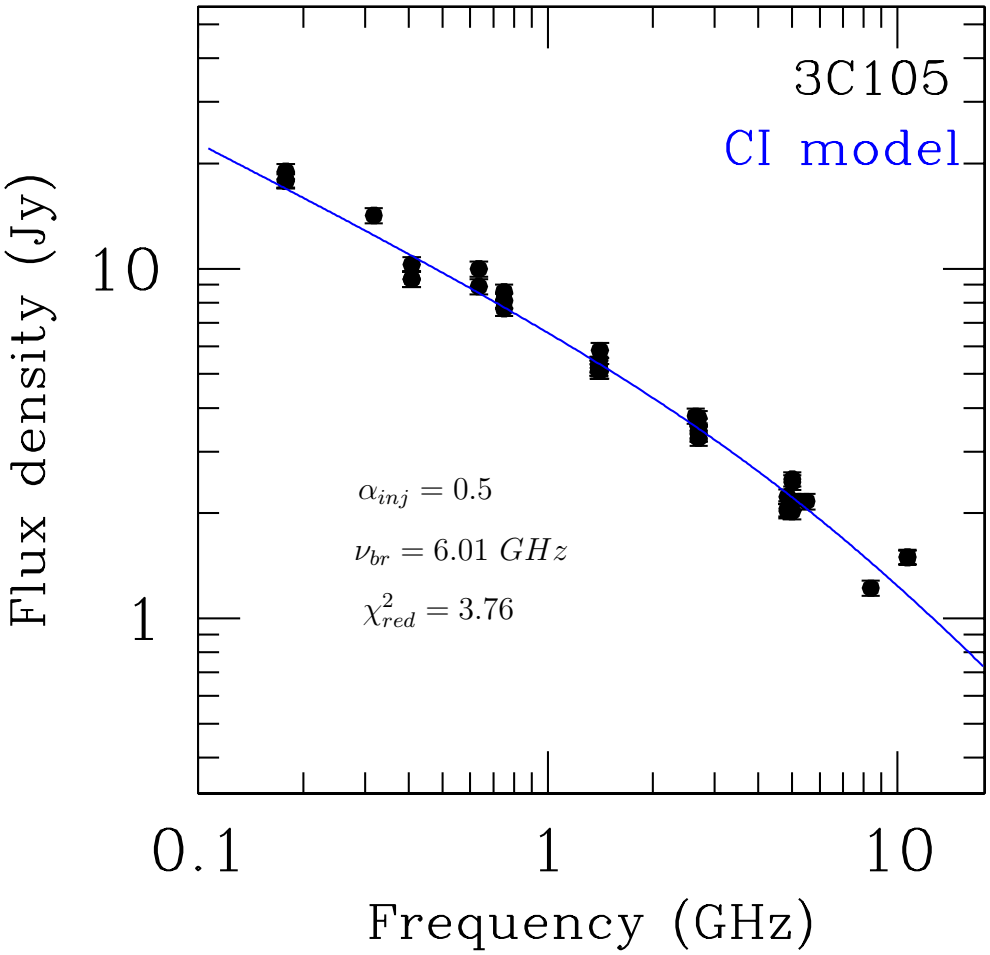

Figure 5.1: The total integrated radio spectrum of 3C 105. The continuous blue fit of the CI model shows the presence of a spectral break at frequency ν_{br}=$6.01^{+0.07}_{-0.08}$ GHz followed by a moderate steepening.

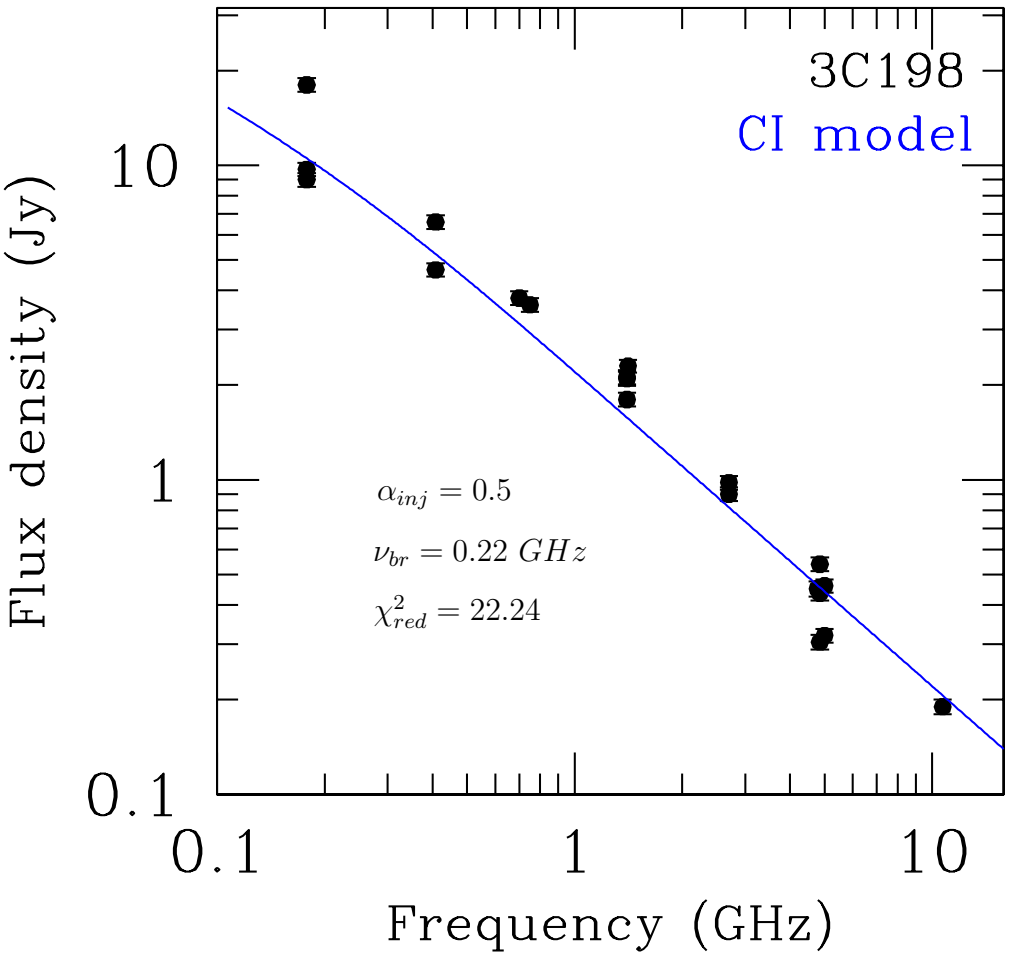

Figure 5.2: The total integrated radio spectrum of 3C 198. The continuous blue fit of the CI model shows the presence of a spectral break at frequency $\nu_{br} = 0.22^{+0.05}_{-0.05}$ GHz.

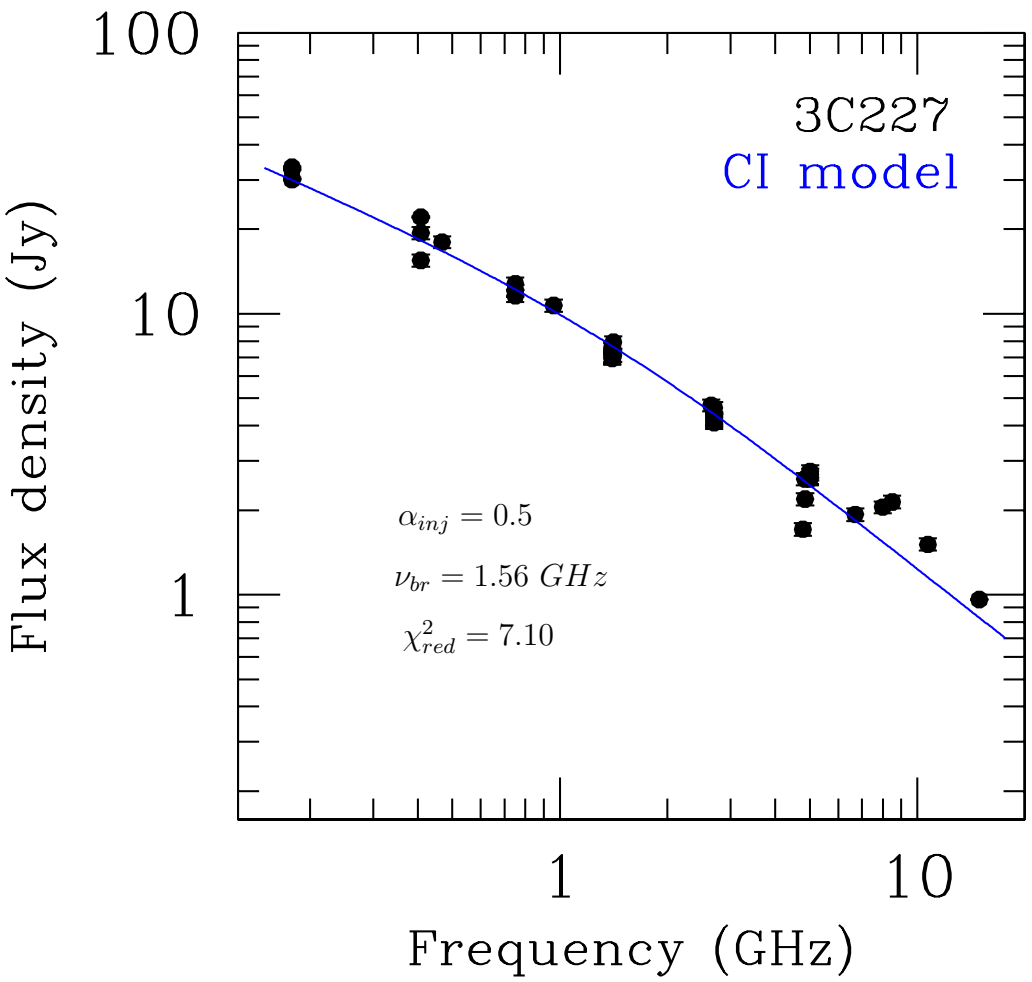

Figure 5.3: The total integrated radio spectrum of 3C 227. The continuous blue fit of the CI model shows the presence of a spectral break at frequency $\nu_{br} = 1.56^{+0.15}_{-0.14}$ GHz.

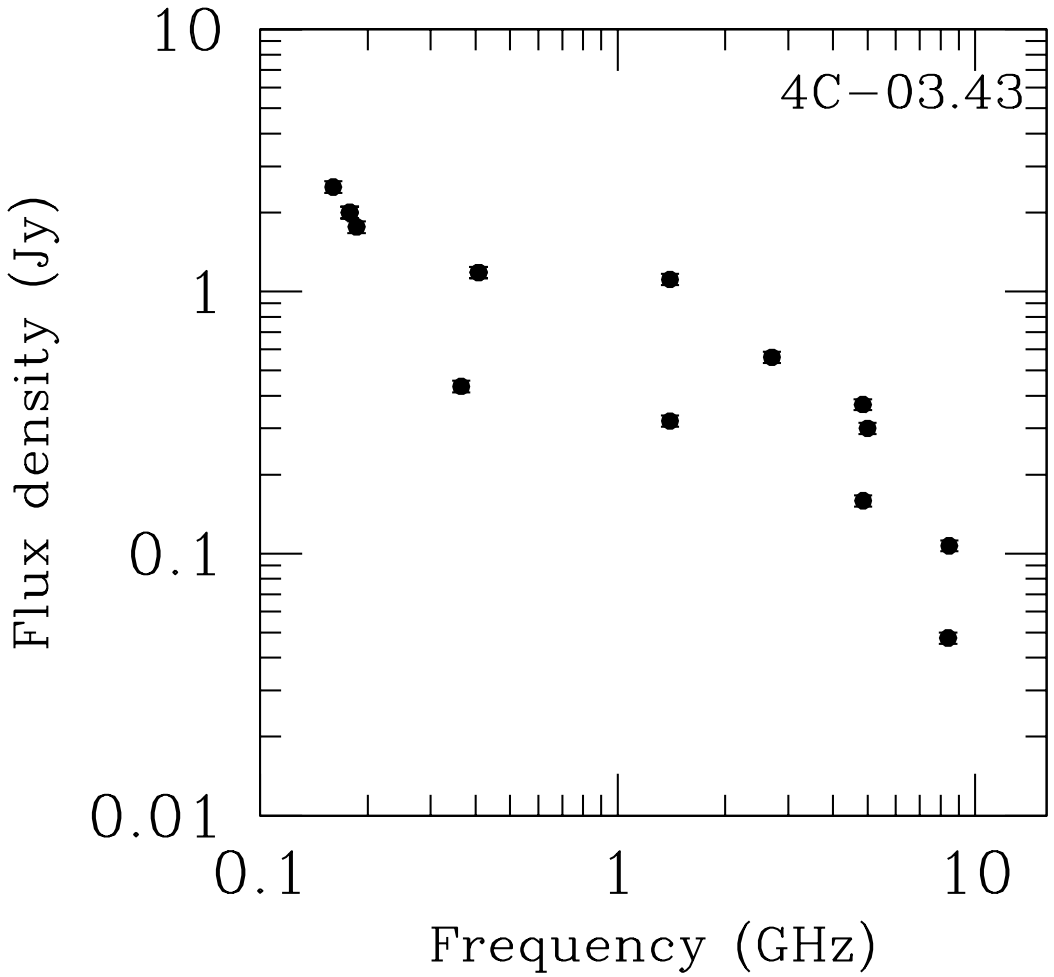

Figure 5.4: The total integrated radio spectrum of 4C-03.43.

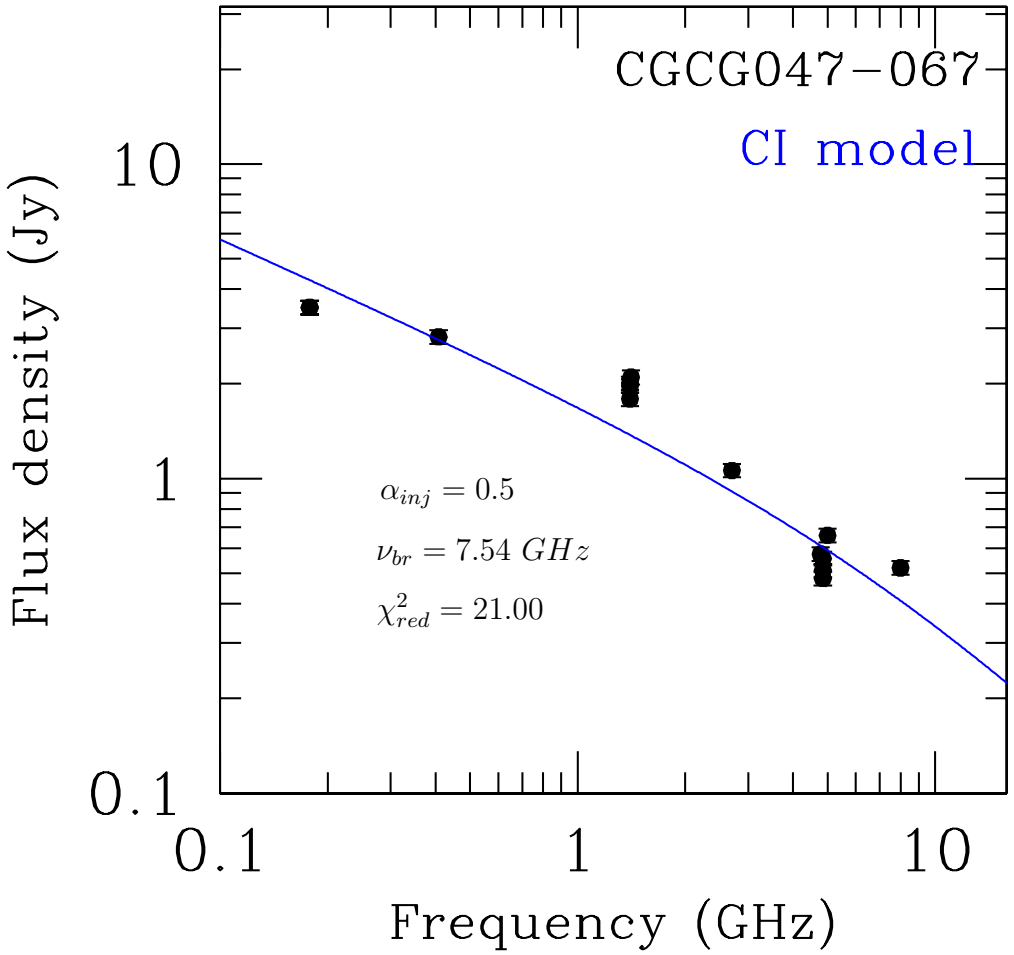

Figure 5.5: The total integrated radio spectrum of CGCG 047-067. The continuous blue fit of the CI model shows the presence of a spectral break at frequency $\nu_{\rm br} = 7.54^{+1.80}_{-1.30}$ GHz.

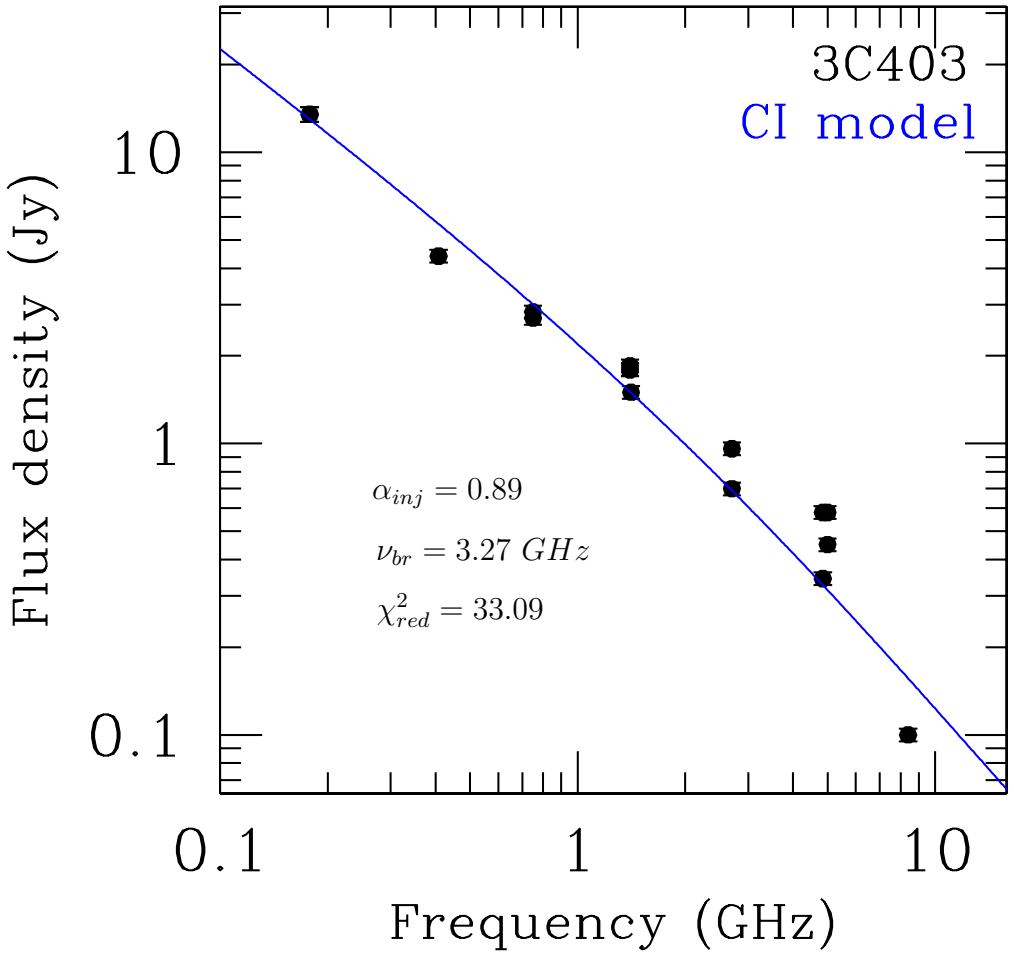

Figure 5.6: The total integrated radio spectrum of 3C 403.1. The continuous blue fit of the CI model shows the presence of a spectral break at frequency $\nu_{br} = 3.27^{+1.50}_{-0.96}$ GHz.

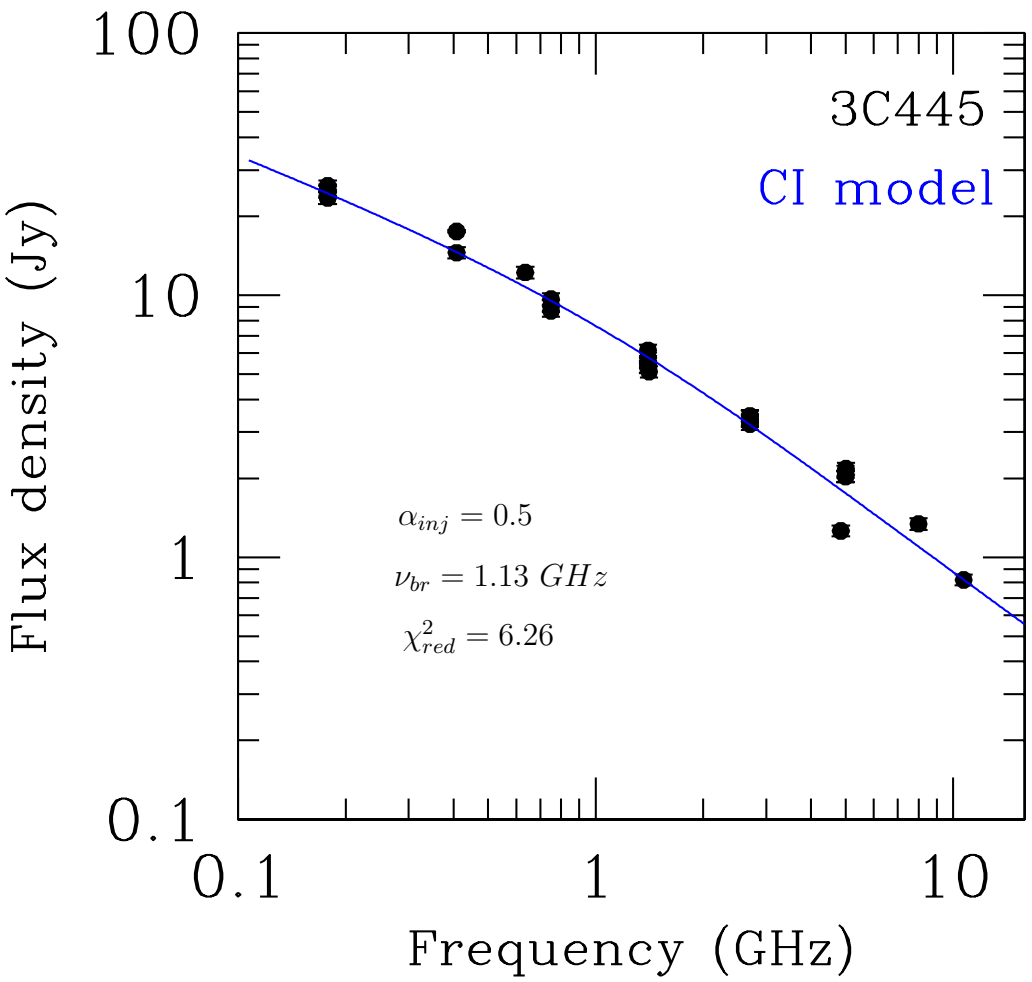

Figure 5.7: The total integrated radio spectrum of 3C 445. The continuous blue fit of the CI model shows the presence of a spectral break at frequency $\nu_{br} = 1.13^{+0.12}_{-0.11}$ GHz.

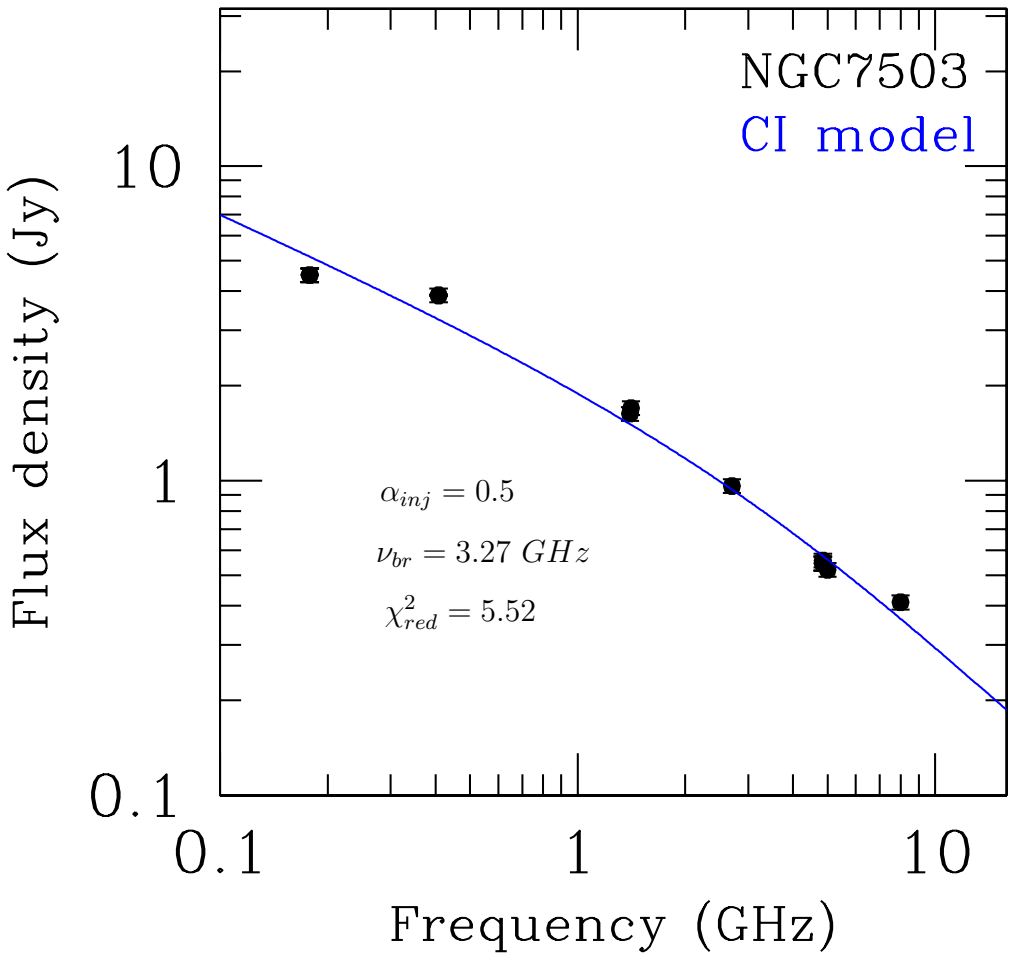

Figure 5.8: The total integrated radio spectrum of NGC 7503. The continuous blue fit of the CI model shows the presence of a spectral break at frequency $\nu_{\rm br} = 3.27^{+0.51}_{-0.42}$ GHz.

5.2.2 General comments

The break frequency differs from case to case and is in the 220 MHz - 7.5 GHz range, hinting at various ages, as discussed in the next Chapter 6. Most sources, such as 3C 198, CGCG -47-067, 3C 445 and NGC 7503 show these clear break frequency. Meanwhile, a single power law can accurately describe sources 3C 105, 3C 227 and 3C 403.1.

The CI model is considered a good fit, albeit the high reduced χ^2_{red} values for some sources are likely due to the underestimated errors in the flux densities rather than issues with the spectral model itself. For a source with continuous particle injection, the injection spectral index increases in steepness to its ultimate value beyond the break frequency. The JP and KP models presume a single injection with particle ageing in disparity with the CI model [Sohn et al., 2003]. Consequently, these models predict a spectral curvature, which we do not see for the radio galaxies in our sample. Visual inspection also suggests that any discrepancies in the fits are more attributed to the estimation errors than the accuracy fit of the model.

3C 105 The spectrum of the source can be described by both a power law with a slope of $\alpha = -0.64 \pm 0.02$ and the CI model, which infers an injected spectral index of $\alpha_{\rm inj} = 0.5$. This spectrum is derived from the literature estimates in Table C.8.

The fit of the CI model to the integrated spectrum is shown in Figure 5.1, which provides a break frequency $\nu_{\rm br} = 6.01^{+0.07}_{-0.08}$ GHz. The estimated equipartition magnetic field of the source following equation 5.8 is $B_{eq} = 4.11$ μG, with a minimum energy of the electrons at $u = 1.56 \times 10^{-12}$ ergs cm^{-3}.

The observed features (see Section 4.1, Figure 4.1) and the spectrum of this source strongly indicate that the radio emission is currently fed by an active nucleus, suggesting a highly efficient replenishment of the lobes, including very efficient transportation of the radio emission. Orienti and Dallacasa [2008] suggested that young radio sources tend to be in equipartition, notably higher than older sources. For detailed radiative age of the source, refer to Section 6 and Table 6.1.

3C 198 The CI model fit to the integrated spectrum is reported in Figure 5.2 and provides a break frequency of $\nu_{\rm br} = 0.22 \pm 0.05$ GHz. The equipartition magnetic field for the radiative electrons is estimated to be $B_{\rm eq} = 1.58$ μG, with an energy density of $u = 2.31 \times 10^{-13}$ ergs cm^{-3}.

The power-law spectrum of the source is steep, with $\alpha = -1.0 \pm 0.02$. This characteristic is further supported by the absence of hotspots, strong jets or a core in Section 4.1 Figure 4.2, indicating that the overall emission is predominantly driven by the radio emission originating from the lobes.

The observed lower break frequency, specifically for the radio emission dominated by the lobes, is a distinct indication of previous cycles of jet activity [Parma et al., 2007]. Its spectrum contributes significantly to determining the source age [Randriamanakoto, 2019].

3C 227 The source spectrum prefers a power-law model. A simple power-law fit gives a $\alpha = -0.78 \pm 0.02$ slope, effectively capturing the high-frequency data points within the spectrum.

The total integrated spectrum of the source, described by the CI model, is shown in Figure 5.3. This model provides a break frequency of $\nu_{\rm br} = 1.56^{+0.15}_{-0.14}$ GHz. The estimated equipartition magnetic field is $B_{\rm eq} = 5.16$ μG, for an energy density of $u = 2.46 \times 10^{-12}$ ergs cm^{-3}.

The high break frequency and the potential high frequency imply a significant contribution from the compact components within the source, such as the hotspots and core.

4C-03.43 Figure 5.4 shows that the integrated spectrum is scattered, likely due to the source's inhomogeneous data acquisition and the telescopes' varying resolutions. Consequently, the fit of the integrated spectrum is deemed inaccurate and unsuitable for further estimations.

However, from the measured power of the source in equation 3.2, $P_{1.4GHz} = 3.11 \times 10^{24}$ WHz^{-1}, the estimated equipartition magnetic field value is $B_{\rm eq}$= 1.33 μG for minimum energy of the electrons of $u = 1.64 \times 10^{-13}$ ergs cm^{-3}.

CGCG 047-067 The best fit of the CI model is reported in Figure 5.5. The fit provides a break frequency of $\nu_{\rm br} = 7.54^{+1.80}_{-1.30}$ GHz and the magnetic field strength is estimated as $B_{\rm eq} = 1.56$ μG, with an energy density of $u = 2.26 \times 10^{-13}$ ergs cm^{-3}.

The source is predominantly influenced by both its jets and lobes. As illustrated in Figure 5.12, there is a noticeable spectral steepening at greater distances, which becomes more pronounced the further one moves from the core. The radiative ageing of relativistic electrons can explain this pattern through synchrotron and Inverse Compton effects [Parma et al., 1998]. Additionally, it is essential to highlight that the spectrum's steepening is attributed to the reduced magnetic field strength resulting from adiabatic expansion [Heesen et al., 2017].

3C 403.1 Interestingly, the CI and power law model exhibit a steep injection spectral index. The spectrum is described as a power law with a value of $\alpha = 0.99 \pm 0.04$. The optimal fit of the integrated spectrum excludes the data point at 8 GHz frequency.

The CI model fit, illustrated by the blue line in Figure 5.6, indicates a break frequency of $\nu_{br} = 3.27^{+1.50}_{-0.96}$ GHz, inferring an injected spectral index of α = -0.89$\pm$0.04. The estimated value for the equipartition magnetic field is $B_{\rm eq}$= 2.67 μG. This estimated B_{eq} value is approximately consistent with that reported in the literature by Missaglia et al. [2022], which measured it at 2.4μG for a minimum energy density value of $u = 6.61 \times 10^{-13}$ ergs cm^{-3}.

3C 445 Figure 5.7 illustrates the integrated spectrum, which is best described by a CI model. The spectrum gives a break frequency of $\nu_{br} = 1.13^{+0.12}_{-0.11}$ GHz. The estimated minimum magnetic field strength is $B_{\rm eq} = 2.51$ μG for $u = 5.86 \times 10^{-13}$ ergs cm^{-3}.

The nature of the source is a DDRG, signifying a restarted activity primarily driven by the emission originating from the older structure of the source (i.e., the majority of the diffuse emission arises from the lobes). Nevertheless, in the context of the overall ν_{br} value and the radiative source age, it presents a combined

result of both the remnant structure and the young radio source, likely giving a lower limit to the age of the oldest emission (see section 6 and Table 6.1).

NGC 7503 Similar to the CGCG 047-067, the jets and lobes dominate the source.

The best fit of the CI model is reported in Figure 5.8. The fit provides a break frequency of $\nu_{\rm br} = 3.27^{+0.51}_{-0.42}$ GHz and the magnetic field strength is estimated as $B_{\rm eq}$ =2.644 μG, with an energy density of $u = 6.49 \times 10^{-13}$ ergs cm^{-3}.

5.2.3 In-band spectral index

One of the key features of MeerKAT and uGMRT is the broadband available in each observing band, which allows for spectral index imaging, i.e., the spectral index distribution along the radio source structure. Moreover, their angular resolution and reasonably comparable u-v coverage allow spectral index imaging between MeerKAT and uGMRT observing bands. Such information allows us to carry out a point-to-point analysis of the spectral index distribution in the sources, potentially showing regions of different ages and sites of re-acceleration. The standard direct method of determining the spectral index between maps $S_{\nu 1}$(x,y) and $S_{\nu 2}$(x,y) at two frequencies ν_1 and ν_2 is given by

$$\alpha_{\nu_1\nu_2}(x,y) = \frac{lnS_{v_1} - lnS_{v_2}}{lnv_2 - lnv_1}. \tag{5.10}$$

To ascertain the spectral indices between ν_1 and ν_2, the u-v planes of the datasets need to have at least the same shortest and same longest baseline, be convolved with the same restoring beam, and possibly have comparable u-v coverages. This process is performed using the *imsmooth* Casa task by executing a Python script. Although the convolution operation eliminates a significant portion of the small-scale visible features in the high-frequency images, it guarantees a distinct identification of emission originating from identical regions in each source. Once the common resolution is attained, it enables a suitable fit for the spectral index. This process is implemented through Spimple [1] (Spectral index fitting made simple) software, specifically utilizing spimple-spifit. This involves convolving to a shared resolution, with the additional option of performing primary beam correction on fly.

We included the eight MeerKAT sub-band images convolved to 10 arcsec in making the in-band spectral index map. The figures 5.9, 5.11, and 5.12 are derived from frequencies in the range of 909.39 to 1658.39 MHz. The threshold enabled a lower value of 6σ. This section outlines the distribution of in-band spectral indices for each source conducted using the Spimple tool.

[1] https://github.com/landmanbester/spimple

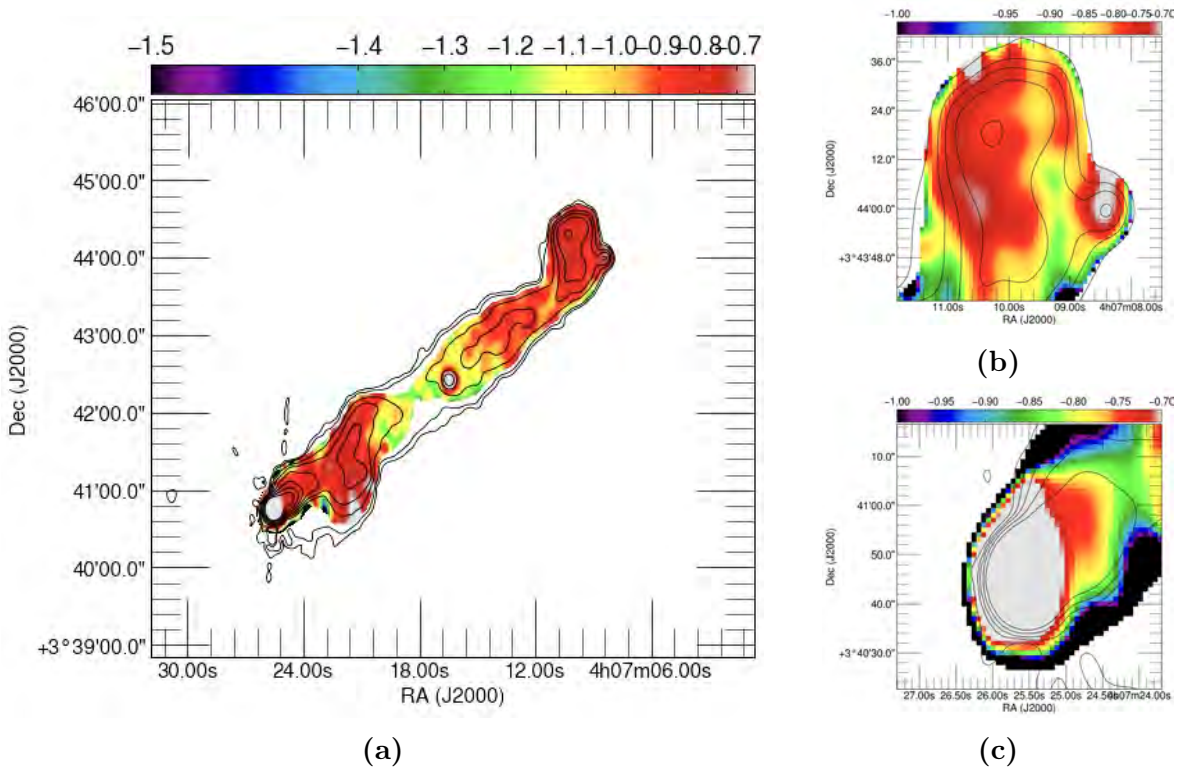

Figure 5.9: The distribution of the spectral index $\alpha(S\nu \propto \nu^{\alpha})$ in range 909.39 to 1658.39 MHz of 3C 105 (main image labelled (a)). The full range of the spectral index is -1.5 to -0.7 plotted in black contours showing the total intensity at $3\sigma \times$ [-1,1,2,4,8,..] with σ_{rms} the noise level (see table 3.3.2). The cutout labelled (b) shows a zoomed-in portion of the northwestern hotspot, and (c) is the zoomed-in region of the southeastern hotspot.

The spectral index image of 3C 105 is given in Figure 5.9 The spectral index trend of the lobes, with α steepening from the hotspots towards the core, clearly shows that the lobes are backflow emission left behind by the hotspots advancing in the ICM. The hotspots in 3C105 have spectral indices of $\alpha \leq -0.5$ between 909.39 to 1658.39 MHz, with gradual steepens of the spectral to the radio indices less than $\alpha \leq -0.8$ in the lobes. The spectral steepening inward from the hotspots is typical in FR II powerful radio galaxies. This effect has been explained as synchrotron radiative 'ageing' of relativistic electrons. The spectra flatten at the core $\alpha \geq -0.5$.

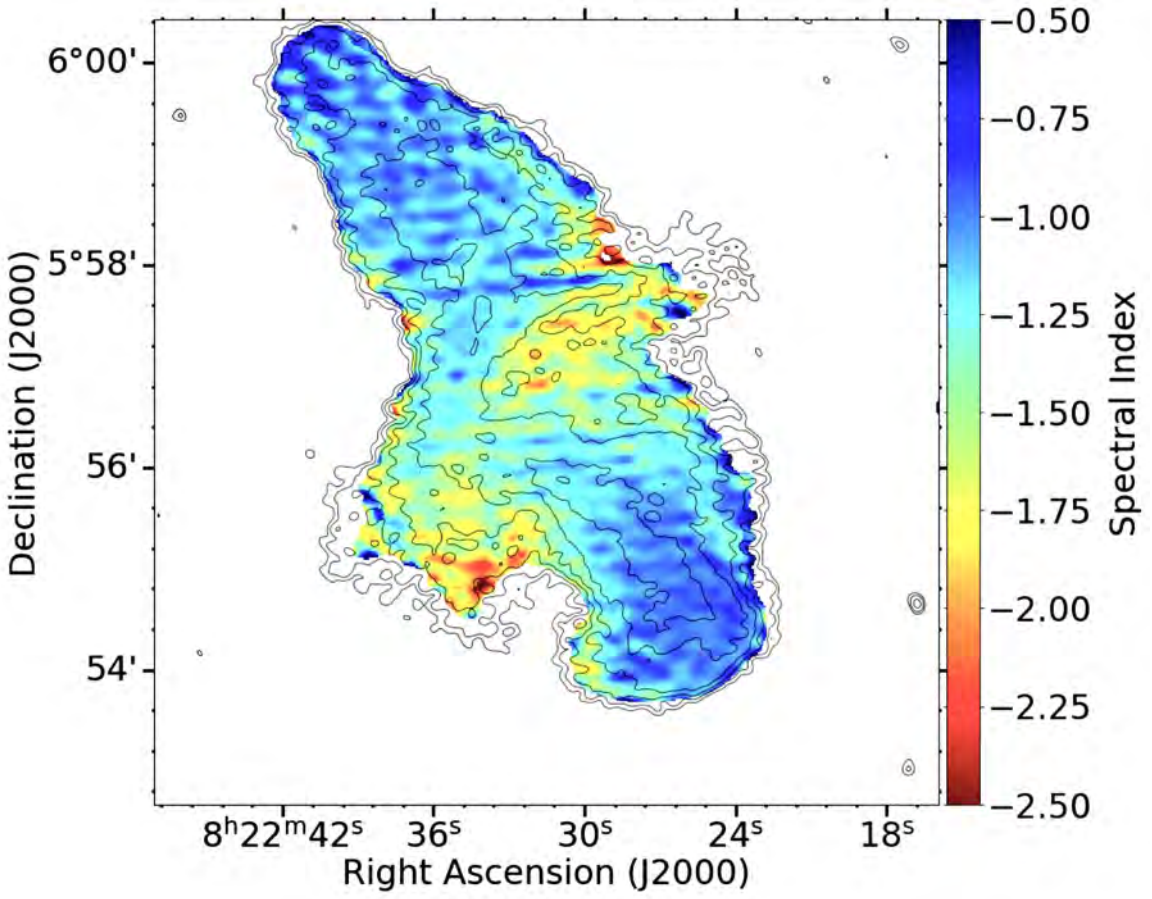

Figure 5.10: The spectral index map of 3C 198 with the MeerKAT radio contours at 1.28 GHz overlayed on the image [Sejake et al., 2023].

For spectral index trend of 3C 198, we used the total intensity images obtained by [Sejake et al., 2023] and produced the spectral index image shown in Figure 5.10. Interestingly, it shows some steepening from the location of the hotspots towards the centre, ranging from $\alpha \sim -0.5$ to $\alpha \sim -1.6$. The spectrum of the NW-SE extension perpendicular to the major axis of the source shows a much steeper spectrum and no obvious trends (the filament is indicated in Figure 4.2). The MeerKAT feature of the horizontal filament does not indicate these features in the spectral index map. For the northwest to Southeast filament, it is rather difficult to determine its spectral index due to the errors portraying a fine line across the image due to sensitivity limitation.

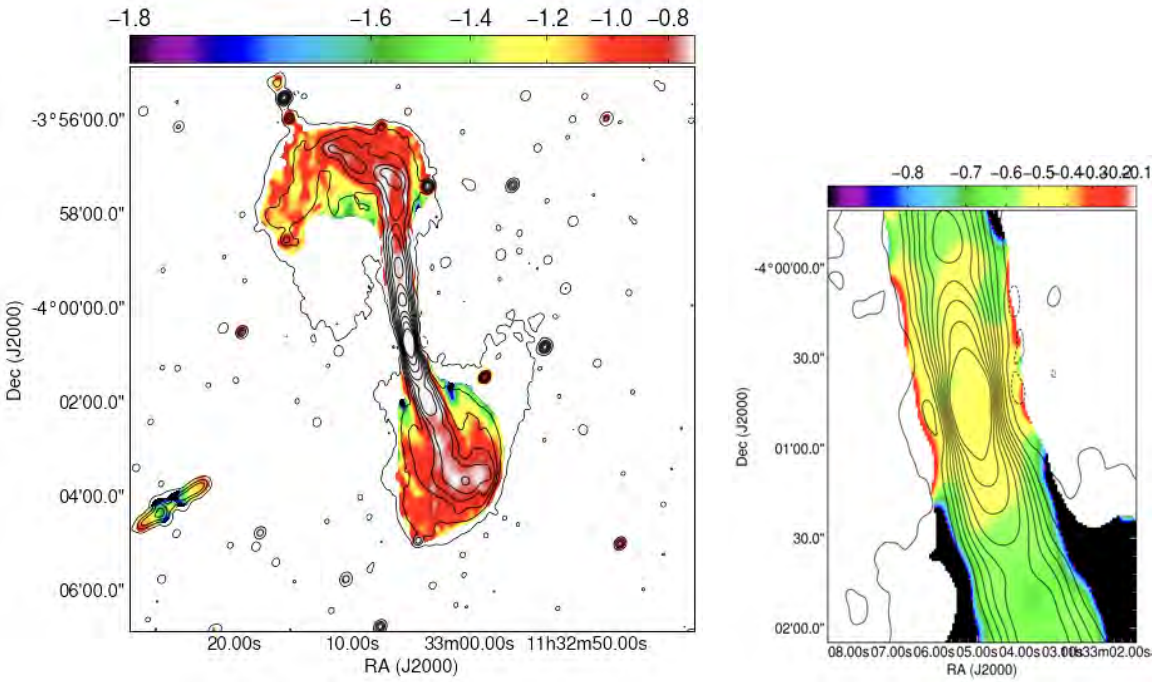

(a) 4C -03.43 **(b)** Zoomed in core region.

Figure 5.11: The spectral index map of 4C -03.43 between 909.39 to 1658.39 MHz. The MeerKAT radio contours at 1.28 GHz are drawn in black at $3\sigma_{rms} \times$ [-1,1,2,4,8,..] with σ_{rms} the noise level (see table 3.3.2). The blank region between closed contours and the colour scale is probably steeper than the plotted colour scale. The right panel shows an inset of the inner jet of the source.

In 4C -03.43, the spectrum steepens along the jets, from the core region to the outer lobes, as typical in FR I radio galaxies. In Figure 5.11, the steepening of the spectral index within the lobes has a moderately steep spectrum in a range $[-0.8, -1.0]$ surrounding the jets. The spectrum in the lobes gradually steepens outward, reaching values of $\alpha \sim -1.5$. The features in the spectral-index maps at the edges of the source, and particularly at the ends of the lobes, are likely to be even steeper than lobes. This behaviour aligns with the expectation that such regions are predominantly dominated by old electrons, which age due to the emitted synchrotron radiation.

Figure 5.12 shows the MeerKAT in-band spectral index of CGCG 047-067. The south-eastern lobe has a fairly uniform and only moderately steep spectrum (α in the range $[-0.8, -1.0]$) throughout its extent. On the other hand, the northern lobe shows two distinct regions: the inner 7 arcmin ($\sim$ 440 kpc) have an average spectral index α $\sim$ –1. The spectrum steepens considerably abruptly beyond this region, with α dropping to values as steep as -1.5. The total intensity images shown in Figure 4.7 show that a sharp drop in brightness occurs at the position where the spectrum steepens.

For the sources 3C 403.1 (uGMRT), 3C 227 (uGMRT), 3C 445 (MeerKAT), CGCG 047-067 (uGMRT) and NGC 7503 (uGMRT), we were unable to derive the spectral images due to large systematic errors and artefacts in the total intensity images.

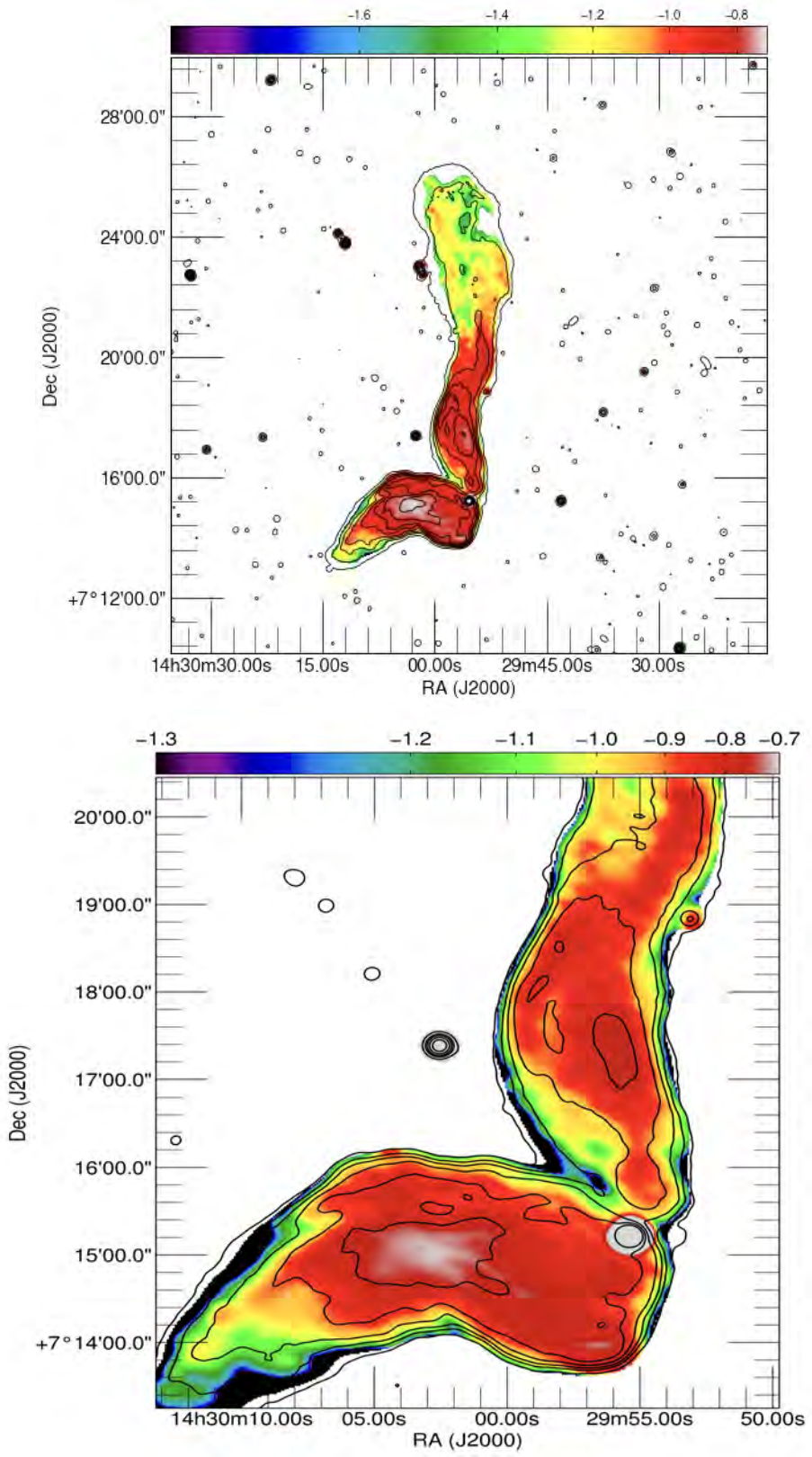

Figure 5.12: The top panel shows a spectral index map of CGC 047-067 between 909.39 to 1658.39 MHz. The MeerKAT radio contours at 1.28 GHz are drawn in black at $3\sigma_{rms}$ × [-1,1,2,4,8,..] with σ_{rms} the noise level (see table 3.3.2). The bottom panel shows the zoomed-in portion of the north and southeast lobe, with contours emphasising a sharp transition.

Chapter 6

Estimate of Ages

The observed trends along spectra are interpreted by radiative ageing of relativistic electrons through synchrotron or Inverse Compton (IC) processes.

By assuming an injected spectral index α_{inj}, thereby obtaining a break frequency ν_{br} under the assumption of equipartition, it is possible to estimate the radiative age of a radio galaxy [Rybicki and Lightman, 1991].

The theoretical synchrotron-loss spectra in this work are computed numerically [Murgia, 1996] following Pacholczyk [1970] synchrotron formulae. Generally, the most considered models are the JP, KP and CI (see Section 5.2). For the JP model, the radiative age is given by

$$t_{rad} = 1590 \, \frac{B^{0.5}}{B^2 + B^2_{CMB} \, [(1+z)\nu_{br}]^{0.5}} \, , \tag{6.1}$$

the KP model

$$t_{rad} = 1060 \, \frac{B^{0.5}}{B^2 + \frac{2}{3} B^2_{CMB} \, [(1+z)\nu_{br}]^{0.5}} \tag{6.2}$$

and the CI model

$$t_{rad} = 1610 \, \frac{B^{0.5}}{B^2 + B^2_{CMB} [(1+z)\nu_{br}]^{0.5}} \, . \tag{6.3}$$

Where t_{rad} is the radiative age in Myr. The break frequency ν_{br} in GHz can be represented more conveniently as

$$\nu_{br} \;\; [GHz] = \frac{2.52 \times 10^9}{B^3 t^2_{rad}} \tag{6.4}$$

and

$$\nu_{br} \;\; [GHz] = \frac{1.12 \times 10^9}{B^3 t^2_{rad}} \tag{6.5}$$

For both the JP and KP models, respectively.

The break frequency $\nu_{\rm br}$ is determined by the time elapsed since the injection of high-energy electrons, as the frequency progressively shifts over time to lower values of the source spectrum.

The magnetic field equivalent B_{CMB} accounts for the Inverse Compton losses with $B_{CMB} = 3.25\ (1+z)^2\ \mu G$ at a given redshift z, adopted equivalently to a black body temperature of 3K.

In particular, we prefer the CI model, considering that the source is fueled at a constant rate [Kardashev, 1962]. Such spectrum results in a break frequency with a steeper power law at higher frequencies, giving a spectral index

$$\alpha_{high} = \alpha_{inj} + 0.5 \tag{6.6}$$

overtime the break frequencies shift to the lower frequencies, and the injected spectral index can be denoted as

$$\alpha_{lower} = \frac{\delta - 1}{2}. \tag{6.7}$$

.

see Section 5.2 for the spectral fitting. The radiative ages of each source are reported in Table 6.1.

Table 6.1: Synchrotron parameters. Column 1: Source name. Column 2: Source redshift. Column 3: Break frequency derived from the fits. Column 4: The equipartition magnetic field computed following section 5.1. Column 5: The source age computed using equation 6.3.

Object ID	z	ν_{br} GHz	B_{eq} μG	t_{rad} Myr
3C 105	0.089	6.01	4.11	40.20
3C 198	0.081	0.22	1.58	242.85
3C 227	0.085	1.56	5.16	68.10
CGCG 047-067	0.05	7.54	1.56	46.13
3C 403.1	0.055	3.27	2.67	70.11
3C 445	0.056	1.13	2.51	119.95
NGC 7503	0.044	3.27	2.64	72.47

The ages of our sources are computed based on the equipartition assumption (see equation 5.5). However, following Ineson et al. [2017] and Mahatma et al. [2020], we acknowledge that B_{eq} can be considered an upper limit; as a consequence, the derived ages should indicatively be considered lower limits. Our analysis is of zero order, relies on the integrated spectra, and does not account for the potential variation in the magnetic fields, which has inherent limitations. Therefore, a degree of uncertainty is associated with the age estimates. Table 6.2 further shows the impact of the magnetic field strength on the age estimate. In particular, we consider two values for the magnetic

Table 6.2: Radiative ages and magnetic field estimates. Column 1: Source name. Column 2: Source redshift, z. Column 3: The equipartition magnetic field computed following section 5.1. Column 4: The lower magnetic field threshold equivalent B_{CMB} scale to the redshift. Column 5: The additive age derived using B_{eq}. Column 6. The radiative age derived using $B_{CMB}/\sqrt{3}$.

Object ID	z	B_{eq} μG	$B_{CMB}/\sqrt{3}$ μG	t_{rad} Myr	t_{rad}(revised) Myr
3C105	0.089	4.11	2.23	40.2	47.41
3C198	0.081	1.58	2.19	243.06	251.7
3C227	0.085	5.16	2.21	68.09	94.13
CGCG047-067	0.0548	1.56	2.09	46.13	47.32
3C403.1	0.055	2.67	2.09	70.11	71.84
3C445	0.0562	2.51	2.09	119.96	121.49
NGC7503	0.044	2.64	2.05	72.47	74.03

field, i.e. the equipartition value computed above and the value obtained from the B_{CMB}, mainly determined by the redshift. The latter is typically smaller than B_{eq}, thus yielding slightly higher radiative ages. This effect is observed across sources as in 3C 227 where the ages extend from 68.09 Myr with B_{eq} to 94.13 Myr with $B_{CMB}/\sqrt{3}$, and in 3C 445 with a range from 119.96 to 121.49 Myr. We thus consider B_{eq} and $B_{CMB}/\sqrt{3}$ as the boundaries for our estimates of the magnetic fields and the radiative ages of the sources in our sample.

Chapter 7

Discussion

The MeerKAT and uGMRT images in this work cover a frequency range of $550 - 1712$ MHz with almost identical angular resolutions and sensitivities, making them ideal for studying radio morphology and spectral features of radio galaxies' jets and lobes. The images acquired with the two arrays for all analysed sources are of similar quality, giving credibility to the imaging processing and calibration of the uGMRT and MeerKAT datasets.

Overall, our images confirm the morphological classification reported in Table 3.1 based on images with lower sensitivity and resolution. An exception exists of 3C 403.1 with characteristics of the FR I and FR II types. Nevertheless, the Fanaroff-Riley classification framework still effectively categorises these sources into FR I and FR II based on the overall morphology.

While the ambiguity of 3C403.1 suggests a deviation from typical Fanaroff-Riley characteristics, several other sources exhibit features that align with their respective FR classes. For instance, 3C 227 displays double hotspots, CGCG 047-067 shows WAT, and 3C 445 and NGC 7503 exhibit well-aligned DDRG and NAT features, respectively. These characteristics are not considered anomalous within their respective Fanaroff-Riley classifications.

Furthermore, using the $P_{178\,\mathrm{MHz}} \sim 10^{25}$ WHz^{-1} threshold [Fanaroff and Riley, 1974] as the dividing line broadly supports the existing classifications. Radio sources with $\leq 10^{25}$ WHz^{-1} fall firmly within the FRI category, consistent with typical FR characteristics [Parma et al., 2002, Capetti et al., 2020]. Of the FR II radio galaxies in our sample, 3C 227 's radio power $P_{700\mathrm{MHz}} > 10^{25}$ WHz^{-1} is an order of magnitude above the canonical FR I and FR II break. This suggests that power alone may not be a sufficient definitive factor for classification, and other factors like morphology may need to be considered (e.g., Ledlow and Owen [1996], Hardcastle et al. [2007a], Saripalli [2012]. As summarized in Table 7.1, most sources in our sample fall within the expected limits for their respective classes, although the boundaries between FR I and FR II are not always clear-cut.

Table 7.1: Summary of the sample properties

Source	Type	Anomalous Properties	Power limits	Nature vs. Nurture
3C 105	FR II	Hammerhead structure in NW hotspot	1.32×10^{26} WHz^{-1} (at 1.28 GHz) - Within FR II range	Recent escape from bounded halo (environment)
3C 198	FR I	No bright hotspots and core, diffuse emission	3.94×10^{25} WHz^{-1} (at 1.28 GHz) - Within FR I range	Diffuse, filamentary emission (possibly environment)
3C 227	FR II	Double hotspots in W, trail in E	2.24×10^{26} WHz^{-1} (at 700 MHz) - Within FR II range	Stream splitting (intrinsic)
4C -03.43	FR I	S-shaped, jet-bending	6.91×10^{24} WHz^{-1} (1.28 GHz) - Within FR I range	Interaction with ICM (environment)
CGCG 046-067	FR I (WAT)	Wide-angle tail (WAT), bright SE lobe	1.71×10^{25} WHz^{-1} (1.28 GHz) - Within FR I range	WAT structure (environment)
3C 403.1	Ambiguous (FR I/II)	Peculiar morphology, diffuse emission	1.39×10^{25} WHz^{-1} (1.28 GHz) - Within FR I range	Diffuse emission, possible nuclear activity (intrinsic/ environment)
3C 445	FR II	Inner double hotspots	4.89×10^{25} WHz^{-1} (1.28 GHz) - Within FR II range	Splatter splitting (intrinsic/ environment)
NGC 7503	FR I (NAT)	Narrow-angle tail, (NAT), hotspot present	1.17×10^{25} WHz^{-1} (700 MHz) - Within FR I range	Narrow-angle tail, jet morphology (environment)
SDSS J09157+1331	FR 0	Compact	1.30×10^{23} WHz^{-1} (1.28 GHz) - Within FR 0 range	
SDSS J1120+0407	FR 0	Compact	4.12×10^{22} WHz^{-1} (1.28 GHz) - Within FR 0 range	

7.1 Spectral properties

Inspection of the integrated spectrum of the sources in Figures 5.1 clearly shows that the spectra of our sources are slightly different in behaviour. A power-law reasonably fits 3C 105 and 3C 227 with $\alpha = -0.64 \pm 0.02$ and $\alpha = -0.78 \pm 0.02$ respectively. The normal-to-flat spectral index values observed in both sources suggest that the radio emission is dominated by the active components, i.e., the hotspots and the core. These components induce ambiguity in the true steepening of the spectra due to energy losses and curvature produced by the absorption process in the components [Murgia et al., 2002].

CGCG 047-067 and NGC 7503 have distinct break frequencies of $\sim 7.53^{+1.80}_{-1.30}$ GHz and $\sim 3.27^{+0.52}_{-0.43}$ GHz, respectively. Both sources' spectra indicate that the radio lobes possess a dominating role. Most radio sources deviate greatly from the classical power-law [Jackson and Wall, 2001]. Figure 5.2 shows a typical example of the spectra of our selected sample of radio galaxies, with $\alpha = -1.00 \pm 0.02$ over a break frequency of $0.22^{+0.05}_{-0.05}$ GHz. Other sources in a sample are flatter than others while steeping above $\sim$ 1.5 GHz (i.e., CGCG 047–067, 3C 403.1 and NGC 7503). Higher frequency curvature indicates radiative ageing of electrons in young sources [Murgia et al., 2002]. Considering a high-frequency break in CGCG 047-067, the estimated age of 46.13 Myr aligns with the typical spectral age range ($6 - 46$ Myr) observed in giant radio sources (GRGs) [Konar et al., 2009]. Further noting the dynamics of FR I radio galaxies are impacted by their interactions with the environment [Machalski et al., 2009]. However, the GRGs FR I source develops in low-density settings, allowing for growth across long distances [Heesen et al., 2017]. This calls out the question of how the extension of the radio source contributes to the global source age. Heesen et al. [2017] states that this effect is either due to the outer tail material not representing the oldest plasma or the particle's ages are underestimated due to the effect of particle acceleration over a large-scale structure.

The inband spectral index maps confirm the source's radiative ageing. Clear, distinct regions were detected within the spectral index of the radio source that gradually steepened from the flat core to the tail's ends. The jets are relatively homogeneous, having a spectral index $\alpha \sim -0.6$, as predicted from synchrotron emission. The transition between the jet's inner area and the tail's outer northern region exhibits a steep shift in the overall intensity and the spectral index $\alpha \sim -1.2$. The sharp transition found in the outer portion of the source varies from $-1.3 \leq \alpha \leq -0.3$, comparable to CGCG 044-046 [Fanaroff et al., 2021]. Furthermore, the sharp transition in CGCG 047-067 might indicate intermittent activity of the AGN's radio emission or radio jet interaction. We identified a steepening from the hotspot to the core and backflow emission in the lobes of 3C 105. This suggests an effective replenishment of the lobes and transmission of radio emission, indicating a young source. The spectral index map is consistent with the hotspot definition in [Croston et al., 2005]. As previously noted, the spectral index of the 3C 198 is consistent from the lobes to the areas of the hotspots, at least in the MeerKAT frequency range. We corroborate the general nature and morphology of the

source in Section 7.2.

7.2 The case of 3C 198: A dying/dead radio galaxy?

The inspection of Figure 5.2 shows that the morphology of 3C 198 is barely elongated in North-East and South-West directions and becomes more diffuse and filamentary.

The amorphous morphology of the source shows a steep spectrum (Figure 5.10), and the age derived in Section 6 indicates 3C 198 is an aged source. The total spectral index covered within our frequency range by our observation shows similar deviations to the 4C 12.03 Fanaroff and Riley [1974], indicating a decline in new particle replenishment.

The physical properties of the source match those of a dead radio galaxy. Whilst situated in a low-richness (poor) cluster, it is classified as a bright cluster galaxy (BCG) included in the W4CGS catalogue noted as GMBCG J125.63314+05.95189 BCG [Runge and Yan, 2018]. Its high surface brightness ($\sim$ 6.82 mJybeam^{-1}) contributes to its notable visibility. The absence of a core and hotspot areas indicates that the source is not refreshed with new particles, indicating a lack of continuous electron injection [Parma et al., 2007, Murgia et al., 2011]. Its filament nature led to the understanding that particle acceleration is slow or no longer occurring. As such, 3C 198 is a dying source.

Our fit model of the spectra is based on the thorough CI model described in Murgia et al. [1999], which accounts for energy losses that shift the break frequency to lower values. The old age is calculated using spectral fitting, considering the time elapsed since the last injection/re-acceleration.

7.3 Properties of the total sample

Indeed, the high-sensitivity and high-resolution images of the radio sources using uGMRT and MeerKAT demonstrate that in almost all cases, barring CGCG 047-067 and CGCG 044-046, the surface brightness declines sharply at the edges of the visible radio lobes and of the low surface brightness features.

The overall sample of sources suggested that the radio sources can be broadly identified into regions [Fanaroff et al., 2021]:

1. The region close to the AGN, where the FR I and FR II are classified.
2. The region of impact between the hotspot and the intergalactic medium, and
3. beyond the hotspot, revealing the interaction between the galaxy tail and the surrounding medium.

The overall radio source sample includes radio galaxies with well-defined structures, a combination of classical double-lobed structures, and more complex morphologies,

i.e., the S/Z-shaped, L-shaped, X-shaped and tailed radio galaxies(WAT and NAT) structure. The morphological details, such as the filaments and multiple hotspots and knots, provide insights into the interactions within the radio galaxies. Such interactions suggest various possibilities, such as contact discontinuities or jet collimation by its surrounding [Hardcastle et al., 2007a].

The spectral index analysis of the overall sources across the sample indicates a variety of behaviours, such as uniform spectral indices (e.g., 3C 198). In other cases, the spectral index maps show substantial steepening, suggesting variable age across the source. An exceptional case in the spectral indexing is the variance between the inner and outer portion of the tails (e.g. CGCG 047-067 and CGCG 044-046), which indicates a sharp transition and episodic character of the jet, consistent with electron ageing.

It is evident that the environment affects the source's direction and, therefore, its projection.

We detected filamentary structures in radio galaxies across the radio lobes. Examples of these features are observed inside the lobes and tails of radio galaxies, particularly in 3C 198 and 4C −03.43, as well as tails CGCG 047-067, CGCG044-046 and NGC 7503. The magneto-hydrodynamics (MHD) simulations of radio galaxies' lobes suggest that these filaments reflect enhancement in the magnetic field distribution within radio galaxies, suggesting the presence of the magnetic field structures' contribution to the observed brightness distribution, [Hardcastle and Krause, 2013]. Polarisation information is available for the sources observed with MeerKAT. A full polarization analysis is planned to address the question of the interaction of the radio plasma with the external medium.

Chapter 8

Conclusion

We have presented the uGMRT and MeerKAT images of ten radio galaxies belonging to a larger sample of 17 (9 FR I, 6 FR II, and 2 FR 0) radio galaxies that are carefully selected with well-defined selection criteria that cover a frequency range from 550 MHz−1712 MHz providing radio images at nearly identical angular resolutions and sensitivities.

The total intensity maps and in-band spectral index calculated at ten arc-sec resolution were also presented. A full description of these maps, as well as precise spectral analyses, were covered in this study. Our data indicate highly intriguing morphological characteristics for radio galaxies, such knots, hotspots, lobes, wiggles, and filaments at the radio μJy beam^{-1} sensitivity and high ($\sim 4''$ to $10''$) angular resolution of the images which have been presented.

8.1 Summary of the results

1. Some tailed radio galaxies are part of the selected sample, such as radio galaxy 4C -03.43 seen face-on, which is a result of ram pressure due to the motion of the galaxy relative to the galaxy cluster Abell 1308 and a possible interaction with a density contact discontinuity, influencing its jet trajectory.

   The L-shaped WAT CGCGC 047-067 also observed edge on. Remarkably, its total size is $\sim$ 950 kpc, regarded as a typical giant radio galaxy.

   We further observed a NAT NGC 7503, whose collimated jet and tails extend $\sim$ 160 kpc in the north direction. The radio emission in tails reveals fine structure at the angular resolution of our observations, displaying wiggles and filaments.

2. Compared to Leahy et al. [1997] our radio images show several high surface brightness compact features emissions along the jet before terminating in 3C 105, parallel ridges of emission from hotspots back to the centre indicating a recent escape of the lobe from a strongly bounded halo surrounding the host galaxy. The emission typically has $-0.5 \leq \alpha \leq -0.7$ and $-0.8 \leq \alpha \leq -0.9$ in the lobes.

3. Our high-resolution images of 3C 227 show evidence of multiple hotspots at the western jet termination point $\sim$ 14.02 pc away from the core reported in Leahy

et al. [1997]. The radio galaxy also shows two clear double peaks as reported in Hardcastle et al. [2007a], resulting from possibilities of propagation of the jet through contact discontinuities of a possible standing shock (describing the primary jet termination point) and a collimated outflow from the primary hotspot (secondary hotspot).

4. The analysis of the spectral index maps reveals that the radio sources are dominated by synchrotron emission. The hotspots and jets exhibit flatter spectra than the material they propagate in, particularly evident in sources 4C −03.43 and 3C 105. This observed spectral steepening is consistent with the theoretical expectation of decreasing particle energy as we move further from the re-acceleration sites.

5. Our detailed study of the spectral index distribution in CGCG 047-067 shows that:

   - the jets are relatively uniform with a spectral index $\alpha \sim -0.6$, which is expected from a synchrotron emission.
   - The transition between the jet's inner region and the tail's outer northern region shows a sharp transition in the total intensity and the spectral index. The sharp transition observed at the outer region of the source varies from $-1.3 \leq \alpha \leq -0.3$ similarly to CGCG 044-046. As stated in Fanaroff et al. [2021], the origin of the sharp transition in the surface brightness are yet unclear. However, it could reflect intermittent activity of the AGN's radio emission or the radio jet's interaction with the external medium.

6. The broad range of frequencies allowed us to perform spectral ageing analysis of the eight sources fitted. In particular:

   - 3C 105 and 3C 227 can be well explained by a simple power law, well fitted over all parts of the frequency range.
   - In 3C 227 (t_{rad} = 68.10 Myr), the spectrum may likely be dominated by the brighter components, causing uncertainty in the genuine steepening of the spectra of the source. An interesting case is the steepness of 3C 198 and the derived age of the sources, t_{rad} = 242.85 Myr, confirmed detection of an old source in its dying state due to slow replenishment of the injected electrons in the source.
   - The magnetic field values in our sample are of the order of $1.5 - 5$ μG. Amongst the reported 3C 198 and CGCG 047-067 have low magnetic field values. However, such low values are not unique to dying radio source [Rudnick, 2004, Parma et al., 2007]. The magnetic field values are likely underestimated for the source CGCG 047-067.

Overall, the quality of the images is similar to that of the uGMRT and MeerKAT images of the fourteen radio galaxies. This gives confidence in the image quality, calibration, and imaging process of the uGMRT and MeerKAT data; as such, the classical morphology can still be applied with the advancement of interferometers. However, the

rich detail of these radio sources suggests new types of interaction between the radio plasma and the surrounding medium. For surveys conducted with radio telescopes with significantly poorer sensitivity to diffuse, low-brightness emission, our work suggests caution when employing source identification techniques for the morphological classification of radio galaxies. As a result, to conduct a thorough study of radio galaxies, high image sensitivity across a wide range of angular scales is required.

8.2 Future work

The work described here and in the earlier work in Fanaroff et al. [2021] have provided much observational information on the hotspots, lobes, jets and filaments in radio galaxies and have, to an extent, made the physics of these objects clearer. As the next step,

We aim to revisit the calibration procedure of the total intensity maps from the uGMRT observation of 3C 198, 3C 227 and NGC 7503 to attain high-resolution images. This observation will then provide an opportunity to derive the spectral index maps. The results will address the nature of the source.

The key to fully addressing the research questions of this present work is the knowledge of the magnetic field strength. The observed synchrotron emission from the radio galaxies in our sample illustrates the presence of the intergalactic magnetic field. As an extension of this work, we obtain polarization information, which is available for the MeerKAT observations to investigate further their orientation and the degree of ordering the magnetic field in the radio sources. This will further enhance our understanding of the underlying physics of the sources.

The environment of radio sources is crucial; this type of data is critical since we know that the environment can impact the behaviour of a radio source on all scales. We intend to supplement our observations with X-ray observations to better understand each source's surroundings.

Appendix A

Reference calibration

A.1 MeerKAT Delay Solutions

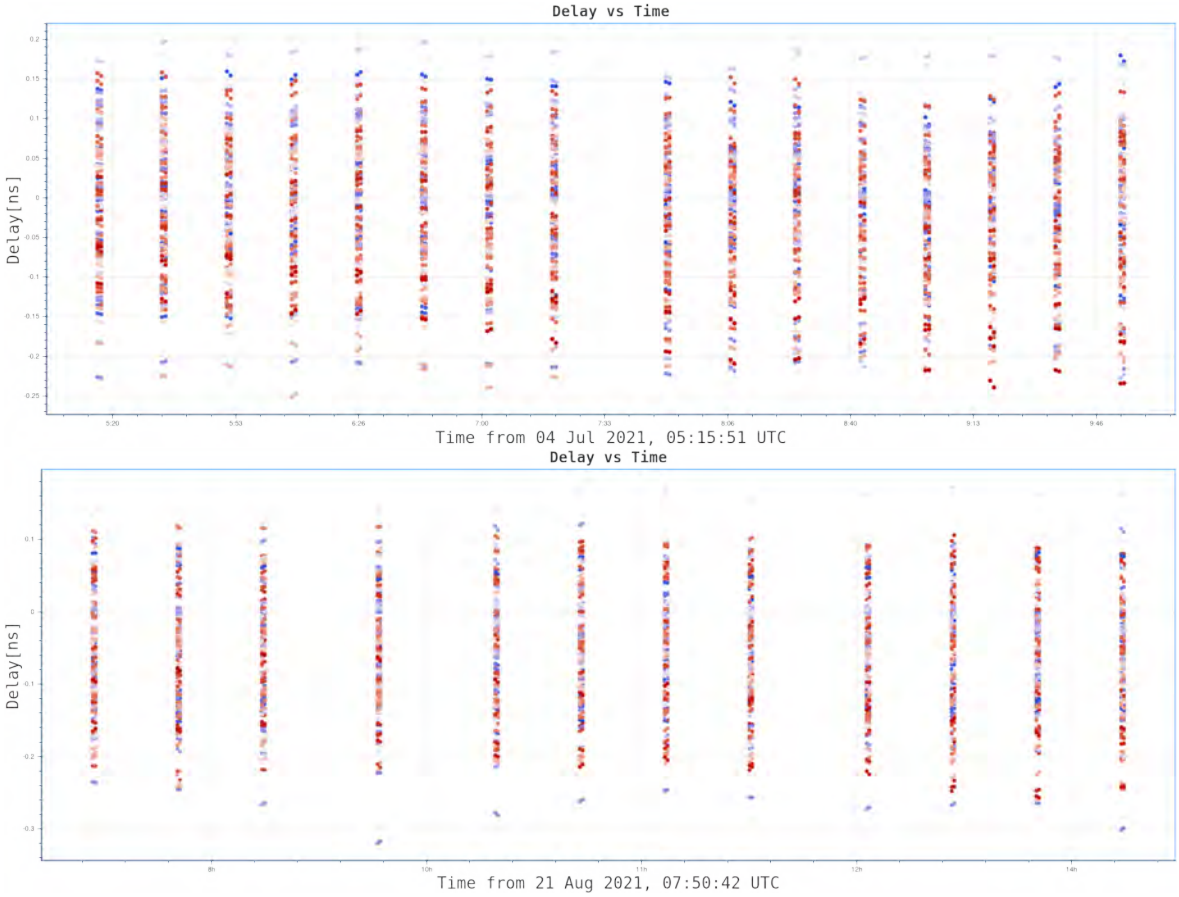

Figure A.1: 3C 105 and 4C -03.43 delays estimated for all antennas for the YY and XX correlated observation of the primary and secondary fields

Figure A.2: 4C -03.43 (top panel), SDSS J 1120+0407 (top panel), CGCG 047-067 (upper-middle panel), 3C 445 (lower-middle panel) and SDSS J 09157+1331 (bottom panel) delays estimated for all antennas for the YY and XX correlated observation of the primary field.

A.2 MeerKAT Bandpass Solutions

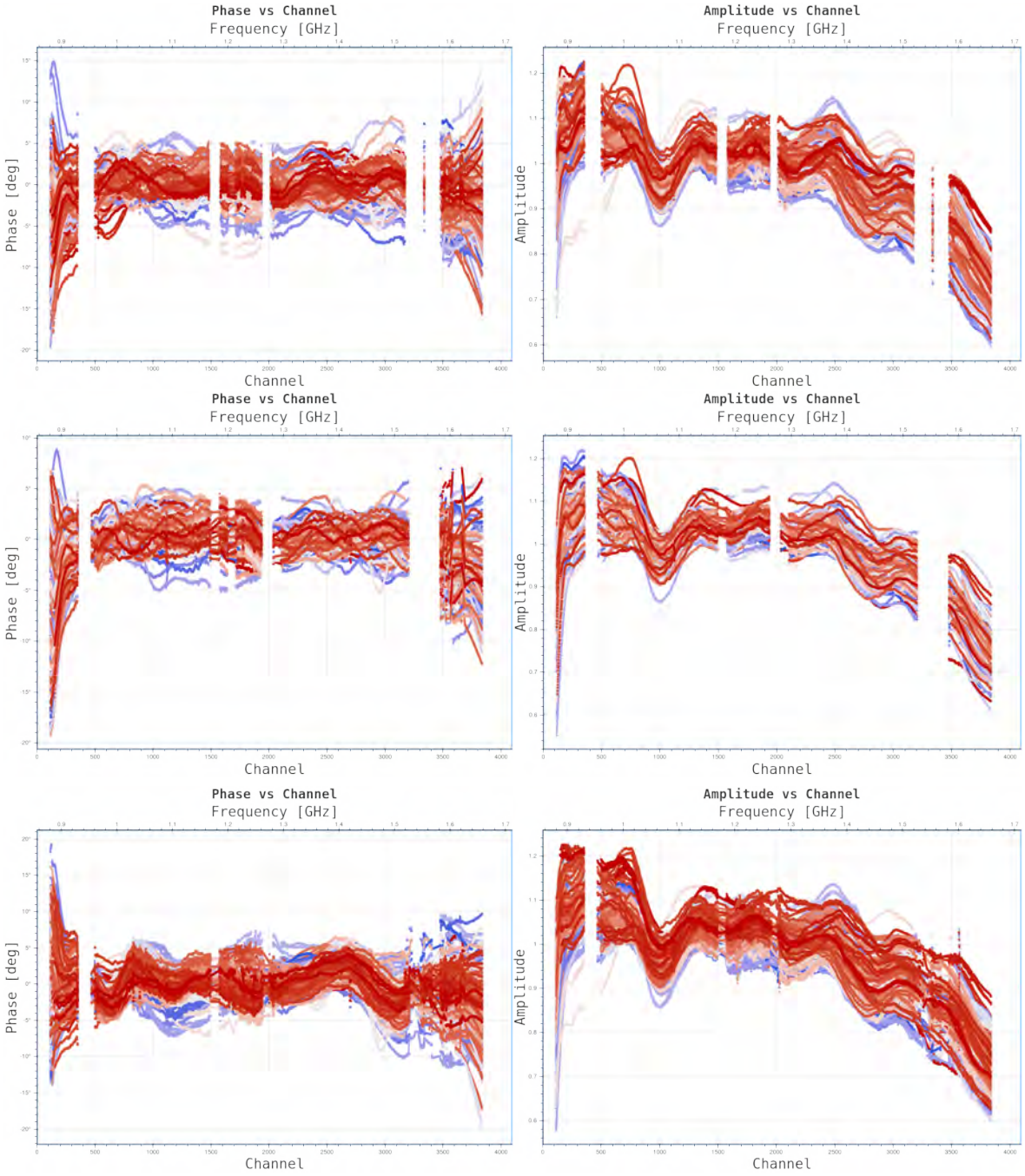

Figure A.3: The 3C 105 (top panel), 4C -03.43 and SDSS J 1120+0407 (middle and bottom panels) bandpass solutions extracted from the primary calibrator. The right panels are the amplitude solutions and the left panel represents the phase solutions as a function of frequency. Each colour represents an antenna in the array. The gaps are where strong RFI has been flagged.

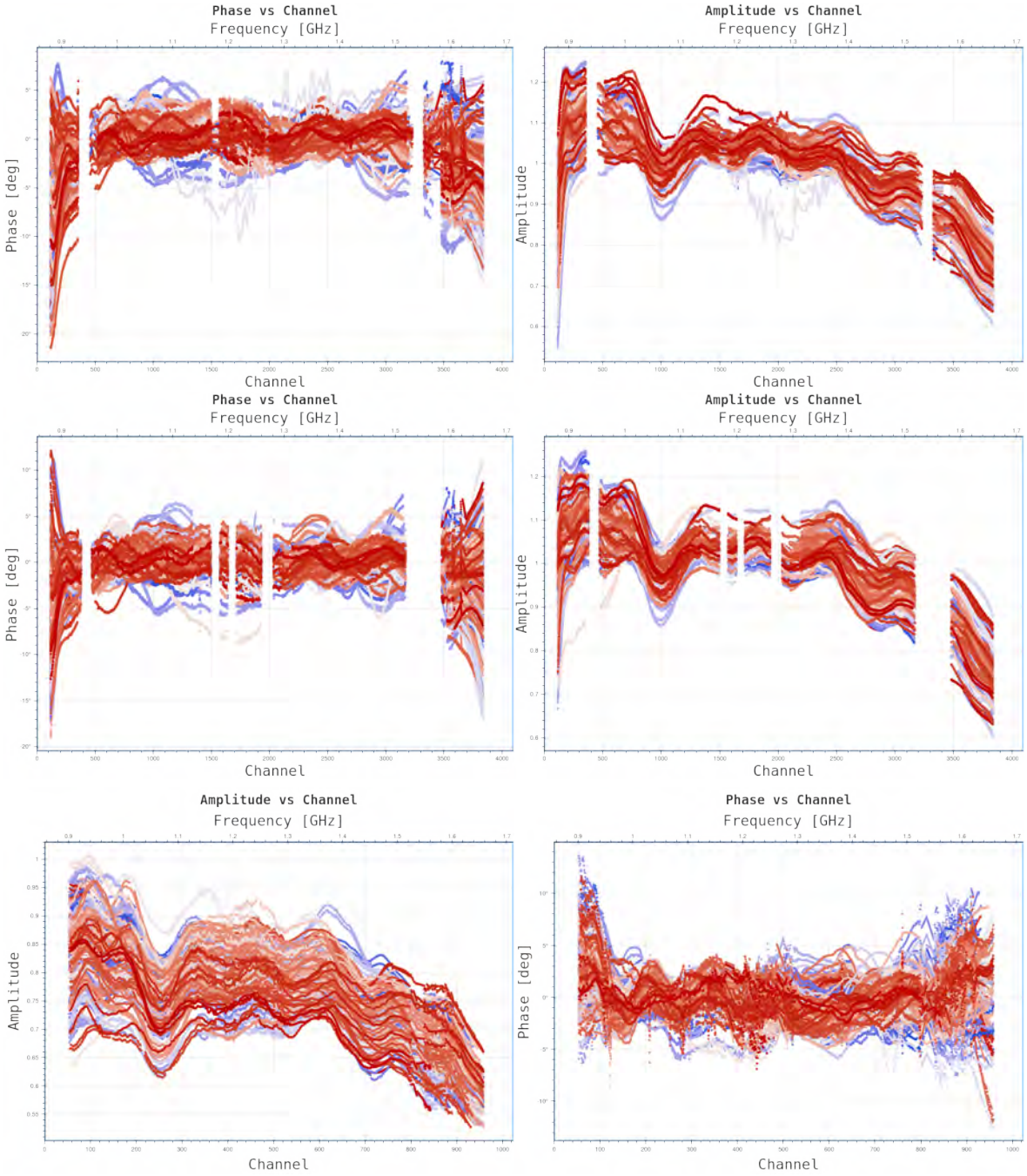

Figure A.4: The CGCG 047-067 (top panel), 3C 445 (middle) and SDSS J 09157+1331 (bottom panel) bandpass solutions extracted from the primary calibrator. The right panels are the amplitude solutions and the left panel represents the phase solutions as a function of frequency. Each colour represents an antenna in the array. The gaps are where strong RFI has been flagged.

A.3 MeerKAT Complex gain solution

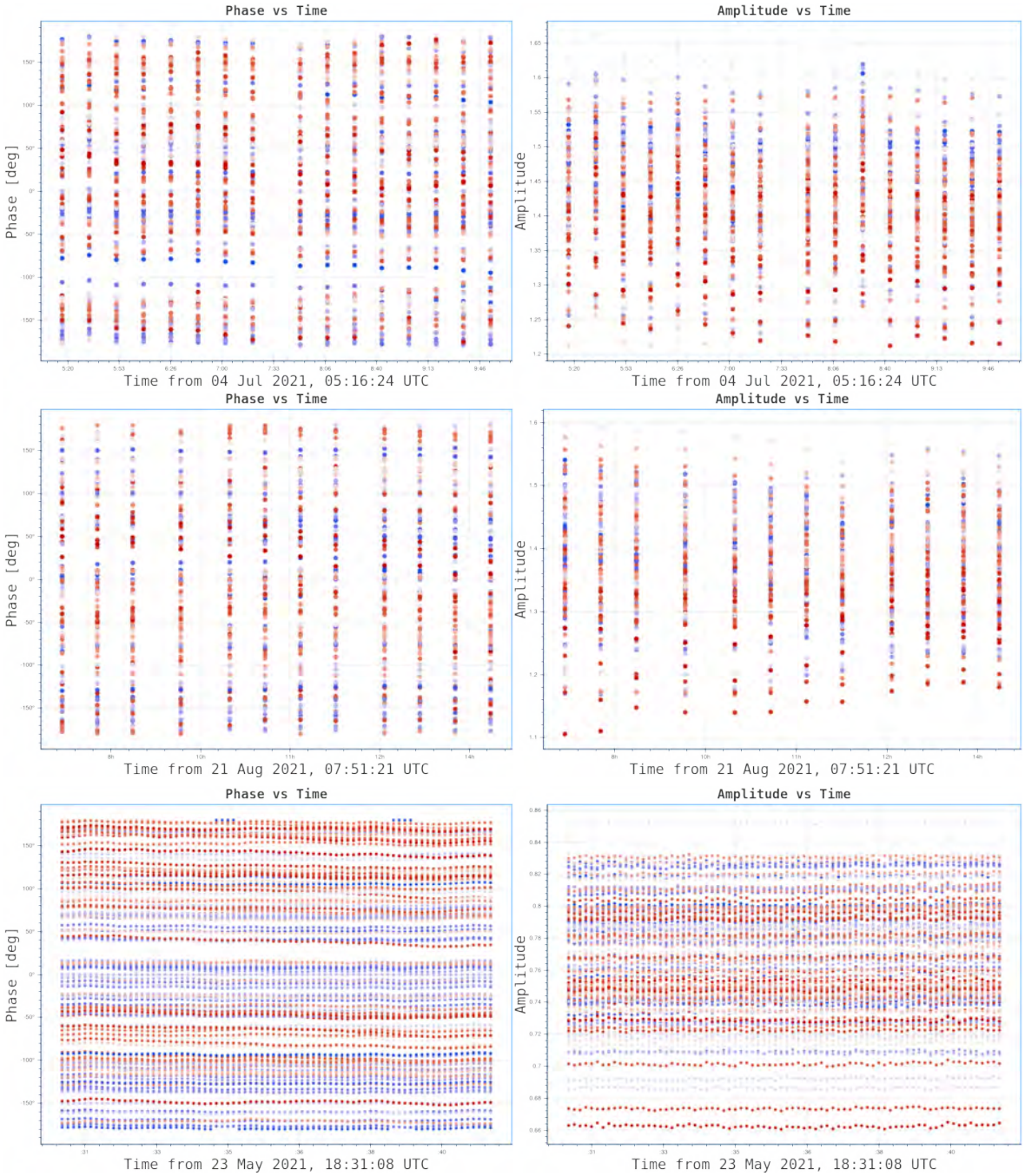

Figure A.5: The complex gain solutions for 3C 105 (top panel), 4C -03.43 and SDSS J 1120+0407 (middle and bottom panels), the right panels are the amplitude solutions, and the left panel represents the phase solution as a function of time.

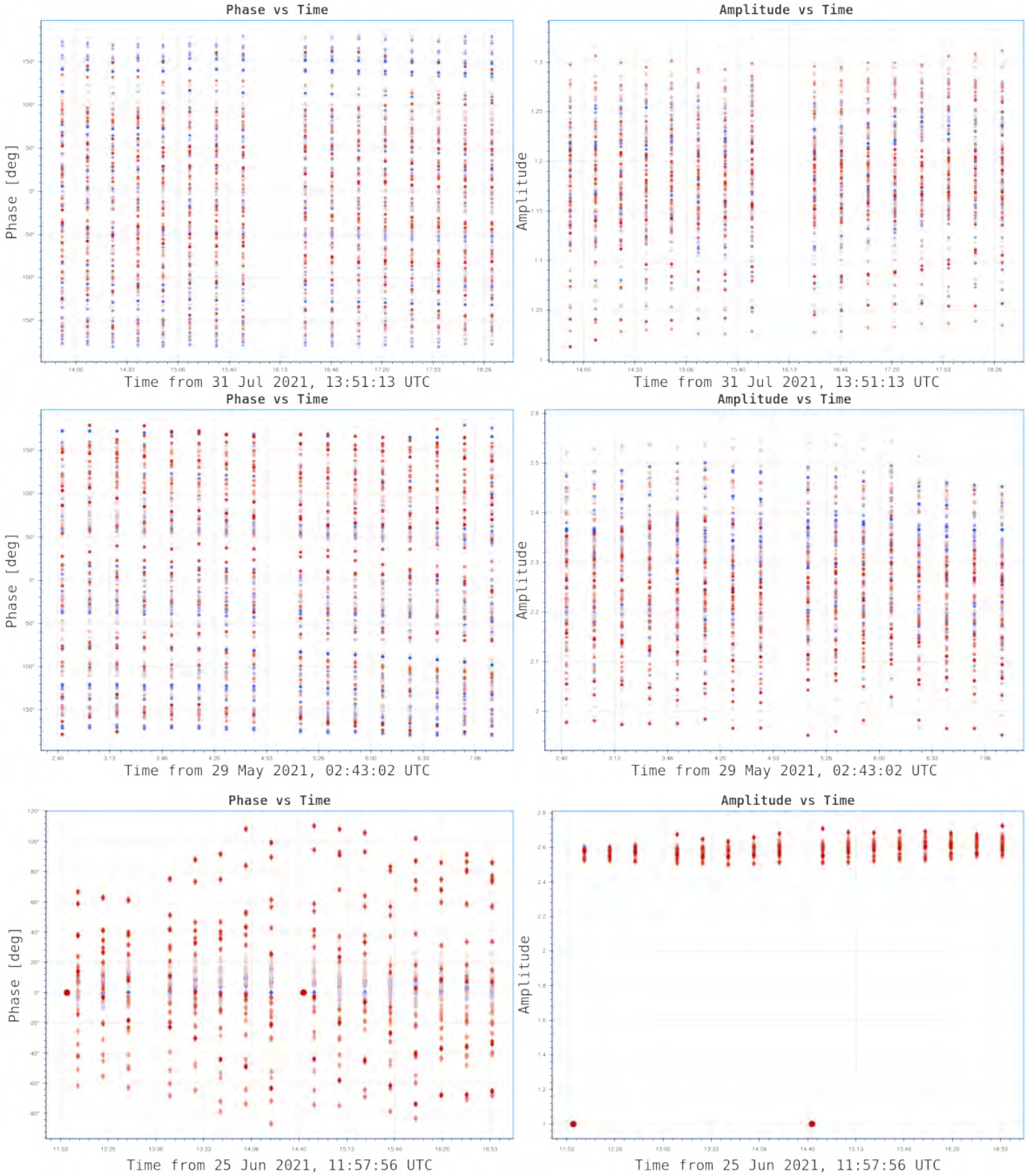

Figure A.6: The CGCG 047-067 (top panel), 3C 445 (middle) and SDSS J 09157+1331 (bottom panel) complex gain solution. Please refer to the caption of figure A.5 for details.

Appendix B

Primary beam corrected full images

B.1 MeerKAT maps

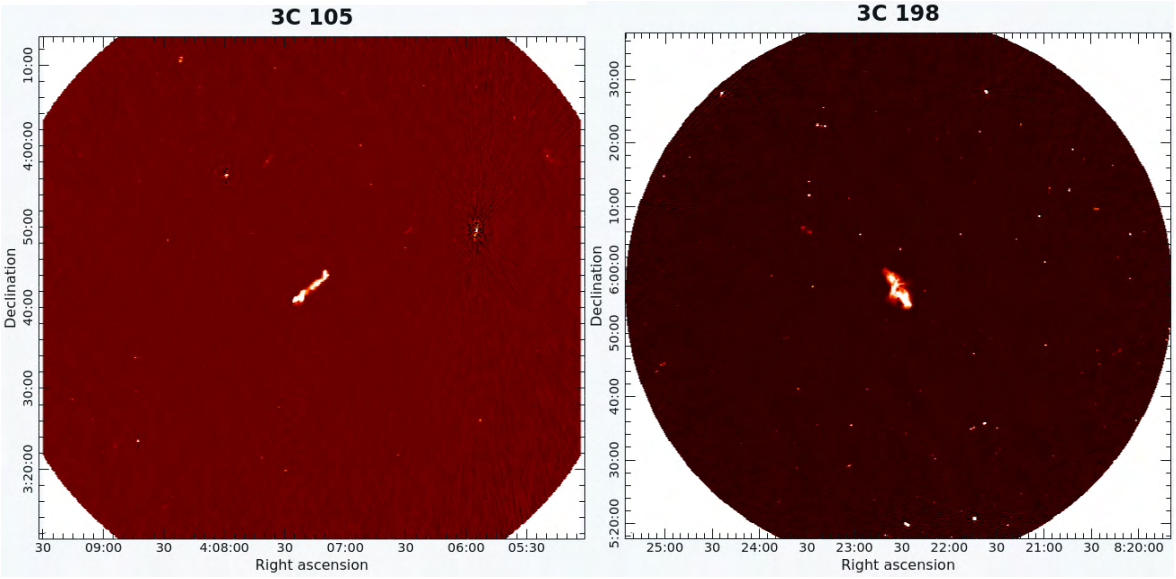

Figure B.1: Primary beam corrected images of the targets 3C 105 and 3C 198 spanning 1.11° and 1.43° with an angular resolution of 7.47″× 5.89″ and 7.84″× 6.87″ respectively.

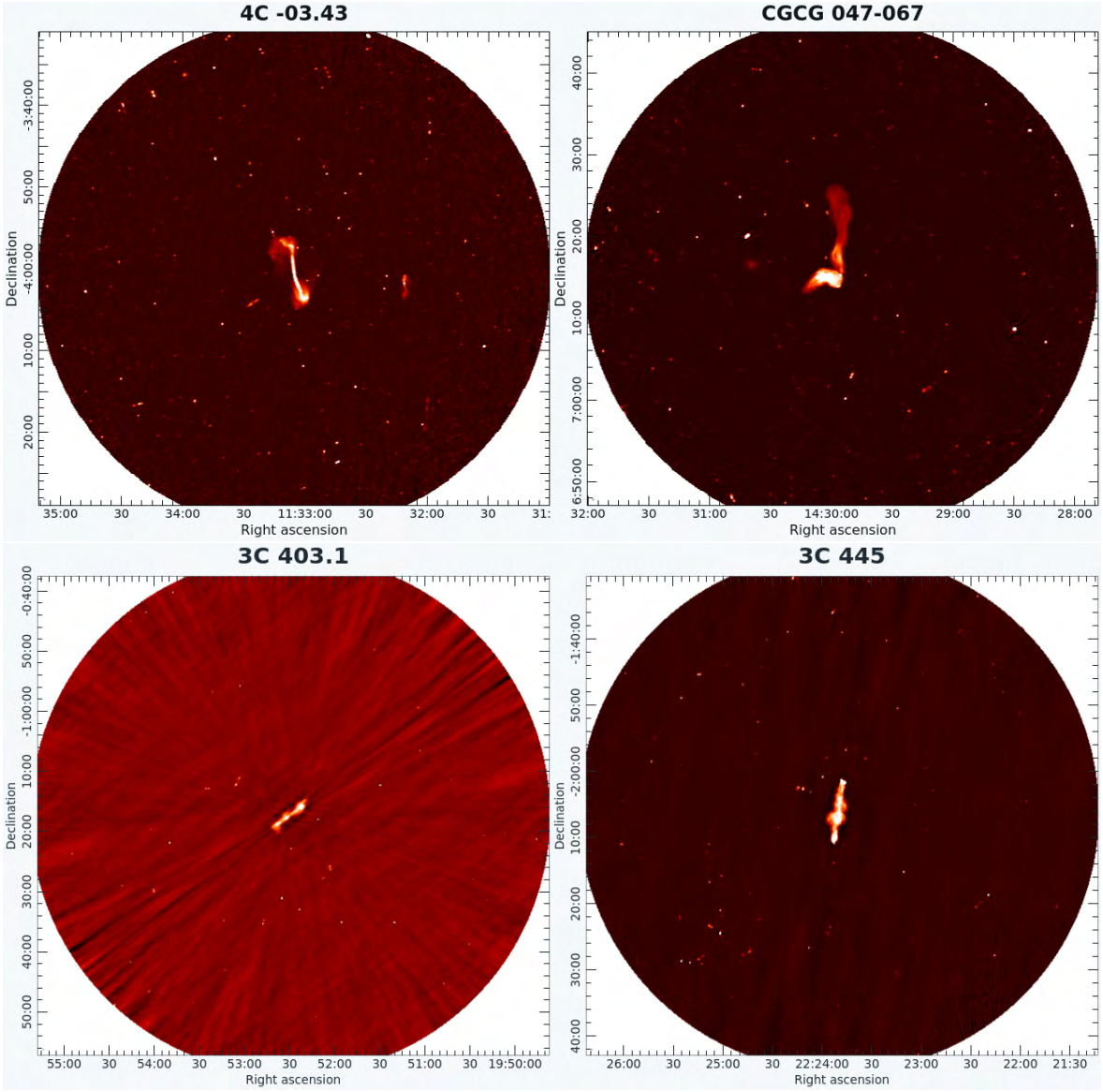

Figure B.2: Primary beam corrected images of the targets 4C-03.43, CGCG-46-067 (top panel) and 3c 403.1, 3C 555 (bottom panel) spanning 1.43° with an angular resolution of 8.64″× 7.11″, 10.02″× 6.93″,7.06″× 6.03″ and 7.38″× 5.68″ respectively.

B.2 uGMRT maps

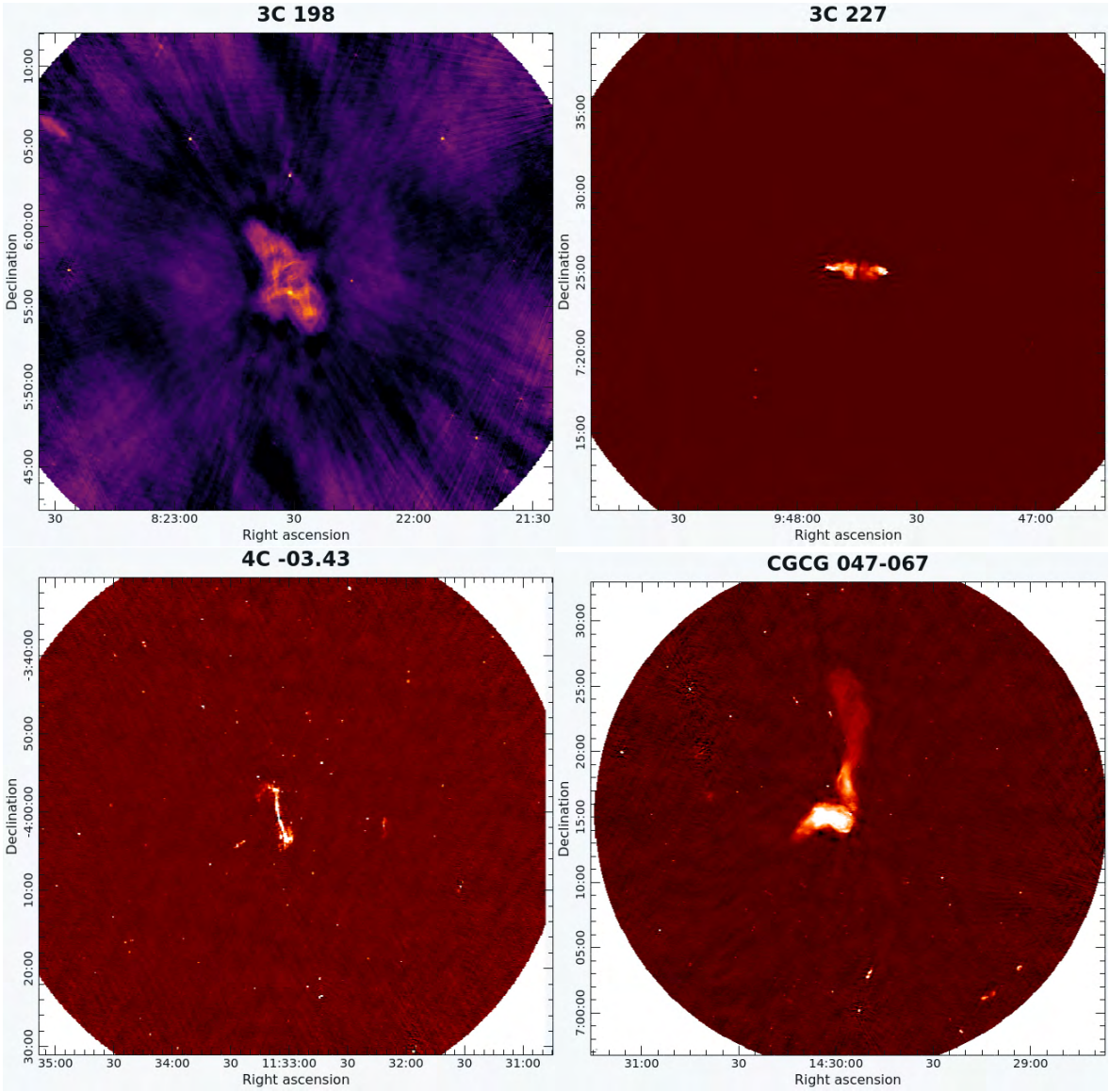

Figure B.3: Primary beam corrected images of the targets 3C 198, 3C 227 (top panel) and 4C -03.43, CGCG -46-067 (bottom panel) spanning 1.11° and 0.65° with an angular resolution of 4.77″× 3.92″, 4.52″× 3.02″, 4.95″× 4.12″ and 3.76″× 3.34″ respectively.

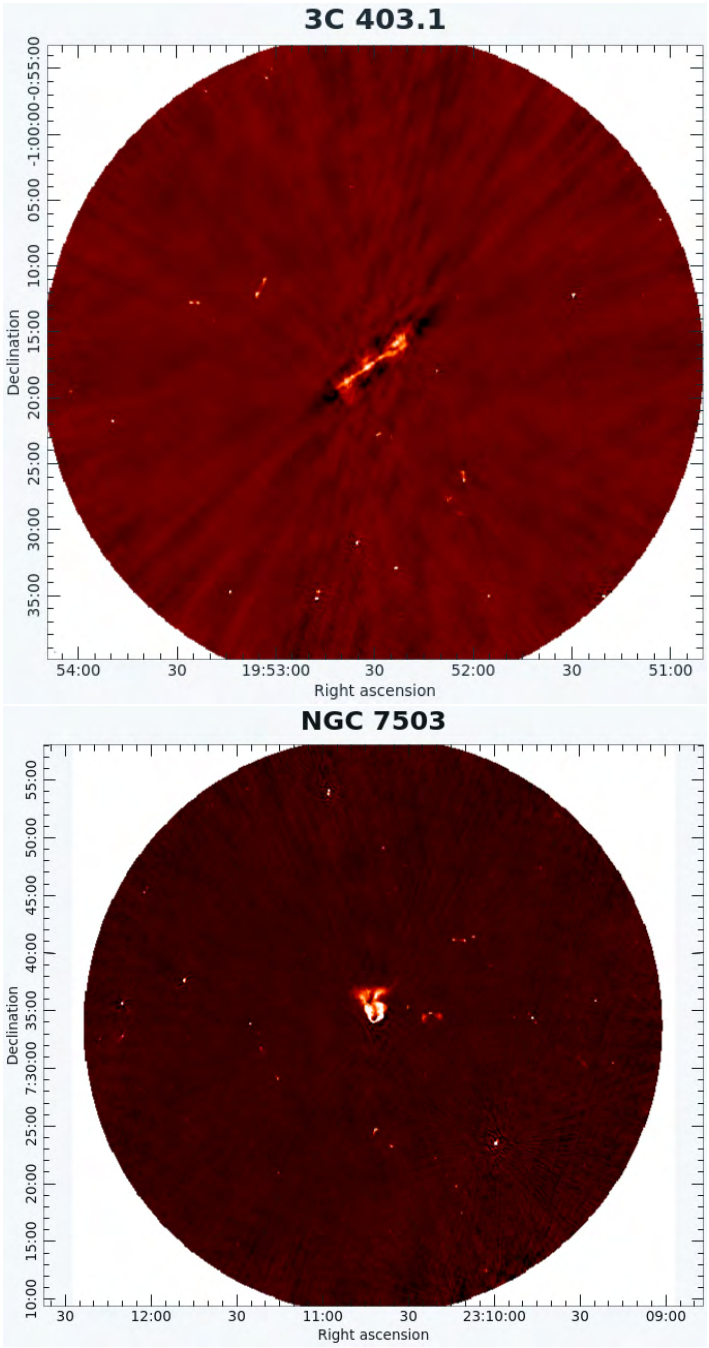

Figure B.4: Primary beam corrected images of the targets 3C 403.1 and NGC 7503 spanning 0.83° and 1.43° with an angular resolution of 3.99″× 3.15″ and 4.43″× 3.53″ respectively.

Appendix C

Flux densities of the radio sources at different frequencies.

Table C.1: The integrated flux densities for 3C 105 at various frequencies presented in the literature.

Frequency GHz	Flux density Jy	Reference
4.000	0.390±0.070	Geldzahler and Witzel [1981]
14.900	0.710±0.010	Genzel et al. [1976]
14.900	0.020±0.001	Dicken et al. [2008]
10.700	1.490±0.100	Kellermann and Pauliny-Toth [1973]
10.700	1.500±0.050	Pauliny-Toth et al. [1978]
8.400	1.220	Wright and Otrupcek [1990]
5.010	2.450±0.100	Kuehr et al. [1981]
5.010	2.500±0.060	Kuehr et al. [1981]
5.000	2.160±0.110	Kellermann et al. [1969]
5.000	2.020	Wright and Otrupcek [1990]
5.000	2.160±0.050	Pauliny-Toth et al. [1972]
5.000	2.140±0.110	Kuehr et al. [1981]
4.850	2.060±0.288	Gregory and Condon [1991]
4.850	2.030±0.305	Becker et al. [1991]
4.850	2.230±0.099	Griffith et al. [1995]
2.700	3.280	Wright and Otrupcek [1990]
2.700	3.440±0.170	Kuehr et al. [1981]
2.700	3.550±0.120	Wall et al. [1971]
2.700	3.740±0.060	Wills [1975]
2.700	3.360±0.170	Kellermann et al. [1969]
2.700	3.400±0.050	Kuehr et al. [1981]

2.650	3.790±0.070	Wills [1975]
1.410	5.100	Wright and Otrupcek [1990]
1.410	5.840±0.190	Kuehr et al. [1981]
1.400	5.340	White and Becker [1992]
1.400	5.210±0.290	Pauliny-Toth et al. [1966]
1.400	5.200±0.500	Kuehr et al. [1981]
1.400	5.310±0.150	Kuehr et al. [1981]
1.400	5.100±0.770	Kellermann et al. [1969]
1.400	0.114±0.004	Condon [1992]
0.750	7.700±0.390	Kellermann et al. [1969]
0.750	8.110±0.190	Pauliny-Toth et al. [1966]
0.750	8.100±0.400	Kuehr et al. [1981]
0.750	8.590±0.200	Kuehr et al. [1981]
0.635	8.900	Wright and Otrupcek [1990]
0.635	10.000±0.360	Kuehr et al. [1981]
0.408	10.300±2.550	Ekers [1969]
0.408	9.350	Wright and Otrupcek [1990]
0.408	9.350±0.290	Large et al. [1981]
0.318	14.200±0.560	Kuehr et al. [1981]
0.178	17.800±1.780	Kellermann et al. [1969]
0.178	18.000±1.800	Kuehr et al. [1981]
0.178	19.000±0.900	Kuehr et al. [1981]
0.178	16.200	Wright and Otrupcek [1990]
0.178	9.900±1.240	Gower et al. [1967]
0.160	23.500	Slee [1995]
0.160	18.000±2.700	Kuehr et al. [1981]
0.145	46.200	Jacobs et al. [2011]

Table C.2: The integrated flux densities for 3C 198 at various frequencies presented in the literature.

Frequency GHz	Flux density Jy	Reference
10.700	0.190±0.050	Kellermann and Pauliny-Toth [1973]
5.000	0.320	Wright and Otrupcek [1990]
5.000	0.460±0.070	Kellermann et al. [1969]
4.850	0.305±0.042	Gregory and Condon [1991]
4.850	0.539±0.081	Becker et al. [1991]
4.850	0.436±0.025	Griffith et al. [1995]
4.780	0.451	Bennett et al. [1986]
2.700	0.900	Wright and Otrupcek [1990]
2.700	0.980±0.150	Kellermann et al. [1969]
1.410	2.300	Wright and Otrupcek [1990]
1.400	2.100±0.100	Kellermann et al. [1969]
1.400	1.800	White and Becker [1992]
1.400	2.120±0.080	Pauliny-Toth et al. [1966]
0.750	3.780±0.060	Pauliny-Toth et al. [1966]
0.750	3.600±0.540	Kellermann et al. [1969]
0.408	4.650±0.310	Large et al. [1981]
0.408	6.600	Wright and Otrupcek [1990]
0.178	18.000	Wright and Otrupcek [1990]
0.178	9.000±1.120	Gower et al. [1967]
0.178	9.700±1.460	Kellermann et al. [1969]
0.16	12.000	Slee [1995]
0.145	16.000	Jacobs et al. [2011]

Table C.3: The integrated flux densities for 3C 227 at various frequencies presented in the literature.

Frequency GHz	Flux density Jy	Reference
31.400	0.530±0.13	Geldzahler and Witzel [1981]
22.400	0.012±3.0E-4	Dicken et al. [2008]
14.900	0.014±3.0E-4	Dicken et al. [2008]
14.900	0.960±0.19	Genzel et al. [1976]
10.700	1.510±0.05	Kellermann and Pauliny-Toth [1973]
8.000	2.050±0.0492	Stull [1971]
6.700	1.930±0.048	Carter et al. [2009]
5.010	2.750±0.110	Kuehr et al. [1981]
5.010	2.680±0.100	Kuehr et al. [1981]
5.000	2.580±0.130	Kuehr et al. [1981]
5.000	2.600	Wright and Otrupcek [1990]
5.000	2.600±0.130	Kellermann et al. [1969]
4.850	2.140±0.322	Becker et al. [1991]
4.850	2.580±0.099	Griffith et al. [1995]
4.850	2.190±0.304	Gregory and Condon [1991]
4.780	1.710	Bennett et al. [1986]
2.700	4.630±0.060	Wills [1975]
2.700	4.260±0.210	Kuehr et al. [1981]
2.700	4.100	Wright and Otrupcek [1990]
2.700	4.160±0.210	Kellermann et al. [1969]
2.700	4.210±0.100	Kuehr et al. [1981]
2.650	4.720±0.070	Wills [1975]
1.410	7.100	Wright and Otrupcek [1990]
1.410	7.920±0.220	Kuehr et al. [1981]
1.400	3.120	Ching et al. [2017]
1.400	7.620	Ching et al. [2017]
1.400	7.100±0.130	Pauliny-Toth et al. [1966]
1.400	6.800±0.340	Kellermann et al. [1969]
1.400	7.000±0.300	Kuehr et al. [1981]
1.400	6.940	White and Becker [1992]
1.400	7.500±0.220	Kuehr et al. [1981]
0.960	10.700±0.180	Kuehr et al. [1981]
0.750	11.600±0.580	Kellermann et al. [1969]
0.750	12.100±0.600	Kuehr et al. [1981]
0.750	12.800±0.140	Kuehr et al. [1981]
0.750	12.100±0.130	Pauliny-Toth et al. [1966]
0.468	18.000±1.460	Kuehr et al. [1981]
0.408	19.400±3.910	Ekers [1969]
0.408	15.500±0.480	Large et al. [1981]
0.408	22.100	Wright and Otrupcek [1990]
0.178	32.600±1.600	Kuehr et al. [1981]
0.178	33.300±3.300	Kuehr et al. [1981]
0.178	30.000	Wright and Otrupcek [1990]
0.178	16.500±1.320	Gower et al. [1967]

1.780	30.400±3.040	Kellermann et al. [1969]
1.600	39.600±5.200	Kuehr et al. [1981]
1.600	45.200	Slee [1995]
1.450	44.200	Jacobs et al. [2011]

Table C.4: The integrated flux densities for 4C -03.43 at various frequencies presented in the literature.

Frequency GHz	Flux density Jy	Reference
22.500	0.0621±0.001	Lin et al. [2009]
19.900	0.108±0.006	Murphy et al. [2010]
8.460	0.107±0.001	Lin et al. [2009]
8.400	0.048	Healey et al. [2007]
5.000	0.300	Wright and Otrupcek [1990]
4.860	0.159±0.002	Lin et al. [2009]
4.850	0.370±0.022	Griffith et al. [1995]
2.700	0.560	Wright and Otrupcek [1990]
1.400	1.110	White and Becker [1992]
1.400	0.320±0.010	Condon et al. [1998]
4.080	1.180	Wright and Otrupcek [1990]
4.080	1.180±0.070	Large et al. [1981]
3.650	0.434±0.054	Douglas et al. [1996]
1.860	1.760±0.036	Tingay et al. [2016]
1.780	2.000	Wright and Otrupcek [1990]
1.780	2.000±0.300	Gower et al. [1967]
1.600	2.500	Slee [1995]
1.550	2.280±0.051	Tingay et al. [2016]

Table C.5: The integrated flux densities for CGCG 047-067 at various frequencies presented in the literature.

Frequency GHz	Flux density Jy	Reference
8.000	0.520±0.0452	Stull [1971]
5.000	0.660	Wright and Otrupcek [1990]
4.850	0.557±0.031	Griffith et al. [1995]
4.850	0.481±0.072	Becker et al. [1991]
4.850	0.511±0.071	Gregory and Condon [1991]
4.780	0.575	Bennett et al. [1986]
2.700	1.060	Wright and Otrupcek [1990]
1.410	2.100	Wright and Otrupcek [1990]
1.400	2.010	Yuan et al. [2017]
1.400	1.790	Lin et al. [2018]
0.408	5.800	Wright and Otrupcek [1990]
0.408	2.820±0.130	Large et al. [1981]
0.178	3.500	Wright and Otrupcek [1990]
0.178	3.500±0.525	Gower et al. [1967]
0.160	7.900	Slee [1995]

Table C.6: The integrated flux densities for 3C 403.1 at various frequencies presented in the literature.

Frequency GHz	Flux density Jy	Reference
8.400	0.100	Wright and Otrupcek [1990]
5.000	0.450±0.110	Kellermann et al. [1969]
5.000	0.580	Wright and Otrupcek [1990]
4.850	0.344±0.021	Griffith et al. [1995]
4.850	0.580±0.087	Becker et al. [1991]
2.700	0.700	Wright and Otrupcek [1990]
2.700	0.960±0.140	Kellermann et al. [1969]
1.410	1.500	Wright and Otrupcek [1990]
1.400	1.800±0.270	Kellermann et al. [1969]
1.400	1.850	White and Becker [1992]
1.400	1.790±0.120	Pauliny-Toth et al. [1966]
0.750	2.830±0.110	Pauliny-Toth et al. [1966]
0.750	2.700±0.410	Kellermann et al. [1969]
0.408	4.400	Wright and Otrupcek [1990]
0.178	13.500	Wright and Otrupcek [1990]
0.178	13.500±2.020	Kellermann et al. [1969]
0.178	3.300±0.825	Gower et al. [1967]
0.160	9.500	Slee [1995]

Table C.7: The integrated flux densities for 3C 445 at various frequencies presented in the literature.

Frequency GHz	Flux density Jy	Reference
22.400	0.0161±0.001	Dicken et al. [2008]
22.000	0.045±0.005	Ricci et al. [2006]
18.500	0.039±0.002	Ricci et al. [2006]
14.900	0.027	Dicken et al. [2008]
10.700	0.820± 0.030	Kellermann and Pauliny-Toth [1973]
8.400	0.320	Wright and Otrupcek [1990]
8.000	1.340± 0.079	Stull [1971]
5.010	2.180±0.090	Kuehr et al. [1981]
5.000	2.040± 0.100	Kellermann et al. [1969]
5.000	2.030± 0.100	Kuehr et al. [1981]
5.000	2.120	Wright and Otrupcek [1990]
4.850	1.260± 0.066	Griffith et al. [1995]
2.700	3.300±0.160	Kuehr et al. [1981]
2.700	3.460 ± 0.120	Wall et al. [1971]
2.700	3.460	Wright and Otrupcek [1990]
2.700	3.340 ± 0.330	Witzel et al. [1971]
2.700	3.220 ± 0.160	Kellermann et al. [1969]
1.410	5.100	Wright and Otrupcek [1990]
1.400	5.750 ± 0.120	Kuehr et al. [1981]
1.400	5.300 ± 0.270	Kellermann et al. [1969]
1.400	5.500 ± 0.300	Kuehr et al. [1981]
1.400	6.160	White and Becker [1992]
1.400	5.330 ± 0.100	Pauliny-Toth et al. [1966]
0.750	8.700 ± 0.430	Kellermann et al. [1969]
0.750	9.670 ± 0.180	Kuehr et al. [1981]
0.750	9.100 ± 0.500	Kuehr et al. [1981]
0.750	9.130 ± 0.170	Pauliny-Toth et al. [1966]
0.635	12.200	Wright and Otrupcek [1990]
0.408	17.500	Wright and Otrupcek [1990]
0.408	14.500 ± 3.180	Ekers [1969]
0.408	7.150 ± 0.180	Large et al. [1981]
0.178	26.100 ± 5.200	Kuehr et al. [1981]
0.178	25.200 ± 3.240	Kuehr et al. [1981]
0.178	23.500	Wright and Otrupcek [1990]
0.178	23.500 ± 1.880	Gower et al. [1967]
0.178	24.800 ± 3.720	Kellermann et al. [1969]
0.160	33.500 ± 4.400	Kuehr et al. [1981]
0.145	36.500	Jacobs et al. [2011]

Table C.8: The integrated flux densities for NGC 7503 at various frequencies presented in the literature.

Frequency GHz	Flux density Jy	Reference
8.000	0.410± 0.039	Stull [1971]
5.000	0.520	Wright and Otrupcek [1990]
4.850	0.544 ± 0.082	Becker et al. [1991]
4.850	0.557± 0.031	Griffith et al. [1995]
4.850	0.547± 0.076	Gregory and Condon [1991]
2.700	0.960	Wright and Otrupcek [1990]
1.410	1.700	Wright and Otrupcek [1990]
1.400	1.630	White and Becker [1992]
0.408	3.880± 0.180	Large et al. [1981]
0.408	3.880	Wright and Otrupcek [1990]
0.178	4.500 ± 0.562	Gower et al. [1967]
0.178	4.500	Wright and Otrupcek [1990]

Appendix D

Morphology of 3C 403.1

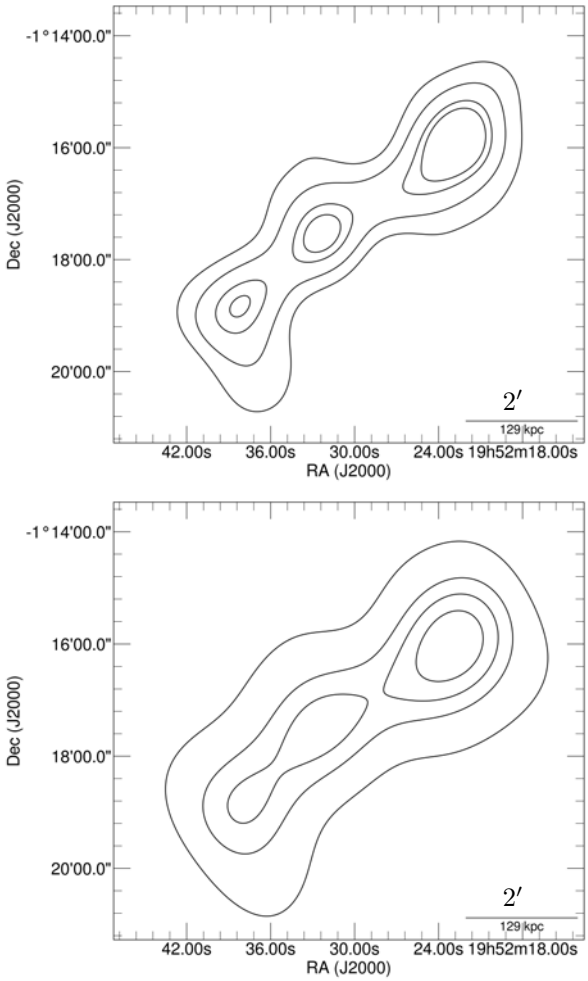

Figure D.1: The radio maps of 3C 403.1 convolved with the GLEAM beam (right panel) with contours drawn at (0.5,0.10,0.20,0.30) $\times\sigma$ and the SRT beam with contours drawn at (0.02,0.04,0.08,1.0,2.0) $\times\sigma$. Note that σ is the background noise level estimation.

Bibliography

M. Ajello, A. Rau, J. Greiner, G. Kanbach, M. Salvato, A. W. Strong, S. D. Barthelmy, N. Gehrels, C. B. Markwardt, and J. Tueller. The Swift BAT X-Ray Survey. III. X-Ray Spectra and Statistical Properties. , 673(1):96–113, January 2008. doi: 10.1086/524104.

R. D. Baldi and A. Capetti. Recent star formation in nearby 3CR radio-galaxies from UV HST observations. , 489(3):989–1002, October 2008. doi: 10.1051/0004-6361:20078745.

Ranieri D Baldi. The nature of compact radio sources: the case of fr 0 radio galaxies. *The Astronomy and Astrophysics Review*, 31(1):3, 2023.

Ranieri D. Baldi, Alessandro Capetti, and Gabriele Giovannini. Pilot study of the radio-emitting agn population: the emerging new class of fr 0 radio-galaxies. *Astronomy amp; Astrophysics*, 576:A38, March 2015. ISSN 1432-0746. doi: 10.1051/0004-6361/201425426. URL `http://dx.doi.org/10.1051/0004-6361/201425426`.

Ranieri D. Baldi, Alessandro Capetti, and Gabriele Giovannini. High-resolution VLA observations of FR0 radio galaxies: the properties and nature of compact radio sources. , 482(2):2294–2304, January 2019. doi: 10.1093/mnras/sty2703.

Ranieri Diego Baldi, Eleonora Torresi, Giulia Migliori, and Barbara Balmaverde. The high energy view of fr0 radio galaxies. *Galaxies*, 7(3):76, 2019.

B. Balmaverde, A. Capetti, A. Marconi, G. Venturi, M. Chiaberge, R. D. Baldi, S. Baum, R. Gilli, P. Grandi, E. Meyer, G. Miley, C. O'Dea, W. Sparks, E. Torresi, and G. Tremblay. The MURALES survey. II. Presentation of MUSE observations of 20 3C low-z radio galaxies and first results. , 632:A124, December 2019. doi: 10.1051/0004-6361/201935544.

B. Balmaverde, A. Capetti, A. Marconi, G. Venturi, M. Chiaberge, R. D. Baldi, S. Baum, R. Gilli, P. Grandi, E. T. Meyer, G. Miley, C. O'Dea, W. Sparks, E. Torresi, and G. Tremblay. The MURALES survey. III. Completing the MUSE observations of 37 3C low-z radio galaxies. , 645:A12, January 2021. doi: 10.1051/0004-6361/202039062.

CJ Bambic, HR Russell, CS Reynolds, AC Fabian, BR McNamara, and PEJ Nulsen. Agn feeding and feedback in m84: from kiloparsec scales to the bondi radius. *Monthly Notices of the Royal Astronomical Society*, 522(3):4374–4391, 2023.

Stefi A. Baum, Esther L. Zirbel, and Christopher P. O'Dea. Toward Understanding the Fanaroff-Riley Dichotomy in Radio Source Morphology and Power. , 451:88, September 1995. doi: 10.1086/176202.

Robert H. Becker, Richard L. White, and Alan L. Edwards. A New Catalog of 53,522 4.85 GHz Sources. , 75:1, January 1991. doi: 10.1086/191529.

C. L. Bennett, C. R. Lawrence, B. F. Burke, J. N. Hewitt, and J. Mahoney. The MIT–Green Bank (MG) 5 GHz Survey. , 61:1, May 1986. doi: 10.1086/191108.

Philip N Best. The environmental dependence of radio-loud agn activity and star formation in the 2dfgrs. *Monthly Notices of the Royal Astronomical Society*, 351(1): 70–82, 2004.

PN Best. Radio source populations: Results from sdss. *Astronomische Nachrichten: Astronomical Notes*, 330(2-3):184–189, 2009.

PN Best and TM Heckman. On the fundamental dichotomy in the local radio-agn population: accretion, evolution and host galaxy properties. *Monthly Notices of the Royal Astronomical Society*, 421(2):1569–1582, 2012.

S. Bhatnagar and T. J. Cornwell. The Pointing Self-calibration Algorithm for Aperture Synthesis Radio Telescopes. *The Astronomical Journal*, 154(5):197, 2017. ISSN 0004-6256. doi: 10.3847/1538-3881/aa8f43.

G. V. Bicknell. A model for the surface brightness of a turbulent low mach number jet. I. Theoretical development and application to 3C 31. , 286:68–87, November 1984. doi: 10.1086/162577.

Geoffrey V. Bicknell. Relativistic Jets and the Fanaroff-Riley Classification of Radio Galaxies. , 101:29, November 1995. doi: 10.1086/192232.

Geoffrey V Bicknell, Michael A Dopita, and Peter J Quinn. The first stromlo symposium: The physics of active galaxies. *The Physics of Active Galaxies*, 54, 1994.

Peter L Biermann, Paul J Wiita, et al. The origin of x-shaped radio galaxies: clues from the z-symmetric secondary lobes. *The Astrophysical Journal*, 594(2):L103, 2003.

R. D. Blandford and M. J. Rees. A "twin-exhaust" model for double radio sources. , 169:395–415, December 1974. doi: 10.1093/mnras/169.3.395.

R. D. Blandford and R. L. Znajek. Electromagnetic extraction of energy from Kerr black holes. , 179:433–456, May 1977. doi: 10.1093/mnras/179.3.433.

EL Blanton, MD Gregg, DJ Helfand, RH Becker, and KM Leighly. The environments of a complete moderate-redshift sample of first bent-double radio sources. *The Astronomical Journal*, 121(6):2915, 2001.

Roy Booth, W. Blok, Justin Jonas, and Bernie Fanaroff. Meerkat key project science, specifications, and proposals. 10 2009.

Alan H Bridle and Richard A Perley. Extragalactic radio jets. *IN: Annual review of astronomy and astrophysics. Volume 22. Palo Alto, CA, Annual Reviews, Inc., 1984, p. 319-358.*, 22:319–358, 1984.

D. S. Briggs. *High Fidelity Deconvolution of Moderately Resolved Sources*. PhD thesis, 1995.

Catherine Brocksopp, CR Kaiser, AP Schoenmakers, and AG De Bruyn. Double–double radio galaxies: further insights into the formation of the radio structures. *Monthly Notices of the Royal Astronomical Society*, 410(1):484–498, 2011.

Geoffrey R Burbidge. On synchrotron radiation from messier 87. *Astrophysical Journal, vol. 124, p. 416*, 124:416, 1956.

J. O. Burns. Stormy Weather in Galaxy Clusters. *Science*, 280:400, April 1998. doi: 10.1126/science.280.5362.400.

Jack O Burns. The radio properties of cd galaxies in abell clusters. i-an x-ray selected sample. *Astronomical Journal (ISSN 0004-6256), vol. 99, Jan. 1990, p. 14-30. Research supported by NASA.*, 99:14–30, 1990.

Jack O Burns, Michael L Norman, and David A Clarke. Numerical models of extragalactic radio sources. *Science*, 253(5019):522–530, 1991.

S. Buttiglione, A. Capetti, A. Celotti, D. J. Axon, M. Chiaberge, F. D. Macchetto, and W. B. Sparks. An optical spectroscopic survey of the 3CR sample of radio galaxies with z $<$ 0.3 . II. Spectroscopic classes and accretion modes in radio-loud AGN. , 509:A6, January 2010. doi: 10.1051/0004-6361/200913290.

F. Camilo, P. Scholz, M. Serylak, S. Buchner, M. Merryfield, V. M. Kaspi, R. F. Archibald, M. Bailes, A. Jameson, W. van Straten, J. Sarkissian, J. E. Reynolds, S. Johnston, G. Hobbs, T. D. Abbott, R. M. Adam, G. B. Adams, T. Alberts, R. Andreas, K. M. B. Asad, D. E. Baker, T. Baloyi, and Bauermeister. Revival of the Magnetar PSR J1622–4950: Observations with MeerKAT, Parkes, XMM-Newton , Swift , Chandra , and NuSTAR . *The Astrophysical Journal*, 856(2):180, 2018. ISSN 1538-4357. doi: 10.3847/1538-4357/aab35a.

A Capetti, F Massaro, and RD Baldi. Large-scale environment of fr 0 radio galaxies. a&a 633: A161, 2020.

Alessandro Capetti, S Zamfir, P Rossi, G Bodo, C Zanni, and Silvano Massaglia. On the origin of x-shaped radio-sources: New insights from the properties of their host galaxies. *Astronomy & Astrophysics*, 394(1):39–45, 2002.

Alessandro Capetti, Francesco Massaro, and Ranieri Diego Baldi. Fricat: a first catalog of fr i radio galaxies. *Astronomy & Astrophysics*, 598:A49, 2017.

Christopher L Carilli, R Perley, DE Harris, and PD Barthel. Physical processes in extragalactic radio sources. *Physics of Plasmas*, 5(5):1981–1990, 1998.

Steven J. B. Carter, Simon P. Ellingsen, Jean-Pierre Macquart, and James E. J. Lovell. Annual cycles in the interstellar scintillation time-scales of PKSB1519-273 and PKSB1622-253. , 396(3):1222–1230, July 2009. doi: 10.1111/j.1365-2966.2009.14824.x.

M Cegłowski, MP Gawroński, and Magdalena Kunert-Bajraszewska. Orientation of the cores of hybrid morphology radio sources. *Astronomy & Astrophysics*, 557:A75, 2013.

Kshitij Chavan, Pratik Dabhade, and D J Saikia. A giant radio galaxy with three cycles of episodic jet activity from lotss dr2. *Monthly Notices of the Royal Astronomical Society: Letters*, 525(1):L87–L92, July 2023. ISSN 1745-3933. doi: 10.1093/mnrasl/slad100. URL `http://dx.doi.org/10.1093/mnrasl/slad100`.

James O Chibueze, Haruka Sakemi, Takumi Ohmura, Mami Machida, Hiroki Akamatsu, Takuya Akahori, Hiroyuki Nakanishi, Viral Parekh, Ruby Rooyen, and Tsutomu T Takeuchi. Jets from MRC 0600-399 bent by magnetic fields in the cluster Abell 3376. *Nature*, 593(May), 2021. ISSN 1476-4687. doi: 10.1038/s41586-021-03434-1. URL `http://dx.doi.org/10.1038/s41586-021-03434-1`.

John H. Y. Ching, Elaine M. Sadler, Scott M. Croom, Helen M. Johnston, Michael B. Pracy, Warrick J. Couch, A. M. Hopkins, Russell J. Jurek, and K. A. Pimbblet. The Large Area Radio Galaxy Evolution Spectroscopic Survey (LARGESS): survey design, data catalogue and GAMA/WiggleZ spectroscopy. , 464(2):1306–1332, January 2017. doi: 10.1093/mnras/stw2396.

J. J. Condon. Radio emission from normal galaxies. , 30:575–611, January 1992. doi: 10.1146/annurev.aa.30.090192.003043.

J. J. Condon, W. D. Cotton, E. W. Greisen, Q. F. Yin, R. A. Perley, G. B. Taylor, and J. J. Broderick. The NRAO VLA Sky Survey. , 115(5):1693–1716, May 1998. doi: 10.1086/300337.

JJ Condon, WD Cotton, SV White, S Legodi, S Goedhart, K McAlpine, SM Ratcliffe, and F Camilo. Threads, ribbons, and rings in the radio galaxy ic 4296. *The Astrophysical Journal*, 917(1):18, 2021.

Tim J. Cornwell. Multiscale clean deconvolution of radio synthesis images. *IEEE Journal of Selected Topics in Signal Processing*, 2(5):793–801, 2008. doi: 10.1109/JSTSP.2008.2006388.

WD Cotton, Kshitij Thorat, JJ Condon, BS Frank, Gyula IG Jozsa, Sarah V White, Roger Deane, N Oozeer, M Atemkeng, L Bester, et al. Hydrodynamical backflow in x-shaped radio galaxy pks 2014- 55. *Monthly Notices of the Royal Astronomical Society*, 495(1):1271–1283, 2020.

CI Cox, SF Gull, and PAG Scheuer. Three-dimensional simulations of the jets of extragalactic radio sources. *Monthly Notices of the Royal Astronomical Society*, 252 (4):558–585, 1991.

Judith H Croston, MJ Hardcastle, DE Harris, E Belsole, M Birkinshaw, and DM Worrall. An x-ray study of magnetic field strengths and particle content in the lobes of fr ii radio sources. *The Astrophysical Journal*, 626(2):733, 2005.

F de Gasperin. Multifrequency study of a new hybrid morphology radio source. *Monthly Notices of the Royal Astronomical Society*, 467(2):2234–2240, 2017.

Charles Dennison Dermer and Berrie Giebels. Active galactic nuclei at gamma-ray energies. *Comptes Rendus. Physique*, 17(6):594–616, 2016.

D. Dicken, C. Tadhunter, R. Morganti, C. Buchanan, T. Oosterloo, and D. Axon. The Origin of the Infrared Emission in Radio Galaxies. I. New Mid- to Far-Infrared and Radio Observations of the 2 Jy Sample. , 678(2):712–728, May 2008. doi: 10.1086/529544.

Rohit Dokara, Govind Nandakumar, Karl Menten, Sarita Vig, Prasun Dutta, Henrik Beuther, Jagadheep Pandian, Michael Rugel, Md Rashid, and Andreas Brunthaler. Metrewave galactic plane with the ugmrt (megaplug) survey: Lessons from the pilot study. *Astronomy Astrophysics*, 678, 08 2023. doi: 10.1051/0004-6361/202347320.

James N Douglas, Frank N Bash, F Arakel Bozyan, Geoffrey W Torrence, and Chip Wolfe. The texas survey of radio sources covering-35.5 degrees< declination< 71.5 degrees at 365 mhz. *Astronomical Journal v. 111, p. 1945*, 111:1945, 1996.

J. W. Dreher and E. D. Feigelson. Rings and wiggles in Hercules A. , 308:43–45, March 1984. doi: 10.1038/308043a0.

JA Eilek, JO Burns, CP O'dea, and FN Owen. What bends 3c 465? *Astrophysical Journal, Part 1 (ISSN 0004-637X), vol. 278, March 1, 1984, p. 37-50. Research supported by Sandia National Laboratories.*, 278:37–50, 1984.

J. A. Ekers. The Parkes catalogue of radio sources, declination zone +20 to -90 . *Australian Journal of Physics Astrophysical Supplement*, 7:3–75, January 1969.

RD Ekers, R Fanti, C Lari, and P Parma. Ngc326—a radio galaxy with a precessing beam? *Nature*, 276(5688):588–590, 1978.

Michael Eracleous and Jules P. Halpern. Double-peaked Emission Lines in Active Galactic Nuclei. , 90:1, January 1994. doi: 10.1086/191856.

Andrew C Fabian. Observational evidence of active galactic nuclei feedback. *Annual Review of Astronomy and Astrophysics*, 50:455–489, 2012.

B. L. Fanaroff and J. M. Riley. The morphology of extragalactic radio sources of high and low luminosity. , 167:31P–36P, May 1974. doi: 10.1093/mnras/167.1.31P.

Bernie Fanaroff, Dharam V Lal, Tiziana Venturi, Oleg M Smirnov, Marco Bondi, Kshitij Thorat, Landman H Bester, I G J Gyula, Dane Kleiner, Francesca Loi, Sphesihle Makhathini, and Sarah V White. A new look at old friends . I . Imaging classical radio galaxies with uGMRT and MeerKAT arXiv : 2105 . 11695v2 [astro-ph . GA] 29 May 2021. 16(June):1–16, 2021.

C Fanti, R Fanti, D Dallacasa, RT Schilizzi, RE Spencer, and C Stanghellini. Are compact steep-spectrum sources young? *Astronomy and Astrophysics*, 302:317, 1995.

E Florido, E Battaner, and ML Sanchez-Saavedra. Spatial distribution of antisymmetrically-curved extragalactic radio-jets. *Astrophysics and space science*, 164:131–137, 1990.

MP Gawroński, A Marecki, M Kunert-Bajraszewska, and AJ Kus. Hybrid morphology radio sources from the first survey. *Astronomy & Astrophysics*, 447(1):63–70, 2006.

B. J. Geldzahler and A. Witzel. 31.4- and 89.6-GHz flux density measurements of extragalactic radio sources. , 86:1306–1311, September 1981. doi: 10.1086/113011.

Melanie A Gendre, PN Best, JV Wall, and LM Ker. The relation between morphology, accretion modes and environmental factors in local radio agn. *Monthly Notices of the Royal Astronomical Society*, 430(4):3086–3101, 2013.

M-L Gendron-Marsolais, Charles LH Hull, Rick Perley, Lawrence Rudnick, Ralph Kraft, Julie Hlavacek-Larrondo, Andrew C Fabian, Elke Roediger, Reinout J van Weeren, Annabelle Richard-Laferrière, et al. Vla resolves unexpected radio structures in the perseus cluster of galaxies. *The Astrophysical Journal*, 911(1):56, 2021.

R. Genzel, I. I. K. Pauliny-Toth, E. Preuss, and A. Witzel. Measurements of the flux densities and spectra of discrete radio sources at centimeter wavelengths. V. The observations at 14.9 GHz (2 cm). , 81:1084–1088, December 1976. doi: 10.1086/111989.

S Giacintucci and T Venturi. Tailed radio galaxies as tracers of galaxy clusters. serendipitous discoveries with the gmrt. *Astronomy & Astrophysics*, 505(1):55–61, 2009.

S Giacintucci, Tiziana Venturi, M Markevitch, H Bourdin, P Mazzotta, Paola Merluzzi, DANIELE Dallacasa, Sandro Bardelli, SP Sikhosana, O Smirnov, et al. A candle in the wind: a radio filament in the core of the a3562 galaxy cluster. *The Astrophysical Journal*, 934(1):49, 2022.

G Giovannini, RD Baldi, A Capetti, M Giroletti, and Rocco Lico. Jets in fr0 radio galaxies. *arXiv preprint arXiv:2302.12657*, 2023.

Gopal-Krishna. Unified Schemes for Radio Loud Active Galactic Nuclei. *Journal of Astrophysics and Astronomy Supplement*, 16:153, June 1995.

Biermann PL Gopal-Krishna, LA Gergely, and PJ Wiita. On the origin of x-shaped radio galaxies. *New Astron. Rev*, 2010.

Joshi Ravi Gopal-Krishna, Paul J. and Patra Dusmanta. A physically-motivated perspective of fanaroff–riley classification of radio galaxies. *Journal of Astrophysics and Astronomy*, 44(1):44, 2023.

Paul J. Gopal-Krishna, Wiita, Ravi Joshi, and Dusmanta Patra. A physically-motivated perspective of Fanaroff-Riley classification of radio galaxies. *Journal of Astrophysics and Astronomy*, 44(1):44, June 2023. doi: 10.1007/s12036-023-09937-9.

Wiita PJ Gopal-Krishna and PJ Wiita. Extragalactic radio sources with hybrid morphology: implications for the fanaroff-riley dichotomy. *A&A*, 363:507–516, 2000.

J. F. R. Gower, P. F. Scott, and D. Wills. A survey of radio sources in the declination ranges —07° to 20° and 40° to 80°. , 71:49, January 1967.

Jf FR Gower. The source counts from the 4c survey. *Monthly Notices of the Royal Astronomical Society*, 133(1):151–161, 1966.

P. Grandi, L. Foschini, N. Masetti, and E. Palazzi. 1WGA J2223.7-0206: A Narrow-Line Quasi-Stellar Object in the XMM-Newton field of view of 3C 445. , 418:907–911, May 2004. doi: 10.1051/0004-6361:20035724.

Paola Grandi, Matteo Guainazzi, Massimo Cappi, and Gabriele Ponti. XMM-Newton unveils the type 2 nature of the BLRG 3C 445. , 381(1):L21–L25, October 2007. doi: 10.1111/j.1745-3933.2007.00358.x.

P. C. Gregory and J. J. Condon. The 87GB Catalog of Radio Sources Covering 0 degrees $<$ delta $<$ +75 degrees at 4.85 GHz. , 75:1011, April 1991. doi: 10.1086/191559.

Mark R. Griffith, Alan E. Wright, B. F. Burke, and R. D. Ekers. The Parkes-MIT-NRAO (PMN) Surveys. VI. Source Catalog for the Equatorial Survey (-9.5 degrees $<$ delta $<$ +10.0 degrees). , 97:347, April 1995. doi: 10.1086/192146.

Y. Gupta, B. Ajithkumar, H. S. Kale, S. Nayak, S. Sabhapathy, S. Sureshkumar, R. V. Swami, J. N. Chengalur, S. K. Ghosh, C. H. Ishwara-Chandra, B. C. Joshi, N. Kanekar, D. V. Lal, and S. Roy. The upgraded GMRT: opening new windows on the radio Universe. *Current Science*, 113(4):707–714, August 2017. doi: 10.18520/cs/v113/i04/707-714.

J. P. Hamaker. Understanding radio polarimetry V. Making matrix self-calibration work: Processing of a simulated observation. *Astronomy and Astrophysics*, 456(1): 395–404, 2006. ISSN 00046361. doi: 10.1051/0004-6361:20065145.

J. P. Hamaker, J. D. Bregman, and R. J. Sault. Understanding radio polarimetry. I. Mathematical foundations. , 117:137–147, May 1996.

M. J. Hardcastle, J. H. Croston, and R. P. Kraft. A Chandra Study of Particle Acceleration in the Multiple Hot Spots of Nearby Radio Galaxies. , 669(2):893–904, November 2007. doi: 10.1086/521696.

Martin J Hardcastle. Jets, hotspots and lobes: what x-ray observations tell us about extragalactic radio sources. *Philosophical Transactions of the Royal Society A: Mathematical, Physical and Engineering Sciences*, 363(1837):2711–2727, 2005.

Martin J Hardcastle, DA Evans, and JH Croston. Hot and cold gas accretion and feedback in radio-loud active galaxies. *Monthly Notices of the Royal Astronomical Society*, 376(4):1849–1856, 2007a.

M.J. Hardcastle and J.H. Croston. Radio galaxies and feedback from agn jets. *New Astronomy Reviews*, 88:101539, 2020. ISSN 1387-6473. doi: https://doi.org/10.1016/j.newar.2020.101539. URL https://www.sciencedirect.com/science/article/pii/S1387647320300166.

MJ Hardcastle and Martin GH Krause. Numerical modelling of the lobes of radio galaxies in cluster environments. *Monthly Notices of the Royal Astronomical Society*, 430(1):174–196, 2013.

MJ Hardcastle, JH Croston, and RP Kraft. A chandra study of particle acceleration in the multiple hot spots of nearby radio galaxies. *The Astrophysical Journal*, 669 (2):893, 2007b.

Jeremy J Harwood, Tessa Vernstrom, and Andra Stroe. Unveiling the cause of hybrid morphology radio sources (hymors). *Monthly Notices of the Royal Astronomical Society*, 491(1):803–822, 2020.

Stephen E Healey, Roger W Romani, Gregory B Taylor, Elaine M Sadler, Roberto Ricci, Tara Murphy, James S Ulvestad, and Joshua N Winn. Crates: an all-sky survey of flat-spectrum radio sources. *The Astrophysical Journal Supplement Series*, 171(1):61, 2007.

Timothy M. Heckman and Philip N. Best. The coevolution of galaxies and supermassive black holes: Insights from surveys of the contemporary universe. *Annual Review of Astronomy and Astrophysics*, 52(1):589–660, August 2014. ISSN 1545-4282. doi: 10.1146/annurev-astro-081913-035722. URL http://dx.doi.org/10.1146/annurev-astro-081913-035722.

V. Heesen, V. Heesen, J. Croston, J. Croston, R. Morganti, R. Morganti, M. Hardcastle, A. Stewart, P. Best, J. Broderick, M. Brüggen, G. Brunetti, K. Chyży, J. Harwood, M. Haverkorn, K. Hess, K. Hess, H. Intema, M. Jamrozy, M. Kunert-Bajraszewska, J. McKean, J. McKean, E. Orr'u, H. Röttgering, T. Shimwell, A. Shulevski, G. White, G. White, E. Wilcots, and W. Williams. Lofar reveals the giant: A low-frequency radio continuum study of the outflow in the nearby fr i radio galaxy 3c 31. *Monthly Notices of the Royal Astronomical Society*, 474:5049–5067, 2017. doi: 10.1093/mnras/stx2869.

RG Hine and MS Longair. Optical spectra of 3cr radio galaxies. *Monthly Notices of the Royal Astronomical Society*, 188(1):111–130, 1979.

M. T. Hogan, A. C. Edge, J. Hlavacek-Larrondo, K. J. B. Grainge, S. L. Hamer, E. K. Mahony, H. R. Russell, A. C. Fabian, B. R. McNamara, and R. J. Wilman. A comprehensive study of the radio properties of brightest cluster galaxies. , 453(2): 1201–1222, October 2015. doi: 10.1093/mnras/stv1517.

J. A. Högbom. Aperture Synthesis with a Non-Regular Distribution of Interferometer Baselines. , 15:417, 1974.

David W. Hogg. Distance measures in cosmology. *arXiv e-prints*, art. astro-ph/9905116, May 1999. doi: 10.48550/arXiv.astro-ph/9905116.

Maya A Horton, Martin GH Krause, and Martin J Hardcastle. New mechanisms for multiple hotspot formation. *Monthly Notices of the Royal Astronomical Society*, 2023.

J. Ineson, J. H. Croston, M. J. Hardcastle, and B. Mingo. A representative survey of the dynamics and energetics of FR II radio galaxies. , 467(2):1586–1607, May 2017. doi: 10.1093/mnras/stx189.

CA Jackson and JV Wall. Radio galaxy spectra. *arXiv preprint astro-ph/0101367*, 2001.

Daniel C. Jacobs, James E. Aguirre, Aaron R. Parsons, Jonathan C. Pober, Richard F. Bradley, Chris L. Carilli, Nicole E. Gugliucci, Jason R. Manley, Carel van der Merwe, David F. Moore, and Chaitali R. Parashare. New 145 MHz Source Measurements by PAPER in the Southern Sky. , 734(2):L34, June 2011. doi: 10.1088/2041-8205/734/2/L34.

WJ Jaffe and GC Perola. Dynamical models of tailed radio sources in clusters of galaxies. *Astronomy and Astrophysics, Vol. 26, p. 423 (1973)*, 26:423, 1973.

Karl G Jansky. Electrical disturbances apparently of extraterrestrial origin. *Proceedings of the Institute of Radio Engineers*, 21(10):1387–1398, 1933.

M. Jarvis, R. Taylor, I. Agudo, J. R. Allison, R. P. Deane, B. Frank, N. Gupta, I. Heywood, N. Maddox, K. McAlpine, M. Santos, A. M. M. Scaife, M. Vaccari, J. T. L. Zwart, E. Adams, D. J. Bacon, A. J. Baker, B. A. Bassett, P. N. Best, R. Beswick, S. Blyth, M. L. Brown, M. Bruggen, M. Cluver, S. Colafrancesco, G. Cotter, C. Cress, R. Davé, C. Ferrari, M. J. Hardcastle, C. L. Hale, I. Harrison, P. W. Hatfield, H. R. Klockner, S. Kolwa, E. Malefahlo, T. Marubini, T. Mauch, K. Moodley, R. Morganti, R. P. Norris, J. A. Peters, I. Prandoni, M. Prescott, S. Oliver, N. Oozeer, H. J. A. Rottgering, N. Seymour, C. Simpson, O. Smirnov, and D. J. B. Smith. The MeerKAT International GHz Tiered Extragalactic Exploration (MIGHTEE) Survey. In *MeerKAT Science: On the Pathway to the SKA*, page 6, January 2016. doi: 10.22323/1.277.0006.

S. Johnston, M. Bailes, N. Bartel, C. Baugh, M. Bietenholz, C. Blake, R. Braun, J. Brown, S. Chatterjee, J. Darling, A. Deller, R. Dodson, P. G. Edwards, R. Ekers, S. Ellingsen, I. Feain, B. M. Gaensler, M. Haverkorn, G. Hobbs, A. Hopkins, C. Jackson, C. James, G. Joncas, V. Kaspi, V. Kilborn, B. Koribalski, R. Kothes, T. L. Landecker, E. Lenc, J. Lovell, J. P. Macquart, R. Manchester, D. Matthews, N. M. McClure-Griffiths, R. Norris, U. L. Pen, C. Phillips, C. Power, R. Protheroe,

E. Sadler, B. Schmidt, I. Stairs, L. Staveley-Smith, J. Stil, R. Taylor, S. Tingay, A. Tzioumis, M. Walker, J. Wall, and M. Wolleben. Science with the Australian Square Kilometre Array Pathfinder. , 24(4):174–188, December 2007. doi: 10.1071/AS07033.

J. Jonas. The MeerKAT SKA precursor telescope. In *Panoramic Radio Astronomy: Wide-field 1-2 GHz Research on Galaxy Evolution*, page 4, January 2009.

Justin L. Jonas. The MeerKAT radio telescope. *Proceedings of Science*, pages 25–27, 2016. ISSN 18248039.

T. W. Jones and F. N. Owen. Hot gas in elliptical galaxies and the formation of head-tail radio sources. , 234:818–824, December 1979. doi: 10.1086/157561.

Gyula "Josh" Jozsa and Simon Perkins. caracal-pipeline/equolver: Doing again, November 2021.

Christian R. Kaiser and Philip N. Best. Luminosity function, sizes and FR dichotomy of radio-loud AGN. , 381(4):1548–1560, November 2007. doi: 10.1111/j.1365-2966.2007.12350.x.

Ruta Kale and C. H. Ishwara-Chandra. Capture: a continuum imaging pipeline for the ugmrt. *Experimental Astronomy*, 51(1):95–108, October 2020. ISSN 1572-9508. doi: 10.1007/s10686-020-09677-6. URL `http://dx.doi.org/10.1007/s10686-020-09677-6`.

Anna D Kapińska, Ivan Terentev, Oiwei Ivy Wong, Stanislav S Shabala, Heinz Andernach, Lawrence Rudnick, Lucas Storer, Julie K Banfield, KylieW Willett, Franco De Gasperin, et al. Radio galaxy zoo: a search for hybrid morphology radio galaxies. *The Astronomical Journal*, 154(6):253, 2017.

N. S. Kardashev. Nonstationarity of Spectra of Young Sources of Nonthermal Radio Emission. , 6:317, December 1962.

K. I. Kellermann and I. I. K. Pauliny-Toth. Measurements of the flux density and spectra of discrete radio sources at centimeter wavelengths. IV. The observations at 10.7 GHz (2.8 cm). , 78:828–847, November 1973. doi: 10.1086/111489.

K. I. Kellermann, I. I. K. Pauliny-Toth, and P. J. S. Williams. The Spectra of Radio Sources in the Revised 3c Catalogue. , 157:1, July 1969. doi: 10.1086/150046.

J S Kenyon, O M Smirnov, T L Grobler, and S J Perkins. cubical – fast radio interferometric calibration suite exploiting complex optimization. *Monthly Notices of the Royal Astronomical Society*, 478(2):2399–2415, May 2018. ISSN 1365-2966. doi: 10.1093/mnras/sty1221. URL `http://dx.doi.org/10.1093/mnras/sty1221`.

Jonathan S Kenyon, Simon Perkins, and Oleg Smirnov. Quartical: Fast radio interferometric calibration. *Astrophysics Source Code Library*, pages ascl–2305, 2023.

I. Klamer, R. Subrahmanyan, and R. W. Hunstead. A binary system of tailed radio galaxies. , 351(1):101–109, June 2004. doi: 10.1111/j.1365-2966.2004.07757.x.

U Klein, K-H Mack, L Gregorini, and M Vigotti. Multi-frequency study of the b3-vla sample-iii. polarisation properties. *Astronomy & Astrophysics*, 406(2):579–592, 2003.

K. Knowles, W. D. Cotton, L. Rudnick, F. Camilo, S. Goedhart, R. Deane, M. Ramatsoku, M. F. Bietenholz, M. Brüggen, C. Button, H. Chen, J. O. Chibueze, T. E. Clarke, F. de Gasperin, R. Ianjamasimanana, G. I. G. Józsa, M. Hilton, K. C. Kesebonye, K. Kolokythas, R. C. Kraan-Korteweg, G. Lawrie, M. Lochner, S. I. Loubser, P. Marchegiani, N. Mhlahlo, and K. Moodley. The MeerKAT Galaxy Cluster Legacy Survey. I. Survey Overview and Highlights. , 657:A56, January 2022. doi: 10.1051/0004-6361/202141488.

S. S. Komissarov and S. A. E. G. Falle. The large-scale structure of FR-II radio sources. , 297(4):1087–1108, July 1998. doi: 10.1046/j.1365-8711.1998.01547.x.

C Konar, DJ Saikia, CH Ishwara-Chandra, and VK Kulkarni. Radio observations of a few giant sources. *Monthly Notices of the Royal Astronomical Society*, 355(3): 845–854, 2004.

C. Konar, D. Saikia, M. Jamrozy, J. M. Iucaa, Pune, India., Ncra, Tifr, J. University, and Poland. Spectral ages of giant radio sources. *arXiv: Cosmology and Nongalactic Astrophysics*, 2009.

P. P. Kronberg, R. Wielebinski, and D. A. Graham. VLA and 100-m telescope observations of two giant galaxies : 0634-20 and 3C 445 (2221-02). , 169:63–70, November 1986.

H. Kuehr, A. Witzel, I. I. K. Pauliny-Toth, and U. Nauber. A Catalogue of Extragalactic Radio Sources Having Flux Densities Greater than 1-JY at 5-GHZ. , 45: 367, September 1981.

Shobha Kumari and Sabyasachi Pal. Search for hybrid morphology radio galaxies from the first survey at 1400 mhz. *Monthly Notices of the Royal Astronomical Society*, 514(3):4290–4299, 2022.

Agnieszka Kuźmicz, Marek Jamrozy, Katarzyna Bronarska, Katarzyna Janda-Boczar, and D. J. Saikia. An Updated Catalog of Giant Radio Sources. , 238(1):9, September 2018. doi: 10.3847/1538-4365/aad9ff.

R Laing. Radio observation of hot spots. In *Hot Spots in Extragalactic Radio Sources: Proceedings of a Workshop Held at Ringberg Castle, Tegernsee, FRG, February 8–12, 1988*, pages 27–44. Springer, 2005.

R. A. Laing and A. H. Bridle. Relativistic jet models for two low-luminosity radio galaxies: evidence for backflow? , 424(2):1149–1169, August 2012. doi: 10.1111/j.1365-2966.2012.21297.x.

RA Laing and AH Bridle. Systematic properties of decelerating relativistic jets in low-luminosity radio galaxies. *Monthly Notices of the Royal Astronomical Society*, 437 (4):3405–3441, 2014.

RA Laing, AH Bridle, P Parma, L Feretti, Gabriele Giovannini, M Murgia, and RA Perley. Multifrequency vla observations of the fr i radio galaxy 3c 31: morphology, spectrum and magnetic field. *Monthly Notices of the Royal Astronomical Society*, 386(2):657–672, 2008.

Robert A Laing and AH Bridle. Dynamical models for jet deceleration in the radio galaxy 3c 31. *Monthly Notices of the Royal Astronomical Society*, 336(4):1161–1180, 2002.

Dharam Vir Lal and A. Pramesh Rao. 3C 129: The GMRT observations. , 420:491–499, June 2004. doi: 10.1051/0004-6361:20035777.

M. I. Large, B. Y. Mills, A. G. Little, D. F. Crawford, and J. M. Sutton. The Molonglo Reference Catalogue of radio sources. , 194:693–704, February 1981. doi: 10.1093/mnras/194.3.693.

J. P. Leahy and P. Parma. Multiple outbursts in radio galaxies. In Jacques Roland, Hilhne Sol, and Guy Pelletier, editors, *Extragalactic Radio Sources. From Beams to Jets*, pages 307–308, January 1992.

J. P. Leahy, A. R. S. Black, J. Dennett-Thorpe, M. J. Hardcastle, S. Komissarov, R. A. Perley, J. M. Riley, and P. A. G. Scheuer. A study of FRII radio galaxies with z<0.15 - II. High-resolution maps of 11 sources at 3.6 CM. , 291(1):20–53, October 1997. doi: 10.1093/mnras/291.1.20.

JP Leahy and AG Williams. The bridges of classical double radio sources. *Monthly Notices of the Royal Astronomical Society*, 210(4):929–951, 1984.

Michael J. Ledlow and Frazer N. Owen. 20 cm vla survey of abell clusters of galaxies. vi. radio/optical luminosity functions. *The Astronomical Journal*, 112:9, July 1996. ISSN 0004-6256. doi: 10.1086/117985. URL `http://dx.doi.org/10.1086/117985`.

Yen-Ting Lin, Bruce Partridge, JC Pober, Khadija El Bouchefry, Sarah Burke, Jonathan N Klein, Joseph W Coish, and Kevin M Huffenberger. Spectral energy distribution of radio sources in nearby clusters of galaxies: Implications for sunyaev–zel'dovich effect surveys. *The Astrophysical Journal*, 694(2):992, 2009.

Yen-Ting Lin, Hung-Jin Huang, and Yen-Chi Chen. An analysis framework for understanding the origin of nuclear activity in low-power radio galaxies. *The Astronomical Journal*, 155(5):188, 2018.

Malcolm S Longair. *High energy astrophysics*. Cambridge university press, 2011.

J. Machalski, M. Jamrozy, D. Univ., Ncra, and Tifr. A multifrequency study of giant radio sources – iii. dynamical age versus spectral age of the lobes of selected sources. *Monthly Notices of the Royal Astronomical Society*, 395:812–822, 2009. doi: 10.1111/j.1365-2966.2009.14516.x.

K. H. Mack, M. A. Prieto, G. Brunetti, and M. Orienti. Near-infrared/optical counterparts of hotspots in radio galaxies. , 392(2):705–717, January 2009. doi: 10.1111/j.1365-2966.2008.14081.x.

Juan P. Madrid, Marco Chiaberge, David Floyd, William B. Sparks, Duccio Macchetto, George K. Miley, David Axon, Alessandro Capetti, Christopher P. O'Dea, Stefi Baum, Eric Perlman, and Alice Quillen. Hubble Space Telescope Near-Infrared Snapshot Survey of 3CR Radio Source Counterparts at Low Redshift. , 164(2): 307–333, June 2006. doi: 10.1086/504480.

V H Mahatma, A Basu, M J Hardcastle, L K Morabito, and R J Van Weeren. A low frequency sub-arcsecond view of powerful radio galaxies in rich-cluster environments: 3C 34 and 3C 320. 16(February):1–16, 2023.

Vijay H. Mahatma, Martin J. Hardcastle, Judith H. Croston, Jeremy Harwood, Judith Ineson, and Javier Moldon. Investigating the spectral age problem with powerful radio galaxies. , 491(4):5015–5034, February 2020. doi: 10.1093/mnras/stz3396.

Andrea Mason, Philip Morrison, and Alberto C. Sadun. The radio rings of Hercules A. , 333(6174):640–642, June 1988. doi: 10.1038/333640a0.

F. Massaro, D. E. Harris, G. R. Tremblay, D. Axon, S. A. Baum, A. Capetti, M. Chiaberge, R. Gilli, G. Giovannini, P. Grandi, F. D. Macchetto, C. P. O'Dea, G. Risaliti, and W. Sparks. Chandra Observations of 3C Radio Sources with z $<$ 0.3: Nuclei, Diffuse Emission, Jets, and Hotspots. , 714(1):589–604, May 2010. doi: 10.1088/0004-637X/714/1/589.

J. P. McMullin, B. Waters, D. Schiebel, W. Young, and K. Golap. CASA Architecture and Applications. In R. A. Shaw, F. Hill, and D. J. Bell, editors, *Astronomical Data Analysis Software and Systems XVI*, volume 376 of *Astronomical Society of the Pacific Conference Series*, page 127, October 2007.

G. Migliori, M. Orienti, L. Coccato, G. Brunetti, F. D'Ammando, K. H. Mack, and M. A. Prieto. Particle acceleration in low-power hotspots: modelling the broad-band spectral energy distribution. , 495(2):1593–1607, June 2020. doi: 10.1093/mnras/staa1214.

GK Miley, GC Perola, PC VAN DER KRUIT, and H VAN DER LAAN. Active galaxies with radio trails in clusters. *Nature*, 237(5353):269–272, 1972.

B Mingo, J H Croston, M J Hardcastle, P N Best, K J Duncan, R Morganti, H J A Rottgering, J Sabater, T W Shimwell, W L Williams, M Brienza, G Gurkan, V H Mahatma, L K Morabito, I Prandoni, M Bondi, J Ineson, and S Mooney. Revisiting the Fanaroff–Riley dichotomy and radio-galaxy morphology with the LOFAR Two-Metre Sky Survey (LoTSS). *Monthly Notices of the Royal Astronomical Society*, 488(2):2701–2721, 07 2019. ISSN 0035-8711. doi: 10.1093/mnras/stz1901. URL `https://doi.org/10.1093/mnras/stz1901`.

B. Mingo, J. H. Croston, P. N. Best, K. J. Duncan, M. J. Hardcastle, R. Kondapally, I. Prandoni, J. Sabater, T. W. Shimwell, W. L. Williams, R. D. Baldi, M. Bonato, M. Bondi, P. Dabhade, G. Gürkan, J. Ineson, M. Magliocchetti, G. Miley, J. C. S. Pierce, and H. J. A. Röttgering. Accretion mode versus radio morphology in the LOFAR Deep Fields. , 511(3):3250–3271, April 2022. doi: 10.1093/mnras/stac140.

H. Miraghaei and P. Best. The nuclear properties and extended morphologies of powerful radio galaxies: the roles of host galaxy and environment. *Monthly Notices of the Royal Astronomical Society*, 466:4346–4363, 2017. doi: 10.1093/mnras/stx007.

Valentina Missaglia, Matteo Murgia, Francesco Massaro, Alessandro Paggi, Ana Jimenez-Gallardo, William Forman, Ralph Kraft, and Barbara Balmaverde. High frequency radio imaging of 3cr 403.1 with the sardinia radio telescope, 07 2022.

M. Murgia. Laurea thesis, 1996.

M. Murgia, C. Fanti, R. Fanti, L. Gregorini, U. Klein, K. H. Mack, and M. Vigotti. Synchrotron spectra and ages of compact steep spectrum radio sources. , 345:769–777, May 1999.

M Murgia, C Fanti, R Fanti, L Gregorini, U Klein, K-H Mack, and M Vigotti. Synchrotron spectra and ages of compact steep spectrum radio sources. *New Astronomy Reviews*, 46(2-7):307–311, 2002.

Matteo Murgia, P Parma, K-H Mack, HR De Ruiter, R Fanti, F Govoni, A Tarchi, S Giacintucci, and M Markevitch. Dying radio galaxies in clusters. *Astronomy & Astrophysics*, 526:A148, 2011.

Tara Murphy, Elaine M Sadler, Ronald D Ekers, Marcella Massardi, Paul J Hancock, Elizabeth Mahony, Roberto Ricci, Sarah Burke-Spolaor, Mark Calabretta, Rajan Chhetri, et al. The australia telescope 20 ghz survey: the source catalogue. *Monthly Notices of the Royal Astronomical Society*, 402(4):2403–2423, 2010.

Claire E. Murray, Snežana Stanimirović, Carl Heiles, John M. Dickey, N. M. McClure-Griffiths, M. Y. Lee, W. M. Goss, and Nicholas Killerby-Smith. The MACH HI Absorption Survey. I. Physical Conditions of Cold Atomic Gas outside of the Galactic Plane. , 256(2):37, October 2021. doi: 10.3847/1538-4365/ac0f0b.

Rendong Nan. Five hundred meter aperture spherical radio telescope (fast). *Science in China series G*, 49:129–148, 2006.

Ramesh Narayan and Insu Yi. Advection-dominated accretion: Underfed black holes and neutron stars. *arXiv preprint astro-ph/9411059*, 1994.

Chris Nolting, TW Jones, Brian J O'Neill, and PJ Mendygral. Interactions between radio galaxies and cluster shocks. i. jet axes aligned with shock normals. *The Astrophysical Journal*, 876(2):154, 2019.

J. E. Noordam and O. M. Smirnov. The MeqTrees software system and its use for third-generation calibration of radio interferometers. *Astronomy and Astrophysics*, 524(2):1–16, 2010. ISSN 00046361. doi: 10.1051/0004-6361/201015013.

Ray P. Norris, A. M. Hopkins, J. Afonso, S. Brown, J. J. Condon, L. Dunne, I. Feain, R. Hollow, M. Jarvis, M. Johnston-Hollitt, E. Lenc, E. Middelberg, P. Padovani, I. Prandoni, L. Rudnick, N. Seymour, G. Umana, H. Andernach, D. M. Alexander, P. N. Appleton, D. Bacon, J. Banfield, W. Becker, M. J.I. Brown, P. Ciliegi, C. Jackson, S. Eales, A. C. Edge, B. M. Gaensler, G. Giovannini, C. A. Hales, P. Hancock, M. T. Huynh, E. Ibar, R. J. Ivison, R. Kennicutt, Amy E. Kimball, A. M. Koekemoer, B. S. Koribalski, R. Lpez-Snchez, M. Y. Mao, T. Murphy, H. Messias, K. A. Pimbblet, A. Raccanelli, K. E. Randall, T. H. Reiprich, I. G. Roseboom, H. Rttgering, D. J. Saikia, R. G. Sharp, O. B. Slee, Ian Smail, M. A. Thompson, J. S. Urquhart, J. V. Wall, and G. B. Zhao. EMU: Evolutionary map of the universe. *Publications of the Astronomical Society of Australia*, 28(3):215–248, 2011. ISSN 13233580. doi: 10.1071/AS11021.

C. P. O'Dea and F. N. Owen. Multifrequency VLA Observations of the Prototypical Narrow-Angle Tail Radio Source, NGC 1265. , 301:841, February 1986. doi: 10.1086/163948.

A. R. Offringa, A. G. de Bruyn, M. Biehl, S. Zaroubi, G. Bernardi, and V. N. Pandey. Post-correlation radio frequency interference classification methods. *Monthly Notices of the Royal Astronomical Society*, 405(1):155–167, 2010. ISSN 00358711. doi: 10.1111/j.1365-2966.2010.16471.x.

A. R. Offringa, J. J. Van De Gronde, and J. B.T.M. Roerdink. A morphological algorithm for improving radio-frequency interference detection. *Astronomy and Astrophysics*, 539(March), 2012. ISSN 00046361. doi: 10.1051/0004-6361/201118497.

AR Offringa and O Smirnov. An optimized algorithm for multiscale wideband deconvolution of radio astronomical images. *Monthly Notices of the Royal Astronomical Society*, 471(1):301–316, 2017.

M. Orienti, M. A. Prieto, G. Brunetti, K. H. Mack, F. Massaro, and D. E. Harris. Complex particle acceleration processes in the hotspots of 3C 105 and 3C 445. , 419 (3):2338–2348, January 2012. doi: 10.1111/j.1365-2966.2011.19882.x.

M. Orienti, G. Migliori, G. Brunetti, H. Nagai, F. D'Ammando, K. H. Mack, and M. A. Prieto. Jansky VLA observations of synchrotron emitting optical hotspots of 3C 227 and 3C 445 radio galaxies. , 494(2):2244–2253, May 2020. doi: 10.1093/mnras/staa777.

Monica Orienti and Daniele Dallacasa. Are young radio sources in equipartition? *Astronomy & Astrophysics*, 487(3):885–894, 2008.

F. N. Owen and M. J. Ledlow. The FRI/II Break and the Bivariate Luminosity Function in Abell Clusters of Galaxies. In Geoffrey V. Bicknell, Michael A. Dopita, and Peter J.

Quinn, editors, *The Physics of Active Galaxies*, volume 54 of *Astronomical Society of the Pacific Conference Series*, page 319, January 1994.

F. N. Owen and L. Rudnick. Radio sources with wide-angle tails in Abell clusters of galaxies. , 205:L1–L4, April 1976. doi: 10.1086/182077.

Christopher P O'Dea and Stefi A Baum. Wide-angle-tail (wat) radio sources. *Galaxies*, 11(3):67, 2023.

AG Pacholczyk. Radio astrophysics wh freeman and company. *San Francisco*, 1970.

Sabyasachi Pal and Shobha Kumari. A new catalog of head-tail radio galaxies from LoTSS DR1. *Journal of Astrophysics and Astronomy*, 44(1):17, June 2023. doi: 10.1007/s12036-022-09892-x.

P Parma, M Murgia, R Morganti, A Capetti, HR De Ruiter, and R Fanti. Radiative ages in a representative sample of low luminosity radio galaxies. *arXiv preprint astro-ph/9812413*, 1998.

P Parma, M Murgia, HR De Ruiter, and R Fanti. The lives of fr i radio galaxies. *New Astronomy Reviews*, 46(2-7):313–325, 2002.

P Parma, M Murgia, HR De Ruiter, R Fanti, K-H Mack, and F Govoni. In search of dying radio sources in the local universe. *Astronomy & Astrophysics*, 470(3):875–888, 2007.

I. I. K. Pauliny-Toth, C. M. Wade, and D. S. Heeschen. Positions and Flux Densities of Radio Sources. , 13:65, May 1966. doi: 10.1086/190137.

IIK Pauliny-Toth, KI Kellermann, MM Davis, EB Fomalont, and DB Shaffer. The nrao 5-ghz radio source survey. ii. the 140-ft" strong"," intermediate", and" deep" source surveys. *Astronomical Journal, Vol. 77, p. 265-284*, 77:265–284, 1972.

IIK Pauliny-Toth, A Witzel, E Preuss, H Kühr, KI Kellermann, EB Fomalont, and MM Davis. The 5 ghz strong source surveys. iv-survey of the area between declination 35 and 70 degrees and summary of source counts, spectra and optical identifications. *Astronomical Journal, vol. 83, May 1978, p. 451-474.*, 83:451–474, 1978.

T. J. Pearson and A. C. S. Readhead. Image Formation by Self-Calibration in Radio Astronomy. , 22:97–130, January 1984. doi: 10.1146/annurev.aa.22.090184.000525.

RA Perley, CJ Chandler, BJ Butler, and JM Wrobel. The expanded very large array: a new telescope for new science. *The Astrophysical Journal Letters*, 739(1):L1, 2011.

Eric S. Perlman, Markos Georganopoulos, Emily M. May, and Demosthenes Kazanas. Chandra Observations of the Radio Galaxy 3C 445 and the Hot Spot X-Ray Emission Mechanism. , 708(1):1–8, January 2010. doi: 10.1088/0004-637X/708/1/1.

Manel Perucho, José María Martí, Robert A Laing, and Philip E Hardee. On the deceleration of fanaroff–riley class i jets: mass loading by stellar winds. *Monthly Notices of the Royal Astronomical Society*, 441(2):1488–1503, 2014.

Manel Perucho, Jose López-Miralles, Nectaria A. B. Gizani, José María Martí, and Bia Boccardi. On the large scale morphology of Hercules A: destabilized hot jets? , 523 (3):3583–3594, August 2023. doi: 10.1093/mnras/stad1640.

R. Piffaretti, M. Arnaud, G. W. Pratt, E. Pointecouteau, and J. B. Melin. The MCXC: a meta-catalogue of x-ray detected clusters of galaxies. , 534:A109, October 2011. doi: 10.1051/0004-6361/201015377.

J. D. H. Pilkington and J. F. Scott. A survey of radio sources between declinations 20° and 40°. , 69:183, January 1965.

Marc Postman and Tod R. Lauer. Brightest Cluster Galaxies as Standard Candles. , 440:28, February 1995. doi: 10.1086/175245.

M. Almudena Prieto, Gianfranco Brunetti, and Karl-Heinz Mack. Particle Accelerators in the Hot Spots of Radio Galaxy 3C 445, Imaged with the VLT. *Science*, 298(5591): 193–195, October 2002. doi: 10.1126/science.1075990.

Mpati Ramatsoku, M Murgia, V Vacca, P Serra, Sphesihle Makhathini, F Govoni, O Smirnov, LAL Andati, E De Blok, GIG Józsa, et al. Collimated synchrotron threads linking the radio lobes of eso 137-006. *Astronomy & Astrophysics*, 636:L1, 2020.

Zara Randriamanakoto. A dying radio AGN in the ELAIS-N1 field. *Proceedings of the International Astronomical Union*, 15(356):342–344, 2019. ISSN 17439221. doi: 10.1017/S1743921320003294.

Urvashi Rau and Tim J Cornwell. A multi-scale multi-frequency deconvolution algorithm for synthesis imaging in radio interferometry. *Astronomy & Astrophysics*, 532: A71, 2011.

Urvashi Rau, Sanjay Bhatnagar, Maxim A. Voronkov, and Tim J. Cornwell. Advances in calibration and imaging techniques in radio interferometry. *Proceedings of the IEEE*, 97(8):1472–1481, 2009. ISSN 00189219. doi: 10.1109/JPROC.2009.2014853.

Travis A. Rector, John T. Stocke, and Erica Ellingson. Quasar Radio Morphology and Clustering Environment at z~1/2. , 110:1492, October 1995. doi: 10.1086/117622.

MJ Rees, MC Begelman, RD Blandford, and ES Phinney. Ion-supported tori and the origin of radio jets. *Nature*, 295(5844):17–21, 1982.

R. Ricci, I. Prandoni, C. Gruppioni, R. J. Sault, and G. de Zotti. High-frequency radio observations of the Kühr sample and the epoch-dependent luminosity function of flat-spectrum quasars. , 445(2):465–469, January 2006. doi: 10.1051/0004-6361:20053797.

JW Rich, WJG De Blok, TJ Cornwell, Elias Brinks, Fabian Walter, Ioannis Bagetakos, and Robert C Kennicutt. Multi-scale clean: A comparison of its performance against classical clean on galaxies using things. *The Astronomical Journal*, 136(6):2897, 2008.

JM Riley. Observations of 3c 272.1 at 2.7 and 5.0 ghz. *Monthly Notices of the Royal Astronomical Society, Vol. 157, p. 349-375 (1972)*, 157:349–375, 1972.

Lawrence Rudnick. Observing magnetic fields on large scales. *arXiv preprint astro-ph/0412629*, 2004.

Lawrence Rudnick. Radio Galaxy Classification : Tags , Not Boxes. 2021.

Lawrence Rudnick, M Brüggen, Gianfranco Brunetti, WD Cotton, William Forman, Thomas W Jones, Chris Nolting, Gerrit Schellenberger, and Reinout van Weeren. Intracluster magnetic filaments and an encounter with a radio jet. *The Astrophysical Journal*, 935(2):168, 2022.

James Runge and Haojing Yan. "Red" but Not "Dead": Actively Star-forming Brightest Cluster Galaxies at Low Redshifts. , 853(1):47, January 2018. doi: 10.3847/1538-4357/aaa020.

George B Rybicki and Alan P Lightman. *Radiative processes in astrophysics*. John Wiley & Sons, 1991.

M Ryle and MD Windram. The radio emission from galaxies in the perseus cluster. *Monthly Notices of the Royal Astronomical Society*, 138(1):1–21, 1968.

Alberto C Sadun and Philip Morrison. Hercules a (3c 348): Phenomenology of an unusual active galactic nucleus. *The Astronomical Journal*, 123(5):2312, 2002.

DJ Saikia. Jets in radio galaxies and quasars: an observational perspective. *Journal of Astrophysics and Astronomy*, 43(2):97, 2022.

DJ Saikia and M Jamrozy. Recurrent activity in active galactic nuclei. *arXiv preprint arXiv:1002.1841*, 2010.

R. M. Sambruna, J. N. Reeves, and V. Braito. The Remarkable X-Ray Spectrum of the Broad-Line Radio Galaxy 3C 445. , 665(2):1030–1037, August 2007. doi: 10.1086/519306.

Lakshmi Saripalli. Understanding the fanaroff–riley radio galaxy classification. *The Astronomical Journal*, 144(3):85, 2012.

Lakshmi Saripalli, Ravi Subrahmanyan, Tanmoy Laskar, and Anton Koekemoer. Restarting engine in an x-shaped radio galaxy. *arXiv preprint arXiv:0806.3518*, 2008.

PAG Scheuer, DS Heeschen, and CM Wade. Extragalactic radio sources. In *IAU Symp*, volume 97, page 163, 1982.

Arno P. Schoenmakers, A. G. de Bruyn, H. J. A. Röttgering, H. van der Laan, and C. R. Kaiser. Radio galaxies with a 'double-double morphology' - I. Analysis of the radio properties and evidence for interrupted activity in active galactic nuclei. , 315 (2):371–380, June 2000. doi: 10.1046/j.1365-8711.2000.03430.x.

Arno P Schoenmakers, AG De Bruyn, HJA Röttgering, and H Van Der Laan. Radio galaxies with a 'double-double'morphology—iii. the case of b 1834+ 620. *Monthly Notices of the Royal Astronomical Society*, 315(2):395–406, 2000.

Precious K. Sejake, Sarah V. White, Ian Heywood, Kshitij Thorat, Hertzog L. Bester, Sphesihle Makhathini, and Bernie Fanaroff. MeerKAT follow-up of enigmatic GLEAM 4-Jy (G4Jy) sources. , 518(3):4290–4309, January 2023. doi: 10.1093/mnras/stac3393.

Nikolai I Shakura and Rashid Alievich Sunyaev. Black holes in binary systems. observational appearance. *Astronomy and Astrophysics, Vol. 24, p. 337-355*, 24:337–355, 1973.

TW Shimwell, HJA Röttgering, Philip N Best, WL Williams, TJ Dijkema, Francesco de Gasperin, MJ Hardcastle, GH Heald, DN Hoang, Andreas Horneffer, et al. The lofar two-metre sky survey-i. survey description and preliminary data release. *Astronomy & Astrophysics*, 598:A104, 2017.

O. B. Slee. Radio sources observed with the Culgoora circular array. *Australian Journal of Physics*, 48:143–186, January 1995. doi: 10.1071/PH950143.

O M Smirnov. Revisiting the radio interferometer measurement equation. 106, 2011a.

O M Smirnov. Revisiting the radio interferometer measurement equation II . Calibration and direction-dependent effects. 107, 2011b.

O. M. Smirnov and A. G. De Bruyn. MeqTrees and direction-dependent effects. *2011 30th URSI General Assembly and Scientific Symposium, URSIGASS 2011*, pages 1–4, 2011. doi: 10.1109/URSIGASS.2011.6051222.

O. M. Smirnov and C. Tasse. Radio interferometric gain calibration as a complex optimization problem. *Monthly Notices of the Royal Astronomical Society*, 449(3): 2668–2684, 2015. ISSN 0035-8711. doi: 10.1093/mnras/stv418.

Anthony G. Smith, Andrew M. Hopkins, Richard W. Hunstead, and Kevin A. Pimbblet. Multiscale probability mapping: groups, clusters and an algorithmic search for filaments in SDSS. , 422(1):25–43, May 2012. doi: 10.1111/j.1365-2966.2012.20400.x.

Eric P. Smith and T. M. Heckman. Multicolor Surface Photometry of Powerful Radio Galaxies. I. Observations and Data Reduction. , 69:365, March 1989. doi: 10.1086/191319.

B. W. Sohn, U. Klein, and K.-H. Mack. The spectral-curvature parameter: An alternative tool for the analysis of synchrotron spectra. *Astronomy and Astrophysics*, 2003. doi: 10.1051/0004-6361:20030435.

G. Speranza, B. Balmaverde, A. Capetti, F. Massaro, G. Tremblay, A. Marconi, G. Venturi, M. Chiaberge, R. D. Baldi, S. Baum, P. Grandi, E. T. Meyer, C. O'Dea, W. Sparks, B. A. Terrazas, and E. Torresi. The MURALES survey. IV. Searching for nuclear outflows in 3C radio galaxies at $z < 0.3$ with MUSE observations. , 653: A150, September 2021. doi: 10.1051/0004-6361/202140686.

S Srikanth, R Norrod, L King, and D Parker. An overview of the green bank telescope. In *IEEE Antennas and Propagation Society International Symposium. 1999 Digest. Held in conjunction with: USNC/URSI National Radio Science Meeting (Cat. No. 99CH37010)*, volume 3, pages 1548–1551. IEEE, 1999.

Andra Stroe, Victoria Catlett, Jeremy J Harwood, Tessa Vernstrom, and Beatriz Mingo. The host galaxies of hybrid morphology radio sources. *The Astrophysical Journal*, 941(2):136, 2022.

M. A. Stull. Flux densities of radio galaxies at 8000 MHz. , 76:1–4, February 1971. doi: 10.1086/111073.

Govind Swarup. Giant metrewave radio telescope (GMRT). In T. J. Cornwell and R. A. Perley, editors, *IAU Colloq. 131: Radio Interferometry. Theory, Techniques, and Applications*, volume 19 of *Astronomical Society of the Pacific Conference Series*, pages 376–380, January 1991.

CN Tadhunter, R Morganti, A Robinson, R Dickson, M Villar-Martin, and RAE Fosbury. The nature of the optical-radio correlations for powerful radio galaxies. *Monthly Notices of the Royal Astronomical Society*, 298(4):1035–1047, 1998.

Greg B Taylor, Chris Luke Carilli, and Richard A Perley. Synthesis imaging in radio astronomy ii. *Synthesis Imaging in Radio Astronomy II*, 180, 1999.

A. Richard Thompson, James M. Moran, and George W. Swenson Jr. *Interferometry and Synthesis in Radio Astronomy.* Wiley, New York, 2nd edition, 2001. ISBN 978-0471254928.

R Timmerman, RJ van Weeren, JR Callingham, WD Cotton, R Perley, LK Morabito, NAB Gizani, AH Bridle, CP O'Dea, SA Baum, et al. Origin of the ring structures in hercules a-sub-arcsecond 144 mhz to 7 ghz observations. *Astronomy & Astrophysics*, 658:A5, 2022.

SJ Tingay, PJ Hancock, RB Wayth, H Intema, P Jagannathan, and K Mooley. A multi-resolution, multi-epoch low radio frequency survey of the kepler k2 mission campaign 1 field. *The Astronomical Journal*, 152(4):82, 2016.

R. Turner and S. Shabala. Energetics and lifetimes of local radio active galactic nuclei. *The Astrophysical Journal*, 806, 2015. doi: 10.1088/0004-637X/806/1/59.

E Valtaoja. Multiple hotspots in radio galaxies. *Astronomy and Astrophysics (ISSN 0004-6361), vol. 140, no. 1, Nov. 1984, p. 148-154.*, 140:148–154, 1984.

M. P. van Haarlem, M. W. Wise, A. W. Gunst, G. Heald, J. P. McKean, J. W. T. Hessels, A. G. de Bruyn, R. Nijboer, J. Swinbank, R. Fallows, M. Brentjens, A. Nelles, R. Beck, H. Falcke, R. Fender, J. Hörandel, L. V. E. Koopmans, G. Mann, G. Miley, H. Röttgering, B. W. Stappers, R. A. M. J. Wijers, S. Zaroubi, M. van den Akker, A. Alexov, J. Anderson, K. Anderson, A. van Ardenne, M. Arts, A. Asgekar, I. M. Avruch, F. Batejat, L. Bähren, M. E. Bell, M. R. Bell, I. van Bemmel, P. Bennema, M. J. Bentum, G. Bernardi, P. Best, L. Bîrzan, A. Bonafede, A. J. Boonstra,

and R. Braun. LOFAR: The LOw-Frequency ARray. , 556:A2, August 2013. doi: 10.1051/0004-6361/201220873.

Velibor Velović, William D Cotton, Miroslav D Filipović, Ray P Norris, Luke A Barnes, and James J Condon. Meerkat view of the dancing ghosts – peculiar galaxy pair pks 2130538 in abell 3785. *Monthly Notices of the Royal Astronomical Society*, 523 (2):1933–1945, May 2023. ISSN 1365-2966. doi: 10.1093/mnras/stad1307. URL `http://dx.doi.org/10.1093/mnras/stad1307`.

Tiziana Venturi, Simona Giacintucci, Paola Merluzzi, Sandro Bardelli, Gianni Busarello, D Dallacasa, Sinenhlanhla P Sikhosana, Josh Marvil, Oleg Smirnov, Herve Bourdin, et al. Radio footprints of a minor merger in the shapley supercluster: From supercluster down to galactic scales. *Astronomy & Astrophysics*, 660:A81, 2022.

J. V. Wall, A. J. Shimmins, and J. K. Merkelijn. The Parkes 2700 MHz Survey. Catalogues for the ±4 declination zone and for the selected regions. *Australian Journal of Physics Astrophysical Supplement*, 19:1–68, January 1971.

Richard L. White and Robert H. Becker. A New Catalog of 30,239 1.4 GHz Sources. , 79:331, April 1992. doi: 10.1086/191656.

Sarah V. White, Thomas M. O. Franzen, Chris J. Riseley, O. Ivy Wong, Anna D. Kapińska, Natasha Hurley-Walker, Joseph R. Callingham, Kshitij Thorat, Chen Wu, Paul Hancock, Richard W. Hunstead, Nick Seymour, Jesse Swan, Randall Wayth, John Morgan, Rajan Chhetri, Carole Jackson, Stuart Weston, Martin Bell, Bi-Qing For, B. M. Gaensler, Melanie Johnston-Hollitt, André Offringa, and Lister Staveley-Smith. The GLEAM 4-Jy (G4Jy) Sample: I. Definition and the catalogue. , 37:e018, June 2020a. doi: 10.1017/pasa.2020.9.

Sarah V. White, Thomas M. O. Franzen, Chris J. Riseley, O. Ivy Wong, Anna D. Kapińska, Natasha Hurley-Walker, Joseph R. Callingham, Kshitij Thorat, Chen Wu, Paul Hancock, Richard W. Hunstead, Nick Seymour, Jesse Swan, Randall Wayth, John Morgan, Rajan Chhetri, Carole Jackson, Stuart Weston, Martin Bell, B. M. Gaensler, Melanie Johnston-Hollitt, André Offringa, and Lister Staveley-Smith. The GLEAM 4-Jy (G4Jy) Sample: II. Host galaxy identification for individual sources. , 37:e017, June 2020b. doi: 10.1017/pasa.2020.10.

Paul J Wiita et al. Hybrid morphology radio sources and the fanaroff–riley dichotomy. *New Astronomy Reviews*, 46(2-7):357–360, 2002.

AG Williams. Numerical simulations of radio source structures. *The Observatory*, 105: 224, 1985.

B. J. Wills. Accurate Spectra of 300 Radio Sources from the Parked Catalogue: Observational Results. *Australian Journal of Physics Astrophysical Supplement*, 38:1, November 1975.

A. Witzel, P. Veron, and M. P. Veron. A Statistically Complete Sample of Radio-Sources at 1400 MHz. , 11:171, March 1971.

A. Wright and R. Otrupcek. Parkes Catalog, 1990, Australia telescope national facility. *PKS Catalog (1990*, page 0, January 1990.

ZS Yuan, JL Han, and ZL Wen. Vizier online data catalog: Brightest cluster galaxies radio luminosity (yuan+, 2016). *VizieR Online Data Catalog*, pages J–MNRAS, 2017.

F Yusef-Zadeh, RG Arendt, and M Wardle. Populations of magnetized filaments in the intracluster medium and the galactic center. *The Astrophysical Journal Letters*, 939(2):L21, 2022.

John ZuHone, Kristian Ehlert, Rainer Weinberger, and Christoph Pfrommer. Turning agn bubbles into radio relics with sloshing: modeling cr transport with realistic physics. *Galaxies*, 9(4):91, 2021.